Development and optimisation of a process for the production of target molecules through the hydrogenation of CO2 using renewable hydrogen

Laura Elizabeth Duran Martinez

Normandie Université

INSA INSTITUT NATIONAL DES SCIENCES APPLIQUÉES ROUEN NORMANDIE

THÈSE

Pour obtenir le diplôme de doctorat

Spécialité **GENIE DES PROCEDES**

Préparée au sein de l'**INSA Rouen Normandie**

Développement et optimisation d'un procédé de production de molécules d'intérêt par hydrogénation du CO2 à partir d'hydrogène renouvelable

Présentée et soutenue par

LAURA ELIZABETH DURAN MARTINEZ

Thèse soutenue le 09/10/2024

devant le jury composé de :

MME ISABELLE POLAERT	PROFESSEUR DES UNIVERSITÉS - INSA Rouen Normandie (INSA)	Directeur de thèse
M. JEAN-MARC COMMENGE	PROFESSEUR DES UNIVERSITÉS - Université de Lorraine	Président du jury
M. ALAIN LEDOUX	MAITRE DE CONFERENCES DES UNIVERSITES HDR - INSA de Rouen Normandie	Membre
MME ISABELLE PITAULT	CHARGÉ DE RECHERCHE HDR - Université Claude Bernard Lyon 1	Membre
MME ANNE-MARIE BILLET	PROFESSEUR DES UNIVERSITÉS - INP ENSIACET, Toulouse	Rapporteur
M. HUBERT MONNIER	CHERCHEUR HDR - INRS, Vandoeuvre lès Nancy	Rapporteur

Thèse dirigée par **ISABELLE POLAERT** (LABORATOIRE DE SECURITE DES PROCEDES CHIMIQUES)

ED 591 PSIME

LSPC Laboratoire de sécurité des procédés chimiques

La vida continúa fluyendo como un río,
mas sin ti, su curso se siente distinto.
Años que nunca podrán regresar,
personas y momentos que no volverán.

Pero los recuerdos fieles quedarán,
como estrellas que siempre brillarán.
Me enseñaste a ser fuerte, a permanecer,
a luchar incluso cuando quise ceder.

Tu voz en mi alma vibra y resuena,
tu amor en mi pecho aún se despliega.
En mi vida fuiste mi guía, mi sostén y alegría,
mi consejera en mis travesías.

En mi corazón tu esencia está,
allí, por siempre, permanecerá.

¡Gracias mami!

¡Siempre te amaré!

Acknowledgements

As I close this chapter of my academic life, I want to express my gratitude to all the people who, in one way or another, contributed to the completion of this doctoral thesis.

First and foremost, I want to thank the One who guided me to this program of study: the Alpha and the Omega, my sustainer, who has always been there. Without Him, this would have been impossible for me.

I extend my heartfelt thanks to my thesis supervisor, Prof. Isabelle Polaert, for her support, collaboration, knowledge, and guidance, which were crucial to bringing this research to its conclusion and allowing me to grow academically and personally.

I sincerely express my deep gratitude to CR HDR Isabelle Pitault, for her unwavering support and guidance throughout this research. Thank you so much for your time, active listening, rigour, patience, constructive criticism, pedagogical insights, and respect. Your support was essential to the successful completion of this work.

I would like to thank Prof. Anne-Marie BILLET from the Laboratoire de Génie Chimique Toulouse-INP and HDR researcher Hubert MONNIER from INRS for their interest in this work and their contributions as reviewers. I would also like to acknowledge the valuable contributions of Prof. Jean-Marc Commenge from the Laboratoire Réactions et Génie des Procédés, ENSIC, Université de Lorraine, who chaired the jury, and MC HDR Alain LEDOUX from LSPC for serving as a jury member.

I am grateful to MESCYT for allowing me to develop professionally beyond borders and for funding this thesis. I am thankful to INSA Rouen Normandie and the Laboratoire de Sécurité des Procédés Chimiques (LSPC) for welcoming me and providing the facilities necessary to carry out this research.

I also express my gratitude to the person who encouraged me to apply to this program, Rosy Valdez, as well as Leonela Martes for facilitating the communication for the interview. My thanks extend to my colleagues and friends at LSPC and Caliope: Gabriela, Patricia, Leonela, Randal, Minda, Alejandra, Gian, Yamily, for creating a pleasant working environment and always being willing to share their knowledge and experiences. The camaraderie and mutual support we shared were essential in overcoming the challenges along the way. Thank you for your empathy.

I would like to acknowledge the permanent staff at LSPC, particularly Maria Pereira, Bruno Daronat, Sylvie Poubelle, and Christine Devouge Boyer, whose support was instrumental in the completion of this research.

There are no words to express my gratitude to the Durán Martínez family, Manuel, Angela, Adoni, Wandy, Nissy, Ambar—for your unwavering trust, unconditional support, and constant presence in my life. Through my highs and lows, doubts and certainties, you have been fundamental in helping me persevere through difficulties until the end. Thank you for encouraging me. Alexandra Martínez, Daniel Martínez, and Brenda Martínez, thank you for your calls. Thank you to the Martínez Álvarez and Durán Durán families for believing in me. Thank you, Ignacia Jiménez, Sonja Boeker and Mariana Torres. Amor Eterno and ERM, your support was essential.

Table of Contents

Acknowledgements ..... **iv**

Table of Contents ..... **vi**

List of Figures ..... **x**

List of Tables ..... **xx**

Nomenclature ..... **xxiii**

Abstract ..... **xxvii**

Résumé ..... **xxviii**

General Introduction **1**

References 7

1. CO_2 hydrogenation products and processes: State of the Art **10**

1.1. The products of CO_2 hydrogenation **10**

1.2. Methane, methanol, and dimethyl ether synthesis description **14**

1.2.1. Methane synthesis 14

1.2.2. Methanol synthesis 14

1.2.3. Dimethyl ether (DME) synthesis 15

1.3. Thermodynamic study **20**

1.3.1. Methane synthesis 21

1.3.2. Methanol synthesis 22

1.3.3. DME synthesis 23

1.4. Catalysts for CO_2 hydrogenation **27**

1.4.1. Methane synthesis 27

1.4.2. Methanol synthesis 29

1.4.3. DME synthesis 33

1.5. Reaction mechanisms **37**

1.5.1. Methane synthesis 37

1.5.2. Methanol synthesis 38

1.5.3. DME synthesis 40

1.6. Kinetic modelling **43**

1.7. CO_2 hydrogenation reactors **51**

1.7.1. Laboratory scale 51

1.7.2. Industrial scale 68

1.8. Process simulations 77
1.8.1. Methanol synthesis 77
1.8.2. DME synthesis 84
1.9. Conclusions **90**
1.10. References **91**
2. Experimental DME synthesis **123**
2.1. Materials **123**
2.2. Installation **125**
2.2.1. Experimental set-up 125
2.2.2. Analytic device 126
2.3. Procedure for one experiment **127**
2.3.1. Reactor preparation 127
2.3.2. Leak test 127
2.3.3. Gas chromatography calibration 128
2.3.4. Catalyst reduction 130
2.3.5. Operating conditions 131
2.3.6. Experimental procedure 132
2.4. Component mass balance **133**
2.5. Catalyst screening **136**
2.5.1. Performance of CZA on methanol synthesis 136
2.5.2. Performance of catalyst mixtures, CZA-zeolite 137
2.6. Catalytic tests for kinetics **144**
2.6.1. Thermodynamics of reaction 144
2.6.2. Experimental results and discussion 148
2.7. Conclusions **161**
2.8. References **163**
3. Kinetic Model **166**
3.1. Reactions and reaction rates **166**
3.2. Transport phenomena **169**
3.2.1. External transfer limitations 169
3.2.2. Internal transfer limitation 172
3.3. Reactor modelling **174**
3.3.1. Preliminary considerations 174
3.3.2. Model equations 178
3.3.3. Parameter estimation algorithm 181

3.3.4. Numerical solution approach 184
3.4. Results of kinetic parameter estimate 185
3.4.1. Initial values 185
3.4.2. Kinetics of methanol synthesis 186
3.4.3. Kinetics of dimethyl-ether synthesis 187
3.4.4. Evaluation of model accuracy 196
3.5. Conclusions 201
3.6. References 202
4. Optimal Temperature Profile 206
4.1. Introduction 206
4.2. Reminder of the OTP principle on one reversible first-order reaction 207
4.3. Adopted approach 213
4.3.1. Study of a single reversible reaction 213
4.3.2. Study of the CO_2 to DME reactions 219
4.4. Simulation of isothermal reactors: Variation of space time (τ) .. 224
4.5. A reactor optimisation by temperature progression 231
4.5.1. Choice of criterion to optimise 231
4.5.2. Effect of inlet temperature 233
4.5.3. Effect of H_2/CO_2 ratio 239
4.5.4. Effect of space time (τ) 244
4.6. Simulation of an OTP scaled-up reactor 246
4.6.1. Optimal dimensions of scaled-up reactors 248
4.6.2. Verification of transfer limitations 250
4.6.3. Comparison of isothermal and OTP reactors 252
4.6.4. Thermal aspects: heat removal and heat exchanger sizing 255
4.7. Conclusions 266
4.8. References 268
5. General Conclusions and Perspectives 272
5.1. General conclusions 272
5.2. Perspectives 274
5.3. References 276
6. Scientific Production 277
APPENDIX A.1
Data and Equations for Transport Phenomena Calculations A.2

Effect of space time (τ) on the OTP B.1

List of Figures

Figure 1.1 Thermodynamic equilibrium a) CO_2 conversion, b) CH_4 and CO yields with increasing temperature for methanol synthesis. Computed using Aspen Plus® RGIBBS reactor with feed molar ratio of H_2/CO_2=4 and P=1 and 40 bar. 21

Figure 1.2 Thermodynamic equilibrium a) CO_2 conversion, b) methanol and CO yields with increasing temperature for methanol synthesis. Computed using Aspen Plus® RGIBBS reactor with feed molar ratio of H_2/CO_2=3 and P=1 and 40 bar..... 22

Figure 1.3 Thermodynamic equilibrium a) CO_2 conversion; b) DME, Methanol and CO yields with increasing temperature. Computed using Aspen Plus® RGIBBS reactor at 40 bar and with different feed molar ratio of H_2/CO_2=1, 3 and 9. 24

Figure 1.4 Thermodynamic equilibrium on a) CO_2 conversion and b) DME, Methanol and CO yields with increasing temperature. Computed using Aspen Plus® RGIBBS reactor with a fixed molar ratio of H_2/CO_2=3 and varying pressure: P=1, 80 and 120 bars..... 25

Figure 1.5 Comparison of methanol formation rates at different calcination and reduction temperatures, and metal loadings. Reaction conditions: CO_2/H_2 = 1/9 and W/F = 0.13 kg·h·m^{-3}. Reproduced from [128]. 33

Figure 1.6 CO_2 methanation pathways: (a) the carbonyl pathway via RWGS+CO hydrogenation and (b) the formate pathway. Reproduced from [64]. 37

Figure 1.7 Diagram of three mechanisms of CO_2 methanation on Ni(111). Reproduced from [144]. 38

Figure 1.8 Potential pathway during conversion of CO_2 under hydrogenation conditions. Reproduced from [153]. 39

Figure 1.9 The methanol synthesis mechanism and kinetics for the methanol synthesis on ZnO. Reproduced from [20]. 39

Figure 1.10 Methanol synthesis pathways over Cu-based catalysts. Reproduced from [11]..... 40

Figure 1.11 Reaction mechanisms for methanol conversion to DME catalysed over H-form zeolite. Reproduced from [155]. 41

Figure 1.12 Reaction mechanism for direct DME synthesis from CO_2 over CZZ(C)/FER catalyst. Reproduced from [156]..... 42

Figure 1.13 (a) Schematic diagram of a multi-stage fluidized bed reactor and (b) its model representation. Reproduced from [194]. 52

Figure 1.14 Illustration of slurry reactor. Reproduced from [206]. 54

Figure 1.15 Schematic diagram of CO_2 photoreduction configuration. Reproduced from [207]. 55

Figure 1.16 a) In-plasma catalysis and b) post-plasma catalysis schematic configurations. Reproduced from [211]. 56

Figure 1.17 Schematics of (a) magnetic field-assisted fixed-bed reactor and (b) magnetic line of force in the north-south direction. Reproduced from [214]. 57

Figure 1.18 Schematic of magnetic field-assisted packed bed reactor under magnetic field direction of north-to-south. Reproduced from [215]. 57

Figure 1.19 Schematics of side cut view of (a) RF-GCR and (c) RF-GCMR and detailed view of (b) RF-GCR and (d) RF-GCMR. Reproduced from [218]. 59

Figure 1.20 Schematic illustration of a membrane contactor reactor. Reproduced from [220]. 60

Figure 1.21 Schematic diagram of a dual-type membrane reactor: a fixed bed reactor with a water perm-selective membrane as the first stage, followed by a fluidized-bed reactor with an H_2 perm-selective membrane. Reproduced from [225]. 61

Figure 1.22 Scheme of the co-current mode for a fluidized bed membrane reactor configuration. Reproduced from [233]. 62

Figure 1.23 Schematic diagram of an axial-flow packed bed reactor (AF-SPBR). Modified from [234] and [235]. 63

Figure 1.24 Condensing liquid out/gas in concept (LOGIC) reactor to convert CO_2 to methanol. TI- are the catalyst in (TI-2), catalyst out (TI-3), condenser out (TI-4) and condenser in (TI-5) temperature indicators, and dP-1 is the differential pressure indicator. The catalyst is randomly packed. Reproduced from [238]. 64

Figure 1.25 a) Design of COx hydrogenation reactor with channels for reaction gas flow and cooling media. b) Axial cross section showing flow streams. Red represents flow for reactant gas and blue coolant media. Reproduced from [243]. 65

Figure 1.26 Design of micro packed bed reactor and core-shell catalyst for DME synthesis. Reproduced from [244]. 67

Figure 1.27 Design of (a) the stacking of reaction and heat exchange oil slits in the three dissimilar integrated micro packed bed reactor-heat exchangers, (b) internal pillar

structure inside the reaction slits of reactors A and B, and (c) pillar structure inside the slits of reactor C. Reproduced from [242]. 67

Figure 1.28 Configuration of Temperature Gradient Reactor. Reproduced from [246]. 68

Figure 1.29 ARC (Advanced Reactor Concept) converter drawing. Reproduced from [250]..... 69

Figure 1.30 Illustration of a) IMC (Isothermal Methanol Converter) reactors: b) Axial-radial steam-raising, c) axial steam-raising and d) axial-radial gas-cooled. Reproduced from [250]..... 69

Figure 1.31 Simplified reactor schemes of (a) Lurgi tubular reactor, (b) Linde Variobar, (c) Toyo MRF, (d) Mitsubishi Superconverter, (e) Methanol Casale IMC, (f) Haldor Topsøe adiabatic reactor, (g) Lurgi MegaMethanol and (h) Air Products LPMEOH. Reproduced from [251]..... 70

Figure 1.32 Methanol and DME synthesis process flow diagram of TOYO Engineering Corporation. Reproduced from [256]..... 74

Figure 1.33 Uhde DME synthesis process flow. Reproduced from [260]. 75

Figure 1.34 DME synthesis plant process flow diagram of JFE Group. Reproduced from [261]. 75

Figure 1.35 Simplified functional diagram of the methanol synthesis and purification section C: Cooler; CP: Compressor; D: Distillation column; F: Flash; H: Heater; M: Mixer; R: Reactor; S: Splitter; TES: Thermal energy storage [269]. 78

Figure 1.36 Diagram of process designed by Van-Dal & Bouallou [270]. R1: adiabatic reactor; KO1, KO2: knock-out drum; TKFL1: tank flash; DT1REB: reboiler. 79

Figure 1.37 Process flow sheet for the simulation of Pérez-Fortes et al., 2016 [252]..... 79

Figure 1.38 CO_2 conversion process flowsheet scheme proposed by Meunier et al., 2020 [40]. HX, REB-CAP, REB: Heat exchanger; REA: Reactor; DISTIL: Distillation column; COOL: Cooler..... 80

Figure 1.39 Reactor configurations developed by Leonzio et al., 2019 [271]: a) once-through equilibrium reactor; b) equilibrium reactor with recycle of CO-CO_2-H_2 and separation of CH_3OH-H_2O by condensation; c) membrane reactor with water separation. 81

Figure 1.40 Schemes of (a) CTM process and (b) methanol converters [273]. 82

Figure 1.41 The optimised process flowsheet of Chiou et al., 2023 [186]. 83

Figure 1.42 Flowsheet diagram of one step methanol dehydration process with a reactive distillation column. Reproduced from [279]. 85

Figure 1.43 Flowsheet diagram of coupled gas-phase reactor and a reactive distillation column for methanol dehydration process. Reproduced from [279]. 85

Figure 1.44 Flowsheet diagram for the identified optimal process result by Giuliano et al., 2021 [283]. 86

Figure 1.45 Flowsheet diagram of the Double Recycling Loop-DME production plant (solid line = reactants-products, dashed line = membrane reactor sweeping gas line; dotted line = reactor cooling line). Reproduced from [288]. 88

Figure 2.1 Schematic representation of the experimental setup for DME and methanol synthesis from CO_2 hydrogenation over CZA+HZSM-5 and CZA alone. 125

Figure 2.2 Schematic representation of the fixed bed reactor. 128

Figure 2.3 Chromatogram from GC-TCD for H_2 and N_2 analyses. 129

Figure 2.4 Chromatogram from GC-FID for CO, CO_2, CH_3OH and CH_3OCH_3 analyses. 129

Figure 2.5 Simplified scheme of the experimental setup of molar and mass flow rates. F, Q and y are respectively molar flow rate, mass flow rate and molar fraction. The indexes t, i, H_2O, in and out are respectively total, specie i, water, input and ouput. 133

Figure 2.6 a) CO_2 conversion and b) methanol and CO yields for CZA-C and CZA-D. Operating conditions: P=36 bars, $H_2/CO_2/N_2$= 67.5/22.5/10, GHSV= 15.3-15.7 $L.gcat-1.h-1$. 137

Figure 2.7 CO_2 conversion as a function of temperature for the mixture of CZA and HZSM5. Operating conditions: P=36 bars, $H_2/CO_2/N_2$= 67.5/22.5/10, GHSV= 7.3-7.8 $L.gcat-1.h-1$. 138

Figure 2.8 a) DME and methanol yields, and b) CO yield for CZA-D and CZA-C mixed with zeolite HZSM5. Operating conditions: P=36 bars, $H_2/CO_2/N_2$= 67.5/22.5/10, GHSV= 7.3-7.8 $L.gcat-1.h-1$. 138

Figure 2.9 CO_2 conversion as a function of temperature for the mixture of CZA and HY. Operating conditions: P=36 bars, $H_2/CO_2/N_2$= 67.5/22.5/10, GHSV= 7.3-7.6 $L.gcat-1.h-1$. 140

Figure 2.10 a) DME and methanol, and b) CO yield of CZA-D and CZA-C mixed with zeolite HY. Operating conditions: P=36 bars, $H_2/CO_2/N_2$= 67.5/22.5/10, GHSV= 7.3-7.6 $L.gcat-1.h-1$ 140

Figure 2.11 Comparison between the CO_2 conversion for CZA-C + HZSM5 and CZA-C + HY. Operating conditions: P=36 bars, $H_2/CO_2/N_2$= 67.5/22.5/10, GHSV= 7.3 $L.gcat-1.h-1$. 141

Figure 2.12 Comparison between the a) DME and methanol, and b) CO yields of the CZA-C + HZSM5 and of the CZA-C + HY. Operating conditions: P=36 bars, $H_2/CO_2/N_2$= 67.5/22.5/10, GHSV= 7.3 $L.gcat-1.h-1$.....141

Figure 2.13 Linear equation of ln (Kj) vs 1/T obtained with REQUIL block results. 147

Figure 2.14 Linear equation of ln (Kj) vs 1/T obtained with RGIBBS block results..... 147

Figure 2.15 CO_2 conversion at equilibrium by two calculation methods of equilibrium constant: equilibrium reactor (REQUIL) and Gibbs reactor (RGIBBS). P=36 bars, $H_2/CO_2/N_2$=3/1/1, EoS: SRK.....148

Figure 2.16 (a) CO_2 conversion, (b) DME yield, (c) methanol yield and (d) CO yield as a function of temperature. Operating conditions: P=36 bars, $H_2/CO_2/N_2$=67.5/22.5/10, GHSV=3.4-3.6 $L.gcat-1.h-1$. Dashes lines represent the chemical equilibrium. Refer to Table 2.8: Experiments 9-10. 150

Figure 2.17 Effect of temperature on (a) CO_2 conversion, (b) DME, (c) methanol and (d) CO yield. Dashes lines represent the chemical equilibrium. Operating conditions: P=36 bars, $H_2/CO_2/N_2$= 81/9/10, GHSV=12.2 $L.gcat-1.h-1$. Refer to Table 2.8: Experiment 6. 151

Figure 2.18 Effect of zeolite on CO_2 conversion. Operating conditions: P=36 bars, $H_2/CO_2/N_2$= 67.5/22.5/10, $GHSV_{CZA\text{-}C}$ =15.3 $L.gcat-1.h-1$, $GHSV_{CZA\text{-}C+HZSM_5}$ =7.3 $L.gcat-1.h-1$. Refer to Table 2.6: Experiments 4-5..... 153

Figure 2.19 Effect of pressure on (a) CO_2 conversion, (b) DME, (c) methanol and (d) CO yield. Dashes lines represent the chemical equilibrium. Operating conditions: $H_2/CO_2/N_2$=67.5/22.5/10, GHSV= 7.3-7.4 $L.gcat-1.h-1$. Refer to Table 2.8: Experiments 1-2. 154

Figure 2.20 Effect of pressure on (a) CO_2 conversion, (b) DME, (c) methanol and (d) CO yield. Dashes lines represent the chemical equilibrium. Operating conditions: $H_2/CO_2/N_2$=67.5/22.5/10, GHSV= 7.3-7.7 $L.gcat-1.h-1$. Refer to Table 2.8: Experiments 1 and 4. 155

Figure 2.21 Effect of feed molar ratio on (a) CO_2 conversion, (b) DME, (c) methanol and (d) CO yield. Dashes lines represent the chemical equilibrium. Operating conditions: P=36 bars, GHSV=3.6 $L.gcat-1.h-1$, N_2=10%. Refer to Table 2.8: Experiments 5 and 10. 156

Figure 2.22 Effect of feed molar ratio on (a) CO_2 conversion, (b) DME, (c) methanol and (d) CO yield. Dashes lines represent the chemical equilibrium. Operating conditions: P=26 bar, H_2/CO_2=3/1, GHSV=7.4 $L.gcat-1.h-1$. Refer to Table 2.8: Experiments 2-3. 158

Figure 2.23 Effect of GHSV on (a) CO_2 conversion, (b) DME, (c) methanol and (d) CO yields. Dashes lines represent the chemical equilibrium. Operating conditions: P=36 bars, $H_2/CO_2/N_2$= 67.5/22.5/10. Refer to Table 2.8: Experiments 1, 9 and 10. 159

Figure 3.1 Temperature gradient of the furnace and fixed bed core as a function of the fixed bed core temperature. Operating conditions: P=26, 31 and 36 bars, T=473.15 – 623.15 K, GHSV=3.6 – 12.2 $L.gcat-1.h-1$. 175

Figure 3.2 a) CO_2 conversion, b) DME, c) methanol and) CO yields as a function of temperature in chemical equilibrium calculated by means of RGIBBS in Aspen Plus. Operating conditions: P=31 and 36 bars, $H_2/CO_2/N_2$=67.5/22.5/10..... 176

Figure 3.3 Comparison of experiments to demonstrate catalyst deactivation. (a) CO_2 conversion, (b) DME, (c) methanol and (d) CO yield. Dashes lines represent the chemical equilibrium. Operating conditions: $H_2/CO_2/N_2$=67.5/22.5/10, GHSV= 7.3-7.7 8 $L.gcat-1.h-1$.....177

Figure 3.4 Moles of CO_2 converted accumulated during all the carried-out experiments as a function of experiment number..... 178

Figure 3.5 Illustration of a plug-flow reactor. 179

Figure 3.6 Representation of program modelling in MATLAB. MSE is the mean squared error. 182

Figure 3.7 Comparison of experimental and calculated data for methanol synthesis. Operating conditions: H_2/CO_2=3, P = 36 bar, GHSV=15.3 $L.gcat-1.h-1$ and N_2=10%. Refer to Table 2.6, Experiment 4.....186

Figure 3.8 Comparison of experimental and calculated conversion and yields for DME synthesis considering chemical equilibrium. Experiment 6. P=36.1 bar, H_2/CO_2=9.7, GHSV=12.2 $L.gcat-1.h-1$ and N_2=10%. 188

Figure 3.9 Comparison of experimental and calculated for DME synthesis not considering chemical equilibrium. Experiment 6. P=36.1 bar, H_2/CO_2=9.7, GHSV=12.2 $L.gcat-1.h-1$, N_2=10%. 189

Figure 3.10 Fitting responses of experimental data for CO_2 conversion and DME, methanol and CO yields: a)- b) H_2/CO_2=3, P=31 bar, GSHV=7.7 $L.gcat-1.h-1$; c)-

d) H_2/CO_2=1, P=36 bar, GSHV=3.6 $L.gcat-1.h-1$; e)-f) H_2/CO_2=9.7, P=36 bar, GSHV=12.2 $L.gcat-1.h-1$. See Table 2.8: Experiments 4-6. 192

Figure 3.11 Fitting responses of experimental data for CO_2 conversion and DME, methanol and CO yields: a)- b) H_2/CO_2=1, P=26 bar, GSHV=3.6 $L.gcat-1.h-1$; c)-d) H_2/CO_2=9, P=26 bar, GSHV=7 $L.gcat-1.h-1$; e)-f) H_2/CO_2=3, P=36 bar, GSHV=3.6 $L.gcat-1.h-1$. See Table 2.8: Experiments 7-9 193

Figure 3.12 Fitting responses of experimental data for CO_2 conversion and DME, methanol and CO yields: a)- b) H_2/CO_2=3, P=36 bar, GSHV=3.4 $L.gcat-1.h-1$. See Table 2.8: Experiment 10 194

Figure 3.13 Fitting responses of experimental data for CO_2 conversion and DME, methanol and CO yields: a)- b) H_2/CO_2=3, P=36 bar, GSHV=7.3 $L.gcat-1.h-1$; c)-d) H_2/CO_2=3, P=26 bar, GSHV=7.4 $L.gcat-1.h-1$; e)-f) H_2/CO_2=3, P=26 bar, GSHV=7.4 $L.gcat-1.h-1$. See Table 2.8: Experiments 1-3. 195

Figure 3.14 Parity plots of experimental vs. calculated a) CO_2 conversion, b) DME, c) CH_3OH and d) CO yields 196

Figure 3.15 Normal and histogram plots of residuals for a) and b) CO_2 conversion, c) and d) DME yield, respectively. 198

Figure 3.16 Normal and histogram plots of residuals for a) and b) CH_3OH, c) and d) CO yields, respectively. 199

Figure 3.17 Residuals versus order plots for a) CO_2 conversion, b) DME, c) CH_3OH and d) CO yields. 200

Figure 4.1 Conversion versus temperature curves iso-τ for an exothermic reversible first-order reaction $A \leftrightharpoons R$ in an isothermal plug flow reactor. Modified from [4]. 209

Figure 4.2 Conversion versus temperature curves iso-r for a reversible first-order reaction $A \leftrightharpoons R$: $k1 = exp17.34 - 48900RT; k2 = exp42.04 - 124200RT$ for $CA0 = 1\ mol.liter-1$ and $CR0 = 0$. Reproduced from [2]. 210

Figure 4.3 Representation of a plug-flow reactor (PFR). 213

Figure 4.4 Optimisation outcomes for a reversible reaction $A \rightleftharpoons B$, where a) and b) resulted from a while loop method, whereas c) and d) were derived from the nonlinear programming solver 'fminunc'. The graphics represents the conversion, X, vs temperature, T (K) of: a), c) all resulted points and b), d) the final conversion at different inlet temperatures To. Refer to Table 4.1 for operating conditions. 218

Figure 4.5 Flowchart of optimal temperature progression optimisation program "while loop" in MATLAB for the DME synthesis from CO_2 hydrogenation. L represents the catalyst bed division.....223

Figure 4.6 Simulation of an isothermal reactor for different set space times (τ) by changing the feed flow rate (F_{total}=0.022-2.178 mol.h^{-1}) for a) $X1$, b) $X2$, c) $X4$, d) $XCO2$ and e) FMDversus temperature. Operating conditions: P=36 bar, T=453.15-553.15 K, $H2/CO2 = 3$, $N_2$2=10%. Refer to Table 4.5.....226

Figure 4.7 Simulation of an isothermal reactor for different set space times (τ) by changing the length of catalyst bed (H_{bed}=0.88-87.86 cm) for a) $X1$, b) $X2$, c) $X4$, d) $XCO2$ and e) FMD versus temperature. Operating conditions: P=36 bar, T=453.15-553.15 K, $H2/CO2 = 3$, $N2 = 10\%$. Refer to Table 4.6. 229

Figure 4.8 Comparison of simulations of an isothermal reactor for different set of space times τ by changing the feed flow rate (F) and by varying the length of catalyst bed (L) for a) $XCO2$ (%), b) Q (W.m^{-2}), c) FMD (mol.h^{-1}) and d) $FMDmcat$ (mol.h^{-1}.kg$_{cat}$) versus the temperature. Refer to Table 4.5 and Table 4.6..... 230

Figure 4.9 Effect of choice of criterion by maximising $X1$, $X4$, $XCO2$ and methanol and DME productivity (FMD) vs temperature. Operating conditions: P=31.1 bar, $F_{t,\ in}$=0.269 mol.h^{-1}, $H2/CO2 = 2.8$, $N2 = 10\%$, m_{cat}=8·10^{-4}kg, T_o=583.15 K and τ=6.8 s. 232

Figure 4.10 Effect of inlet temperature by optimising X1: a) $X1$, b) $X2$, c) $X4$, d) methanol and DME productivity (FMD) e) $FMDmcat$ and f) $XCO2$ vs temperature. Operating conditions: P=31.1 bar, $F_{t,\ in}$=0.269 mol.h^{-1}, $H2CO2 = 2.8$, N2=10%, m_{cat}=8·10^{-4}kg and τ=6.1-7.1 s. 234

Figure 4.11 Effect of inlet temperature by optimising X1: local heat flux (qk) vs the axial position (z) for a)T=523.15-563.15 K and b)T=573.15-608.15 K. Operating conditions: P=31.1 bar, $F_{t,\ in}$=0.269 mol.h^{-1}, $H2/CO2 = 2.8$, $N2 = 10\%$, m_{cat}=8·10^{-4}kg and τ=6.1-7.1 s.....235

Figure 4.12 Effect of inlet temperature by optimising $X1$: $X1$ vs temperature at the reactor outlet. Operating conditions: P=31.1 bar, $F_{t,\ in}$=0.269 mol.h^{-1}, $H2/CO2 = 2.8$, $N2 = 10\%$, m_{cat}=8·10^{-4}kg and τ=6.7-6.8 s. 236

Figure 4.13 Effect of feed molar $H2/CO2$ ratio vs length of reactor (z): at a fixed input total flow a) $X1$, b) $X2$, c) $X4$, and at a fixed $CO2$ input flow rate d) $X1$, e) $X2$ and f) $X4$. See Table 4.8 for details on operating conditions. 241

Figure 4.14 Effect of feed molar $H2/CO2$ratio vs length of reactor (z): at a fixed input total flow a) $XCO2$, b) FMD, and at a fixed $CO2$ input flow rate c) $XCO2$, and d) FMD. See Table 4.8 for details on operating conditions. 243

Figure 4.15 Effect of particle Reynolds number (Re) on X_{CO_2} and FMD throughout the reactor. Fixed parameters: $P = 36$ bar, $H2/CO2 = 3$, $Ft, in = 3.79 \cdot 105 mol.h - 1$ and $dp = 2 \cdot 10 - 3m$. Refer to Table 4.11 for more details. 250

Figure 4.16 Simulated a) $CO2$ conversion profile, b) combined methanol and DME production profile and evolution of c) X_{CO_2} and d) F_{MD} throughout the reactor in the scaled-up isothermal (IsoT) and OTP reactors. Fixed parameters: P=36 bar, $H2/CO2 = 3$, $Ft, in = 3.79 \cdot 105 mol.h - 1$ and $dp = 2 \cdot 10 - 3$ m. Refer to Table 4.13 for more details. 254

Figure 4.17 Simulated temperature and local heat flux qk profiles in the scaled-up isothermal (IsoT) and OTP reactors. Fixed parameters: P=36 bar, $H2/CO2 = 3$, $Ft, in = 3.79 \cdot 105 mol.h - 1$ and $dp = 2 \cdot 10 - 3$ m. Refer to Table 4.13 for more details. 255

Figure 4.18 Profile of the product of a) the overall heat transfer coefficient and the heat transfer area $UdA$and b) the overall heat transfer coefficient along the simulated OTP reactor. Fixed parameters: P=36 bar, $H2/CO2 = 3$, $Ft, in = 3.79 \cdot 105 mol.h - 1$, $dp = 2 \cdot 10 - 3$ m, $\Delta z = 0.11\, m$ and $Tcoolant = 423.15\, K$. Refer to Table 4.13 for more details. 257

Figure 4.19 Evolution of the heat transfer surface area dAthroughout the OTP reactor. Fixed parameters: P=36 bar, $H2/CO2 = 3$, $Ft, in = 3.79 \cdot 105 mol.h - 1$, $dp = 2 \cdot 10 - 3$ m and $Tcoolant = 423.15\, K$. Refer to Table 4.13 for more details. 258

Figure 4.20 Evolution of coolant temperature along the OTP reactor. Fixed parameters: P=36 bar, $H2/CO2 = 3$, $Ft, in = 3.79 \cdot 105 mol.h - 1$ and $dp = 2 \cdot 10 - 3$ m. Refer to Table 4.13 for more details. 259

Figure 4.21 Evolution of coolant temperature along the OTP multi-tubular reactor. Fixed parameters: P=36 bar, $T0 = 531.15\, K$, $H2/CO2 = 3$, $Ft, in = 3.79 \cdot 105 mol.h - 1$, $dp = 2 \cdot 10 - 3$ m, $dtube = 0.04\, m$, $Lr = 11\, m$, $\Delta z = 0.1\, m$, $Ntubes = 958$, $U = 455\, W.m - 2.K - 1$, $Re = 100$ and $\tau = 102.6\, s$. 261

Figure 4.22 Comparison of the evolution of coolant temperature along the OTP multi-tubular reactor and the single-tube reactor. Fixed parameters: P=36 bar, $T0 = 531.15\, K$, $H2/CO2 = 3$, $Ft, in = 3.79 \cdot 105 mol.h - 1$, $dp = 2 \cdot 10 - 3$ m, $Lr = 11\, m$,

$\Delta z = 0.1\,m$, $U = 455\,W.m-2.K-1$, $Re = 100$ and $\tau = 102.6\,s$. For multi-tubular: $dtube = 0.04\,m$, $Ntubes = 958$. For single-tube: $dr = 1.24\,m$. 262

Figure 4.23 Profiles of a) the temperature and local heat flux qk and b) CO_2 conversion and combined methanol and DME production in the OTP multi-tubular reactor. Fixed parameters: P=36 bar, $T0 = 531.15\,K$, $H2/CO2 = 3$, $Ft,in = 3.79 \cdot 105 mol.h-1$, $dp = 2 \cdot 10-3$ m, $dtube = 0.04\,m$, $Lr = 11\,m$, $\Delta z = 0.1\,m$, $Ntubes = 958$, $U = 455\,W.m-2.K-1$, $Re = 100$ and $\tau = 102.6\,s$. 262

Figure 4.24 Evolution of a) $CO2$ conversion and b) combined methanol and DME production as a function of the temperature in the OTP multi-tubular reactor. Fixed parameters: P=36 bar, $T0 = 531.15\,K$, $H2/CO2 = 3$, $Ft,in = 3.79 \cdot 105 mol.h-1$, $dp = 2 \cdot 10-3$ m, $dtube = 0.04\,m$, $Lr = 11\,m$, $\Delta z = 0.1\,m$, $Ntubes = 958$, $U = 455\,W.m-2.K-1$, $Re = 100$ and $\tau = 102.6\,s$. 263

Figure B.1 Optimisation of $X1$ at 563.15 K: Effect of space time (τ) vs temperature by varying the total feed flow rate from 0.091 – 2.013 mol.h^{-1} for $H2/CO2 = 3$ and P=36 bar at a fixed catalyst mass a) X_1, b) X_2, c) X_4, d) X_{CO2} and e) F_{MD}. Refer to Table B.1 for specific operating conditions. B.3

Figure B.2 Optimisation of X_1 at 563.15 K: Effect of space time (τ) along the entire reactor by varying the total feed flow rate from 0.09 – 2.01 mol.h^{-1} for $H2/CO2 = 3$, T=563.15 K and P=36 bar at a fixed catalyst mass a) X_1, b) X_2, c) X_4, d) X_{CO2}, e) F_{MD} and f) qk. Refer to Table B.1 for specific operating conditions..... B.4

Figure B.3 Optimisation of $X1$ at 563.15 K: Effect of space time (τ) along the entire reactor vs temperature by changing the length of catalyst bed (z) from 0.89 – 22.36 cm for $H2/CO2 = 3$, T=563.15 K and P=36 bar at a fixed molar flow a) X_1, b) X_2, c) X_4, d) X_{CO2} and e) F_{MD}. Table B.2 outlines the specific operating parameters. B.6

Figure B.4 Optimisation of $X1$ at 563.15 K: Effect of space time (τ) along the entire reactor by changing the length of catalyst bed (z) from 0.89 – 22.36 cm for $H2/CO2 = 3$, T=563.15 K and P=36 bar at a fixed molar flow a) X_1, b) X_2, c) X_4, d) X_{CO2}, e) F_{MD} and f) qk. Table B.2 outlines the specific operating parameters. B.7

List of Tables

Table 1.1 Summary of applications, processes, catalysts, and reaction conditions for CO_2 hydrogenation into several products. 12

Table 1.2 Physical and chemical properties of DME and other fuels. 17

Table 1.3 Methanol synthesis catalysts from CO_2 hydrogenation. 30

Table 1.4 Summary of the performance of catalysts for direct DME synthesis from CO_2 hydrogenation. 34

Table 1.5 Kinetic models for DME synthesis. 43

Table 1.6 Existing or planned plants for methanol production from CO_2 and H_2. Reproduced from [41]. 71

Table 2.1 Structural composition of the CZA catalysts. 123

Table 2.2 Zeolites properties. 123

Table 2.3 CO_2, CO, H_2, N_2 calibration parameters 130

Table 2.4 Main target product depending on catalysts. 131

Table 2.5 Plan of experiments: operating conditions. 131

Table 2.6 Chronology of catalyst screening. 136

Table 2.7 Enthalpies and Gibbs energies of formation at 298.15 K and 1 bar. 144

Table 2.8 Experiments of DME synthesis with CZA-C+HZSM-5 in chronological order. 149

Table 3.1 Parameters to estimate the external resistance fraction. 170

Table 3.2 Parameters to estimate the external heat transfer limitation. 171

Table 3.3 Mears Criterion for CO_2 and H_2. 171

Table 3.4 Parameters to estimate the internal mass transfer limitation for the CZA catalyst. 173

Table 3.5 Global material balances of the species. 180

Table 3.6 Reactor configuration and operating conditions 182

Table 3.7 Initial parameters for methanol synthesis. 185

Table 3.8 Initial parameters for DME synthesis 185

Table 3.9 Optimised parameters for methanol synthesis. 187

Table 3.10 Optimised parameters values considering equilibrium. 188

Table 3.11 Initial parameters values with backward reaction $k5, E5$ not considering equilibrium. 189

Table 3.12 Optimised final kinetic parameters. 190
Table 3.13 Summary of kinetic parameters from literature. 190
Table 4.1 Inlet parameters for optimisation of a first order reversible reaction $A \rightleftharpoons B$ in a PFR. 215
Table 4.2 Final outputs of both methods: while loop and fminunc. 216
Table 4.3 Reaction rates constants. 219
Table 4.4 Global material balances of the species 220
Table 4.5 Inlet conditions set to simulate an isothermal reactor for different set space times (τ) by changing the total feed flow rate at a pressure of 36 bar. 224
Table 4.6 Inlet conditions set to simulate an isothermal reactor for different set space times (τ) by varying the length of catalyst bed at pressure of 36 bar. 224
Table 4.7 Simulation results when varying feed flow rate and the amount of catalyst mass. 228
Table 4.8 Inlet condition set to evaluate the effect of the feed molar ratio: $H2/CO2$. H_{bed}=0.059 m, and P=36 bar. 239
Table 4.9 Comparison of FMD, the global power Q, the outlet global heat flux Q and the local qk heat flux of both methods for the varied space-time τ. 244
Table 4.10 Operating conditions of the reactor and particle diameter parameter. 248
Table 4.11 Effect of space time and Reynolds number on reactor dimensions in a laboratory reactor and scaled-up OTP reactors. Fixed parameters: $P = 36\,bar$, $H2/CO2$=3, $Ft, in = 3.79 \cdot 105\,mol.h - 1$ and $dp = 2 \cdot 10 - 3$ m. The fixed parameters for the reference (first line): $P = 36\,bar$, $H2/CO2$=3, $Ft, in = 2.71 \cdot 10 - 1\,mol.h - 1$ and $dp = 2 \cdot 10 - 4$ m. 248
Table 4.12 Effect of space time and Reynolds number on reactor dimensions and transfer coefficients in two scaled-up OTP reactors. Fixed parameters: $P = 36$ bar, $H2/CO2 = 3$, $Ft, in = 3.79 \cdot 105 mol.h - 1$, $\tau = 100\,s$ and $dp = 2 \cdot 10 - 3m$. 251
Table 4.13 Comparison of reactor dimensions and transfer coefficients of a scaled-up OTP reactor (#1) and an isothermal reactor (#2). Fixed parameters: $P = 36$ bar, $H2/CO2 = 3$, $Ft, in = 3.79 \cdot 105 mol.h - 1$ and $dp = 2 \cdot 10 - 3m$. 253
Table 4.14 Comparison of the outcomes with literature data. 264
Table A.1 Gas properties [1]. A.3
Table A.2 Vapor Thermal Conductivity of Components $W.m - 1.K - 1$ [6]. A.4
Table A.3 Ideal Gas Heat Capacities at 298.15 K $J.mol - 1\,K - 1$ [1] A.5

Table B.1 Inlet conditions set to evaluate the effect of changing total feed flow rate for a feed molar flow ratio of $H2/CO2 = 3$, T=563.15 K and P=36 bar. B.1

Table B.2 Inlet conditions set to evaluate the effect of changing the length of catalyst bed for a feed molar ratio of $H2/CO2 = 3$, T=563.15 K and P=36 bar. B.5

Nomenclature

Physical constants	**Definition**	**Value**
R	Gas constant	$8.3145\ J.mol^{-1}.K^{-1}$
Properties	**Definition**	**Units**
A	External surface	m^2
a	Activity coefficient	Dimensionless
C	Concentration	$mol.m^{-3}$
C_M	Mears criterion $\left(\frac{\lvert-\Delta H_{rx}\rvert r_{obs} E_{obs}}{hRT^2}\frac{d_p}{6} < 0.15\right)$	Dimensionless
Cp	Heat capacity	$J.mol^{-1}.K^{-1}$
d	Diameter	m
D	Diffusivity	$m^2.s^{-1}$
df	Deactivation function	Dimensionless
$\Delta_f G_i^o$	Gibbs energy change of formation at standard state	$kJ.mol^{-1}$
$\Delta_r G°$	Standard Gibbs energy change of reaction	$kJ.mol^{-1}$
ΔH_{rx}	Heat of reaction	$kJ.mol^{-1}$
$\Delta_f H_i^o$	Enthalpy energy change of formation at standard state	$kJ.mol^{-1}$
$\Delta_r H°$	Standard heat change of reaction	$kJ.mol^{-1}$
ΔS_i^0	Standard entropy change	$kJ.mol^{-1}.K^{-1}$
E	Activation energy	$J.mol^{-1}$
F	Molar flow rate	$mol.h^{-1}$
f	Fraction of resistance	Dimensionless
$GHSV$	Gas hourly space velocity	$m^{-3}.g_{cat}^{-1}.h^{-1}$
h	Heat transfer coefficient	$W.m^{-2}.K^{-1}$
H	Height	m
K	Pre-exponential factor	Variable
k_D	External mass transfer coefficient	$m.s^{-1}$
K_i	Adsorption equilibrium constant	bar^{-1}

K_j	Chemical reaction equilibrium constant	Dimensionless
L	Length	m
M	Molar mass	$g.mol^{-1}$
m	Mass	kg
$\dot{m}$	Mass flow rate	$g.h^{-1}$
n	Number of moles	mol
N	Flux density	$mol.m^2.s^{-1}$
N_{tubes}	Number of tubes	Dimensionless
Nu	Nusselt number $\left(2 + 1.8Re^{\frac{1}{2}}Pr^{\frac{1}{3}}\right)$	Dimensionless
OF	Objective function	Dimensionless
P	Total pressure	Bar
p_i	Partial pressure	Bar
Pr	Prandlt number $\left(\mu_m C_{p,m} C_m / \rho \lambda_m\right)$	Dimensionless
Q	Global power	W
$\dot{Q}$	Heat flux	$W.m^{-2}$
q_k	Power at the segment wall	W
$\dot{q_k}$	Local heat flux through the reactor wall	W
r	Reaction rate	$mol.kg^{-1}.s^{-1}$
R_i	Production rate	$mol.kg^{-1}.s^{-1}$
Re	Reynolds number $((u\rho d\_p) \,/\, \mu\_m\,)$	Dimensionless
S	Section	m^2
S_k	Segment surface	m^2
S_W	Reactor wall surface	m^2
Sc	Schmidt number $(\mu_m / \rho D_{m,i})$	Dimensionless
Sh	Sherwood number $\left(k_D d_p / D_{m,i}\right)$	Dimensionless
T	Temperature	K
U	Overall heat transfer coefficient	$W.m^{-2}.K^{-1}$
u	Superficial velocity	$m.s^{-1}$
V	Volume	m^3
X	Conversion	%
y	Molar fraction	Dimensionless
Y	Product yield	%

z	Axial position in the catalyst bed	m

Greek letters	**Definition**	**Units**
α	Deactivation factor	mol^{-1}
ε	Porosity	Dimensionless
η	Internal effectiveness factor	Dimensionless
λ	Thermal conductivity	$W.m^{-2}.K^{-1}$
μ	Dynamic viscosity	$Pa.s$
ν	Stoichiometric number	Dimensionless
ρ	Density	$kg.m^{-3}$
τ	Space time	s
τ_p	Tortuosity	Dimensionless
ϕ	Thiele modulus	Dimensionless
Ω	Cross-sectional area	m^2

Subscripts	**Definition**
0	Inlet
ad	Adsorption
b	Bulk
bed	Catalyst bed
c	Chromatogram
cal	Calculated
cat	Catalyst
e	Effective
exp	Experimental
ext	External
f	Final
i	Specie
in	Input
j	Reaction
k	Wall area
m	Mixture

MD	Methanol plus DME
obs	Observed
opt	Optimal
out	Output
p	Particle
r	Reactor
s	Surface
t	Total
w	Wall

Abbreviations	**Definition**
BET	Brunauer, Emmett and Teller
CTM	CO_2 to methanol
CZA-C	$CuO/ZnO/Al_2O_3/MgO$
CZA-D	$CuO/ZnO/Al_2O_3$
DME	Dimethyl-Ether
FID	Flame ionization detector
GC	Gas chromatography
LHV	Lower heating value
LPG	Liquefied petroleum gas
MeOH	Methanol
OTP	Optimal temperature profile
PFR	Plug Flow Reactor
RWGS	Reverse Water Gas Shift
SNG	Synthetic natural gas
SRK	Soave-Redlich-Kwong
TCD	Thermal conductivity detector
TRL	Technology readiness level

Abstract

Rising levels of atmospheric carbon dioxide, which drives additional greenhouse effects, underscore the pressing need for sustainable alternatives. Converting CO_2 into value-added molecules (energy carriers) offers a promising solution to reduce reliance on fossil fuels.

This thesis explores the potential of catalytic CO_2 hydrogenation to produce value-added chemicals, specifically methane (CH_4), methanol (CH_3OH), and dimethyl ether (DME). These processes not only provide a route to lower CO_2 emissions but also support sustainable fuel production. The primary goal is to enhance CO_2 conversion (X_{CO2}) through thermal catalysis, a highly efficient and industrially viable approach. Literature shows that the production of CH_4 and CH_3OH via CO_2 hydrogenation is well-developed (TRL>8). However, DME synthesis remains comparatively less explored, thus becoming the central focus of this PhD thesis.

A combination of two catalysts—copper-zinc on alumina and H-ZSM5 zeolite—was selected for DME production at the laboratory scale using a fixed-bed reactor. Experimental trials across a broad range of operating conditions provided the data needed to develop a kinetic model for this complex reaction. Comprising four consecutive reactions, DME synthesis via CO_2 hydrogenation was modelled, and the kinetic parameters were estimated. A Langmuir-Hinshelwood type model was proposed for methanol synthesis, while an innovative model was introduced for methanol dehydration to DME. The study demonstrates that the latter reaction is not in equilibrium under the examined conditions, allowing for the simultaneous production of methanol and DME and CO2 conversion beyond thermodynamic equilibrium values.

An Optimal Temperature Profile (OTP) reactor, integrating the developed kinetic model, was simulated and studied to achieve precise temperature control and maximise X_{CO2}. Simulations and optimisations confirmed that longer residence times, adjusted by catalyst mass, are more effective for increasing X_{CO2}. Reactor inlet temperature is also a critical parameter and must be optimised for each scenario. Extrapolation to an industrial CO_2 feed flow (100 tonnes per day) was performed, and the OTP reactor was compared to an optimised isothermal reactor. While the advantages in terms of X_{CO2} were minimal (<1%), the combined productivity of DME and methanol improved by over 4.4% compared to the isothermal reactor. An OTP multi-tubular reactor with variable coolant temperature, comprising 958 tubes, achieved a CO_2 conversion of 34.18% per tube, approaching thermodynamic equilibrium without recirculation.

Keywords: Carbon dioxide, CO_2 hydrogenation, Dimethyl ether (DME), Methanol, Kinetics, CZA, HZSM-5, Simulation, Optimisation, Optimal Temperature Profile (OTP).

Résumé

L'augmentation des niveaux de dioxyde de carbone atmosphérique responsables de l'effet de serre additionnel souligne la nécessité pressante d'alternatives durables. La conversion du CO_2 en molécules à valeur ajoutée (vecteurs d'énergie) offre une solution prometteuse pour réduire la dépendance aux combustibles fossiles.

Cette thèse explore le potentiel de l'hydrogénation catalytique du CO_2 pour produire des produits chimiques à valeur ajoutée, en particulier le méthane (CH_4), le méthanol (CH_3OH) et l'éther di-méthyl éther (DME). Ces processus offrent non seulement une voie pour réduire les émissions de CO_2, mais soutiennent également la production de carburants durables. L'objectif principal est d'améliorer la conversion du CO_2 (X_{CO_2}) grâce à la catalyse thermique, une approche à la fois très efficace et viable industriellement. La littérature montre que la production de CH_4 et de CH_3OH par hydrogénation du CO_2 est bien développée (TRL>8). Cependant, la synthèse de DME reste comparativement moins étudiée, devenant ainsi le sujet central de cette thèse de doctorat.

La combinaison de deux catalyseurs, à base de Cuivre-Zinc sur alumine et une zéolithe H-ZSM5 a été sélectionnée pour la production de DME à l'échelle de laboratoire dans un réacteur à lit fixe. Des essais expérimentaux réalisés dans une large gamme de conditions opératoires ont fourni les données nécessaires au développement d'un modèle cinétique de cette réaction complexe. Composée de 4 réactions consécutives, la synthèse du DME par hydrogénation du CO_2 a été modélisée et les paramètres cinétiques estimés. Un modèle cinétique de type Langmuir- Hinshelwood a été proposé pour la synthèse du méthanol, et un modèle novateur a été introduit pour la déshydratation du méthanol en DME. L'étude démontre que cette dernière réaction n'est pas à l'équilibre dans nos conditions ce qui permet une production de méthanol et de DME et une conversion de CO_2 au-delà des valeurs d'équilibres thermodynamiques.

Un réacteur à Profil Optimal de Température (POT), intégrant le modèle cinétique développé, a été simulé et étudié pour obtenir, pour chaque condition de fonctionnement, le profil optimal précis de la température qui maximise X_{CO_2}. Les simulations et optimisations ont confirmé que des temps de résidence plus longs, ajustés par la masse de catalyseur, sont plus efficaces pour augmenter X_{CO_2}. La température à l'entrée du réacteur est également un paramètre clé et doit être optimisée sur chaque cas. L'extrapolation à un débit industriel d'alimentation en CO_2 (100 tonnes par jour) a été réalisée et le réacteur POT a aussi été comparé à un réacteur isotherme optimisé. Des avantages minimes (<1 %) en termes de X_{CO_2} mais la productivité combinée de DME et de méthanol s'est améliorée de plus de 4,4 % par rapport au réacteur

isotherme. Un réacteur multitubulaire POT avec température de refroidissement variable, comprenant 958 tubes, a atteint une conversion de CO_2 de 34,18 % par tube, se rapprochant de l'équilibre thermodynamique sans recirculation.

Mots-clés : Dioxyde de carbone, Hydrogénation du CO_2, Di-méthyl éther (DME), Méthanol, Cinétique, CZA, HZSM-5, Simulation, Optimisation, Profil Optimal de Température (POT).

General Introduction

In recent years, the research and implementation of the transition from fossil fuels to renewable energy production have become imperative. Fossil fuels, including coal, oil, and gas, significantly contribute to global climate change, responsible for over 75% of global greenhouse gas emissions and almost 90% of carbon dioxide emissions [1]. These greenhouse gases emissions have undeniably resulted in global warming, leading to a global surface temperature increase of 1.1°C above the 1850-1900 baseline during the period from 2011 to 2020 [2].

The global average atmospheric carbon dioxide measurements at National Oceanic and Atmospheric Administration's (NOAA) Mauna Loa Atmospheric Baseline Observatory recorded an historic high of 417.06 parts per million (ppm) in 2022. This marked an increase of 2.13 ppm of carbon dioxide from 2021, making it the 11th consecutive year with an annual rise exceeding 2 ppm [3]. Figure 1 displays how the atmospheric concentration of carbon dioxide (blue line) has risen in tandem with human emissions (grey line) since the onset of the Industrial Revolution in 1750. Emissions gradually increased to approximately 5 gigatons (one gigaton equals a billion metric tons) annually in the mid-20th century before sharply escalating to over 35 billion tons per year by the end of the century. To effectively curb climate change, it is imperative to decrease reliance on fossil fuels and adopt new sustainable methods for capturing, storing and utilizing CO_2, thereby exploring alternative approaches for producing fuels and energy vectors [4]–[7].

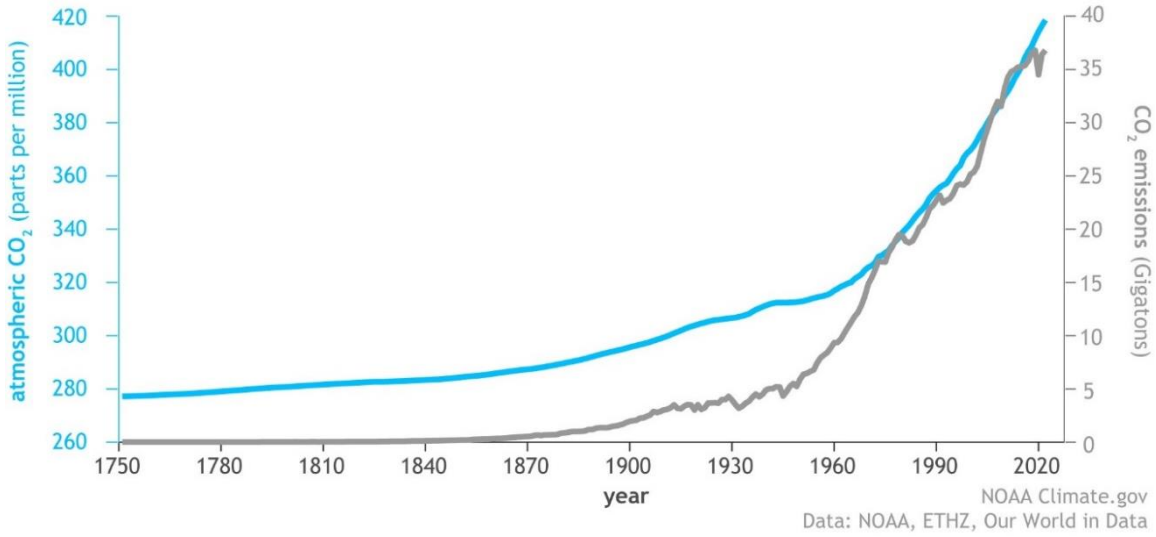

Figure 1 Global atmospheric carbon dioxide compared to annual emissions (1751-2022). Reproduced from NOAA Climate.gov [3].

The Intergovernmental Panel on Climate Change (IPCC) reported that achieving net zero CO_2 emissions is essential to mitigate the impact of human-induced global warming [2]. The endeavour to find a solution to this mitigation led to Carbon Capture, Utilization and Storage (CCUS). This technology enables deployment in existing industries, tackles emissions, supports decarbonization and removes CO_2 from the air. According to the International Energy Agency (IEA), the CCUS is subdivided into four: CO_2 Capture and Utilisation (CCU), CO_2 Transport and Storage, Direct Air Capture (DAC) and Bioenergy with Carbon Capture and Storage [8]. CCU describes a variety of processes where CO_2 is directly (i.e., enhanced oil recovery, dry ice, cooling systems, beverages) or indirectly (i.e., production of synthetic fuels, solvents, proteins, cement, concrete, and aggregates) captured and used. Additionally, the IEA established that supporting research, development and demonstration can be crucial to the implementation of promising CO_2-derived goods and services that are scalable and have a strong chance of eventually becoming competitive.

The core of the climate challenge lies in energy, and it is pivotal to the solution. Achieving net-zero (no GHG emissions) by 2050 requires moving away from fossil fuels and an investment in alternative energy sources that are clean, accessible, affordable, sustainable, and reliable, such as sunlight, wind, water, waste, and Earth's heat, the United Nations explains. Renewable energy is presently the most cost-effective power option in many parts of the world.

Power-to-X (P2X) is envisaged as one of the technologies able to transform CO_2 into e-fuel (energy carrier) from renewable energy, displacing fossil fuels. X products can be liquid, compressed gas fuels, or chemicals. P2X involves converting electricity into alternative forms like green hydrogen or e-fuels, using renewable sources such as wind or solar energy for electrolysis. This technology diverts electricity from production to sectors like transportation or chemicals. Green hydrogen, emission-free and made from renewable sources, offers a promising path to emission reduction in industry and transport. With wind and solar costs declining, green hydrogen becomes economically viable and competitive with traditional coal, gas, and nuclear power, according to Ørsted A/S [9]. Generally, CO_2 conversion demands high-energy processes or feedstocks. H_2 is a high energy feedstock capable of reacting with CO_2 [10].

Catalytic hydrogenation of CO_2 refers to the process of converting carbon dioxide into value-added molecules using hydrogen (H_2). During the generation of desired products from carbon dioxide, energy is required due to the thermodynamically stable nature of CO_2. According to this, a thermodynamic evaluation must be carried out to determine suitable operating conditions before achieving the chosen transformation. In general, high temperatures and pressures are required to convert CO_2. Hydrogen is employed as a reductive reagent, especially in thermal catalysis, as it is an energy carrier. Catalytic reduction of CO_2 can be

achieved by thermal, electrochemical, biochemical, photocatalysis or a combination of these processes (i.e. photoelectrochemical catalysis).

One of the most promising routes to recovery is the synthesis by catalytic hydrogenation. CO_2 valorisation remains an industrial challenge due to the chemical stability of CO_2 and the complexity and intensity of the process to reach meaningful yields. Some of the products obtained from CO_2 hydrogenation include syngas (CO/H_2), methane (CH_4), methanol (CH_3OH), formic acid ($HCOOH$), formaldehyde ($HCHO$), di-methyl ether (CH_3OCH_3), light olefins ($C_2 - C_4$) and higher hydrocarbons (C_{5+}). Figure 2 shows a representation of all the possible reactions with the associated catalysts. The generation of the desired product depends on factors such as the process, catalyst, operating conditions and duration of the reaction. The catalyst development is crucial to the selective synthesis of each product. Likewise, the synthesis routes play a key role in catalyst design, considering whether it will be direct or indirect (products subsequently transformed into the main molecule). In order to design, develop and test catalysts for a target product, many investigations have been conducted.

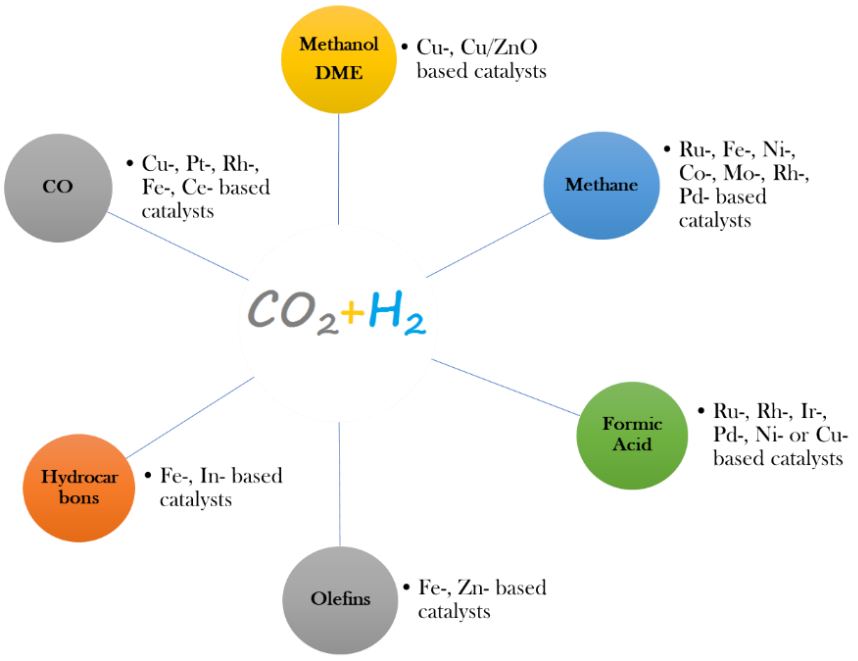

Figure 2 Reaction products of the hydrogenation of CO_2 into different products and catalysts often used.

The thermal catalysis has been extensively studied, particularly through heterogeneous catalysis, and scaled-up industrially. The thermal catalysis hydrogenation stays as the best

option owing to its higher efficiency and easier industrialization, despite its high energy consumption and the catalyst regeneration requirement.

Nowadays, a variety of processes are used to obtain the mentioned products, including the direct catalytic hydrogenation of CO_2, Reverse Water Gas Shift (RWGS), Sabatier reaction, hydroformylation, and a combination of them.

$$CO_2 + H_2 \rightleftharpoons CO + H_2O \qquad \textit{RWGS reaction} \qquad (1)$$

$$CO_2 + 4H_2 \rightleftharpoons CH_4 + 2H_2O \qquad \textit{Sabatier reaction} \qquad (2)$$

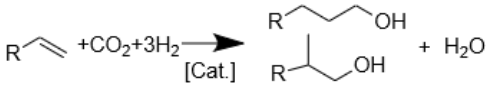

Hydroformylation (3)

For instance, CO is obtained by the RWGS reaction and, when combined with H_2, can be used in the production of hydrocarbons, aromatics, and olefins. This occurs through the RWGS–Fischer-Tropsch (FT) tandem reaction. Syngas has been used for more than 80 years in the FT and HF processes to produce aldehydes, olefins, higher alcohols iso-paraffins, aromatics, liquid fuels, etc.

Methane constitutes the primary component of synthetic natural gas (SNG). SNG denotes substitutes for natural gas designed to closely resemble its composition and properties. SNG derived from captured CO_2 holds significant promise as an energy carrier due to its compatibility with existing natural gas infrastructure, offering a pathway to transition to eco-friendly, renewable methane [11], [12]. The CO_2 methanation (Sabatier reaction, reaction (2)) is a highly exothermic process favoured at low temperatures and high pressures. Despite the inherent stability of CO_2, efficient catalysts are required to enhance the kinetics of its conversion into CH_4.

Olah, 2005 [13] and Olah et al., 2009 [14] proposed the concept of a "Methanol Economy", advocating for the chemical transformation of CO_2 into methanol, dimethyl ether, and further into synthetic hydrocarbons and their products. This approach provided a novel means to make fuels renewable and environmentally sustainable, potentially offsetting or even reversing carbon emissions. Methanol and DME, beyond serving as transportation fuels, are established and progressively employed as initial compounds for generating ethylene and propylene through the methanol to olefin (MTO) process [14].

The synthesis of methanol from carbon dioxide comprises two exothermic reactions (4) and (5), along with the concurrent presence of an endothermic reaction (RWGS) producing CO as a by-product.

$$CO_2 + 3H_2 \rightleftharpoons CH_3OH + H_2O \qquad \Delta H_{rx,298K} = -49.25\ kJ.mol^{-1} \qquad (4)$$

$$CO_2 + H_2 \rightleftharpoons CO + H_2O \qquad \Delta H_{rx,298K} = 41.16\ kJ.mol^{-1} \qquad (1)$$

$$CO + 2H_2 \rightleftharpoons CH_3OH \qquad \Delta H_{rx,298K} = -90.41\ kJ.mol^{-1} \qquad (5)$$

The typical synthesis process for DME involves two steps: 1) the synthesis of methanol from syngas, and 2) the dehydration of methanol. Thus, the formation of DME from CO_2 involves four chemical reactions: hydrogenation of CO_2 to methanol (4), Reverse Water Gas Shift (1), hydrogenation of CO (5) and methanol dehydration (6).

$$2CH_3OH \rightleftharpoons CH_3OCH_3 + H_2O \qquad \Delta H_{rx,298K} = -24.04\ kJ.mol^{-1} \qquad (6)$$

Most of the CO_2 transformations, on a laboratory scale, are carried out in fixed-bed reactors. But there are still some challenges such as the hot spot occurring because of the exothermic nature of reactions. In like manner, the literature shows the aim to address the deactivation or loss of catalysts throughout the processes. Therefore, to improve production, it is necessary to maximise the conversion of reactants. For this target, we can work on different aspects: the catalyst is one way (this is the job of the catalysis specialists) and the reactor design is another. Several investigations have been conducted to develop new catalysts to produce methane, methanol and, to a lesser extent, DME. Hence this thesis, once we have chosen the reaction to work on, we are going to study the possibilities of maximising CO_2 conversion by optimising the reactor design.

This thesis research is part of a collaboration program with the Ministry of Higher Education Science and Technology, MESCYT, from Dominican Republic, which has been in existence since 2016, aiming to train Dominican doctors in Process Engineering on sustainable development issues. A collaboration with the Automation, Process Engineering and Pharmaceutical Engineering Laboratory (LAGEPP) has also been established to leverage the complementary skills of LAGEPP and the Chemical Process Safety Laboratory (LSPC) in a subject that combines experimental science, simulation, and modelling.

Regarding the valorisation of CO_2, this thesis follows two theses conducted at LSPC: Bachar Alrafei's thesis, defended on 28/10/2019, entitled "Catalytic and kinetic study of CO_2 methanation in a fixed bed under microwave plasma" and Maxwell Quezada's thesis, entitled "Catalytic hydrogenation of CO_2 to methanol in a fixed bed under conventional heating and DBD plasma" defended on 15/10/2020. These two theses have led to the development of an experimental pilot for the hydrogenation of CO_2 into valuable products, studying kinetics, and designing innovative processes by using microwave plasma in methanation, DBD plasma for methanol synthesis, and precisely studying the performance of methanol production through simulation using ASPEN+.

These theses have demonstrated the interest in valorising CO_2 into methane and/or methanol. They have also highlighted the limitations and drawbacks of these pathways. Concerning methane, limitations lie in temperature control in the reactor and catalyst deactivation. The catalytic hydrogenation process into methane is mature, well-studied, and industrial units are already operational. For methanol, thermodynamic equilibrium strongly limits the conversion of CO_2, and deactivation can also occur. Through this thesis, we will seek to produce a higher value-added molecule than methanol through CO_2 hydrogenation while maximising CO_2 conversion.

Initially, this thesis will focus on researching a molecule to produce and a synthesis pathway to consume a maximum of CO_2 by shifting the thermodynamic equilibrium. In the second part, we will aim to optimise operating conditions and the reactor, always with the same objective, and evaluate the maximum performance we can achieve in terms of conversion and yield towards the sought-after molecule.

Thus, this thesis is structured into five chapters:

I. The first chapter provides a review of the literature on the potential products of CO_2 hydrogenation. The thermodynamics of three molecules (methane, methanol and DME), as well as the catalysts used and their reaction mechanisms, are examined, followed by the existing kinetic models. Typical industrial and laboratory-scale reactors are also described. The final section focuses on process simulations of methanol and DME syntheses.
II. The second chapter describes laboratory reactor experiments that have been conducted to obtain experimental data on CO_2 conversion and product yields. The materials, setup, experimental methodologies, and protocols are showed, and results are discussed.
III. The kinetic modelling of the selected reaction is presented in the third chapter. The description of the model includes the assumptions considered for parameter estimation and data fitting. Furthermore, the accuracy of the model is evaluated.
IV. Chapter fourth is dedicated to the simulation and optimisation of a reactor through its precise temperature control.
V. Finally, chapter fifth provides a summary of the key findings on this thesis research and proposes potential future perspectives.

References

[1] United Nations, “Causes and Effects of Climate Change.” https://www.un.org/en/climatechange/science/causes-effects-climate-change (accessed Jan. 06, 2024).

[2] IPCC, “Climate Change 2023: Synthesis Report. Contribution of Working Groups I, II and III to the Sixth Assessment Report of the Intergovernmental Panel on Climate Change [Core Writing Team, H. Lee and J. Romero (eds.)]. IPCC, Geneva, Switzerland.,” Jul. 2023. doi: 10.59327/IPCC/AR6-9789291691647.

[3] R. Lindsey and E. Dlugokencky, “Climate Change: Atmospheric Carbon Dioxide | NOAA Climate.gov,” 2023. https://www.climate.gov/news-features/understanding-climate/climate-change-atmospheric-carbon-dioxide (accessed Dec. 08, 2023).

[4] O. Tursunov, L. Kustov, and A. Kustov, “A Brief Review of Carbon Dioxide Hydrogenation to Methanol Over Copper and Iron Based Catalysts,” *Oil Gas Sci. Technol. – Rev. d’IFP Energies Nouv.*, vol. 72, no. 5, p. 30, Sep. 2017, doi: 10.2516/OGST/2017027.

[5] A. Ateka, M. Sánchez-Contador, A. Portillo, J. Bilbao, and A. T. Aguayo, “Kinetic modeling of CO_2+CO hydrogenation to DME over a CuO-ZnO-ZrO2@SAPO-11 core-shell catalyst,” *Fuel Process. Technol.*, vol. 206, p. 106434, Sep. 2020, doi: 10.1016/j.fuproc.2020.106434.

[6] J. Schmidt *et al.*, “A new perspective on global renewable energy systems: why trade in energy carriers matters,” *Energy Environ. Sci.*, vol. 12, no. 7, pp. 2022–2029, Jul. 2019, doi: 10.1039/C9EE00223E.

[7] A. Rafiee, K. Rajab Khalilpour, D. Milani, and M. Panahi, “Trends in CO_2 conversion and utilization: A review from process systems perspective,” *J. Environ. Chem. Eng.*, vol. 6, no. 5, pp. 5771–5794, Oct. 2018, doi: 10.1016/J.JECE.2018.08.065.

[8] S. Budinis, M. Fajardy, and C. Greenfield, “Carbon Capture, Utilisation and Storage - Energy System - IEA,” *July*, 2023. https://www.iea.org/energy-system/carbon-capture-utilisation-and-storage (accessed Jan. 11, 2024).

[9] Ørsted, “Decarbonizing the U.S. Economy with Power-to-X,” 2023. https://us.orsted.com/renewable-energy-solutions/power-to-x (accessed Feb. 09, 2024).

[10] M. Matzen and Y. Demirel, “Methanol and dimethyl ether from renewable hydrogen

and carbon dioxide: Alternative fuels production and life-cycle assessment," *J. Clean. Prod.*, vol. 139, pp. 1068–1077, Dec. 2016, doi: 10.1016/J.JCLEPRO.2016.08.163.

[11] A. Borgschulte *et al.*, "Sorption enhanced CO_2 methanation," *Phys. Chem. Chem. Phys.*, vol. 15, no. 24, pp. 9620–9625, May 2013, doi: 10.1039/C3CP51408K.

[12] L. Gómez, I. Martínez, M. V. Navarro, and R. Murillo, "Selection and optimisation of a zeolite/catalyst mixture for sorption-enhanced CO_2 methanation (SEM) process," *J. CO_2 Util.*, vol. 77, p. 102611, Nov. 2023, doi: 10.1016/J.JCOU.2023.102611.

[13] G. A. Olah, "Beyond Oil and Gas: The Methanol Economy," *Angew. Chemie Int. Ed.*, vol. 44, no. 18, pp. 2636–2639, Apr. 2005, doi: 10.1002/ANIE.200462121.

[14] G. A. Olah, A. Goeppert, and G. K. S. Prakash, "Chemical recycling of carbon dioxide to methanol and dimethyl ether: From greenhouse gas to renewable, environmentally carbon neutral fuels and synthetic hydrocarbons," *J. Org. Chem.*, vol. 74, no. 2, pp. 487–498, Jan. 2009, doi: 10.1021/JO801260F/ASSET/IMAGES/LARGE/JO-2008-01260F_0001.JPEG.

Chapter 1

1. CO_2 hydrogenation products and processes: State of the Art

1.1. The products of CO_2 hydrogenation

Catalytic reduction of CO_2 can be achieved by thermal, electrochemical, biochemical [1], [2], photocatalysis [3] or a combination of these processes (i.e. photoelectrochemical catalysis [4]). Thermal catalysis has been extensively studied, particularly through heterogeneous catalysis, and scaled-up industrially. Despite its high energy consumption and the need for catalyst regeneration, thermal catalytic hydrogenation remains the preferred option due to its superior efficiency and easier industrial implementation. It is the oldest and most established technology in this field [5], [6].

Electrochemical catalysis permits CO_2 reduction at low temperatures using electrode potentials. Yaashikaa et al., 2019 [1] cited some metal complexes such as Ni(II), Rh, Co(II), Re(I) and Ir(III) used as catalysts in electrochemical CO_2 transformation. The authors said that this technology could be simply scaled up. Notwithstanding, it reduced efficiency and it came at a high cost [1], [3]. Correspondingly, although photocatalysis is carried out by light irradiation, it requires a meaningful energy input to have weak selectivity and low reaction activity [1], [7].

Biochemical catalysis uses enzymes to convert CO_2 in value-added molecules. Some microbial species explored for the production of bio-alcohols, bio-plastics, bio-diesel and other products are: S*ynechococcus elongates, Rhodobacter capsulatus, Ideonella sp., Phaeodactylum tricornutum, Chlorella vulgaris, Nannochloropsis oculate, Synehocystis sp., Trichosoporon moniliiforme, Ralstonia eutropha, Porphyridium aerugineum* [1]. Carbonic anhydrase contains zinc in its active site allowing the CO_2 transformation to bicarbonates ions, but its instability blocks its industrial application [2]. Review articles are available for those concerned in this field [1], [8].

Table 1.1 presents the mentioned CO_2 hydrogenation products and their utilization, as well as the process by which they can be formed. Two types of catalyst are used for the CO_2 conversion: homogeneous and heterogeneous [9]. Industrially, the latter is preferred. A few

investigations have been performed with homogeneous catalysts, compared with heterogeneous catalytic systems [10]. Homogenous catalysts are most commonly used for formic acid and aldehyde synthesis. [11]. Table 1.1 also gives several catalysts and operating conditions.

Harnessing renewable energy to convert CO_2 into fuels and chemicals, with the potential of replacing fossil feedstocks in the chemical industry, is an outstanding alternative to mitigate greenhouse gas emissions and reduce reliance on fossil fuels. At the LSPC there is a facility used to perform two research theses for CO_2 hydrogenation, one for methane production [12] and the other for methanol synthesis [13]. Hence, we decided to focus our research on the three valuable molecules: methane, methanol, and dimethyl ether syntheses to develop a more efficient process.

Table 1.1 Summary of applications, processes, catalysts, and reaction conditions for CO_2 hydrogenation into several products.

Product	**Uses**	**Process**	**Catalyst**	**T (°C)**	**P (bar)**	**Ref.**
Syngas	Chemicals, fuel and hydrogen production, power generation.	Reverse water gas shift (RWGS) reaction	Cu-, Au-, Ce-, Fe-, Ir-, Pd-, Pt-, Rh-, AuPd-, NiFe-, NiK-, NiCu-, NiCo-, PtPd-, PtCo-, KPt-, PdIn- based catalysts	200-850	1-20	[14], [15]
CH_4	Fuel (internal combustion engines, fuel cells) and as a feedstock for industrial processes.	Sabatier reaction	Ni-, Co-, Ru- based catalysts, Ni-based catalysts + zeolites, Ni-based catalysts + siliceous materials	180-470	1-30	[15]–[19]
CH_3OH	Fuel (internal combustion engines, fuel cells), and as a feedstock for chemicals.	Direct or indirect (RWGS reactor + MeOH reactor) synthesis	Cu-, CuZn-, NiGa-, Pd-, CoGa-, In_2O_3- based catalysts	100-450	0.1-100	[5], [20]–[23]
HCOOH	Production of leather, rubber, textiles, food industry, and pharmaceuticals.	Direct synthesis or hydro-thermal process	Ru-, Rh-, Ir-, Pd-, Au-, Ni-based catalysts	40-100	30-180	[5], [24], [25]
HCHO	Production of glues, resins, plastics, chemicals, and textiles.	Direct synthesis	Pt-, Ru- based catalysts	25-90	20-70	[26], [27]
CH_3OCH_3	Fuel (diesel engines), aerosol propellant, refrigerant, chemical feedstock, and as LPG substitute.	Direct or indirect synthesis (MeOH synthesis + MeOH dehydration)	Methanol catalysts + zeolite or + γ-Al_2O_3	190-350	10-50	[28]–[31]
C_2-C_4	Production of plastics, synthetic rubber, fuel (gasoline, diesel fuel, jet fuel and LPG), textiles, and adhesives.	Direct or indirect (MeOH synthesis + MeOH to olefins or RWGS + Fischer-Tropsch (FT) to olefins) synthesis	Fe-, Co-, Cu-, Na-, K-, Cs-, Mn- based catalysts	200-400	5-50	[3], [32], [33]

C_5+	Fuel (petrochemical feedstock, power generation), production of plastics, solvents, lubricants, chemicals, adhesives, and wax.	Direct or indirect synthesis (RWGS+FT, MeOH + MTH)	Na-/zeolite, methanol or RWGS catalysts + zeolite-based catalyst (Zr-, In_2O_3-, Zn-, Cu-, Cr_2O_3-, Fe- based catalysts + HZSM5 or + SAPO-34 or + γ-Al_2O_3)	280-350	10-40	[33]–[36]

1.2. Methane, methanol, and dimethyl ether synthesis description

1.2.1. Methane synthesis

CO_2 methanation (Sabatier reaction) is a mature catalytic process used to produce synthetic natural gas (SNG). This process was proposed in 1897 by the French chemists Paul Sabatier and Jean-Baptiste Senderens. The reaction involves the transformation of CO_2 combined with H_2 to form methane (CH_4) and water (H_2O). The chemical equation is:

$$CO_2 + 4H_2 \rightleftharpoons CH_4 + 2H_2O \quad \Delta H_{298K} = -164.65\ kJ \cdot mol^{-1} \quad \Delta G_{298K} = -113.26\ kJ \cdot mol^{-1} \qquad (1.1)$$

The reaction is typically accompanied by the RWGS reaction.

$$CO_2 + H_2 \rightleftharpoons CO + H_2O \quad \Delta H_{298K} = 41.16\ kJ \cdot mol^{-1} \quad \Delta G_{298K} = 28.65\ kJ \cdot mol^{-1} \qquad (1.2)$$

Methane represents a good storage fuel option of Power-to-Gas (PtG). Since, compared to H_2, it is easy to transport, has lower storage costs, and higher energy density (smaller tank needed) [37]. Besides, existing gas infrastructure can be used for methane distribution. In addition, the International Energy Agency (IEA) informed that the natural gas production in 2020 was 4.01 trillion cubic meters, accounting for about a quarter of global electricity generation [38]. It has a technology readiness level (TRL) of 9, meaning that it has been proven in an operational environment. Some examples are HELMETH (Integrated High-Temperature Electrolysis and Methanation, Germany, 2014-2017), MINERVE (Management of Intermittent & Nuclear Electricity by High Efficiency Electrochemical Reactor for the Valorisation of CO_2 in flexible Energies, Germany, 2013-2016), Jupiter 1000 (GRTgaz, 2020), DEMETHA and METHAMAG projects (the SOLIDIA platform, France, 2018-2022), Storengy (Pau, France) and Audi e-gas plant (Werlte, Germany).

1.2.2. Methanol synthesis

Hydrogenation of CO_2 to methanol (CTM) is a combined process resulting from three reactions, Eq. (1.2)-(1.4). In these reactions, the preferred direct formation of methanol (Eq. (1.3)) from CO_2 may be accompanied by a combination of RWGS (Eq. (1.2)) followed by the hydrogenation of CO (Eq. (1.4)) to methanol. The relative occurrence of these parallel or consecutive reactions is difficult to quantify under operating conditions. It is generally a

function of the thermodynamic conditions of the process and the chemical nature of the catalyst [39].

$$CO_2 + 3H_2 \rightleftharpoons CH_3OH + H_2O \qquad \Delta H_{298K} = -49.25\ kJ \cdot mol^{-1} \qquad \Delta G_{298K} = -8.90\ kJ \cdot mol^{-1} \qquad (1.3)$$

$$CO_2 + H_2 \rightleftharpoons CO + H_2O \qquad \Delta H_{298K} = 41.16\ kJ \cdot mol^{-1} \qquad \Delta G_{298K} = 28.65\ kJ \cdot mol^{-1} \qquad (1.2)$$

$$CO + 2H_2 \rightleftharpoons CH_3OH \qquad \Delta H_{298K} = -90.41\ kJ \cdot mol^{-1} \qquad \Delta G_{298K} = -25.17\ kJ \cdot mol^{-1} \qquad (1.4)$$

Methanol is a Power-to-Liquid (PtL) alternative. It is easy to transport, due to its liquid state at ambient conditions. Methanol has a wide range of applications in chemical and energy fields. In chemical sector, methanol is used for the synthesis of acetic acid, methyl tertiary butyl ether (MTBE), MTO/MTP, methylamines, dimethyl ether, and formaldehyde. Besides, it is a primarily organic industrial solvent. Its high octane rating enables it to be used as fuel for heat engines and fuel cells. [40]

The technology of methanol synthesis from CO_2 and H_2 is mature (TRL 8-9). Its current production cost is estimated by the International Renewable Energy Agency (IRENA) in the range USD 800–2400 per ton, depending on the technology applied to capture the CO_2 (bioenergy with carbon capture and storage [BECCS] or direct air capture [DAC]). Nonetheless, a decrease is anticipated between USD 250-630 per ton by 2050. [41]

1.2.3. Dimethyl ether (DME) synthesis

DME is the simplest of the ethers produced directly from syngas ($CO/CO_2/H_2$ or CO/H_2) or by methanol dehydration on acid systems [42]. This chemical compound is mainly used as an aerosol propellant as alternative to the Chlorofluorocarbons (CFCs) compounds. In like manner, DME is used as refrigerant gas, as raw material for the production of methylation agents, polishing products, methyl acetate, diethyl sulphate, ethanol, light olefins, aromatics, gasoline and other chemicals [43], [44]. Since DME is non-carcinogenic molecule and has a minimal toxicity level [45], it can replace methanol in processes such as methanol to olefins (MTO) and methanol to gasoline (MTG) [46]. In addition, DME is non-corrosive, non-teratogenic, neither mutagenic [47].

In the hydrogenation of CO_2, dimethyl ether (DME) generation demonstrates superior energy efficiency compared to the production of hydrocarbons or alcohols [48]. DME is an ecological and economical option fuel for future applications [49]. It lacks of Carbon-Carbon bond [49], which results in low emissions of particulates, SO_x, NO_x [44], [49], because smoke particles

rely exclusively on carbon-carbon bonds. Its combustion does not produce soot [43] and will not deplete the ozone layer [47]. DME, with a high cetane number, is a promising ultra-clean fuel substitute to diesel and liquefied petroleum gas (LPG) [43], [47], [48]. Its autoignition temperature, which is lower than that of other fuels, makes DME the cleanest high-efficiency compression ignition fuel [47]. Nonetheless, the downsides of the DME use are low viscosity, which can cause leakage, low lubricity requiring lubricating agent [50], and low lower heating value (LHV) compared to LPG, gasoline and diesel [43] (1.2 litres of DME are equivalent to 1 litre of diesel based on the LHV [47]). Table 1.2 displays the comparison of physical and chemical properties of DME and methanol with other fuels.

Table 1.2 Physical and chemical properties of DME and other fuels.

Properties	**Unit**	**DME CH_3OCH_3**	**Methanol CH_3OH** [51]	**LPG C_2-C_5**	**Gasoline C_4-C_{12}** [51]	**Diesel C_8-C_{25}** [51]
Vapor pressure at 293.15 K	Bar	5.3 [44]	0.12-0.14	2.1-8.1 [52]	0.34-1.03	≈0
Boiling point temperature	K	248 [47]	338	231 [47]	300-498	453-613
Flash point temperature	K	269 [53]	284	169 [52]	230	333-353
Auto-ignition temperature	K	508 [44]	737	638-743 [52]	530	≈589
LHV	$MJ \cdot kg^{-1}$	28.99 [47]	19.93-20.09	50.03 [47]	41.87-44.19	41.87-44.19
Cetane number	-	55-60 [47]	5 [47]	5 [47]	4-20 [47]	40-55 [47]
Stoichiometric air/fuel ratio	wt./wt.	9.6 [44]	6.45	15.4 [54]	14.7	14.7
Liquid density at 288.71 K	$kg \cdot m^{-3}$	0.67* [47]	0.79	0.49* [47]	0.72-0.78	0.80-0.89
Relative vapor density (air=1)	-	1.6 [53]	1.1	1.9 [52]	3-4	>3
Carbon	wt.%	52.2 [44]	37.5	82-83 [54]	85-88	87
Hydrogen	wt.%	1-3 [44]	12.6	17-18 [54]	12-15	13
Oxygen	wt.%	34.8 [44]	49.9	0 [54]	0	0

*at 293 K.

According to several investigations, the LPG technologies used for transport and storage could be converted for the use of DME thanks to their close physical and chemical properties, what enable to apply the same safety measures [43], [44], [49]. In 1995, Amoco (currently British Petroleum), Haldor Topsøe and Navistar International Corporation researched and demonstrated the reliability of DME as fuel for diesel engines[43], [44]. Since then, DME has been certified as a non-polluting ultra-clean fuel by California Ultra Low Emission Vehicle (ULEV) [43], [44].

Methanol Institute [55] informed that global dimethyl ether market volume approximated to be 3,740.46 KT in 2014. DME can be used directly in boilers, burners, engines, or blended with other liquified gases without requiring any change to existing devices. It allows a partial decarbonation of industrial technologies and LPG vehicles. Similarly, with existing cookers and heaters, domestic and non-domestic heating is possible with a blend of up to 20% DME with LPG or renewable LPG. [56]. Primarily in China, DME is used as a propane supplement in bottled cooking gas [55]. Besides, DME is a hydrogen carrier which is simple to separate and make it available as a fuel [56]. In addition, Isuzu Trucks, Auto manufacturers Shanghai Diesel Co, Nissan Diesel, and AB Volvo are actively developing DME fueled heavy duty vehicles [55].

Nowadays, world production of DME stands at nearly 5 million t/year, mainly via methanol dehydration [55]. Most of DME production is in China [47], [55]. In Japan, South Korea, Brazil, Egypt, India, Indonesia, Iran, Uzbekistan, Vietnam, the United Kingdom, the United States and in Europe, there are established or under development DME production plants [47], [55], [56]. Oberon Fuels [57] was the first company to build a commercial scale plant to produce DME from syngas or renewable methanol. They project over 200 million gallons per year later this decade.

DME is typically synthesized in two steps: 1) methanol synthesis from syngas and 2) methanol dehydration. For methanol synthesis, commercial CZA ($CuO/ZnO/Al_2O_3$) catalyst is generally used, and to dehydrate the methanol, acid catalysts [43] such as zeolites [58], γ-Al_2O_3 or silica-modified alumina are employed [31], [42], [49], [59]–[61].

In direct hydrogenation of CO_2 to DME, methanol is formed as an intermediate which dehydrates to DME. Reactions (1.2) to (1.4) are potentially involved. As a result, methanol is synthesized and successively dehydrated following Eq. (1.5), in a single reactor containing bifunctional catalysts. The thermodynamic properties of the last reaction are given below. CO is a by-product of the process as shown in reactions (1.2) and (1.4).

$$2CH_3OH \rightleftharpoons CH_3OCH_3 + H_2O \qquad \Delta H_{298K} = -24.04\ kJ \cdot mol^{-1} \qquad \Delta G_{298K} = -16.73\ kJ \cdot mol^{-1} \qquad (1.5)$$

Summarizing, methane, methanol and DME synthesized from the hydrogenation of CO_2 are exothermic reactions occurring simultaneously with an endothermic reaction (RWGS) which results in CO as a by-product at high temperature. Water is also produced in all three syntheses. Based on the TRL values (8-9) for methane and methanol syntheses, these are mature processes. Fuel options for Power-to-X technology include methane, methanol, and DME.

1.3. Thermodynamic study

Thermodynamics have been reported for CH_4, methanol and DME. Although known from the literature, we decided to perform our own simulations under the conditions we wanted to compare.

In order to visualize the thermodynamic equilibrium obtained if methane or methanol or DME is the desired product, simulations of the equilibrium through CO_2 conversion and product yields were carried out by the Gibbs free energy minimisation method. Gibbs free energy minimisation facilitates computation of the equilibrium molar fraction of a reaction. The RGIBBS reactor of Aspen Plus® uses this basis to calculate equilibrium compositions where the involved components i must be indicated without specifying possible reactions. Eq. (1.6) gives formula of the reaction the equilibrium constant (K_{eq}) at a given temperature, pressure and feed used for calculation. The Equation of State used was Soave–Redlich–Kwong (SRK).

$$K_{eq} = \frac{\prod_{i=products} a_i}{\prod_{i=reactants} a_i} \equiv exp\left(\frac{-\Delta_r G_j^o}{RT_0}\right) \tag{1.6}$$

where $\Delta_r G_j^o$ is the Gibbs free energy of reaction j, and a_i is the activity coefficient of species i, R is the molar gas constant and T_0 is the temperature. The activity coefficient is defined by Eq. (1.7),

$$a_i = f_i(mixture)/f_i(pure\ standard\ state) \tag{1.7}$$

where f_i is the fugacity of species i. As a result, chemical equilibrium is calculated as:

$$K_{eq} = \frac{\prod_{i=products} f_i}{\prod_{i=reactants} f_i} \tag{1.8}$$

CO_2 conversion and product yields were evaluated from composition results considering molar flows (F) and from stoichiometric coefficients (ν) for yields (see Eq. (1.9)-(1.10)).

$$X_{CO_2} = \frac{F_{CO_2,in} - F_{CO_2,out}}{F_{CO_2,in}} \cdot 100 \tag{1.9}$$

$$Y_i = \frac{F_{i,out}}{F_{H_2,in}} \left|\frac{\nu_{H_2}}{\nu_i}\right| \cdot 100 \tag{1.10}$$

1.3.1. Methane synthesis

Methanation reaction (Eq. (1.1)) is equilibrated and exothermic. Brooks et al., 2007 [62] explained that low temperature favours the overall reaction (1.1), but a catalyst must be used owing to kinetic limitations. Additionally, per Le Chatelier's principle, elevated pressures are favourable for CO_2 methanation. Catalytic methanation is generally carried out in a range of temperature [200-550 °C] and of pressure [1-100 bar] [63].

Figure 1.1 depicts the thermodynamic equilibrium results of CO_2 methanation at 1 and 40 bars for a stoichiometric feed. CO_2 conversion and CH_4 yields are higher at lower temperatures, consistent with the exothermic character of the reaction. Likewise, increasing pressure favours the methanation of CO_2 and decrease the yield of CO. Hence, it confirms the preference for working at low temperatures and high pressures.

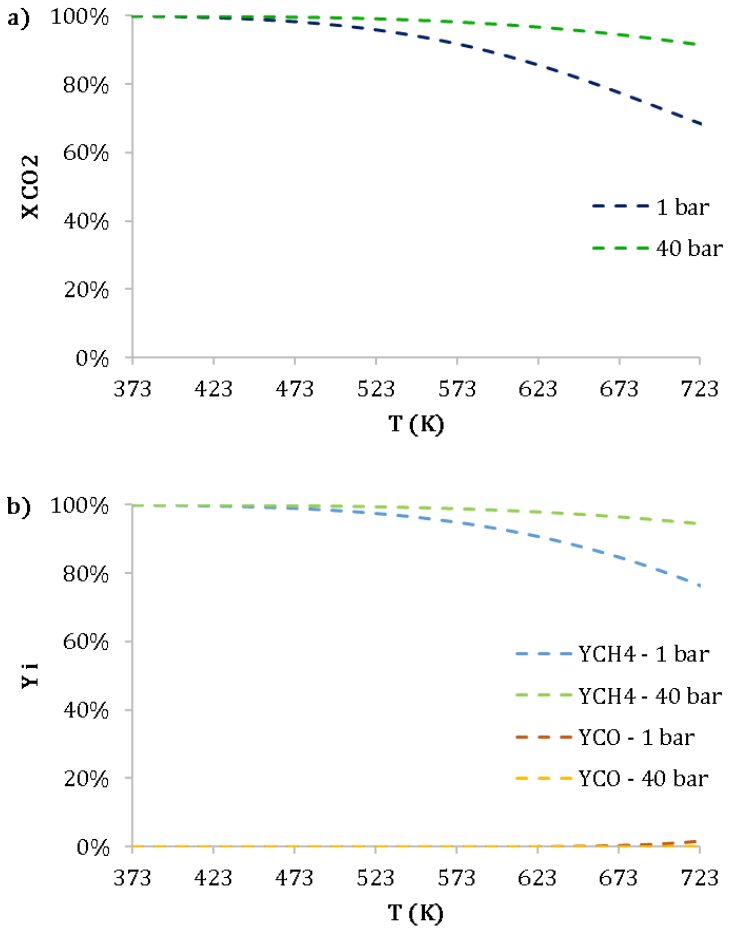

Figure 1.1 Thermodynamic equilibrium a) CO_2 conversion, b) CH_4 and CO yields with increasing temperature for methanol synthesis. Computed using Aspen Plus® RGIBBS reactor with feed molar ratio of H_2/CO_2=4 and P=1 and 40 bar.

The catalysts must be chosen based on the stability of CO_2 at ambient conditions and the exothermicity of the reaction. This is to attain high CO_2 conversions and high CH_4 yields and

then avoid or reduce the coke deposition causing the catalyst deactivation. Further, the water generated needs to be examined, since it inhibits CO_2 methanation at catalyst active sites.

1.3.2. Methanol synthesis

The methanol production reaction from CO_2 and CO (Eq. (1.3) and Eq. (1.4)) are exothermic reactions, favoured by low temperatures and high pressures, in which molecular reduction occurs. This is confirmed by the enthalpy and Gibbs free energy values (Eq. (1.3) and Eq. (1.4)) have a ΔH_{298K} of -49.25 kJ.mol^{-1} and -90.41 kJ.mol^{-1}, respectively). In contrast, Eq. (1.2) (RWGS) is endothermic where the number of moles remains constant. As CO_2 is kinetically inert and thermodynamically very stable at 298K and atmospheric pressure, it requires an active catalyst to react with it. Increasing the temperature (e.g., >473.15 K) would lead to CO_2 activation and methanol formation. Thus, the overall process becomes a limited equilibrium process in which thermodynamics interacts to control conversion and product selectivity.

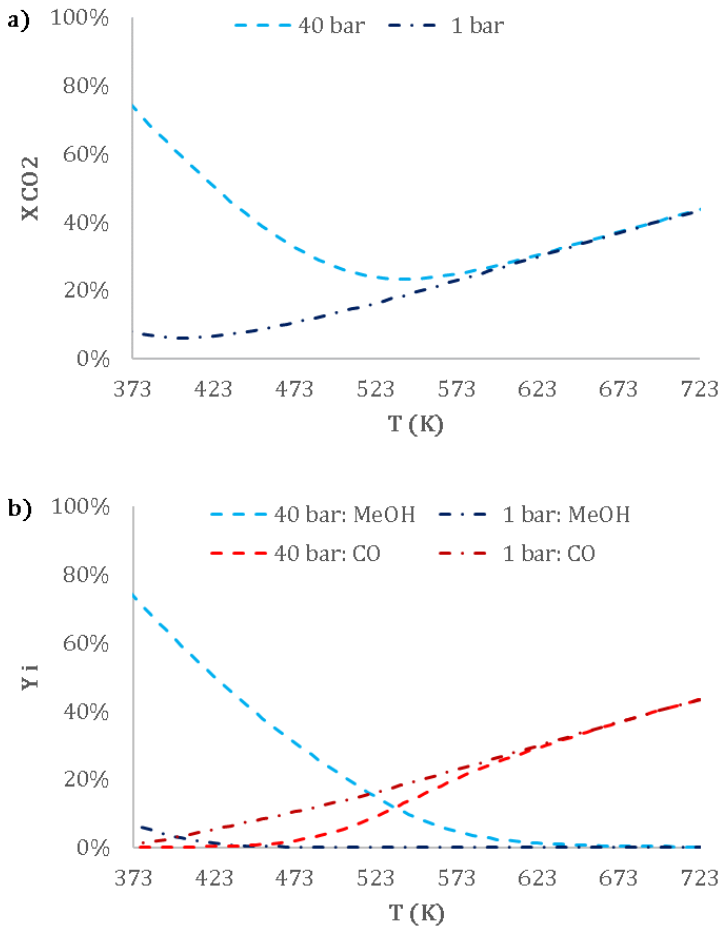

Figure 1.2 Thermodynamic equilibrium a) CO_2 conversion, b) methanol and CO yields with increasing temperature for methanol synthesis. Computed using Aspen Plus® RGIBBS reactor with feed molar ratio of H_2/CO_2=3 and P=1 and 40 bar.

Like CO_2 methanation, methanol synthesis is thermodynamically favoured by high pressure and moderate temperature as displayed in Figure 1.2. At 1 bar and with stoichiometric feed ratio, the trend is to produce carbon monoxide more than methanol and with a lower CO_2 conversion. On the other hand, increasing pressure influences CO_2 conversion and methanol yield positively and decreases CO yield.

1.3.3. DME synthesis

The thermodynamics equilibria of reactions involved in the synthesis of CO_2 to DME were evaluated in Aspen Plus® RGIBBS reactor as explained in section 1.3.1 but considering the reagents and products of the reactions Eq. (1.2)-(1.4). Figure 1.3 illustrates the effect of temperature and feed molar ratio (H_2/CO_2) at a specified pressure (40 bar) on the CO_2 conversion and product yields. The same behaviour for CO_2 conversion is observed for all feed molar ratios (Figure 1.3a). It decreases until it reaches approximately 548 K, where it begins to increase again. However, CO_2 conversion and DME and MeOH yields are unfavoured by the diminution of H_2/CO_2 molar ratio. Operating at temperatures below 548 K favours DME and MeOH yields. Conversely, higher temperatures promote the rise in by-product, as observed in the CO yield in Figure 1.3b. The highest CO_2 conversion and DME yield are noticed at 373 K over the studied range.

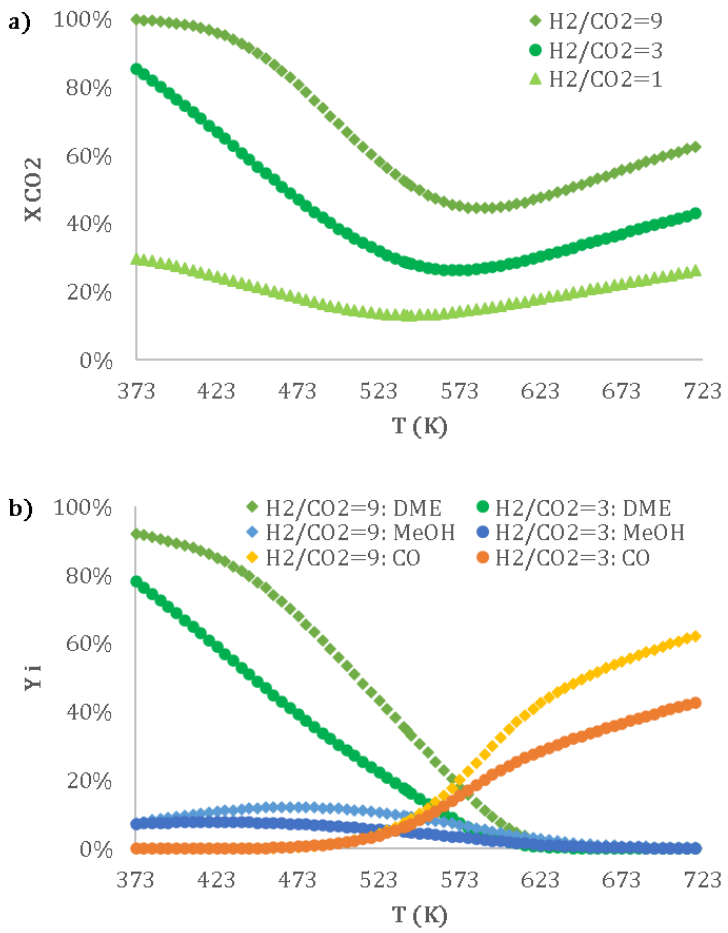

Figure 1.3 Thermodynamic equilibrium a) CO_2 conversion; b) DME, Methanol and CO yields with increasing temperature. Computed using Aspen Plus® RGIBBS reactor at 40 bar and with different feed molar ratio of H_2/CO_2=1, 3 and 9.

Figure 1.4 illustrates the effect of temperature and pressure at a molar ratio of H_2/CO_2=3 on a) CO_2 conversion and b) product yields at thermodynamic equilibrium. Figure 1.4a displays that at atmospheric pressure, CO_2 conversion is minimal when compared to higher pressures. Additionally, the product obtained is basically CO. CO_2 conversion and DME and MeOH yields rise with pressure. At 80 and 120 bars and temperatures above 603 K, the CO_2 is mostly transformed into CO. Thus, direct DME synthesis is favoured at high pressure and mild temperatures. Based on Le Chatelier's principle, as the formation of DME from methanol (Eq. (1.5)) is exothermic, low temperatures are expected to lead to a higher yield of DME and a lower yield of CO, as the latter is an endothermic reaction (RWGS). Likewise, considering the discrepancy of moles between reactants and products of CO_2 hydrogenation to methanol and methanol dehydration, high pressures are suitable for CO_2 to DME. This is what is shown in Figure 1.4.

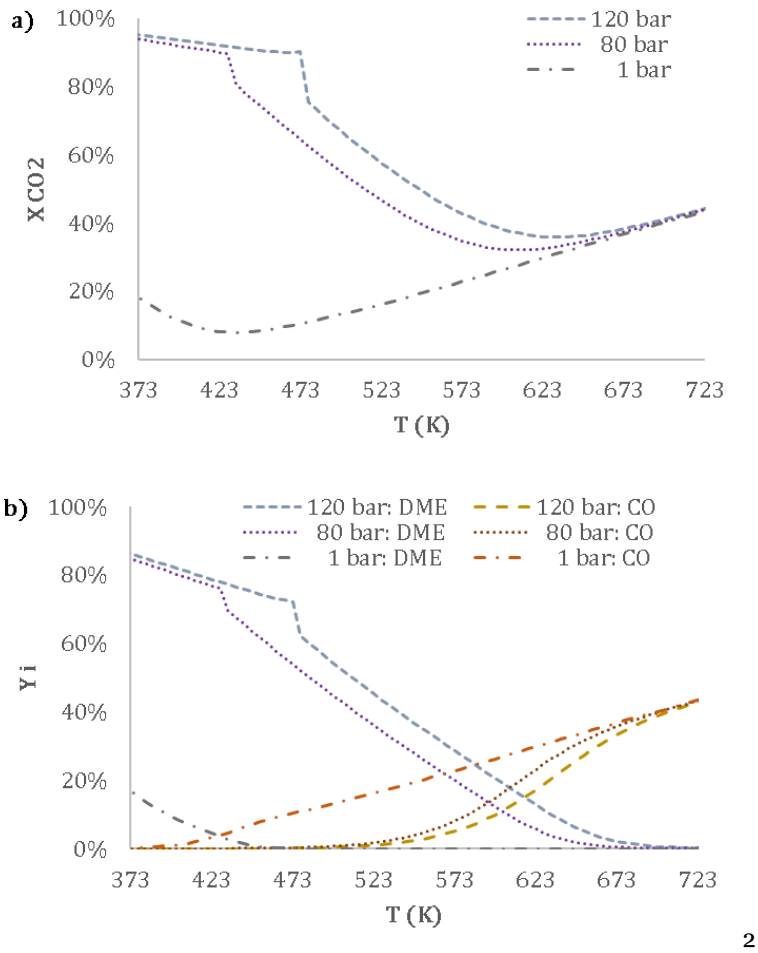

Figure 1.4 Thermodynamic equilibrium on a) CO_2 conversion and b) DME, Methanol and CO yields with increasing temperature. Computed using Aspen Plus® RGIBBS reactor with a fixed molar ratio of H_2/CO_2=3 and varying pressure: P=1, 80 and 120 bars.

In accordance with the bubble point and dew point curves for a reacting mixture of H_2/CO_2=3/1 to MeOH/DME/CO/H_2O presented by Stangeland et al., 2018 [60], the change in the curves at temperatures below 483 K and at higher pressures (Figure 1.4) is related to the phase change from vapour to liquid.

Chang Liu & Liu, 2022 [48] compared the compositions at the thermodynamic equilibria for the direct CO_2 to DME process (in one reactor) and the indirect process (two steps: methanol synthesis followed by dehydration in separate reactors). They concluded that DME yield is greater via the direct process than the indirect CO_2 hydrogenation to DME. Therefore, thermodynamically, CO_2 to DME is more advantageous [48]. Besides, one step CO_2 to DME synthesis is recommended to lower production costs [47].

Comparing the thermodynamic equilibria, the highest CO_2 conversions and desired product yields are obtained for the methane synthesis. For the DME synthesis, the CO_2 conversions and desired product yields are lower, but they are higher than those obtained for the methanol synthesis alone. In all cases, the increase in pressure led to an increase in CO_2 conversion and

a decrease in CO yield. For the DME synthesis, the lower feed molar ratio, $H_2/CO_2=1$, implies the lower CO_2 conversion.

1.4. Catalysts for CO_2 hydrogenation

1.4.1. Methane synthesis

The hydrogenation of CO_2 to methane was studied using transition and noble metals [15]–[19], [64]. Numerous investigations have been performed with bifunctional catalysts (metal + support) for SNG. Nickel (Ni-) based catalysts are usually preferred for CO_2 methanation, since it is low-cost with respect to other metal catalysts and has high activity and selectivity. Though, $Ni(CO)_4$ appears causing sintering, poisoning and carbon deposition, and subsequently catalyst inactivation.

Previous published research organized CO_2 methanation catalysts according to their activity, Co < Fe < Ni < Rh < Ru, and selectivity, Ni < Rh < Co < Fe < Ru [65]. Besides, other transition metals (Mo, Ag, Os, Ir, Pt) have been tested in experiments up to 800 °C [66]. Ridzuan et al., 2022 [67] and Younas et al., 2016 [65] agreed that Ru-based catalysts are more active and have prominent CH_4 yield. Nevertheless, its use is limited due to its high cost and limited availability [65], [67]. For instance, in the HELMETH project, nickel and ruthenium catalysts were tested and optimised. But, due to costs, the Ru-based catalysts were excluded in the initial project phase [68]. Moreover, Stangeland et al., 2017 [69] expressed that other catalysts produce simultaneously CH_4, CH_3OH and CO (RWGS) in CO_2 hydrogenation to methane, unlike Ni and Ru based catalysts which produce almost exclusively CH_4. Hence, the predominance of Ni based catalysts is proven.

It is crucial to design and develop a Ni-based catalyst capable of boosting the catalytic performance and thus CO_2 conversion and CH_4 yield at lower temperatures (below 400 °C) to attenuate sintering resulting from Ni carbonyl activity at high temperatures [17]. The application of alloying, metal doping, metal-support interaction regulation, support design, morphology engineering, and encapsulation of metallic nanoparticles in porous materials are among the approaches used for the aim [70].

Wenhui Li et al., 2018 [71] explained that loading of the metal affects the state of the active metal on the supports, which in turn affects the reaction pathways. Alrafei et al., 2020 [72] demonstrated the effect of varying Ni loading on catalytic activity and selectivity. The authors concluded that Ni loading from 5 to 20% increases catalytic activity. Addition of Co to high Ni-loaded catalysts exhibited better reducibility, but worse dispersion of active species [72]. They reported a very good stability of their novel Ni and Ni-Co catalyst over 200h-run tests.

Metal oxides (Al_2O_3, SiO_2, CeO_2, TiO_2, Y_2O_3, Sm_2O_3, La_2O_3 and ZrO_2) and carbon-based materials (e.g. CNT, CNF and rGO) are the prevailing supports explored, which afford high

surface areas and heat-resistance properties [3], [67]. Ni/Al_2O_3 and Ni/SiO_2 have been broadly studied, where Ni/Al_2O_3 is mostly commercially used [69]. Likewise, particular zeolites (e.g. ZSM-5, USY, BEA, SBA-15, MCM-41 adopted zeolites, and ETS-10) have been studied for Sabatier reaction [17], [19], [67]. Basically, a support is added to the catalyst to improve the dispersion of Ni nanoparticles (active sites augmentation) and CO_2 adsorption and to decrease sintering [67]. C. H. Tan et al., 2022 [19] pointed out that it is possible to modify the characteristics of Ni-based catalysts by selecting different methods of catalyst synthesis, catalyst pre-treatment, supports, and promoters.

Wenhui Li et al., 2018 [71] also explained that lately novel materials have attracted attention to produce heterogeneous catalysts, including perovskite, hydrotalcite, multi-metal composite oxides, and metal–organic framework (MOF)-based catalysts. Furthermore, ammonia evaporation, double flame spray pyrolysis, robocasting (three dimensional fibre deposition) and dielectric barrier discharge plasma are some of the innovative techniques to prepare the catalyst to amend the existing challenges in impregnation and co-precipitation methods [71].

The addition of a promoter to the catalyst is expected to improve catalyst performance (activity, selectivity and stability) owing to its involvement in the reaction [67]. Dębek et al., 2019 [73] suggested that the application of an appropriate promoter may enhance all catalyst properties (basicity, CO_2 adsorption capacity, Ni dispersion, Ni particle size and resistance to sintering). According to their study, the promoters and their effect could be divided into groups: noble metals, alkali and alkali earth metals, lanthanides and bimetallic catalysts consisting of two transition metals (e.g. Ni/Fe, NiCu) [73]. Nieß et al., 2022 [66] specified that promoters could act structural or electronically for thermal stability and metal dispersion. Promoters can also modify the acid/basic sites on the catalyst surface [66]. Mohd Ridzuan et al., 2022[67] noted that, among the different promoters evaluated, the addition of Mg, Fe or Ru showed better catalytic performances.

Further, the effect of active metal particles has been investigated with different catalysts. Ra et al., 2020 [64] discussed the relationship between catalyst particle sizes and catalyst activity and CO selectivity. They pointed out that diverse authors revealed that after working with catalysts such as Rh, Ru, Ni and Co, CO intermediates improved while metal particle sizes were lesser. Consequently, the CO selectivity increased with the diminution of metal particle size, whereas the CH_4 selectivity decreased. H. C. Wu et al., 2015 [74] suggested that the smaller size of Ni particles boosted CO selectivity. Also, they assessed the effect of Ni loading and determined that increasing Ni loading increased CH_4 selectivity.

1.4.2. Methanol synthesis

Many catalysts for CO_2 hydrogenation to methanol have been studied and tested. Most of them have been evaluated on a copper basis, using other metals as promoters (Zn, Zr, Al, Ce, Cr, In, Pd, Ti, La, etc.) [75]–[80]. In methanol synthesis, Cu-based materials and metal oxides supports are usually used [3]. The catalyst of choice for the industry is the CZA catalyst ($Cu/ZnO/Al_2O_3$), that was introduced by ICI in 1966 [20].

Kamsuwan et al., 2021 [81] compared the performance CZA catalysts with different copper loadings in methanol synthesis from CO_2 hydrogenation. A significant Cu loading was correlated with higher catalytic activity, according to the results. In another study, Kamsuwan et al., 2022 [82] found the same behaviour after testing a CZA catalyst at 250 °C and varying the Cu loading. This was attributed to the deactivation caused by changes in the catalyst structure, arrangement of metal sites, and the coke formation. Similarly, Karelovic & Ruiz, 2015 [83] found higher methanol selectivities over catalysts with more Cu. Witoon et al., 2016 [84] worked on modifying the chemical composition of a $CuO/ZnO/ZrO_2$ (CZZ) catalyst. They identified that increasing the Cu/Zn ratio from 0.69 to 1.33 exhibited an increasing trend in CO_2 conversion. Notwithstanding, a decrease in CO_2 conversion was also noted for further Cu/Zn ratio increases (e.g., 2.5 and 6.3). All this confirms that Cu is the principal active component in CZA catalyst which is improved by the addition of oxides.

Bowker, 2019 [20] suggested to make academic efforts to synthesize new types of catalysts using Pd for methanol synthesis (although this is not economical or environmentally friendly), or use cheaper element as Ni or Co. Tursunov et al., 2017 [85] found very few papers containing Fe for the methanol synthesis from CO_2. Ren et al., 2022 [86], Zhong et al., 2020 [87] and Guil-López et al., 2019 [11] reviewed other catalysts for CTM. They agreed that Cu-based catalysts are still predominant in research. Nevertheless, Pd-based (Pd/Zn/CNTs, Pd/ZnO, Pd/plate Ga2O, $Pd/ZnO\text{-}Al_2O_3$, Pd/In_2O_3, PdZn-400), Au-based (Au/ZnO, Au/Al_2O_3, Au/TiO_2, Au/Fe_2O_3, Au/CeO_2), bimetallic ($Pd\text{-}Cu/SiO_2$, Pd-Cu/SBA-15, RhW, PtCo), intermetallic ($Cu11In9\text{-}In_2O_3$, PdZnAl, Ni_5Ga_3/SiO_2, In-Pd, Pd-Ga) and hybrid oxide ($ZnO\text{-}ZrO_2$, Ga_aZrO_x, In_2O_3-based catalysts, $MnO_x/m\text{-}Co_3O_4$) catalysts were cited as tested for methanol synthesis from CO_2 hydrogenation [11], [86], [87]. As well, they reported that MoS_2 and MoS_2-based materials, metal–organic frameworks (MOFs)-based catalysts and Co_4N nanosheets have been studied for this process. Ren et al., 2022 [86] mentioned that solid solution catalysts are another promising catalyst for methanol synthesis.

In addition to the Cu-ZnO catalysts, research has also been carried out to identify other combinations of Cu with other oxides that could be more efficient and stable for the methanol synthesis process. For instance, ZrO_2 when combined with Cu gives a very active, stable and

selective catalyst [11]. Chaoheng Liu et al., 2016 [88] conducted experiments with TiO_2-modified Cu catalysts with different amounts of MgO prepared by the impregnation method. The authors concluded that MgO modification enhances basic sites properties of Cu/TiO_2 catalysts, improving CO_2 conversion and CH_3OH selectivity. The maximum methanol yield occurred at 1% MgO loading due to synergistic effects and optimal basicity [88].

Quezada, 2020 [13] tested six Cu-based catalysts, four of them were supported on zeolite (HZSM-5). Among the catalysts studied, $CuZn/Al_2O_3$ consistently demonstrated superior performance at all temperatures tested. However, the author saw similar performance of $CuZn/Al_2O_3$ and CuZn/Z23. This underlines the potential of zeolites, suggesting that, with further research, they could surpass the methanol yields achieved by the commercial $CuZn/Al_2O_3$ catalyst [13].

Further experiments with different catalysts and their respective temperature, pressure, molar ratio (H_2/CO_2), CO_2 conversion and CH_3OH selectivity are summarized in Table 1.3.

Table 1.3 Methanol synthesis catalysts from CO_2 hydrogenation.

Catalyst	$\boldsymbol{T}$ $(\boldsymbol{K})$	$\boldsymbol{P}$ $(\boldsymbol{bar})$	$\boldsymbol{H_2/CO_2}$	$\boldsymbol{GHSV}$ $\boldsymbol{or}$ $\boldsymbol{WHSV}$	$\boldsymbol{X_{CO_2}}$ (%)	$\boldsymbol{S_{CH_3OH}}$ (%)	$\boldsymbol{Ref.}$
$CuO/ZnO/Al_2O_3$	568	36	3	$15\ L.g^{-1}.h^{-1}$	15.8	12.0	[13]
$CuO/ZnO/Al_2O_3$-C-1.25*	513	30	3	$3600\ h^{-1}$	16.2	63.8	[89]
10Cu-/ZnCr	523	20	3	$6\ L.g^{-1}.h^{-1}$	10.9	48.0	[76]
$CuO/ZnO/CeO_2$	513	1	9	$1\ L.h^{-1}$	20.0	90.0	[75]
$CuO/ZnO/ZrO_2$	513	30	3	$3600\ h^{-1}$	12.1	54.1	[90]
10%CuZn/rGO	523	15	3	$2400\ h^{-1}$	26.0	5.1	[91]
CuZnGa	543	30	3	$3000\ h^{-1}$	15.9	–	[92]
Cu/SiO_2	593	30	4	$16\ L.g^{-1}.h^{-1}$	28.0	21.3	[93]
Cu/ZrO_2	493	30	3	$3600\ h^{-1}$	4.2	53.9	[94]
Cu-Ce-Zr-450	553	30	3	$10000\ h^{-1}$	13.2	71.8	[95]
$Cu/1\%MgO/TiO_2$	493	30	3	$4800\ h^{-1}$	5.2	37.9	[88]
$CuNi_2/CeO_2$-NT	533	30	3	$6000\ h^{-1}$	17.8	78.8	[96]
Cu/ZrO_2/CNF	453	30	3	n/s	11.0	–	[97]
Cu/ZrO_2/CNT	533	30	3	$3600\ h^{-1}$	16.3	43.5	[98]
$CuZnZr/CuBr_2$	523	50	3	$3\ L.g^{-1}.h^{-1}$	10.7	97.1	[99]
110°C-Ni_5Ga_3	473	30	3	$0.37\ L.g^{-1}.h^{-1}$	3.2	100.0	[100]
Ni/In_2O_3	573	50	4	$21\ L.g^{-1}.h^{-1}$	18.5	> 54.0	[101]
Ni_7In_3/SBA-15	573	50	3	$4.7\ h^{-1}$	17.0	86.8	[102]
Rh/In_2O_3	573	50	4	$21\ L.g^{-1}.h^{-1}$	17.1	56.1	[103]
Co_5Ga_3	523	30	3	n/s	1.0	63.0	[104]
5%Pd/ZnO	523	20	3	$3.6\ L.g^{-1}.h^{-1}$	10.7	60.0	[105]
$9\%In_2O_3/ZrO_2$	573	50	4	$16000\ h^{-1}$	5.2	99.8	[106]
Fe–Cu/MCM-41	473	10	3	$4.8\ L.g^{-1}.h^{-1}$	2.0	–	[107]

*Catalyst using citric acid/salts = 1.25 (molar ratio). n/s: not specified.

ZnO, as a support, strongly influences catalytic activity [108]. Toyir et al., 2001 [109] explained that ZnO improves dispersion and stabilization of copper sites. Schittkowski et al., 2018 [108] agreed with this announcement. According to Schumann et al., 2015 [110], the synergistic effects of Cu and ZnO have been debated for a long time. They mentioned research groups that proposed a hydrogen spill-over mechanism, in which ZnO acts as a hydrogen reservoir, facilitating hydrogenation on adjacent Cu surfaces. Strong metal-support interaction (SMSI) has also been considered [108], causing the wetting of ZnO in a reduced environment, coating Cu particles and leading to morphological changes or providing Zn atoms to the copper surface [110].

Other authors reported that catalytic activity could also be negatively affected by an overload of ZnO in the CZA catalyst [111]–[113], even though ZnO is the main promoter for enhancing the activity of the system [114]. From Lei et al., 2016 [89], Tursunov et al., 2017 [85] inferred that CZA catalytic activity and the Cu surface area are deeply related. Consequently, the loading of bimetallic compounds Cu and Zn directly influences the catalyst performance. It is necessary to identify an optimum ratio to increase the metal dispersion and improve the surface area. Thus, a catalyst tune of compounds is required to obtain the highest catalytic performance.

There are two categories of promoters that can be differentiated by their effect on the catalyst, namely physical (structural: affects active sites and stabilization of active phase) and electronic (bonding: affects the nature of the active sites) [115]. In a Cu/Zn:Al, the Al promoter affects phase formation of the precursor by a geometric effect. This can also be achieved by adding Ga, Cr, or Mg. The Al or Ga or Cr also affect, by dynamical strong metal support interaction, the electronic structure of the catalytically active Cu surface. [116]

Al_2O_3 plays the role of a structural promoter [117]. In reaction conditions, Al_2O_3 improves the exposure and stabilization of Cu-active centres [11]. The inclusion of Al atoms boosts the catalyst activity and stability, owing to an upgrade in the BET surface area and the Cu dispersion [87], [116], [117].

Enhancing CO_2 conversion to methanol by adding promoters to the CZA catalyst has also been investigated. Promoting a heterogeneous catalyst (i.e., adding small amounts of one or more extra elements to a proven catalyst system) can have a huge impact on the catalytic properties [103], [104], and most industrially applied catalysts are promoted in one way or another [92]. The incorporation of noble metals such as Pd, Au, Rh or Pt increases the activity of Cu catalysts during the reaction. However, their prices and the post-reaction catalyst recycling makes them unsustainable [11]. Previtali et al., 2020 [118] tested the effect of Mg, Ca and Sr as basic

promoters. The best performance was attributed to the catalyst without promoter, but the literature reports a low lifetime for these catalysts.

Zhang et al., 2017 [119] showed that incorporating magnesium into the CZA catalyst improved its BET surface area and the copper dispersion. By stabilizing Cu° (or Cu+) species against oxidation, Nishida et al., 2009 [120] identified a positive effect of MgO present on the surface on catalyst activity in the Water Gas Shift (WGS) reaction. Endorsing these statements, Cheng et al., 2021 [121] found that the synergy of copper and ZnO was augmented after adding Mg resulting in an increased stability and catalytic activity.

Xaba et al., 2021 [122] reported on the role of ZrO_2 and Ga_2O_3 promoters. They identified that the introduction of ZrO_2 and Ga_2O_3 modifiers enhance the methanol production. But a higher CO_2 adsorption, resulting in higher methanol yield was observed while working with ZrO2. Other investigators experimented with Ga^{3+}[109], [110], [116], [123], Al^{3+}[110], [116], Mg^{2+}[110], [118], Zn[124], K, Na[125], SiO_2, TiO_2, SiO_2-TiO_2[126], ZrO_2[99], [127], F[127], etc., to improve the catalytic performance and stability.

Díez-Ramírez et al., 2017 [128] studied the influence of calcination and reduction temperatures, and the metal loading on the Cu/ZnO catalyst (Figure 1.5). After carrying out four calcination temperatures: 300, 350, 400 and 600°C with copper loadings of 10 wt%, they identified 350°C as the most appropriate calcination temperature. Regarding the reduction temperature, they tested five reduction temperatures (150, 200, 250, 300 and 400°C) for the 10 wt.%CuZnO catalyst calcined at 350°C. In the reduction step, the highest CH_3OH formation was obtained at 200°C. Regarding the metal loading, the authors indicated that a higher metal loading leads to a superior methanol formation rate and greater CO_2 conversion. This was related to the dual site mechanism (dissociative H_2 adsorption on ZnO sites and CO_2 adsorption on Cu active sites) for methanol formation. Optimal performances were achieved for a metal loading of about 20 wt.%.

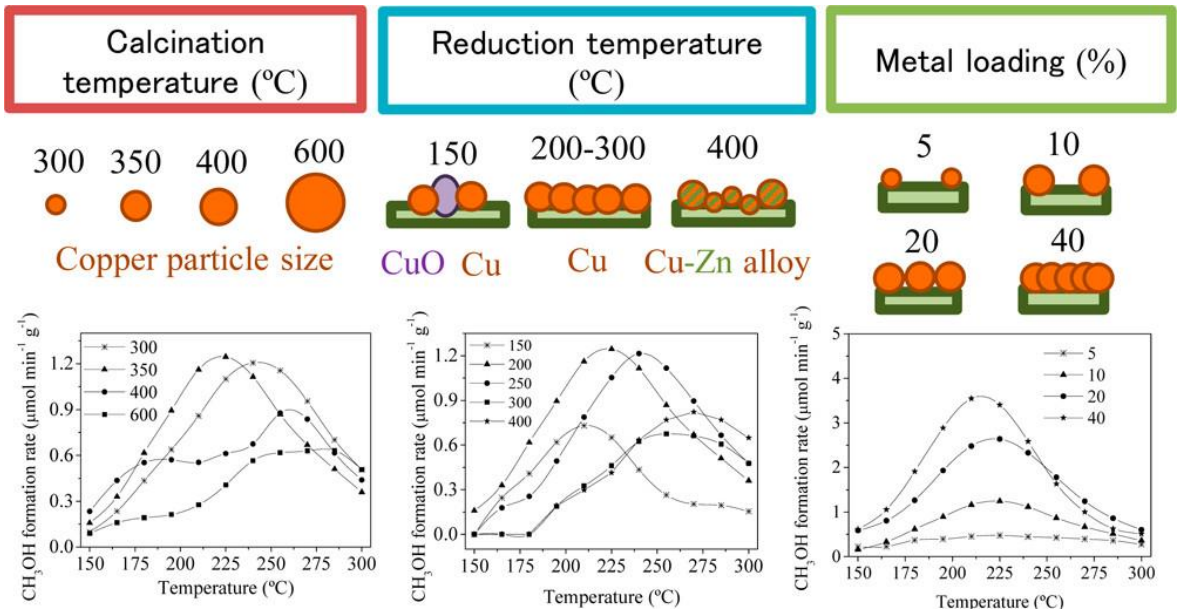

Figure 1.5 Comparison of methanol formation rates at different calcination and reduction temperatures, and metal loadings. Reaction conditions: CO_2/H_2 = 1/9 and W/F = 0.13 kg·h·m^{-3}. Reproduced from [128].

Most Cu-based catalysts used for CO_2 hydrogenation are prepared by co-precipitation [11], [20], [108]. The active catalyst has Cu^0 or Cu^+ nanoparticles coating the ZnO or partly reduced ZnOx phases, which are suitable for the methanol synthesis [11]. Sol-gel method allows also the synthesis of catalysts with large specific surface areas and high CuO dispersions [128]. Allam et al., 2019 [75] prepared Cu- and Zn- based catalysts by the polyol method (with polyethylene glycol as solvent). They observed that the morphology, as well as the metal oxide dispersion and a variety of metal and metal oxides species on the surface were enhanced. M. Ren et al., 2022 [86] cited other methods such as the ammonia evaporation (AE), flame spray pyrolysis (FSP), and the aerosol-assisted sol–gel (AASG). Ultrasound-assisted, solid-state [129], wetness impregnation, sol immobilization [105] and fractional-precipitation [119] are other methods employed.

1.4.3. DME synthesis

For direct CO_2 to DME process, the challenge lies in catalysing both the methanol synthesis and the methanol dehydration simultaneously [59]. The water production during the CO_2 hydrogenation and the methanol dehydration induces a thermodynamic constraint, resulting in lower DME yields compared to using CO [44], [47]. Park et al., 2022 [58] proposed the use of hybrid catalysts that enable simultaneous methanol and DME production, overcoming equilibrium limitations and significantly enhancing methanol productivity. Designing an

effective bifunctional catalyst for one-step CO_2 hydrogenation to DME is a key focus, with efforts aimed at developing a robust, water-resistant catalyst with minimal coke formation.

In order to address catalyst activity and stability challenges, various strategies have been proposed, including replacing active metals, modifying promoters, reducing particle size, altering pre-treatment methods, and exploring different combinations of metals and supports [61]. Creating a hybrid catalyst that ensures exceptional contact between catalysts for methanol synthesis and dehydration is deemed essential, considering factors such as preparation methods, sintering of copper particles and catalyst deactivation [47].

Cu-based catalysts combined with acid catalysts (pure or doped silica, zeolites, clay) are commonly used in the direct synthesis of CO_2 to DME. Cu sites play a crucial role in the preliminary step of DME synthesis from CO_2 hydrogenation [48], and researchers debate whether Cu^+ or Cu^0 species are the active sites. After reviewing other investigations, Chang Liu & Liu, 2022 [48] established that both Cu^+ and Cu^0 species can participate in CO_2 hydrogenation to DME.

Table 1.4 summarises the conversion, selectivity and DME and methanol yields obtained by various authors for the catalysts discussed in this section.

Table 1.4 Summary of the performance of catalysts for direct DME synthesis from CO_2 hydrogenation.

Catalyst	$\boldsymbol{T}$ $(\boldsymbol{K})$	$\boldsymbol{P}$ $(\boldsymbol{bar})$	$\boldsymbol{X_{CO_2}}$ (%)	$\boldsymbol{GHSV}$ $\boldsymbol{or}$ $\boldsymbol{WHSV}$	$\boldsymbol{S_{DME}}$ (%)	$\boldsymbol{S_{CH_3OH}}$ (%)	**Ref.**
$10Cu_5Ga$/SBA-15	523	25	3.0	30000 h^{-1}	29.0	71.0	[130]
CZA/ZSM-5-HM	498	30	2.1	48 $NL.g^{-1}.h^{-1}$	77.5	22.5	[31]
CZA/ZSM-5	513	27.6	23.6	1.5– 2.8 $NL.g^{-1}.h^{-1}$	56.4	n/s	[131]
C-CZA-CP-1/HZSM-5	533	30	24.0	2.4 $L.g^{-1}.h^{-1}$	32.0	n/s	[132]
C-CZA-HT-1/HZSM-5	533	30	28.0	2.4 $L.g^{-1}.h^{-1}$	48.0	n/s	[132]
CuZnO/γ-Al_2O_3 4%Si	543	30	13.0	0.23 h^{-1}	7.0	10.0	[133]
CuZnO/γ-Al_2O_3 8%Si	543	30	12.0	0.23 h^{-1}	16.0	17.0	[133]
5CuZnO/PTA	533	30	21.5	12 h^{-1}	68.9	7.0	[61]
CuO–ZnO/ZSM-5	533	20	n/s	200 h^{-1}	65.0	n/s	[134]
CuZnOZrO_2/H-ZSM5	513	30	16.1	10 $NL.g^{-1}.h^{-1}$	33.9	11.8	[59]
CuZnZr/ferrierite8	533	30	22.0	8.8 $NL.g^{-1}.h^{-1}$	38.5	14.0	[135]
CZZA/HZSM-5	513	27.6	26.5	823 h^{-1}	69.2	n/s	[136]
CuO/ZrO_2 + montmorillonite K10	533	40	3.0	n/s	51.0	38.0	[137]
PdZn/TiO_2 + ZSM-5	543	20	11.0	3500 h^{-1}	32.3	5.9	[138]
PdZn/ZSM-5	543	20	13.7	3500 h^{-1}	30.4	4.2	[138]
Pd/ZnO+bio-ZSM-5	573	30	10.8	12 $L.g^{-1}.h^{-1}$	31.0	n/s	[139]
In_2O_3/Al-MCM-41/HNT	523	40	4.0	12000 h^{-1}	53.0	n/s	[140]

n/s: not specified.

S. Ren et al., 2020 [136] studied the atomic ratio of Cu/Zn/Zr/Al (CZZA) on DME synthesis. They suggested that a low Al loading and a Zr loading of 1.0 yield better catalyst performance. They cited that the hydrophobic nature of Zr in the CZA catalyst improved the stability. Kornas et al., 2017 [137] highlighted the importance of the metallic function synthesis method for CuO/ZrO2, with the citric method leading to a better connectivity between the support and the active phase.

Other investigators [61] explained that varying the weight percentage of acid sites (PTA) on a halloysite nanotube-supported CuZn-PTA@HNT catalyst influenced the DME and water selectivities, with the catalyst with the lowest Cu content having the highest acidity and stable catalytic performance. Xia et al., 2023 [132] demonstrated the impact of metal content and synthesis methods on the distribution of hydrotalcite-containing precursor phases in a Cu-based catalyst. The hydrothermal synthesis method showed superior catalytic results.

Bahruji et al., 2018 [138] emphasized the influence of zeolite catalyst modifications on methanol dehydration rates, favouring HZSM-5 over γ-Al_2O_3 due to its relative stability and controllable hydrophobic/hydrophilic properties. PdZn/TiO_2-ZSM-5 was found to be superior, attributed to the blocking of essential Brönsted acid sites when PdZn is directly supported on the zeolite surface.

Several reports [39], [42], [44], [49], [138], [141] suggest that the dehydration rates depend on both Lewis and Brönsted acid sites. High Brönsted acidity was associated with increased dehydration activity, facilitating the formation of dimethyl ether, while strongly acidic catalysts could lead to the formation of coke and the catalyst deactivation [49]. Lewis acid sites were found to strongly adsorb water, inhibiting DME formation, with Brönsted acid sites playing a predominant role [141]. The hydrophilic nature of γ-Al_2O_3 and the hydrophobic nature of HZSM-5 were highlighted [141]. Moderate/medium acidic sites were identified as providing optimal DME production, with Brönsted site acidity remaining unaffected by water [39].

Modifications to alumina, incorporating Si atoms, enhanced the acid sites, leading to increased DME and methanol yields [133]. CuO–ZnO/ZSM-5 catalytic performance at lower pressure and temperature, but greater space velocity exhibited higher CO_2 conversion and DME+methanol yield compared to other conditions [134]. Krim et al., 2023 [31] pointed out that γ-Al_2O_3 showed lower activity than HZSM-5 in the moderate temperature range (513-553 K).

A research team [142] analysed the effects of drying techniques and calcination temperature on alumina-supported copper catalysts. Infrared drying showed the highest DME space-time yield and excellent stability over 24 hours. S. Ren et al. (2019) [131] discussed the effects of

mixing methods of bifunctional catalysts on stability, with Method 'pressed then mixed' proving more stable. Fan et al. (2021) [143] explored the interaction between components in CZZA/HZSM-5 bifunctional catalysts, noting that particle size and mixing method influenced stability by affecting active site availability. Reducing CZZA improved HZSM-5 stability, correlated with a decreased MeOH production. Separating HZSM-5 and CZZA led to faster deactivation.

Bonura et al., 2013 [59] found no advantage in separating catalytic beds (Cu–ZnO–ZrO_2 and H-ZSM5), with physically mixed catalysts showing superior results. In a subsequent study [29], using a Cu/Zn/Zr metal-oxide phase, the long-term stability of six homemade zeolites was tested. They found that the zeolite characteristics influenced the metallic properties and, the acidity and distribution of acid sites, showing that the density of acid sites is crucial for the conversion of methanol to DME.

The same research group [135] evaluated the Si/Al ratio and effects of the grain size on the acid capacity of ferrierite-based hybrid catalysts. They confirmed that higher crystallization induced lower acidity. Hengne et al., 2018 [130] found that a mesoporous-silica-supported Cu-Ga nanocomposite catalyst enhanced methanol and DME selectivity, despite low CO_2 conversion (<5%). Pechenkin et al., 2021 [140] investigated In_2O_3 catalysts for methanol production, with experiments showing promising DME selectivity and stability for at least 40 hours.

In brief, the direct conversion of CO_2 to dimethyl ether (DME) presents challenges in concurrently catalysing methanol synthesis and dehydration due to thermodynamic constraints linked to water production. Hybrid catalysts have been proposed as a solution to enhance methanol productivity by facilitating simultaneous methanol and DME production. The focus of research efforts has been on designing effective bifunctional catalysts for one-step CO_2 hydrogenation to DME. Emphasis has been placed on developing robust, water-resistant catalysts with minimal coke formation. Cu-based catalysts, often in combination with acid catalysts, are commonly employed in direct CO_2 to DME synthesis. While challenges persist, promising developments in catalyst design have been achieved, and further research holds the potential for enhancing DME yield and overall process efficiency.

1.5. Reaction mechanisms

1.5.1. Methane synthesis

There are two main reaction pathways identified for Sabatier-Senderens reaction (Figure 1.6) [39], [64], [65], [67], [73], [144]. One is going through the RWGS reaction, from CO_2 dissociation, and ensuing CO hydrogenation to form CH_4, also called carbonyl route. The other is the formate route, where CH_4 is directly produced from CO_2 ($*CO_2 \rightarrow HCOO* \rightarrow HCOOH \rightarrow CH_4$). Researchers do not agree about the reaction route for CO_2 methanation.

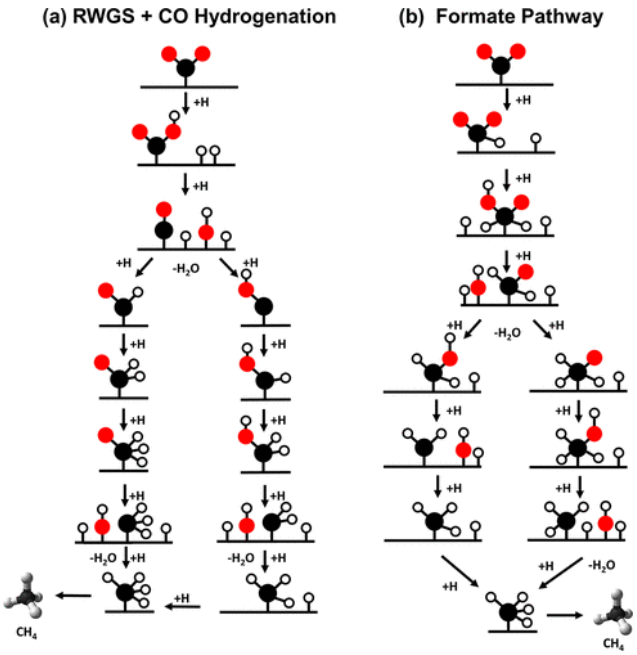

Figure 1.6 CO_2 methanation pathways: (a) the carbonyl pathway via RWGS+CO hydrogenation and (b) the formate pathway. Reproduced from [64].

Karelovic & Ruiz, 2013 [145] observed by Diffuse Reflectance Infrared Fourier Transform Spectroscopy (DRIFTS) cell the CO_2 dissociation as reaction mechanism over Rh catalysts. On the other hand, Zhao et al., 2022 [144] presented three possible mechanisms of CO_2 methanation on Ni(111) surfaces (Figure 1.7). Wenhui Li et al., 2018 [71] explained how different authors agree with carbonyl pathway over catalysts such as Ni(111), Ni(110), USY zeolites-supported Ni catalysts. Correspondingly, Vogt et al., 2018 [146] pointed out the CO_2 dissociation as the main active route over Ni catalyst at 400 °C.

Huang et al., 2019 [147] identified two formate pathways via the intermediates H_2COO^* on Ni/MgO surface, and $HCOOH^*$ on Ni(111) by density functional theory (DFT) calculations. Other authors reported formate route on Ni/CeO_2 [148] and on Ni/TiO_2 [144].

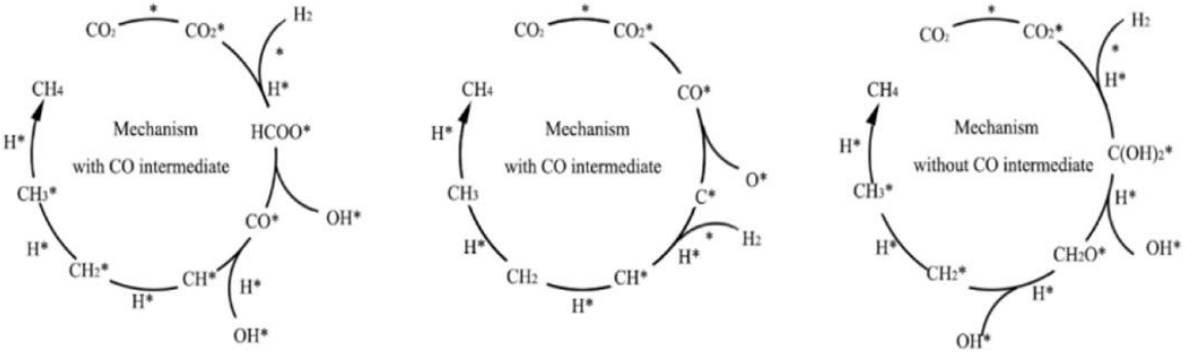

Figure 1.7 Diagram of three mechanisms of CO_2 methanation on Ni(111). Reproduced from [144].

In short, there is a lack of agreement among researchers regarding the specific reaction pathway for CO_2 methanation, either the RWGS + CO hydrogenation route or the formate route.

1.5.2. Methanol synthesis

For several years the predominance of CO hydrogenation for methanol synthesis was assumed as the main pathway [149]. Recently, it has been noted by Chinchen et al., 1987 [150] that methanol is principally produced via CO_2 hydrogenation under industrial conditions. In their study, Grabow and Mavrikakis, 2011 [151] said that under typical methanol synthesis conditions over a $Cu/ZnO/Al_2O_3$ (CZA) catalyst, both CO and CO_2 hydrogenation pathways are active. They also stated that 2/3 of methanol synthesis is from CO_2 hydrogenation under typical industrial operating conditions [151]. Likewise, Gaikwad et al., 2020 [152] affirmed that methanol formation over CZA could be through CO or CO_2 hydrogenation, for the first ($CO_2 \rightarrow CO \rightarrow CH_3OH$) at 260-340 °C and for the latter ($CO_2 \rightleftharpoons CH_3OH;\ CH_3OH \longrightarrow CO \rightarrow CO_2$) at low temperatures (180 °C). Schittkowski et al., 2018 [108] explained that the use of kinetic measurements in conjunction with isotopic tracer techniques enabled the demonstration that CO_2 hydrogenation over the industrial catalyst CZA proceeds much more rapidly than the hydrogenation of CO [108].

Furimsky, 2020 [153] hypothesised that the activated adsorption of CO over carbon-supported catalysts could be more challenging than that of CO_2. This is true when the form of active site considered is similar to the one presented in Figure 1.8 [153]. Bowker, 2019 [20] described a

mechanism of the reaction on ZnO (Figure 1.9) where the formate is identified as the common intermediate. On the other hand, according to Guil-López et al., 2019 [11] two mechanisms are mainly accepted for the synthesis of methanol in Cu/ZnO: formate mechanism and RWGS and posteriori CO hydrogenation. In the formate mechanism, the formate (HCOO) is the intermediate, while in the RWGS and CO hydrogenation, the reaction occurs via formyl (HCO) and formaldehyde (HCHO) intermediates (Figure 1.10) [11]. For both intermediates, HCOO and HCO, diverse researchers found evidence to support each reaction mechanism over other catalysts [108], [154].

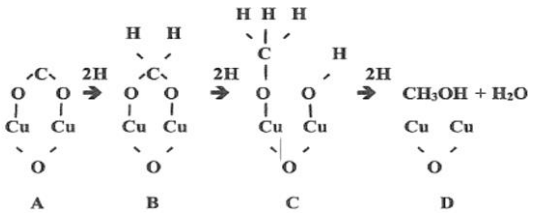

Figure 1.8 Potential pathway during conversion of CO_2 under hydrogenation conditions. Reproduced from [153].

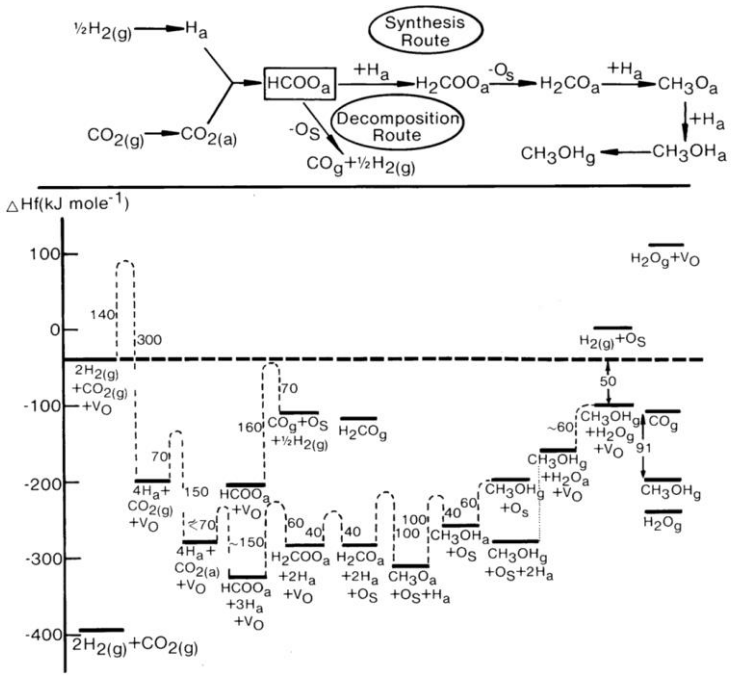

Figure 1.9 The methanol synthesis mechanism and kinetics for the methanol synthesis on ZnO. Reproduced from [20].

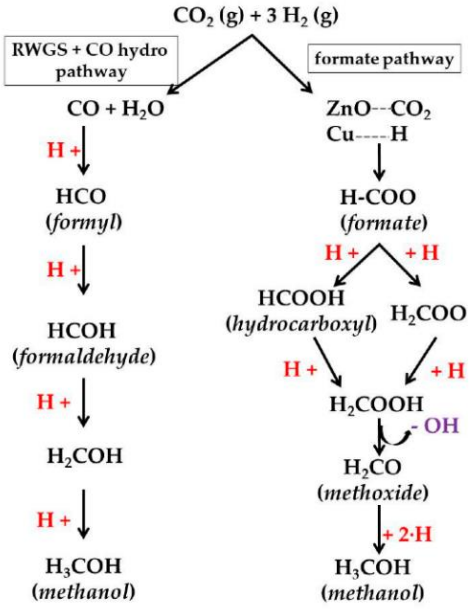

Figure 1.10 Methanol synthesis pathways over Cu-based catalysts. Reproduced from [11].

In short, the mechanism involved depends very much on the catalyst used, and even for Cu/ZnO, two pathways seem possible, with no real consensus on the issue from the authors.

1.5.3. DME synthesis

Two pathways for methanol dehydration are commonly described for H-form zeolites (Figure 1.11), associative and methoxy-mediated dissociative, which requires Brönsted acid sites, explained Ghorbanpour et al., 2016 [155]. In the dissociative route, a methanol molecule is adsorbed at the Brönsted acid site, after a water molecule is eliminated. This is followed by the nucleophilic attack of a second methanol molecule, forming DME. In the associative route, DME and water production appears from the co-adsorption of two methanol molecules at the Brönsted acid site. Depending on reaction conditions, regardless of the acid site location, the dissociative route prevails [155]. Mota et al., 2021 [43] elucidated that the reaction mechanism relying on Lewis acidity assumes the occurrence of a reaction between a methanol molecule adsorbed on an acidic site and an alkoxide anion adsorbed on a basic site. For this reaction to take place, it is necessary to have neighbouring acid-base pair sites on the catalyst surface.

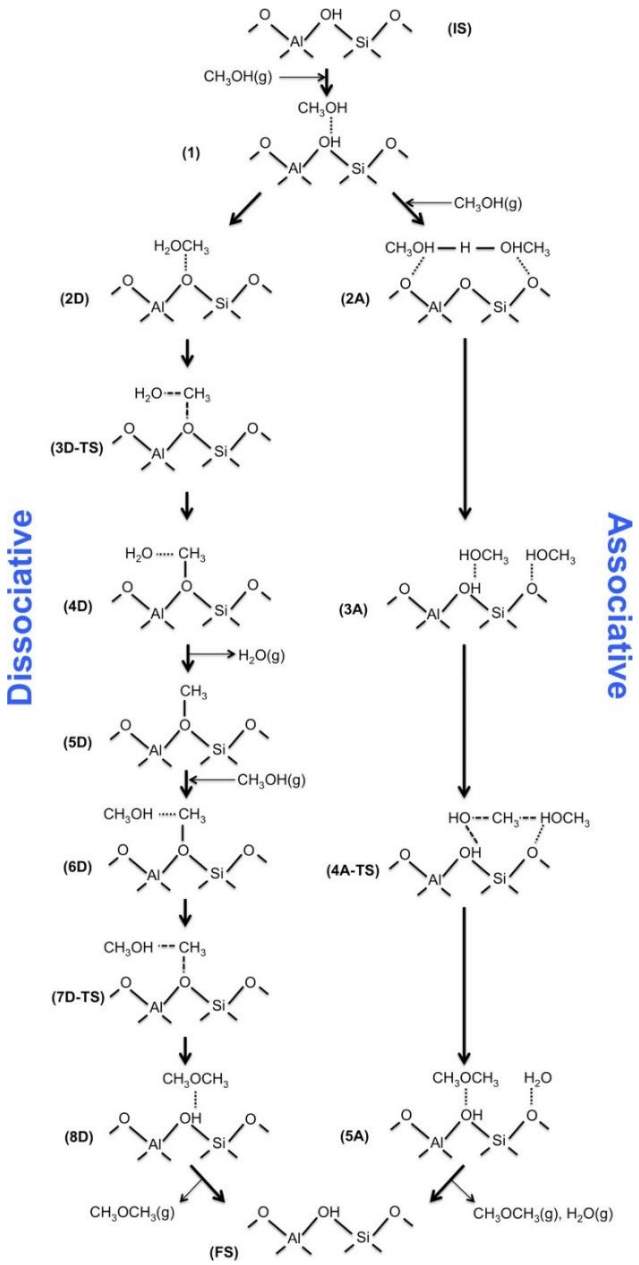

Figure 1.11 Reaction mechanisms for methanol conversion to DME catalysed over H-form zeolite. Reproduced from [155].

Sheng et al., 2020 [156] presented a reaction mechanism based on several literature references for CuZnZr/FER catalyst (Figure 1.12). Dissociatively adsorbed CO_2 directly reacts with surface atomic H, in the upper route, coming from the dissociation of adsorbed H_2 on metallic Cu sites which leads to the formation of b-HCOO and m-HCOO (intermediate formate species), and in parallel the adsorption of CO_2* with O* occurs (lower route: carbonate pathway) [156].

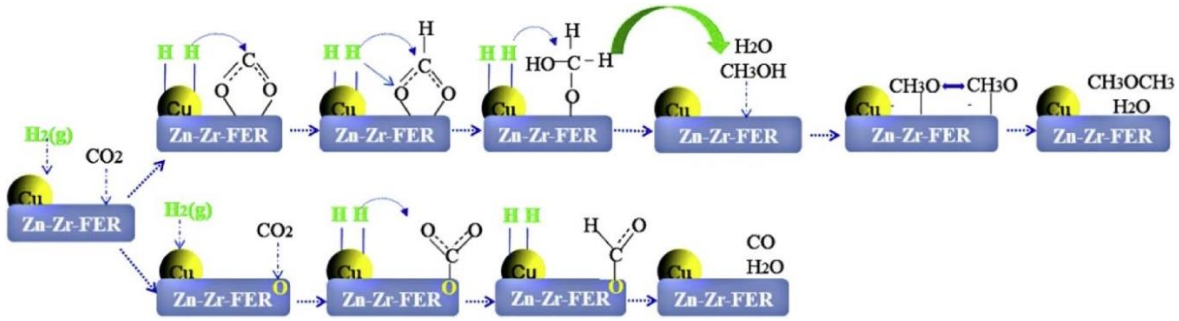

Figure 1.12 Reaction mechanism for direct DME synthesis from CO_2 over CZZ(C)/FER catalyst. Reproduced from [156].

In conclusion, for both methane and methanol synthesis there is no unanimity on the reaction routes, with two routes being considered: RWGS + CO hydrogenation route or the formate route. In the case of methanol dehydration, dissociative and associative reaction mechanisms are possible.

1.6. Kinetic modelling

Most of the kinetic models presented in the literature for CO_2 hydrogenation to methane, to methanol and to DME considered isothermal reactors (no heat balance equations are shown). Table 1.5 displays some kinetic expressions found in literature for DME synthesis with their respective technology, feedstock, and catalyst.

Table 1.5 Kinetic models for DME synthesis.

Kinetic rate expressions	**Feed-stock**	**Reactor**	**Catalyst**	**Ref.**
$r_{CO_2} = k_1 p_{H_2} p_{CO_2} \left(1 - \frac{p_M p_W}{K_{eq1} p_{CO_2} p_{H_2}^3}\right) \theta^3$ $r_{RWGS} = k_5 p_{CO_2} \left(1 - \frac{p_{CO} p_W}{K_{eq2} p_{CO_2} p_{H_2}}\right) \theta$ $r_{DME} = \frac{k_6 K_M^2 \left(C_M^2 - \frac{C_W C_{DME}}{K_{eq3}}\right)}{\left(1 + 2\sqrt{K_M C_M} + K_W C_W\right)^4}$ $\theta = \frac{1}{1 + \frac{K_2 P_W}{P_{H_2}} + \sqrt{K_3 P_{H_2}} + K_4 P_W}$	CO_x/H_2	Continuous gradient-less internal-recycle	CZA + γ-Al_2O_3	[157]
$r_{CO_2} = k_1 P_{CO_2} P_{H_2} (1 - P_W P_M / K_1 P_{CO_2} P_{H_2}^3) \theta^3$ $r_{RWGS} = k_2 (P_W - P_{CO_2} P_{H_2} / K_2 P_{CO})$ $r_{DME} = k_3 \left(\frac{P_M^2}{P_W} - \frac{P_{DME}}{K_3}\right)$ $\theta = \frac{1}{1 + K_{CO_2} P_{CO_2} + K_{CO} P_{CO} + \sqrt{K_{H_2} P_{H_2}}}$	$CO_2/CO/H_2/N_2$	Fluidized bed	CZA/HZSM-5	[158]
$r_{CO} = k_1 f_{CO} f_{H_2}^2 (1 - f_M / K_{f_1} f_{CO} f_{H_2}^2) \theta^3$ $r_{CO_2} = k_2 f_{CO_2} f_{H_2}^3 (1 - f_M f_W / K_{f_2} f_{CO_2} f_{H_2}^3) \theta^4$ $r_{DME} = \frac{k_3 f_M (1 - f_{DME} f_W / K_{f_3} f_M^2)}{\left(1 + \sqrt{K_M f_M}\right)^2}$ $\theta = 1/(1 + K_{CO} f_{CO} + K_{CO2} f_{CO_2} + K_{H_2} f_{H_2})$	$CO_2/CO/CH_4/H_2/N_2$	Iso-thermal fixed-bed	Commercial	[159]

$r_{CO} = k_1(p_{CO}p_{H_2}^2 - p_M/K_1)\theta$ $r_{CO_2} = k_2(p_{CO_2}p_{H_2}^3 - p_M p_W/K_2)\theta$ $r_{WGS} = k_3(p_{CO}p_W - p_{CO_2}p_{H_2}/K_3)$ $r_{DME} = k_4(p_M^2 - p_{DME}p_W/K_4)$ $r_{HC} = k_5(f_{CO}f_{H_2}^3 - f_{HC}f_W/K_5)\theta$ $\theta = 1/(1 + K_W f_W + K_{CO_2}p_{CO_2})$	CO_2/CO /H_2	Fixed bed	CuO-ZnO-MnO/SAPO-18	[160]
$r_{CO_2} = k_1(f_{CO_2}f_{H_2}^3 - f_M f_W/K_1)\theta^3$ $r_{WGS} = k_2(f_W - f_{CO_2}f_{H_2}/K_2 f_{CO})\theta$ $r_{DME} = k_3(f_M^2 - f_{DME}f_W/K_3)$ $\theta = \frac{1}{1 + \sqrt{K_{H_2}f_{H_2}} + K_{CO_2}f_{CO_2} + K_{CO}f_{CO}}$	CO_2/CO/ H_2	Fixed bed	CZA + γ-Al_2O_3	[161] – [163]
$r_{CO} = k_1 K_{CO}(f_{CO}f_{H_2}^{1.5} - f_M/(f_{H_2}^{0.5}K_1))\theta$ $r_{CO_2} = k_2 K_{CO_2}(f_{CO_2}f_{H_2}^{1.5} - f_M f_W/(f_{H_2}^{1.5}K_2))\theta$ $r_{RWGS} = k_3 K_{CO_2}(f_{CO_2}f_{H_2} - f_W f_{CO}/K_3)\theta$ $r_{DME} = \frac{k_4 K_M^2 C_M^2(1 - C_W C_{DME}/C_M^2 K_4)}{(1 + 2\sqrt{K_M C_M} + K_W C_W)^4}$ $\theta = \frac{1}{(1 + K_{CO_2}f_{CO_2} + K_{CO}f_{CO})(f_{H_2}^{0.5} + K_W f_W/K_{H_2})}$	CO_2/CO/ H_2	Fixed bed	CZA/HZSM-5	[164]
$r_{CO} = k_1 K_{CO}(f_{CO}f_{H_2}^{1.5} - f_M/K_1 f_M^{0.5})\theta$ $r_{CO_2} = k_2 K_{CO_2}(f_{CO}f_{H_2}^{1.5} - f_W f_M/K_2 f_{H_2}^{1.5})\theta$ $r_{WGS} = k_3 K_{CO_2}(f_{CO}f_W/K_3 - f_{CO_2}f_{H_2})\theta$ $r_{DME} = \frac{k_4 K_M^2(C_M^2 - C_W C_{DME}/K_4)}{(1 + 2\sqrt{K_M C_M} + K_{W,DME}C_W)^4}$ $\theta = \frac{1}{(1 + K_{CO_2}f_{CO_2})(1 + \sqrt{K_{H_2}f_{H_2}} + K_W f_W)}$	CO_2/CO/ H_2/N_2	Fixed bed	CZA/ ferrierite	[58]
$r_{DME} = \frac{k K_M^2 p_M^2}{(1 + K_M p_M + K_{DME}p_{DME} + K_W p_W)^2}$	CH_3OH	Flow	Cation exchange resin (Dowex 50 X-8)	[165]

$r_{DME} = k^2 K_M p_M \theta^2$ $r_{DME} = k^3 K_M p_M^2 \theta^3$ $r_{DME} = k^4 K_M p_M^2 \theta^4$ $\theta = 1/\left(1 + 2\sqrt{K_M p_M} + K_{DME} p_{DME} + K_W p_W\right)$	CH_3OH	CSTR	Sulphonated styrene-divinyl benzene copolymer	[166]
$r_{DME} = \frac{k_s C_M^2}{\frac{K_W}{K_M} C_W + C_M}$	CH_3OH	Batch	Amberlyst 35	[167]
$r_{DME} = \frac{k P_M (1 - P_{DME} P_W / K)}{1 + K_M P_M + (P_W / K_W)}$	CH_3OH	Fixed bed	γ-Al_2O_3	[168]
$r_{DME} = \frac{k_2 K_M^2 (P_M^2 - P_{DME} P_W / K)}{(1 + K_M p_M + K_W p_W)^2}$	CH_3OH/ H_2O/N_2	Fixed bed	Modified ZSM-5	[169]
$r_{DME,LH} = \frac{k K_M^2 C_M^2}{(1 + K_M C_M)^2}$ $r_{DME,ER} = \frac{k K_M^2 C_M^2}{1 + K_M C_M}$	CH_3OH	Autoclave batch	Zeolites & ion exchange resins	[170]
$r_{DME,\gamma-Al_2O_3} = k_1 C_M - k_2 C_W$ $r_{DME,HZSM-5} = \frac{k K_M P_M (1 - P_{DME} P_W / K)}{1 + K_M P_M + K_W P_W}$	CH_3OH	Fixed bed	γ-Al_2O_3 & HZSM-5	[171]
$r_{DME,G\&J} = \frac{k_1 (K_M p_M)^2 (1 - p_{DME} p_W / p_M^2 K)}{(1 + K_M p_M + K_W p_W)^2}$ $r_{DME,K\&S} = \frac{k_1 K_M p_M (1 - p_{DME} p_W / p_M^2 K)}{\left(1 + 2\sqrt{K_M p_M} + K_W p_W\right)^2}$ $r_{DME,Ha\ et\ al.} = \frac{k_1 K_M p_M (1 - p_{DME} p_W / p_M^2 K)}{1 + K_M p_M + K_W p_W}$	CH_3OH/ DME/N_2	Fixed bed	ZSM-5	[172]

W: water, M: methanol, DME: dimethyl ether, HC: hydrocarbon. LH: Langmuir–Hinshelwood, ER: Eley–Rideal, G&J: Gates & Johanson [165]*, K&S: Klusáček & Schneider* [166]*, Ha et al.* [169].

For carbon dioxide methanation, the model of Xu and Froment, 1989 [173] is well detailed and widely used in the literature [12]. The model equations were derived for the methane steam reforming over a $Ni/MgAl_2O_4$ catalyst. This considers numerous reaction mechanisms with thermodynamic analysis aiding in their refinement. Depending on the rate-determining steps, they selected 21 sets of three rate equations and underwent model discrimination and parameter estimation. The resulting best model yielded statistically significant parameter

estimates that were thermodynamically coherent. Weatherbee and Bartholomew, 1982 [174] developed another detailed model over a Ni/SiO2 catalyst (Langmuir-Hinshelwood type mechanism).

Falbo et al., 2018 [175] studied a model based on the empirical approach of Lunde and Kester, 1973 [176], which is only based on thermodynamic equilibrium, but with an order of reaction of 1.064 instead of 1.575. Both investigations were performed over a 0.5wt.% Ru/Al_2O_3 catalyst. Falbo et al., 2018 [175] took into account the effect of water by integrating a new parameter (α) in the reaction rate expression proposed in [176] to alter the kinetic relationship with respect to the partial pressure of H_2O, thus they have better agreement of results. Similarly, Alrafei, 2019 [12] coupled a kinetic model derived from the Lunde and Kester, 1973 [176] model to a reactor model to incorporate thermal phenomena in the reactor. Ni-based catalysts were employed. More recently, Schmider et al., 2021 [177] evaluated several reaction kinetics over Ni-based catalysts. They developed a detailed model for the surface kinetics of CO and CO2 methanation using theoretical estimations and fine-tuned to match a wide variety of datasets from both in-house and literature studies at a wide range of operating conditions [177].

The Langmuir-Hinshelwood analysis forms the basis for the simplified treatment of kinetics on heterogeneous catalysts [178]. This kinetic model aims to establish an expression for the reaction rate containing the binding of the catalyst surface active sites (molecules or dissociative atoms) and the gas reactants adsorbed. The slowest of these steps is referred to as the kinetically decisive step, and it is its speed that controls the rate at which the final product is produced [13]. This mechanism also includes adsorption and desorption steps on the catalyst (see Eq. (1.11)). While the adsorption term considers the adsorption constants and the partial pressures of reactants and products, the driving force only considers the partial pressure of the reactants and the equilibrium constant of the reaction. The kinetic term represents the Arrhenius equation. On the other hand, power law models permit a simple representation of a reaction when very little information on the reaction mechanism is available and a law with partial pressures is therefore sufficient to explain the experimental reaction rates [13]. Quezada, 2020 [13] disclosed that microkinetic models provide more in-depth conclusions on reaction mechanisms; although, their complexity of computing and writing limits their use. Three mechanisms for methanol synthesis are explained in detail by Quezada, 2020 [13].

$$r = \frac{kinetic\ term\ (driving\ force)}{adsorption\ term} \tag{1.11}$$

Power law model for methanol synthesis on a CZA catalyst was described by Quezada, 2020 [13]. But modelling results could not fit well the experimental data and he finally proposed Langmuir-Hinshelwood (LH) model for methanol synthesis (Eq. (1.5)-(1.7)) over $Cu/Zn/Al_2O_3$ with a feed of CO_2/H_2 at 26-36 bar and 473.15-598.15 K. The author evaluated two Langmuir–Hinshelwood models with a single type of active sites (Cu^0 active site for CO_2 and ZnO as promoter) and with two types of active sites (Cu^0 for CO_2 and ZnO for hydrogen). First, he considered the thermodynamic equilibrium and product and reactant inhibition by competitive adsorption on a unique type of sites (Eq. (1.12)-(1.14)).

$$CO_2 + 3H_2 \rightleftharpoons CH_3OH + H_2O \quad (1.6)$$

$$CO_2 + H_2 \rightleftharpoons CO + H_2O \quad (1.5)$$

$$CO + 2H_2 \rightleftharpoons CH_3OH \quad (1.7)$$

$$r_{CO_2,CH_3OH} = \frac{k_1 e^{-\frac{E_1}{RT}} \left(P_{CO_2} P_{H_2}^3 - \frac{P_{CH_3OH} P_{H_2O}}{K_{eq,1}}\right) / P_{H_2}^{3-\frac{\nu_1}{2}}}{\left(1 + \sqrt{K_{H_2} P_{H_2}} + K_{H_2O} P_{H_2O} + K_{CO_2} P_{CO_2} + K_{CH_3OH} P_{CH_3OH} + K_{CO} P_{CO}\right)^3} \quad (1.12)$$

$$r_{RWGS} = \frac{k_2 e^{-\frac{E_2}{RT}} \left(P_{CO_2} P_{H_2} - \frac{P_{CO} P_{H_2O}}{K_{eq,2}}\right) / P_{H_2}^{1-\frac{\nu_2}{2}}}{\left(1 + \sqrt{K_{H_2} P_{H_2}} + K_{H_2O} P_{H_2O} + K_{CO_2} P_{CO_2} + K_{CH_3OH} P_{CH_3OH} + K_{CO} P_{CO}\right)^2} \quad (1.13)$$

$$r_{CO,CH_3OH} = \frac{k_3 e^{-\frac{E_3}{RT}} \left(P_{CO} P_{H_2}^2 - \frac{P_{CH_3OH}}{K_{eq,3}}\right) / P_{H_2}^{2-\frac{\nu_3}{2}}}{\left(1 + \sqrt{K_{H_2} P_{H_2}} + K_{H_2O} P_{H_2O} + K_{CO_2} P_{CO_2} + K_{CH_3OH} P_{CH_3OH} + K_{CO} P_{CO}\right)^2} \quad (1.14)$$

where superscripts ν_1, ν_2 and ν_3 are function of the rate determining steps of reactions (1.2)-(1.4), respectively. In this case, best results were obtained with $\nu_1 = 2$, $\nu_2 = 1$ and $\nu_3 = 4$.

Second, he considered two types of adsorption sites. The basis of his kinetic model used the mechanism proposed by Graaf et al., 1988 [179]. The H_2 adsorption sites are represented by s_1 for H_2 adsorption and the CO_2 by s_2. Only the determining steps are numbered. For CO_2 hydrogenation to methanol (reaction (1.6)):

$$H_2 + 2s_1 \leftrightarrow 2H^{s_1}$$

$$CO_2 + s_2 \leftrightarrow CO_2^{s_2}$$

$$CO_2 + H^{s_1} \leftrightarrow HCO_2^{s_2} + s_1 \ (1)$$

$$HCO_2 + H^{s_1} \leftrightarrow H_2CO_2^{s_2} + s_1 \ (2)$$

$$H_2CO_2^{s_2} + H^{s_1} \leftrightarrow H_3CO_2^{s_2} + s_1 \ (3)$$

$$H_3CO_2^{s_2} + H^{s_1} \leftrightarrow H_2CO^{s_2} + H_2O^{s_1} \ (4)$$

$$H_2CO^{s_2} + H^{s_1} \leftrightarrow H_3CO^{s_2} + s_1 \ (5)$$

$$H_3CO^{s_2} + H^{s_1} \leftrightarrow CH_3OH^{s_2} + s_1 \ (6)$$

$$CH_3OH^{s_2} \leftrightarrow CH_3OH + s_2$$

$$H_2O^{s_1} \leftrightarrow H_2O + s_1$$

For the RWGS reaction (*1.5*):

$$H_2 + 2s_1 \leftrightarrow 2H^{s_1}$$

$$CO_2 + s_2 \leftrightarrow CO_2^{s_2}$$

$$CO_2^{s_2} + H^{s_1} \leftrightarrow HCO_2^{s_2} + s_1 \ (1)$$

$$HCO_2^{s_2} + H^{s_1} \leftrightarrow CO_2^{s_2} + H_2O^{s_1} \ (2)$$

$$CO^{s_2} \leftrightarrow CO + s_2$$

$$H_2O^{s_1} \leftrightarrow H_2O + s_1$$

For the hydrogenation of CO (reaction (1.7)):

$$CO + s_2 \leftrightarrow CO^{s_2}$$

$$H_2 + 2s_1 \leftrightarrow 2H^{s_1}$$

$$CO^{s_2} + H^{s_1} \leftrightarrow HCO_2^{s_2} + s_1 \ (1)$$

$$HCO^{s_2} + H^{s_1} \leftrightarrow H_2CO^{s_2} + s_1 \ (2)$$

$$H_2CO^{s_2} + H^{s_1} \leftrightarrow H_3CO^{s_2} + s_1 \ \ (3)$$

$$H_3CO^{s_2} + H^{s_1} \leftrightarrow CH_3OH^{s_2} + s_1 \ \ (4)$$

$$CH_3OH^{s_2} \leftrightarrow CH_3OH + s_2$$

The rate expressions were derived from the previous equations based on any arbitrary determining step, represented by v. Thus, it was possible to formulate Eq. (1.15)-(1.17) for two active sites and one for Eq. (1.12)-(1.14). The first (Eq. (1.12)-(1.14)) proved to be more consistent with his experimental results, where $s_1 = s_2$. [13]

$$r_{CO_2,CH_3OH} = \frac{k_1 e^{-\frac{E_1}{RT}} \left(P_{CO_2} P_{H_2}^3 - \frac{P_{CH_3OH} P_{H_2O}}{K_{eq,1}}\right) / P_{H_2}^{3-\frac{\nu_1}{2}}}{\left(1 + \sqrt{K_{H_2} P_{H_2}} + K_{H_2O} P_{H_2O}\right)^2 \left(K_{CO_2} P_{CO_2} + K_{CH_3OH} P_{CH_3OH} + K_{CO} P_{CO}\right)} \quad (1.15)$$

$$r_{RWGS} = \frac{k_2 e^{-\frac{E_2}{RT}} \left(P_{CO_2} P_{H_2} - \frac{P_{CO} P_{H_2O}}{K_{eq,2}}\right) / P_{H_2}^{1-\frac{\nu_2}{2}}}{\left(1 + \sqrt{K_{H_2} P_{H_2}} + K_{H_2O} P_{H_2O}\right)\left(K_{CO_2} P_{CO_2} + K_{CH_3OH} P_{CH_3OH} + K_{CO} P_{CO}\right)} \quad (1.16)$$

$$r_{CO,CH_3OH} = \frac{k_3 e^{-\frac{E_3}{RT}} \left(P_{CO} P_{H_2}^2 - \frac{P_{CH_3OH}}{K_{eq,3}}\right) / P_{H_2}^{2-\frac{\nu_3}{2}}}{\left(1 + \sqrt{K_{H_2} P_{H_2}} + K_{H_2O} P_{H_2O}\right)\left(K_{CO_2} P_{CO_2} + K_{CH_3OH} P_{CH_3OH} + K_{CO} P_{CO}\right)} \quad (1.17)$$

Concerning methanol dehydration into DME, the Langmuir–Hinshelwood (LH) [165] or Eley–Rideal (ER) [180] kinetic models are commonly used as basis where DME and water have inhibiting effects in the reaction [6], [170], [181]. Hosseininejad et al., 2012 [170] explained that in the Eley–Rideal model proposed by Kiviranta-Pääkkönen et al., 1998 [180], a single methanol molecule adsorbs on the acid site and reacts with another molecule from the liquid bulk phase. A. Ateka et al., 2022 [181] mentioned that the combination of two stages, methanol synthesis (mostly from syngas) and methanol dehydration to DME, led to the first kinetic models for the direct synthesis of DME. Some kinetic models are the combination of models proposed in the literature. For instance, J. Park et al., 2022 [58] combined the models of Ng et al., 1999 [157] for DME dehydration and N. Park et al., 2014 [182] for methanol synthesis. Likewise, Guffanti et al., 2021 [164] adopted the reaction rates from Graaf et al. [179] for methanol synthesis and from Ng et al., 1999 [157]. Delgado Otalvaro et al., 2020 [163] proposed rate expressions based on the general formulation of Hougen-Watson and on the model proposed by Lu et al., 2004 [158], but using fugacities (f_i) instead of partial pressures (p_i).

From the experiments carried out by Ateka et al., 2018 [160] for one-step DME synthesis, they recommended kinetic equations for the specific reactions of hydrogenation of CO_2 and CO to methanol, WGS, dehydration of methanol to DME and hydrocarbon formation (HC: $C_1 - C_4$). Ortega et al., 2018 [172] evaluated nineteen kinetic models (both power law and Langmuir-Hinshelwood-Hougen-Watson (LHHW) type) from the literature and found three [165], [166], [169] performing better during their kinetic analysis. They modified the models by including a driving force term and identified the modification of the model of Klusáček & Schneider [166] as the most robust. Tavan et al., 2013 [171] developed two kinetic models, one for γ-Al_2O_3 and one for HZSM-5. This model differs from the ones suggested by Mollavali et al., 2008 [168] for γ-Al_2O_3 and Ha et al., 2011 [169] for HZSM-5. In 2005, Nie et al. [159] worked with the intrinsic kinetics of DME from syngas over commercial mixed catalysts (for methanol

synthesis and for methanol dehydration) and considering methanol production from CO and CO_2 hydrogenation. They did not observe the WGS reaction. An et al., 2004 [167] analysed the kinetics of DME synthesis from methanol over an ion exchange resin (Amberlyst 35) working with concentration (C_i) of products and reagent.

All in all, the reaction rates afore described for methanol dehydration are very similar. A particular difference is observed in the adsorption term, where some investigators consider methanol dissociation while others do not. Moreover, in the driving force, the amount of methanol molecules estimated as adsorbed differentiates one equation from another. It is also noticed that computations of rate expressions are performed as function of partial pressures, fugacities or concentrations. On the other hand, the adsorption of DME on the catalyst (K_{DME}) was negligible in all cases.

Taking into consideration that methane synthesis from CO_2 has been extensively studied and is the most mature technology (TRL 9), and the fact that methanol synthesis follows in TRL position, and that methanol is an intermediate to produce DME from CO_2 hydrogenation, this research from now on is going to be focus on the processes of methanol and DME syntheses.

1.7. CO_2 hydrogenation reactors

1.7.1. Laboratory scale

Researchers are investigating technologies to enhance CO_2 conversion and methanol and/or DME selectivity and preserve catalyst lifetime. The most common reported technology for methanol synthesis from CO_2 is a tubular continuous fixed bed reactor with heterogeneous catalysts. However, the water generation by the reaction (1.3) limits DME production and water removal is still a challenge.

Reactor systems for DME synthesis include traditional and high-tech reactors [183]. As for methanol synthesis, fixed bed reactors are mostly found in literature. Currently, the objective of developing new technologies is to solve the issue of deactivation and/or catalyst loss during the processes [183]. Heat removal and temperature control is also another challenging subject of research.

1.7.1.1. Fixed bed reactor

Fixed-bed reactors have a simple design, consisting of catalyst pellets/particles loaded and uniformly packed into a bed of a cylindrical vessel. These reactors are easy to scale up. There are two types of fixed-bed reactors, adiabatic and multi-tubular for very highly endothermic (exothermic) reactions [178]. Their disadvantages can be: (i) the decreasing activity of solid-supported catalysts over time, (ii) the failure on sieves to retain the catalyst in bed, (iii) the blockages due to catalyst crushing, reactor plugging and/or catalyst attrition [184]. When assessing the advantages and disadvantages of fixed-bed reactors, the former generally outweigh the latter, establishing fixed-bed reactors as the preferred tool for catalysing reactions in gas or liquid process streams [184]. Most of research on CO_2 hydrogenation to methanol and/or to DME were conducted on fixed-bed reactors [29], [98], [140], [163], [185]–[190].

1.7.1.2. Fluidized bed reactor

Fluidized bed reactors have favourable heat transfer, temperature uniformity, high effectiveness factors, low pressure drop, and ability to add/remove catalyst [191]. Certain of their drawbacks are entrainment, attrition, wear, non-uniform residence time distributions, unpredictability [191]. Thus, it is necessary to weigh their advantages and disadvantages for application.

Moreover, the incorporation of a heat exchanger has been demonstrated to exert a profound impact on the steady states of the reactor, leading to notable alterations in its configuration. Wang et al., 2011 [192] evaluated Cu-Zr-Zn catalysts in a fluidized bed reactor for methanol synthesis. They pointed out a good catalytic stability during the process. Tabiś, 2001 [193] preheated the feed stream with an external heat exchanger before the fluidized-bed reactor in methanol synthesis process. The investigators concluded that the heat exchanger altered the steady states of the reactor, resulting in autothermicity improvement. Lu et al., 2004 [158] assessed the performance of DME synthesis from syngas ($CO/CO_2/H_2/N_2$) in a fluidized bed reactor and they obtained better CO conversion and DME selectivity (48.5% and 97%) compared with fixed bed (10.7% and 91.9%) or slurry (17% and 70%) reactors. The findings indicated that the ideal H_2/CO_2 ratio in the feed gas is approximately 1.4 and the optimal temperature was within 280-290 °C, but at high temperature significant deactivation may occur. Abashar, 2017 [194] simulated a multi-stage fluidized bed reactor potentially applied for enhancement of DME synthesis. A two-bed configuration yielded 32.67% more DME than a single-bed configuration, with a selectivity close to 100%. The two-bed configuration enhances performance by using distinct feed compositions and catalyst loadings in each bed. While the first bed maintains an optimal composition (52/48), the second bed's composition varies using three bifunctional catalyst loadings: methanol synthesis-rich (80/20), equal (50/50), and methanol dehydration-rich (20/80). Likewise, other investigators studied the DME production in fluidized bed reactors [195], [196].

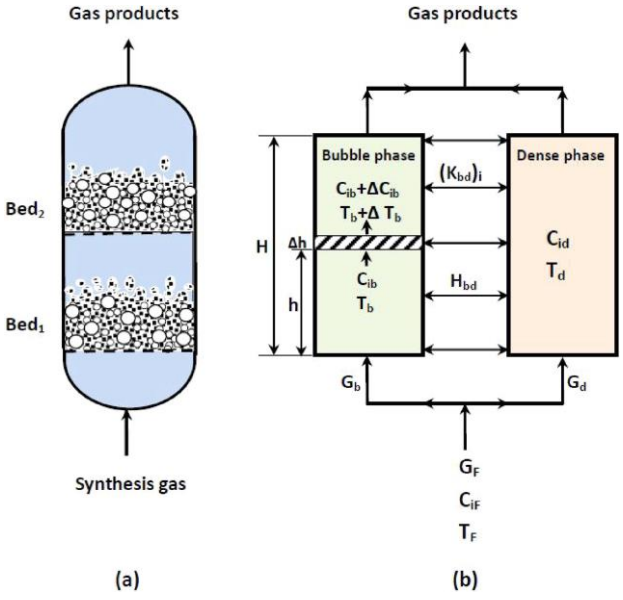

Figure 1.13 (a) Schematic diagram of a multi-stage fluidized bed reactor and (b) its model representation. Reproduced from [194].

1.7.1.3. Slurry reactor

Slurry reactors use a liquid as the fluidizing medium, operating akin to fluidized beds. Slurry stirred tank reactors have become common in methanol and DME synthesis research [197]. The simplicity of construction and temperature control (efficient heat transfer with the heat exchanger tubes, avoiding the generation of hot spots) make stirred or bubbling slurry reactors interesting for direct synthesis of exothermic gas-liquid-solid reactions [181]. Some of the drawbacks are (i) the complexity of the system as it requires a recycling system and a solid-liquid separator, (ii) a higher catalyst deactivation owing to sintering of the Cu crystallites, (iii) the severe mass transfer limitation between phases due to the necessary solubility of gases in the liquid and (iv) the loss of catalyst particles [6], [198].

A slurry Parr Instrument Company reactor was used to convert CO_2 to methanol over Cu/CNT catalysts with ethanol as the medium of the reaction, obtaining 75 $g_{meth} \cdot kg_{cat}^{-1} \cdot h^{-1}$ at 30 bar and 220 °C [199]. Likewise, Din et al., 2018 [97] carried out experiments in a three phase autoclave slurry reactor (Parr 4593) with a Cu/ZrO_2/CNF catalyst, also using ethanol as the reaction medium. Their results showed methanol productivity from 20 to 18 $g_{meth} \cdot kg_{cat}^{-1} \cdot h^{-1}$. Zhang et al., 2016 [189] tested a micro-spherical $Cu/ZnO/Al_2O_3/ZrO_2$ catalyst in a slurry phase reactor with continuous flow. The weight time yield (WTY) of CH_3OH was about 3.5 to 6 times lower than in the tested fixed-bed reactor. Nonetheless, high activity and high stability were observed in a continuous-flow slurry reactor [189]. Other investigations were conducted with slurry reactors for methanol synthesis from CO_2 hydrogenation [200]–[202]. However, a limitation of this approach is that the reaction must be conducted in a liquid solvent that is not methanol or DME. This is because, in such cases, thermodynamic equilibrium would not favour the production of methanol or DME. The use of a liquid solvent (such as ethanol or other suitable alternatives) necessitates the introduction of an additional separation step within the overall process.

Various researchers have used this technology for the synthesis of DME. For instance, Yagi et al., 2010 [203] simulated a slurry reactor to produce 3000 ton·day^{-1} of DME from synthesis gas with a single reactor. Naik et al., 2011 [204] synthetized DME from CO_2/H_2 with two catalysts ($6CuO\text{-}3ZnO\text{-}Al_2O_3/\gamma\text{-}Al_2O_3$ and $6CuO\text{-}3ZnO\text{-}1Al_2O_3$/HZSM-5) in a fixed-bed and slurry reactors. The stability of the $6CuO\text{-}3ZnO\text{-}Al_2O_3/\gamma\text{-}Al_2O_3$ was demonstrated in the fixed bed reactor, although the DME selectivity was low and the CO yield was high. The $6CuO\text{-}3ZnO\text{-}1Al_2O_3$/HZSM-5 catalyst exhibited superior performance in both slurry and fixed-bed reactors [204]. Khadzhiev et al., 2017 [205] reviewed the prospects for using the slurry technology in the large-scale production of DME from syngas ($CO/H_2/CO_2$). In line with their assessment, performing methanol dehydration in a slurry reactor avoids the acid catalyst deactivation by water, a common issue in fixed-bed reactors for DME synthesis. The γ-Al2O3 catalyst

maintained its crystalline structure and stability during methanol dehydration at at 300°C, 2–3 MPa, 1100 rpm stirring, 1.5 g catalyst, 1.18 mol/L methanol, and 2-hour reaction time [205]. Additionally, it simplifies ultrafine catalyst preparation techniques and introduces new catalyst systems like boehmite suspensions [205].

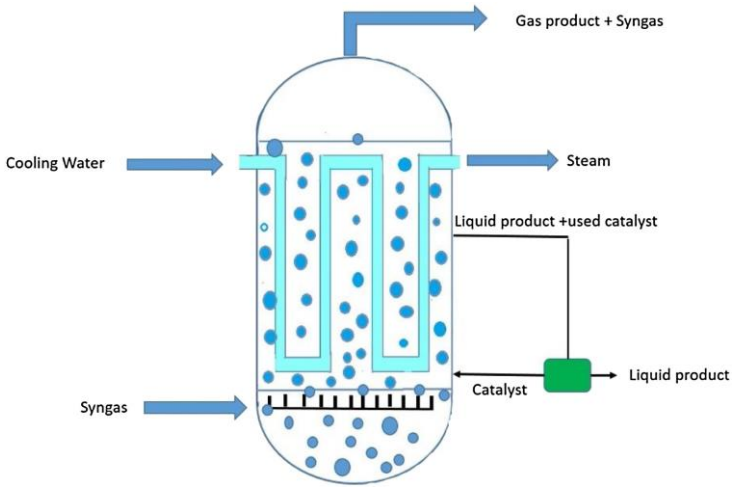

Figure 1.14 Illustration of slurry reactor. Reproduced from [206].

1.7.1.4. Photocatalytic reactor

Furthermore, the potential of CO_2 photoconversion has been assessed. In a review of the literature on CO_2 photoconversion, Li et al., 2014 [207] identified several key findings. The authors distinguished between fluidized and fixed bed reactors, which they categorized as two distinct types of photoreactors. The fluidized bed batch reactor is the most prevalent type of reactor (Figure 1.15). Nevertheless, this technology presents significant challenges, particularly in terms of reducing costs and designing an efficient reaction system, given the need to understand the underlying chemical processes. Photocatalytic CO_2 conversion represents a promising approach for reducing carbon dioxide emissions by harnessing abundant solar energy. The improvement of photoreduction efficiency presents a significant challenge, necessitating extensive research into the development of low-cost, robust artificial photocatalysts and effective reaction systems [207].

More recently, He et al., 2020 [208] performed a photothermal methanol synthesis from CO_2 hydrogenation over $CoO/Co/TiO_2$ catalyst in aqueous medium at 1 bar in an autoclave. Methanol selectivity was 99.9% with a forming rate of methanol of 39.6 $\mu mol \cdot g_{cat}^{-1} \cdot h^{-1}$. Tripathi et al., 2021 [209] explained that special emphasis has been placed on the photocatalytic approach adopted for the conversion of the carbon oxides into methanol/DME. Though, the economic viability of photo-catalysis for CO_2 conversion is hindered by their time or geographic dependence [210].

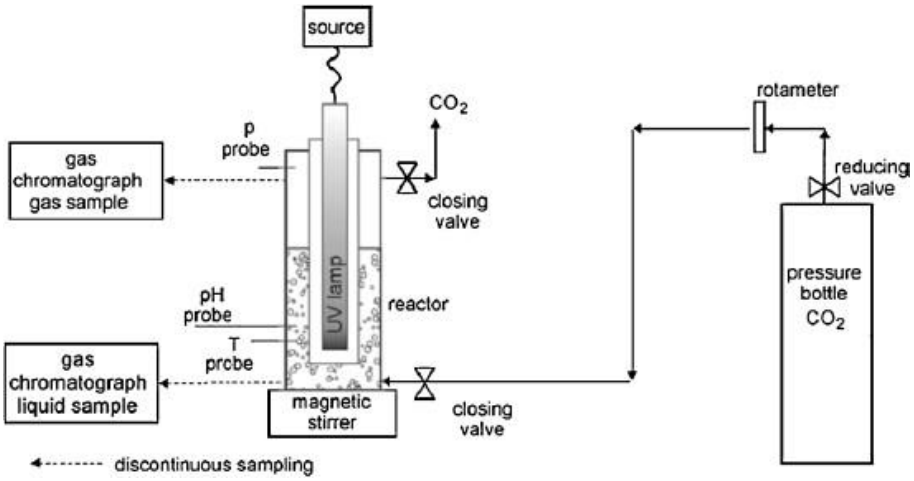

Figure 1.15 Schematic diagram of CO_2 photoreduction configuration. Reproduced from [207].

1.7.1.5. Plasma and magnetic field reactors

George et al., 2021 [211] reviewed non-thermal plasma (NTP) technology. In-plasma catalysis (IPC) and post-plasma catalysis (PPC) are the two most common reactor configurations for plasma-assisted catalysis (Figure 1.16). NTP allows operation in mild conditions. Nevertheless, the maximum methanol selectivity and yield reported were 53.7% and 11.3%, respectively, with IPC over Cu/γ-Al_2O_3 catalyst at atmospheric pressure and room temperature [211], [212]. Iliuta & Larachi, 2020 [21], presented a simulated process combining a microwave-induced plasma and a fixed bed reactor for methanol synthesis. They found 82% CO_2 conversion with H_2/CO_2=3. Even so, the energy efficiency declines significantly (from 7.3% to 2.5%) as the H_2/CO_2 ratio increases. On the other hand, Quezada, 2020 [13] performed experiments with several catalysts as well as plasma DBD (IPC). He obtained a maximum CO_2 conversion of 34% and, methanol and CO yields of 0.2% and 32.7%, respectively, over Al_2O_3 catalyst. Su et al., 2016 [213] studied the intrinsic kinetics of dimethyl ether synthesis from plasma activation of CO_2 hydrogenation. They indicated a reduction of activation energy of the hydrogenation reaction and an improvement of the DME yield. In conclusion, this is a challenging technology that needs further evaluation before implementation.

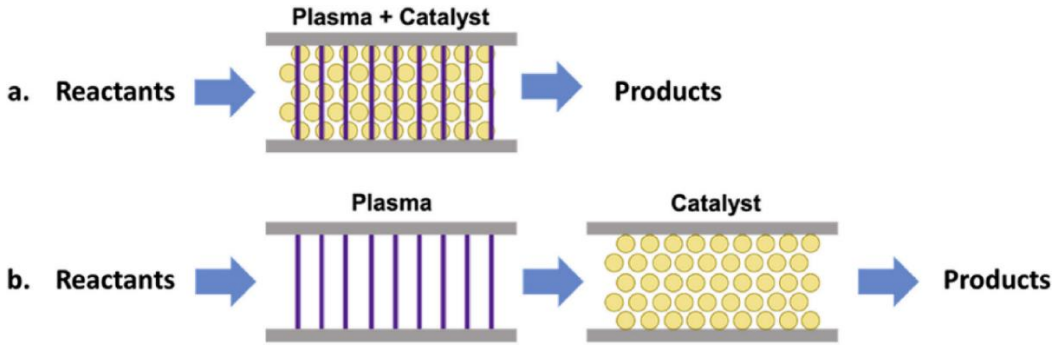

Figure 1.16 a) In-plasma catalysis and b) post-plasma catalysis schematic configurations. Reproduced from [211].

Magnetic field has also been explored in catalytic CO_2 hydrogenation. According to Donphai et al., 2016 [214], magnetic field enables a carbon-neutral CO_2 conversion process. They applied an external magnetic field in the catalytic hydrogenation of CO_2 over Cu-ZnO/ZrO_2 catalyst. Under a magnetic field intensity of 20.8 militesla (mT) in the S-N direction (counter-flow), the maximum CO_2 conversions was 2.7 time greater than that achieved without a magnetic field at 180 °C. The magnetic field improved the reactivity of the Cu-ZnO/ZrO_2 catalyst, reducing the activation energy and operating temperature. The magnetic field lowered operating temperatures by 1.03-1.23 times, enhancing catalysis by magnetizing catalysts and promoting CO_2 reactant adsorption, improving reaction performance [214]. Correspondingly, Sriakkarin et al., 2018 [215] tested Cu-Fe/HZSM-5 catalyst in a magnetic field assisted reactor. They identified an increase of methanol selectivity and CO_2 conversion by 2.24 and 1.7 times, respectively, at 220°C. Both groups found that the activity of the catalysts was improved, and apparent activation energies and operating temperatures were reduced when an external magnetic field was used. Moreover, it presented a lower environmental impact compared to conventional reactor, achieving a carbon neutral CO_2 conversion[214]. Figure 1.17 and Figure 1.18 show schematics representation of magnetic field reactors.

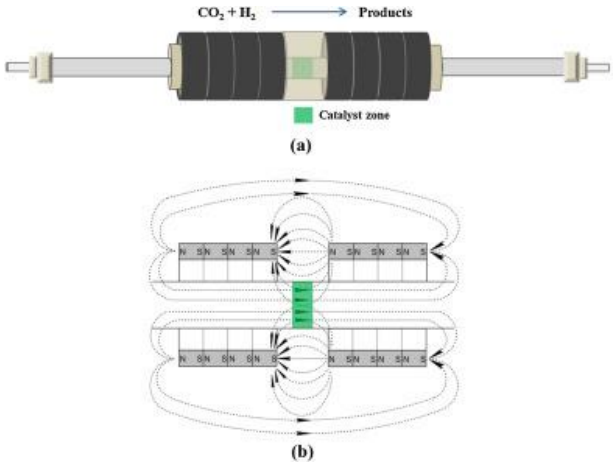

Figure 1.17 Schematics of (a) magnetic field-assisted fixed-bed reactor and (b) magnetic line of force in the north-south direction. Reproduced from [214].

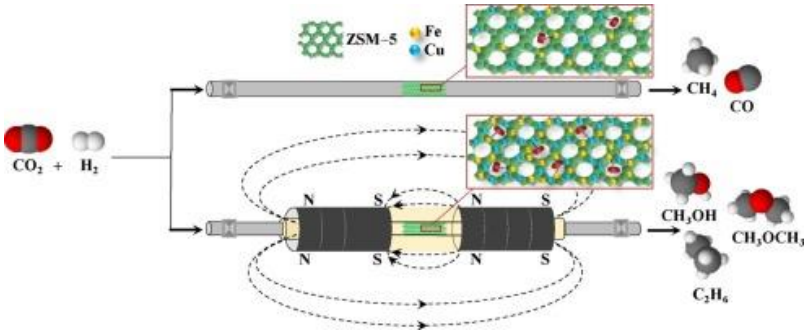

Figure 1.18 Schematic of magnetic field-assisted packed bed reactor under magnetic field direction of north-to-south. Reproduced from [215].

1.7.1.6. Membrane reactor

Process intensification using membranes for water removal, and for lowering catalyst deactivation in DME and methanol syntheses have been acknowledged as a promising process. Several investigations show the advantages of membrane reactors (MR). Gallucci et al., 2014 [216] carried out an experimental analysis of methanol production from CO_2 hydrogenation involving a zeolite membrane reactor. The membrane reactor demonstrated higher CO_2 conversion and methanol selectivity than a conventional reactor. Similarly, Raso et al., 2020 [217] tested numerous zeolite membranes (zeolite A, mordenite, zeolite T, chabazite and Ti-Chabazite) and found better results than conventional reactor.

Dehghani et al., 2021 [218] simulated a steady state Radial Flow Gas-Cooled Reactor (RF-GCR) and a Radial Flow Gas-Cooled Membrane Reactor (RF-GCMR) and compared them with a Conventional Gas-Cooled reactor (CGCR). RF-GCMR and RF-GCR consist of annular packed

beds (subsections) and annular cooling-chambers exhibited excellent heat transfer area, negligible pressure drop along the catalytic beds and higher methanol production rates than CGCR. In CGCR, both reacting and synthesis gases flow axially in counter-current mode. In RF–GCR, the gas-cooled reactor comprises two sections: annular packed-beds of CuO/ZnO/ Al_2O_3 and annular cooling chambers filled with synthesis gas, facilitating heat exchange and pre-heating for methanol synthesis in water-cooled reactors (see Figure 1.19(a) and (b)). In RF–GCMR, annular cooling-chamber walls feature hydrogen perm-selective membrane layers (Pd–Ag membrane, 6 μm thick), allowing hydrogen permeation from synthesis gas to reacting gas due to the partial pressure gradient (see Figure 1.19(c) and (d)). This flow occurs through the annular cooling-chambers and radial direction through the annular packed-beds. The reactors were evaluated at 76 bar and 401 K of pressure and temperature, respectively. Among the three reactors evaluated, RF–GCMR presented higher methanol production rate (5630.4 ton·day^{-1}).

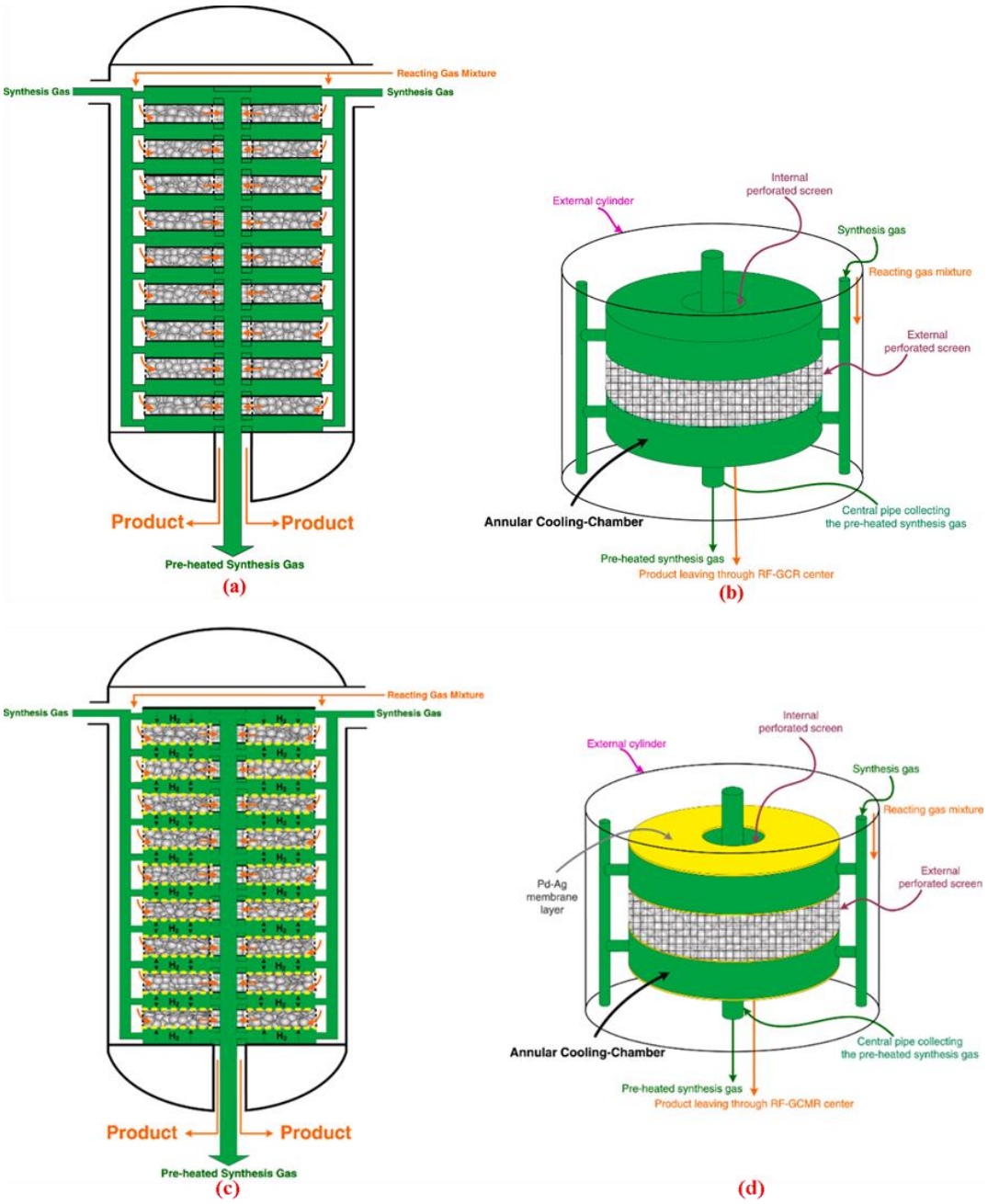

Figure 1.19 Schematics of side cut view of (a) RF-GCR and (c) RF-GCMR and detailed view of (b) RF-GCR and (d) RF-GCMR. Reproduced from [218].

High pressure MR with liquid sweep [219] and, membrane-contactor reactor (Figure 1.20) with ionic fluids (IL) and tetra-ethylene glycol dimethyl ether (TGDE) were also investigated for methanol synthesis revealing high carbon conversion [220]–[223].

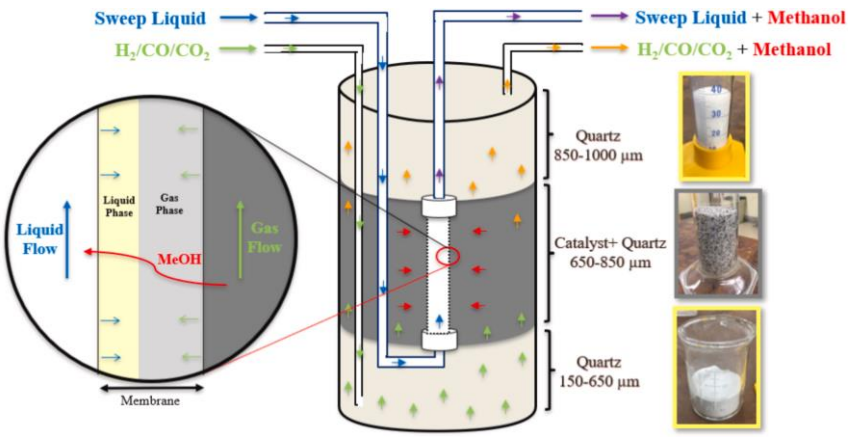

Figure 1.20 Schematic illustration of a membrane contactor reactor. Reproduced from [220].

Rahimpour et al., 2010 [224], using dynamic simulation, compared the performance of a conventional dual-type methanol reactor (CDMR), a fluidized-bed membrane dual-type methanol reactor (FBMDMR) and a cascade fluidized-bed membrane methanol reactor (CFBMMR). The dual-type reactor system allows a high temperature in the first reactor and a low temperature in the second, combining an isothermal water-cooled reactor with a gas-cooled reactor for partial synthesis gas conversion to methanol. In the CFBMMR, both reactors are fluidized beds and catalyst temperature can be controlled. Both FBMDMR and CFBMMR systems exposed lower pressure drop, overcoming mass transfer limitations, achieving higher conversion. The simulation results exhibited improved performance with the cascade fluidized-bed hydrogen permselective membrane methanol reactor.

Similarly, Saeidi et al., 2014 [225] explained that the introduction of dual-type membrane minimises energy consumption and breaks the reaction equilibrium. They used two permeable reactors (Figure 1.21). This system employs a dual-type membrane reactor, which integrates fluidized bed and fixed bed reactors. The walls of the second reactor and the vertical tubes of the first reactor (layered with a selective water-permeable membrane H-SOD, hydroxy sodalite) were filled with catalyst, which improves H_2 permeation. The H_2 perm-selective walls control the stoichiometry. The perm-selective water tubes of the first reactor facilitate the RWGS reactions, and the cooling water removes excess heat. The product then flows into the second reactor for further reactions, achieving higher CO_2 conversion and advancing FT hydrocarbon synthesis. Permselective water and hydrogen membranes improve the overall reactor performance [163].

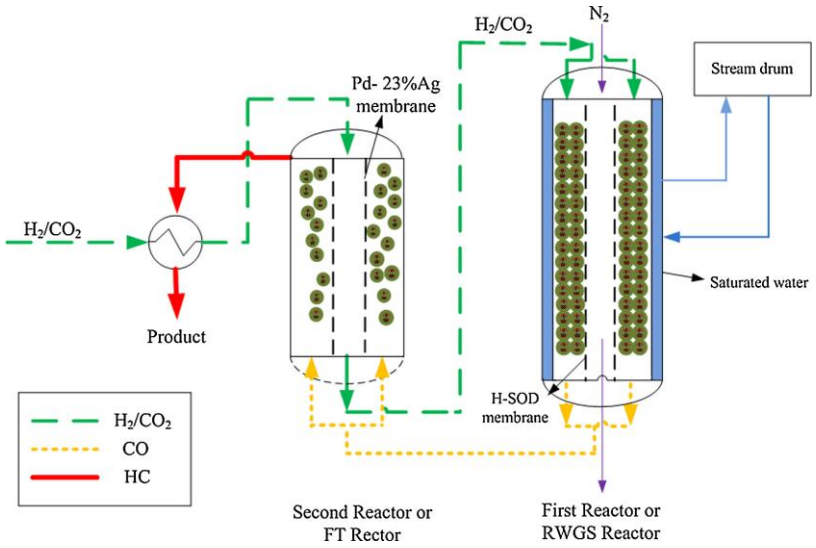

Figure 1.21 Schematic diagram of a dual-type membrane reactor: a fixed bed reactor with a water perm-selective membrane as the first stage, followed by a fluidized-bed reactor with an H_2 perm-selective membrane. Reproduced from [225].

Fedosov et al., 2015 [226] evaluated the methanol dehydration process in a NaA zeolite membrane reactor. Their zeolite membrane reactor (ZMR) achieved a maximum conversion of 88% at 250 °C, surpassing conventional reactors by 8%. Zhou et al., 2016 [227] dehydrated the methanol over a double-layer FAU–LTA zeolite sandwich membrane, having 100% DME selectivity and 90.9% methanol conversion at 310 °C, with better performance than the conventional reactor and PBMR.

In 2016, Farsi et al. [228] modelled a dual membrane reactor at steady-state condition to convert syngas to DME and obtained a 17.2% improvement in DME production capacity compared to the conventional reactor. Ateka et al., 2020 [229] tested a hydrophilic LTA zeolite membrane and validated a model for the simulation of the DME synthesis in a packed bed membrane reactor (PBMR). The PBMR enhanced DME yield and CO_2 and CO conversions compared to those obtained with the non-membrane systems, owing to the shift of thermodynamic equilibrium through the partial separation of H_2O. The higher DME yield per run is an economic advantage because recirculation is not required. Poto et al., 2021 [230] modelled and simulated a membrane reactor to produce DME from CO_2/H_2. They considered co-current sweep gas flow, non-isothermal operation, and non-ideal separation. Water and heat removal were favoured by the co-current mode. In addition, high sweep gas flow rates also favoured water removal and consequently DME synthesis. CO_2 conversion and DME yield were improved by 36% and 46%, respectively, over a conventional packed bed reactor. Beltermann et al., 2023 [231] used computational fluid dynamics (CFD) to simulate Lurgi-

type reactor and MR. In agreement with other researchers, they concluded that in-situ removal of water improves the productivity of the reaction.

Mardanpour et al., 2012 [232] proposed a model for a shell and tube fluidized bed membrane reactor (FBMR) to synthesize DME. Their simulation showed an improvement of DME production and CO conversion using fluidized bed membrane reactor instead of conventional reactor. More recently, Sadeghi & Karimi, 2023 [233] simulated a gas-cooled fluidized bed membrane reactor (Figure 1.22). They disclosed that the presence of membranes enhanced the DME production.

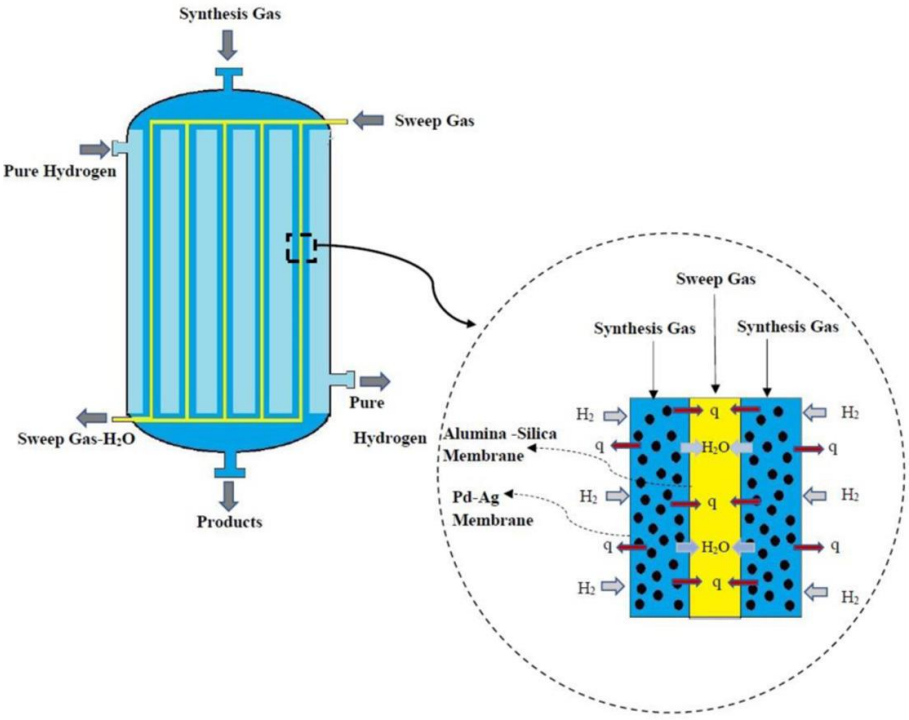

Figure 1.22 Scheme of the co-current mode for a fluidized bed membrane reactor configuration. Reproduced from [233].

1.7.1.7. Spherical reactor

Rahimpour et al., 2011 [234] and Samimi et al., 2013 [235] explained that spherical reactors are designed to solve some disadvantages found in conventional reactors such as undesirable pressure drop, high fabrication cost, diffusion limitation of larger catalyst size with lower effectiveness factor and low production capacity. Depending on the reagents flow through a catalyst bed, these reactors are classified into radial and axial reactors. Rahimpour et al., 2011 [234] simulated an axial-flow spherical packed bed reactor (AF-SPBR) for methanol synthesis to reduce pressure drop and related recompression costs and enhance methanol production rate. Its comparison with a conventional tubular packed bed reactor showed that the AF-SPBR

three and four stages improved the methanol production rate for the steady state condition by 4.4 and 7.7%, respectively. In a previous work, Rahimpour et al., 2009 [236] conducted a theoretical investigation to evaluate the optimal operating conditions and methanol production enhancement in a radial-flow spherical bed methanol synthesis reactor (RF-SPBR). They determined an optimal inlet temperature and an optimal temperature profile along the three-stage methanol synthesis reactors. The inner and outer radius ratio of one-stage reactor was variable to maximise total methanol production. Nonetheless, it remained uncertain whether there existed a singular optimal value for the radius ratio. In like manner, for DME synthesis from methanol, Samimi et al., 2013 [235] proposed an axial-flow spherical packed bed membrane reactor (AF-SPMR). The AF-SPMR consisted of two concentric spheres in which the surface of the inner sphere was coated with H-SOD. The optimised AF-SPMR decreased the pressure drop and achieved 13.5% more DME production than an AF-SPBR and a conventional reactor. Farsi, 2014 [237] modelled a simulation of methanol dehydration in radial flow spherical membrane reactors. He reported an improvement in DME production against conventional reactor, a lower pressure drop (dP in the membrane one-stage, two-stage, and tubular reactors was 0.18, 0.34, and 0.8 bar, respectively), a shift of the thermodynamic equilibrium and a reduction of purification cost in the distillation section. Figure 1.23 displays a schematic representation of an axial-flow spherical reactor.

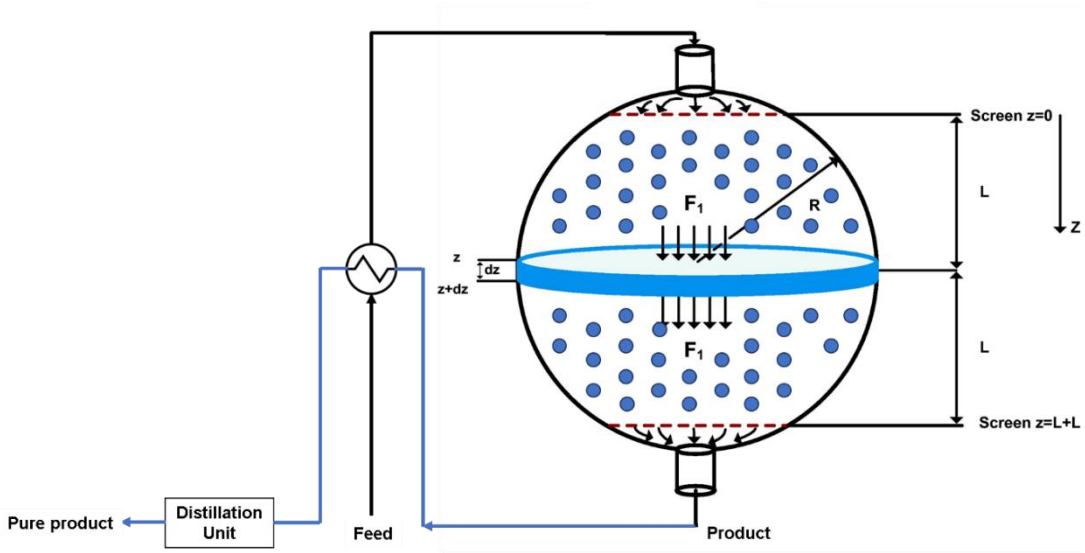

Figure 1.23 Schematic diagram of an axial-flow packed bed reactor (AF-SPBR). Modified from [234] *and* [235].

1.7.1.8. Simple cooled reactor

Considering thermodynamics and exothermicity of reactions Eq. (1.3) and Eq. (1.4), working at low temperatures is thermodynamically favourable to DME production. A compromise

must be found between hydrogenation rates and equilibrium. Bos et al., 2019 [238] characterized a condensing liquid out/gas in concept (LOGIC) reactor for CO_2 conversion to methanol by experiments and modelling (Figure 1.24). They found that this can be optimised by identifying the most optimal operating conditions for reactor and condenser, including reactor dimensions (catalyst dimension and necessary heat transfer area) to favour methanol production. Optimal productivity in adiabatic operation is achieved at 50 bars with a catalyst inlet temperature of 230–250 °C and a condenser temperature < 70 °C. High catalyst outlet temperatures restrict productivity, suggesting that (partial) removal of the heat of reaction from the catalyst bed could improve reactor productivity.

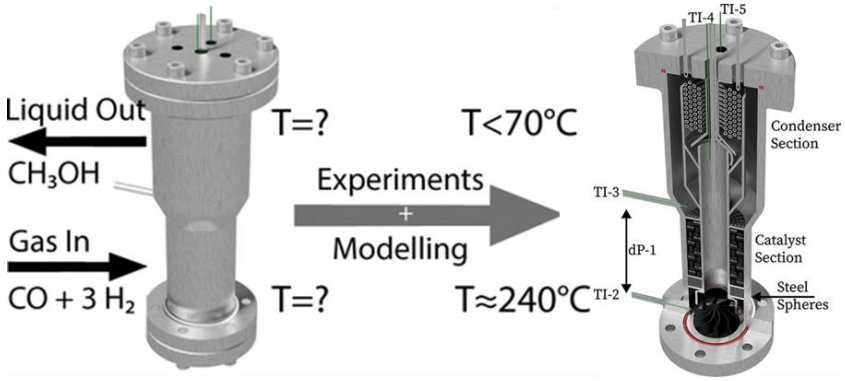

Figure 1.24 Condensing liquid out/gas in concept (LOGIC) reactor to convert CO_2 to methanol. TI- are the catalyst in (TI-2), catalyst out (TI-3), condenser out (TI-4) and condenser in (TI-5) temperature indicators, and dP-1 is the differential pressure indicator. The catalyst is randomly packed. Reproduced from [238].

1.7.1.9. Heat exchanger and micro-reactors

Phan et al., 2016 [239] synthesised methanol from syngas ($H_2/CO/CO_2/N_2$ = 65 :25 :5 :5) in a microreactor of 14 structured foils in a fixed-bed reactor at 80 bar and 300 °C. The dimensions of the structured foils in the microreactor were as follows: channel width and height of 200 µm, foil length of 150 mm, foil width of 25 mm, channel volume of the stacked foils of 4,200 mm^3, and coated surface of 63,000 mm^2. The foils were coated with a Pd/CeO_2 catalyst. They quoted that this technology may have interesting offshore potential. Besides, the advantages of microreactors were discussed in general terms. These include the narrow reaction volumes significantly boost heat and mass transfer compared to conventional reactors; quasi-isothermal conditions or controlled temperature gradients are possible; a longer catalyst lifetime due to the elimination of hot spots; a potential reduction of the extent of undesirable side reactions, thus increasing product yield; and higher energy efficiency, which leads to diminished capital costs [198], [239]–[241]. In addition, Azizi et al., 2014 [198] described that

the microreactors allow laminar flow behaviour, compactness and parallel processability. The possible disadvantages of micropacked bed reactors may include high pressure drop and maldistribution between reaction channels [242].

Li et al., 2021 [243] designed and constructed an additively manufactured reactor for methanol production from CO_2 capable to operate at 200 °C and with pressure up to 10 bar. The microstructure reactor consisted of honeycomb-like channels, some of which were utilised as reaction channels and others as cooling channels (Figure 1.25). The cooling media flows counter to syngas, ensuring a uniform 200 °C temperature across reactor zones, optimised by outer layer channels for efficiency. The surface of the internal channels was coated with catalyst for carbon dioxide hydrogenation. They explained that additive manufacturing expands configuration options, overcoming manufacturability constraints. Successful fabrication of carbon dioxide hydrogenation reactors and a CFD model optimises future designs [243].

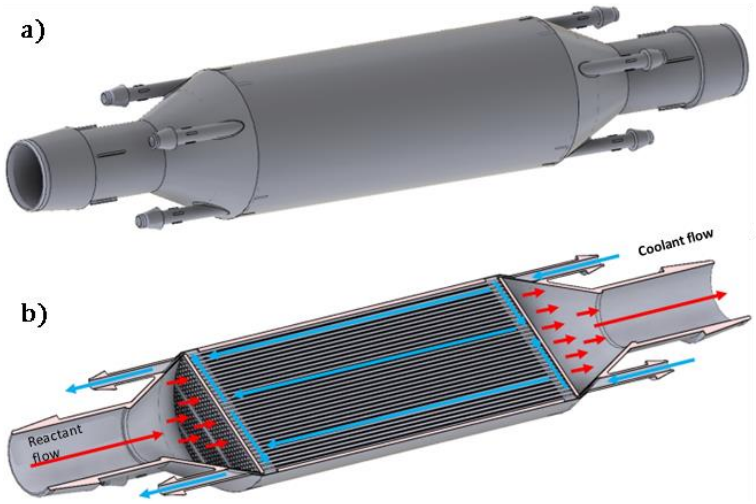

Figure 1.25 a) Design of COx hydrogenation reactor with channels for reaction gas flow and cooling media. b) Axial cross section showing flow streams. Red represents flow for reactant gas and blue coolant media. Reproduced from [243].

Ding et al., 2015 [244] synthesized a spherical microsized core-shell catalyst (CuO/ZnO/ Al_2O_3@H-ZSM-5) for the one-step DME synthesis from syngas in a micro packed bed reactor (Figure 1.26). They cited that the micro packed bed reactors are good at controlling temperature, which enables a very high heat exchange performance. The DME selectivity reached approximately 60% at 40 bar and 250 – 280 °C; GHSV=900 $mL_{STP}g_{cat}^{-1}h^{-1}$; N_2:H_2: CO:CO_2 = 10:57.6:28.8:3.6. They concluded that the shell lacks sufficient thickness and activity to fully convert methanol produced within the core. The H-ZSM-5 core-shell catalyst showed lower activity compared to conventional hydrothermal synthesis method.

In the literature, researchers have evaluated the effects of catalyst loading and process conditions on the microreactor performance [240], and of the content of wash-coated catalyst over microchannels [241] for the direct synthesis of DME from syngas. Allahyari et al., 2015 [240] exposed an increase in the catalyst loading, with a notable thickening from 20 μm to 60 μm, resulted in a change in morphology. Higher loading enhances active site count but may hinder performance due to increased diffusion distance. Catalytic comparison at 275 °C, 40 bar, $H_2/CO=2$, a flow rate of 60 mL.min^{-1} and GHSV=18,000 cm^{3}g^{-1}.h^{-1} showed that, despite a rise in catalyst loading (0.02, 0.025, and 0.03), the microreactor results surpassed those of a packed bed reactor. A rise in catalyst loading from 0.025 g to 0.03 g showed no significant change in CO conversion and DME yield [240]. In 2014, the same research team [241] investigated the impact of solid concentration in the catalyst slurry on the synthesis gas to DME in a wash-coated microreactor. Three washcoating levels (10%, 20%, and 30 wt.% $CuO/ZnO/Al_2O_3$/HZSM-5, CZAZ, catalyst slurry) were examined. According to their findings, the quality of deposited washcoat significantly influences microreactor activity. The 20 wt.% washcoating excels in CO conversion and DME yield due to optimal morphology and dispersion, ensuring improved heat and mass transfer. This is especially evident at high flow rates, where the fixed-bed reactors experience pressure drop and diffusion issues that are reduced in the microreactors. Despite slurry concentration, the microreactor consistently outperforms the fixed-bed reactors in reactivity [241].

Hayer et al., 2013 [242] examined in detail three different integrated micro packed bed reactor-heat exchangers for the one-step DME synthesis from synthesis gas over CuO-ZnO-Al_2O_3 and γ-Al_2O_3 catalysts to analyse the effect of changing the number, cross-section and internal geometry of reaction slits (Figure 1.27). The three micro packed bed reactors differ in the number of reaction slits, slit cross-section, and internal pillar arrangement. Reactor C has pillars across all 8 slits, while A and B feature three rows of pillars only at the slit input and output. Cooling channels with Thermal H350 Heat Transfer Oil remove reaction heat, ensuring a temperature gradient below 1 K, and an external insulation minimises heat loss. All reactors achieve near-equilibrium CO conversion for DME synthesis, with slight differences in conversion and DME yield observed, especially at high temperatures. Catalyst particle size fractions and varying conditions confirm the absence of internal mass limitations in micro packed beds, concluding that external mass transfer is not a limiting factor under the studied conditions. They obtained a maximum CO conversion and DME yield of 96% and 53%, respectively at 280 °C, 50 bar and GHSV = 7500 NmL·g_{cat}^{-1}·h^{-1}. The research team suggested that the direct synthesis of DME could potentially be scaled up thanks to the characteristic features of micro-structured reactors.

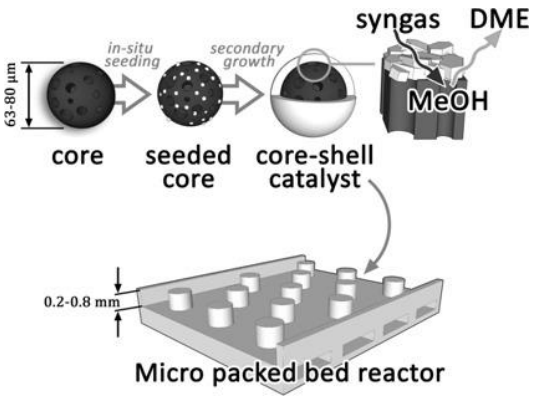

Figure 1.26 Design of micro packed bed reactor and core-shell catalyst for DME synthesis. Reproduced from [244].

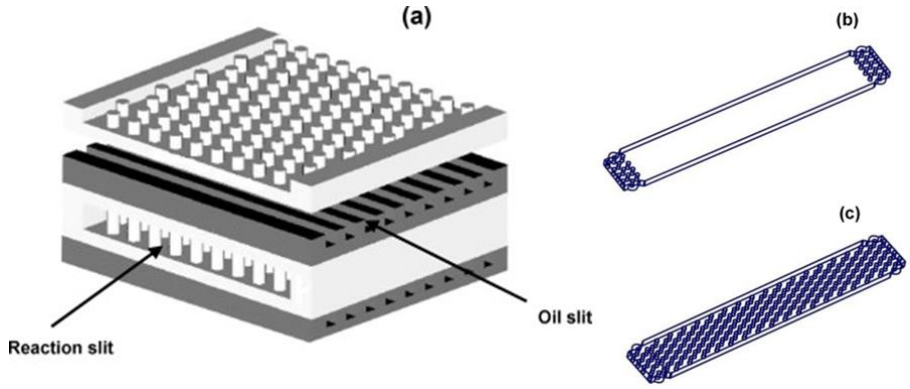

Figure 1.27 Design of (a) the stacking of reaction and heat exchange oil slits in the three dissimilar integrated micro packed bed reactor-heat exchangers, (b) internal pillar structure inside the reaction slits of reactors A and B, and (c) pillar structure inside the slits of reactor C. Reproduced from [242].

1.7.1.10. Temperature gradient reactor

Omata et al., 2002 [245] designed and tested a DME synthesis process in a temperature-gradient reactor (TGR). Their experimental results displayed that the TGR was able to overcome the equilibrium conversion limit, thus the catalyst performance was much higher than that in a conventional isothermal fixed bed reactor. The TGR inlet temperature was high inlet and decreased along the reactor with the down flow of reaction gas. As thermodynamic equilibrium conversion was attained close to the TGR input, the conversion increased gradually along the reactor following the temperature-equilibrium curve until the colder zone. At 513 K, 2 MPa, $H_2/CO/CO_2/N_2$=60:30:5:5, CO conversion was about 80% at a short contact time (W/F) of 30 g.h.mol^{-1} in an isothermal reactor, while in the TGR at 550–513 K, W/F=15 g.h.mol^{-1} gave the same conversion. After, the catalyst bed was divided into five zones in series consistent of five outer ring heaters controlled by individual temperature controllers as illustrated in Figure 1.28. They performed a temperature gradient optimisation. Besides, they

accelerated the evolution of the temperature profile using a genetic algorithm (GA) and neural network to have 71% CO conversion at 1 MPa and with W/F=50 g_{cat}·h·mol^{-1} [246]. In 2009, the same group [247] optimised the temperature profile of TGR by means of artificial neural network (ANN) and grid search aided optimisation (to find the optimum temperature setting to obtain high CO conversion) attaining a 82% CO conversion at 1 MPa and W/F=50 g_{cat}·h·mol^{-1} with a mixture of Cu-Zn-Al-Ti-Nb-V-Cr catalysts and γ-alumina.

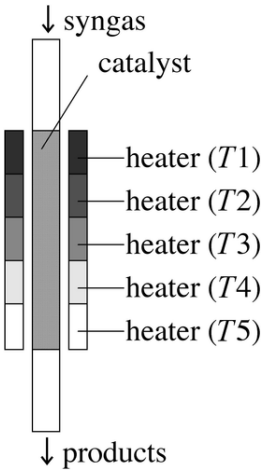

Figure 1.28 Configuration of Temperature Gradient Reactor. Reproduced from [246].

1.7.2. Industrial scale

1.7.2.1. Methanol synthesis

For industrial methanol synthesis, there are various patents using copper catalysts, including Johnson Matthey PLC (ICI, US5424335A), Metallgesellschaft AG (Lurgi, US5631302A) and Mitsubishi Heavy Industries Ltd. (EP1008577A1). Moreover, Haldor Topsoe, Linde and Casale are companies licensing their own technologies to convert syngas into methanol [248]. Mitsubishi used conventional adiabatic reactors in its methanol plants [248] operating at temperatures ranging from 200 to 280 °C with a pressure of 50-150 atm. The catalyst bed temperature is controlled by means of a quench-type converter and by the reaction heat recovery in an intermediate stage boiler [249]. In the ICI process, methanol is also synthesized in adiabatic reactors with quench points, inject part of the feed stream into the reactor for direct cooling. Lurgi and Linde used an isothermal reactor consisting in a shell-and-tube heat exchanger: in the shell circulates boiling water and the tubes are packed with a catalyst for methanol synthesis [248]. Air Liquide is a methanol licensor using Lurgi MegaMethanol™ to convert natural gas into methanol. But they also offer the technology to produce methanol from CO_2 conversion.

Casale proposes a reactor portfolio with ARC (Advanced Reactor Concept) and IMC (Isothermal Methanol Converter) technologies. The ARC is a 4-bed reactor renovated from the ICI quench lozenge converter (Figure 1.29). There are two types of IMCs (Figure 1.30): steam-raising reactors and gas-cooled reactors. Both quasi-isothermal converters consist of exchanger plates containing cooling media with axial and axial-radial catalyst beds. These have a single isothermal bed, traversed by the process gas in downward direction (axial) or axial- radial path. In the IMC steam-raising reactors, the catalyst temperature is kept under control by the cooling plates in which boiler feed water flows in counter-current or crossflow to the gas flow. In the IMC gas-cooled reactors, the bed is split in two regions: an adiabatic zone and an isothermal zone. The adiabatic region is not cooled by heat exchange. The isothermal region is cooled by heat exchanger plates vertically immersed inside the catalyst mass. The plate design ensures the co-current flow. [250]

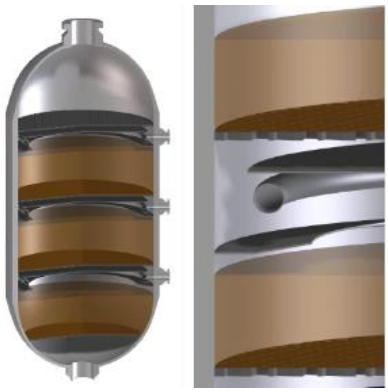

Figure 1.29 ARC (Advanced Reactor Concept) converter drawing. Reproduced from [250].

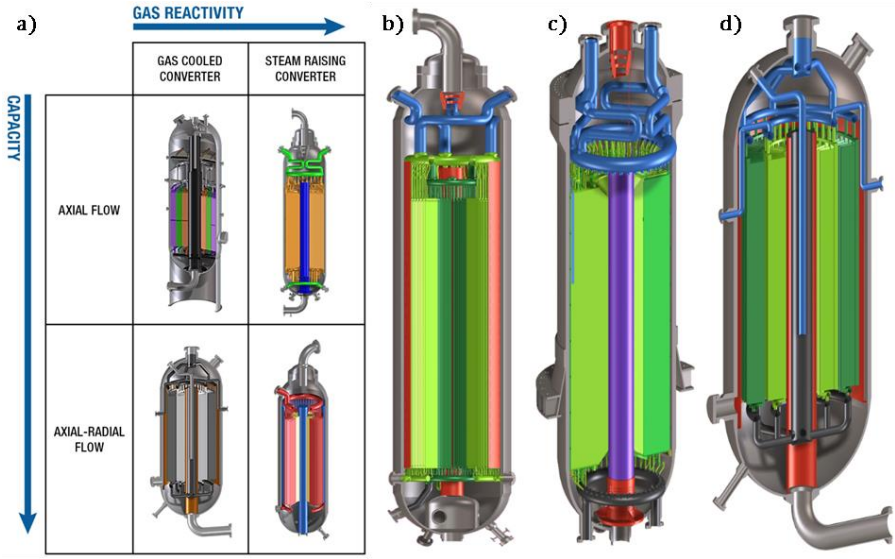

Figure 1.30 Illustration of a) IMC (Isothermal Methanol Converter) reactors: b) Axial-radial steam-raising, c) axial steam-raising and d) axial-radial gas-cooled. Reproduced from [250].

Dieterich et al., 2020 [251] gathered the commercial designs and processes for methanol synthesis. In Figure 1.31, they illustrated the corresponding simplified reactor layouts.

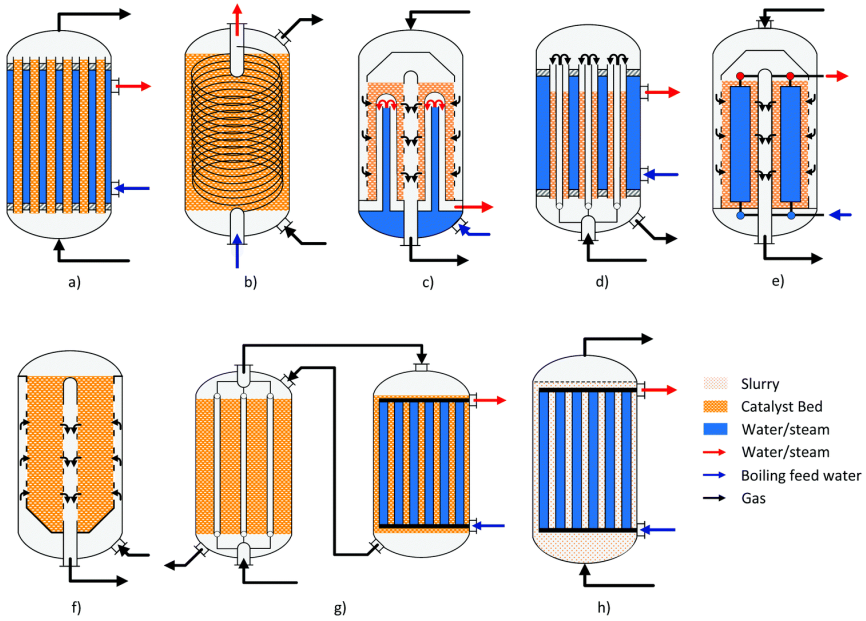

Figure 1.31 Simplified reactor schemes of (a) Lurgi tubular reactor, (b) Linde Variobar, (c) Toyo MRF, (d) Mitsubishi Superconverter, (e) Methanol Casale IMC, (f) Haldor Topsøe adiabatic reactor, (g) Lurgi MegaMethanol and (h) Air Products LPMEOH. Reproduced from [251].

Today, some plants produce methanol from CO_2 hydrogenation. Tursunov et al., 2017 [85] explained that in Japan in 1996 was built the first pilot plant generating 50 $kg \cdot h^{-1}$ of methanol from CO_2 and H_2. It used a CuO/ZnO catalyst supported on modified SiO2. In 2008, Mitsui Chemicals Inc. invested in the construction of a pilot plant to produce about 100 tons of methanol per year from CO_2 and H_2 [252]. Since 2010, this Mitsui Chemicals pilot plant has been operational at the R&D site (Osaka Works). It synthesizes methanol, using CO_2 emitted from plants and hydrogen obtained by photolysis of water [252]. Sud-Chemie and Lurgi AG achieved one of the fundamental milestones, developing a highly selective and active catalyst for CO_2 conversion to methanol at 260°C. For the US DOE National Energy Technology Laboratory, Air Products Liquid Phase Conversion Company has announced the development of a liquid-phase synthesis of methanol for the first time, enabling CO_2 and H_2 to be converted into methanol of approximately 95% with high selectivity in one step. [85]

In 2011, Carbon Recycling International (CRI) commissioned the first commercial demonstration plant in Iceland, which aimed to improve the plant economics for larger plants and to gain operation expertise. Its capacity was about 5 $Mton_{CH_3OH} \cdot year^{-1}$ [252]. Innogy (GER) is another commercial company involved in renewable methanol production. Other feasibility and R&D companies' feasibility and R&D companies involved in methanol synthesis from CO_2

and H_2 are Advanced Chemical Technologies (CAN), Asahi Kasei (Japan), Blue Fuel Energy (Canada), bse Engineering (Germany), Catalytic Innovations (USA), CRI (Canada /Germany), Gensoric (Germany), Infraserv (Germany), Liquid Wind (Sweden), MefCO_2 (Germany), Neo-H_2 (USA), Port of Antwerp (Belgium), Quantiam Technologies (Canada), STEAG (Germany), Swiss Liquid Future (Switzerland), Thyssenkrupp (Germany), USC (USA), ZASt (Germany) [253].

IRENA [41] presented a table (Table 1.6) of existing and projected facilities, with a possible global production of over 700 000 ton ·year^{-1}. They reported five technology providers: CRI (Iceland), Thyssenkrupp/Swiss Liquid Future (Germany), bse engineering/BASF (FlexMethanol, Germany), Haldor Topsoe (Denmark), and Johnson Matthey (United Kingdom) who develop and license CTM solutions [41]. Additionally, ENN Natural Gas Co., Ltd. currently has a capacity of producing 1.2 million tonnes of methanol per year with two production units [254].

Table 1.6 Existing or planned plants for methanol production from CO_2 and H_2. Reproduced from [41].

Country	**Company**	**Start-up year**	**Capacity (ton·y^{-1})**	**Feedstock**
Iceland	CRI	2011	4000	Geothermal CO_2 and H_2 from water electrolysis
China	Dalian Institute of Chemical Physics	2020	1000	CO_2 and H_2 from water electrolysis (PV)
Sweden	Liquid Wind	2023 (plan for 6 facilities by 2030)	45000	Upcycled industrial CO_2 and H_2 from water electrolysis
Australia (Tasmania)	ABEL	2023	60000	Biogenic CO_2 and H_2 from water electrolysis
China	Henan Shuncheng Group/CRI	2022	110000	CO_2 from limekiln and H_2 from coke oven gas
Norway	Swiss Liquid Future/ Thyssenkrupp	n/k	80000	CO_2 from ferrosilicon plant and H_2 from water electrolysis (hydropower)
Norway	Consortium of companies/CRI	2024	100000	CO_2 and H_2 from water electrolysis
Canada	Renewable Hydrogen Canada (RH2C)	n/k	120000	CO_2 and H_2 from water electrolysis (hydro)
Belgium	Consortium at the port of Antwerp	n/k	8000	CO_2 and H_2 from water electrolysis

Belgium	Consortium at the port of Ghent	n/k	46000-180000	Industrial CO_2 and H_2 from water electrolysis
Netherlands	Consortium Nouryon/ Gasunie/ BioMCN and three others	n/k	15000	CO_2 and H_2 from water electrolysis
Germany	Dow	n/k	200000	CO_2 and H_2 from water electrolysis
Denmark	Consortium of companies	2023-2030	n/k	CO_2 from MSW and biomass. H_2 from water electrolysis (offshore wind). Up to 1.3 GW electrolyser capacity by 2030
Germany	Consortium	n/k	n/k	CO_2 from cement plant and H_2 from water electrolysis (wind)

n/k: not known.

As a conclusion, tubular boiling-water reactor, quench reactor and series adiabatic reactors (spherical adiabatic reactors) are the three most common used reactors for conventional methanol production in the industrial fields [87]. In the first reactor, the heat generated in the catalytic process is dissipated via the boiling water [11], [87]. Its configuration enables temperature regulation, high conversion, and catalyst stability. Several adiabatic catalyst beds are installed in series in one pressure vessel of the ICI quench-cooled converter. However, catalyst is partially used owing to the reaction preferential pathways. The spherical adiabatic reactors have higher methanol production rate and lower cost compared to cylindrical reactors [87].

1.7.2.2. DME synthesis

Several patents have been found associated with dimethyl ether production process, including: JPS59199647A (Mitsubishi Kasei Corp.), JPH0285224A (Mitsui Toatsu Chemicals, Inc.), EP0324475A1 (Air Products and Chemicals, Inc.), US5389689A and US6147125A (JFE Holdings, Inc.), US6191175B1 (Haldor Topsoe, AS), US6608114B1 (Air Products and Chemicals, Inc.), EP1396483A1 (Toyo Engineering Corp.) and, CN101941892A (Southwest Research and Design Institute of Chemical Industry, Haohua Chemical Science and Technology Corp Ltd).

DME is produced industrially in indirect (methanol production followed by its dehydration) or direct route (one-step DME synthesis with bifunctional catalyst). Azizi et al., 2014 [198] explained that Toyo, Mitsubishi Gas Chemical, Lurgi and Uhde (thyssenkrupp) have their own

indirect processes, while Haldor Topsoe, JFE Holdings, Korea Gas Corporation, and Air Products have direct processes for DME production.

Toyo Engineering Corporation (TOYO) developed indirect DME production technology consisting of methanol synthesis from synthesis gas, and DME synthesis processes [255]. They operate at an inlet temperature of 220-250 °C and outlet temperature of 300-350 °C and a pressure of 1.0-2.0 MPaG, with a methanol conversion of 75-80% in the reactor of the methanol dehydration section (Figure 1.32). They awarded and completed four licensing contracts for DME production in China: Lutianhua Group Inc., Shenhua Ningxia Coal Group Co., Ltd., and Shanxi Lanhua Clean Energy Co., Ltd. [255], [256]. TOYO claims that a single train JumboDME® plant can be realised with a DME capacity of 3500 ton·day^{-1} and that a radial flow reactor like the MRF-Z® methanol with a capacity of up to 6000 ton·day^{-1} is feasible. This technology was jointly taken over by four companies (Toyota Tsusho, INPEX, JAPEX and Total) [257]. Mitsubishi Gas Chemical/Mitsubishi Heavy Industry developed their process using super converter (SPC) instead of conventional quench process [245]. Mitsubishi Gas Chemical Company (MGC), Mitsubishi Corporation (MC) and Mitsubishi Heavy Industries Engineering (MHIENG) partnered with the National Gas Company of Trinidad and Tobago (NGC) and Massy Holdings (Massy) to launch commercial operations of a methanol and dimethyl ether (DME) plant [258]. The expected production rate was 20 000 ton·year^{-1} DME.

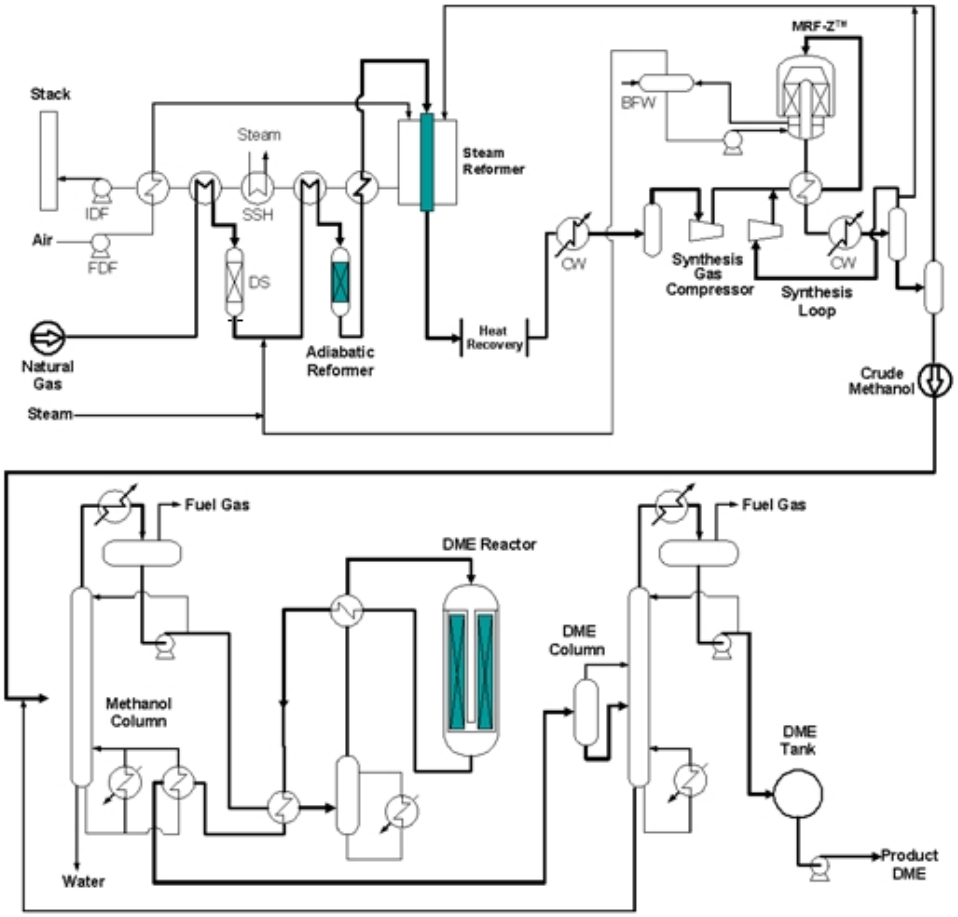

Figure 1.32 Methanol and DME synthesis process flow diagram of TOYO Engineering Corporation. Reproduced from [256].

The Lurgi MegaDME® process involves a simple adiabatic or cooled fixed-bed reactor operating at 1-30 bar and 250-360 °C with 70-85% methanol conversion, and the methanol vaporizer and the DME column are coupled becoming the reboiler or overhead condenser of the other [251], [259]. Uhde AG has a methanol dehydration process in a reactor operating between 260-310 °C. In the next step, DME is separated from water, non-condensable components and impurities to achieve fuel-grade (over 98%) [260]. In Figure 1.33 is presented their DME process flow.

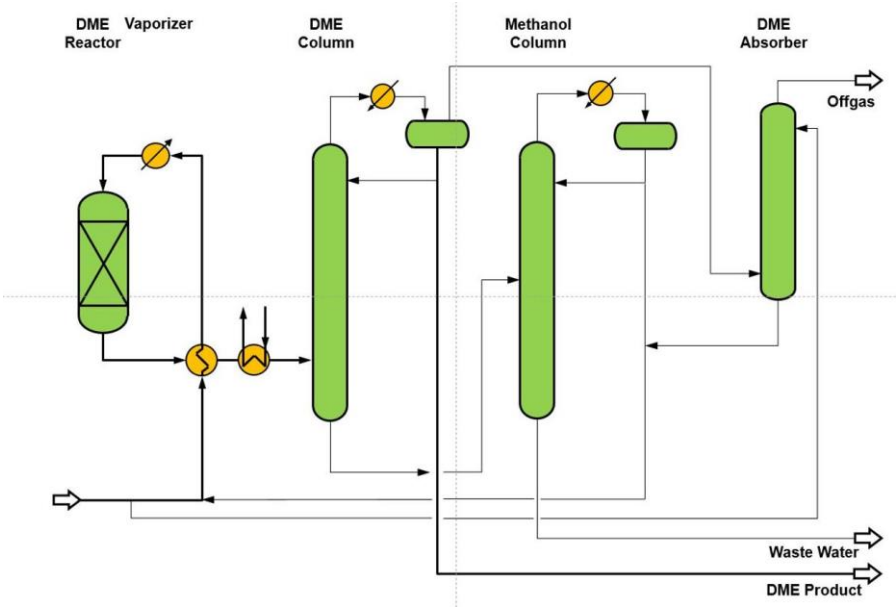

Figure 1.33 Uhde DME synthesis process flow. Reproduced from [260].

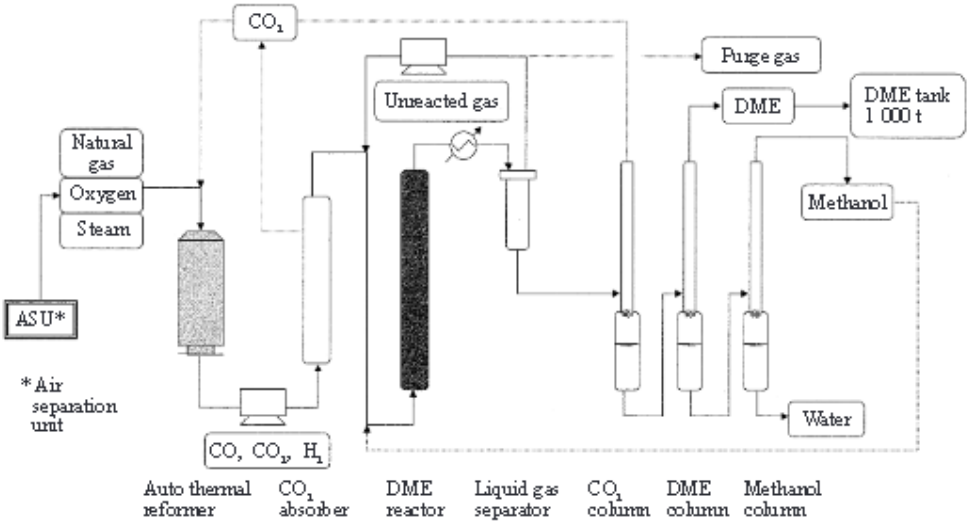

Figure 1.34 DME synthesis plant process flow diagram of JFE Group. Reproduced from [261].

JFE Group synthesized DME directly from syngas in a 100 ton·day^{-1} pilot plant (Figure 1.34) at a reaction temperature of 260 °C and pressure of 5 MPa in a slurry bed reactor, obtaining 99.6% DME purity, 93% DME selectivity, and 96% syngas conversion [261]. Yagi et al., 2010 [203] explained that they employed two reactors in parallel: the first one had an inner diameter of 2.3 m and a height of 22 m and the second one, an inner diameter of 0.65 m and a height of 28 m. The internal coils of the heat exchanger allow the reaction heat removal and steam generation. The by-products (CO_2 and methanol) were recycled to the reactor. This

demonstration plant generated 19,520 tons in 346 days (from 2003-2006). Through simulation, a process capable of producing 3 000 ton·day^{-1} was developed with a single reactor of 7 m diameter and 50 m height [203]. Afokin & Magomedova, 2021 [262] cited that Korea Gas Corporation (KOGAS) launched a DME demo-plant of 10 ton·day^{-1} and worked 78 days in 2008. This technology made possible 99.6 wt.% DME purity. Their process is oriented towards the recovery and removal of CO_2, which is achieved by using three columns (an absorber, a desorber and a CO_2 extractor). For DME synthesis, a water-cooled shell-and-tube heat exchanger reactor at 6.0 MPa is used. DME is only recovered from the liquid phase by distillation [262].

In 1999, Air Products ran a Liquid Phase Dimethyl Ether (LPDME™) process demonstration in a single high-pressure slurry bubble column reactor (SBCR) on a 10 ton·day^{-1} scale. DME production rate was 5.1 ton·day^{-1} versus 4.8 ton·day^{-1} expected. The higher productivities were perhaps because of multiple CSTRs in the SBCR [263]. In 2020, Air Products and Haldor Topsoe signed an alliance agreement to develop a potential DME plant project [264], [265]. In 2019, Sichuan Lutianhua Co., Ltd. planned to invest and built a direct syngas conversion to DME plant developed by BASF and Linde [266]. Sichuan Lutianhua Luyuanchun Industrial Corp. has a DME production of 100 000 Mton·year^{-1} [267]. Besides, Johnson Matthey (JM) licenses its own methanol dehydration process with a feature of the DAVY™ process controlling the methanol conversion to a level below equilibrium, significantly reducing by-product formation and therefore the loss of methanol [268].

In summary, DME is industrially produced through indirect or direct routes. Existing processes are based on syngas hydrogenation or methanol dehydration and not on CO_2 hydrogenation. Fixed-bed reactors, slurry bed reactors and water-cooled shell-and-tube heat exchanger reactors are used on industrial scale for the synthesis of DME. Zeolite materials within 250–400 °C and pressures up to 18 bar appear suitable as solid-acid catalysts in methanol dehydration and they are extensively used in industry as catalyst, adsorbent and ion exchanger [198].

It can be inferred that zeolite materials, within a temperature range of 250–400 °C and under pressures up to 18 bar, are suitable candidates to serve as solid-acid catalysts in the methanol dehydration process.

1.8. Process simulations

Process simulations play a crucial role in understanding and optimising methanol and DME syntheses. Process simulations typically involve modelling the intricate reactions and the underlying thermodynamics within the process. The simulation aims to anticipate the behaviour of the system under different operating conditions, thereby providing insights into process performance, efficiency, and potential enhancements. Several researches have been done concerning the simulation of methanol and DME production process from CO_2 conversion.

1.8.1. Methanol synthesis

Lonis et al., 2019 [269] proposed a design for methanol production on commercial Cu/ZnO/Al_2O_3 catalyst by hydrogenation of captured and recycled CO_2. Figure 1.35 shows the diagram of the methanol synthesis section they presented. Here, a hydrogen-rich stream (13M) is heated up (HX1M) to feed the adiabatic reactor (R1M) and then pass through a separation process that consists of two stages: 1-separation of unreacted gases (F1M), mainly composed of hydrogen (22M), from the water/liquid methanol mixture (17M); and 2-separation of non-condensable residual gases (F2M), primarily composed of CO_2 (25M); followed by a temperature rise (HX2M) to finally proceed with distillation (D1M) of the mixture. Aspen Plus was used for the simulation of the reactor (RPlug) and the distillation column (RadFrac). The authors reported a production rate of about 600 $kg \cdot h^{-1}$ of methanol. Thermal energy storage system, recovered from another process stage (Solid Oxide Fuel Cell (SOFC) exhaust gases), generated 93% of the thermal power required in the process.

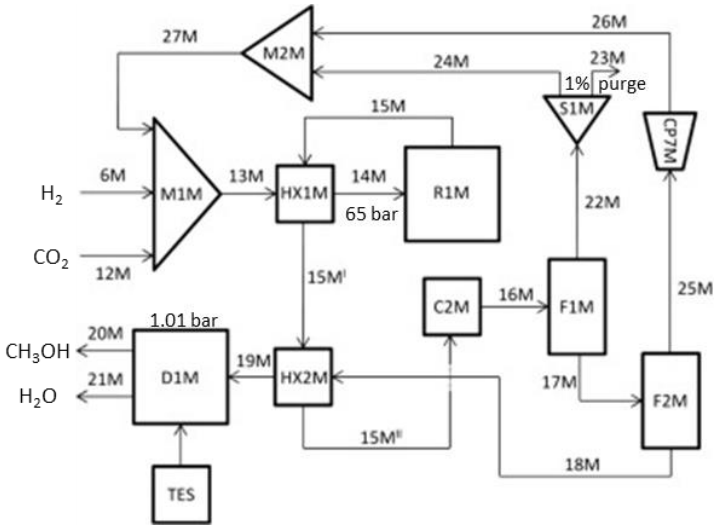

Figure 1.35 Simplified functional diagram of the methanol synthesis and purification section C: Cooler; CP: Compressor; D: Distillation column; F: Flash; H: Heater; M: Mixer; R: Reactor; S: Splitter; TES: Thermal energy storage [269].

On the other hand, Pérez-Fortes et al., 2016 [252] described a simulation in CHEMCAD with technological, economic and environmental analysis. Their simulation was based on the process designed and simulated with Aspen Plus by Van-Dal & Bouallou, 2013 [270] (Figure 1.36). Both processes were simulated and optimised with the commercial catalyst Cu/ZnO/ Al_2O_3. In the Van-Dal & Bouallou, 2013 [270] process, H_2 and CO_2 are introduced at high pressure into a mixer and passed through a series of heat exchangers to achieve the desired temperature at the reactor input. The gases leave the reactor then pass through further heat exchangers before entering the high-pressure separator and then a second low-pressure separator where the feed to the distillation tower would exit to obtain the methanol. Pérez-Fortes et al., 2016 [252] proposal has a more complex heat exchange network than Van-Dal & Bouallou's, by adding exchangers 11 and 13 (Figure 1.37). The recycle stream is heated in heat exchanger 13 with hot water from the intercoolers, the partial condenser of the distillation column and the final condenser 25. The reactor reached equilibrium for reactions (1.3) and (1.2) at approximately the midpoint of the process. The conversion of CO_2 to CH_3OH is about 22% in the reactor, but 94% in the whole process and about 0.4% of the incoming CO_2 is converted to CO. Based on their conclusions, this is a feasible project for Carbon Capture and Utilisation (CCU) plant.

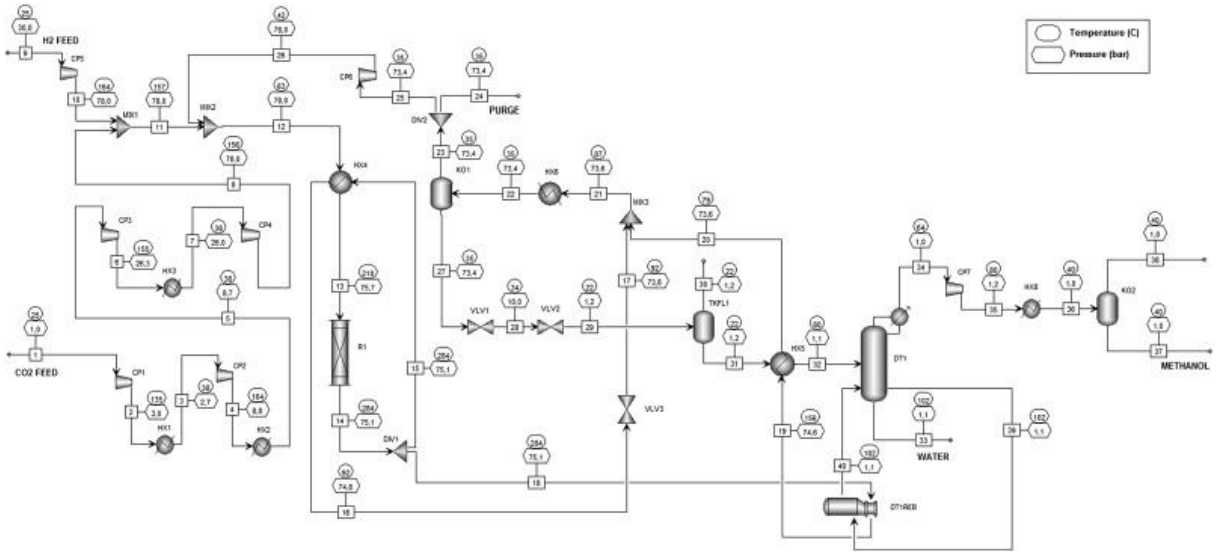

Figure 1.36 Diagram of process designed by Van-Dal & Bouallou [270]. *R1: adiabatic reactor; KO1, KO2: knock-out drum; TKFL1: tank flash; DT1REB: reboiler.*

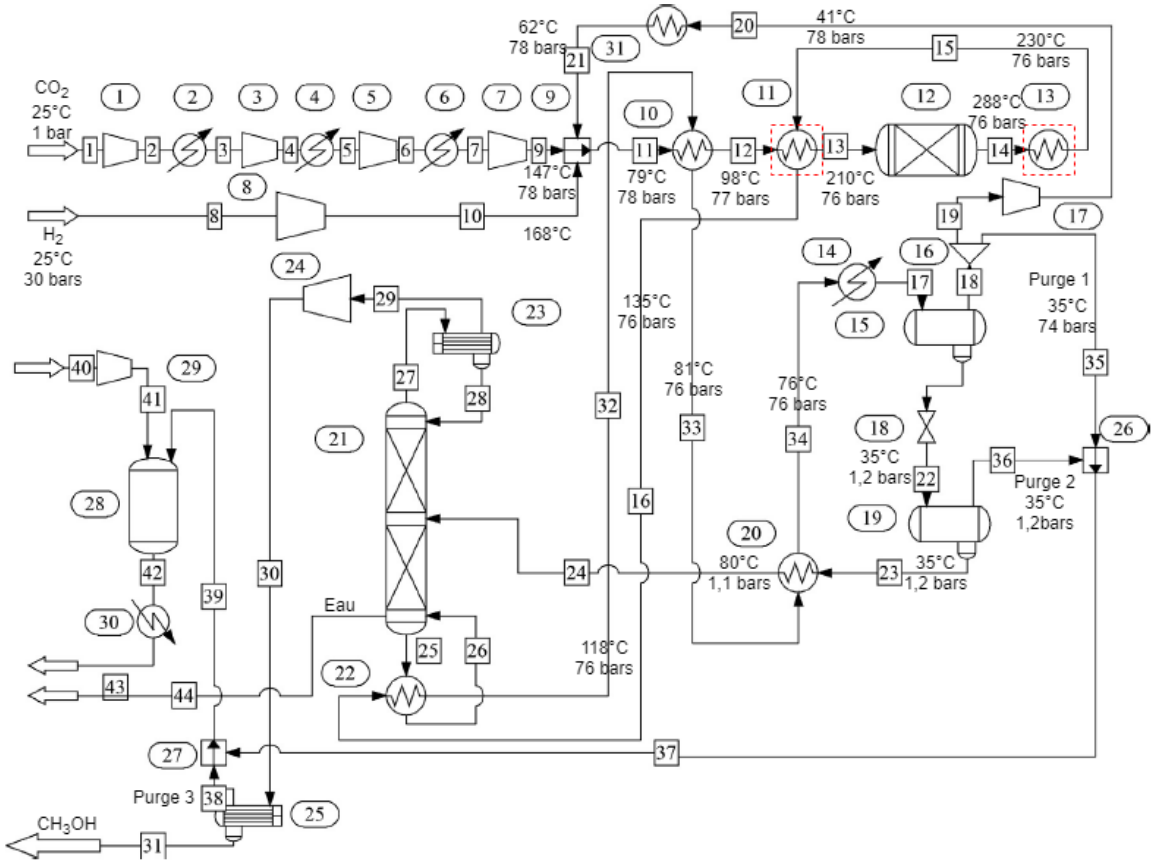

Figure 1.37 Process flow sheet for the simulation of Pérez-Fortes et al., 2016 [252].

More recently, Meunier et al., 2020 [40], based on the approaches of Van-Dal & Bouallou, 2013 [270] and Pérez-Fortes et al., 2016 [252], designed a process scheme for the production

of methanol from industrial CO_2, using same CZA catalyst (Figure 1.38). The operating pressure was 80 bar and the temperature at the reactor input was 250°C. The reactor processed 2 475 tons of CO_2 per day and produced 1 546 tons of methanol per day, implying a methanol yield of 90%. The reactors used in the various documents cited are adiabatic. Despite the optimisation of the process, it is still economically unviable, given the price of electricity [40].

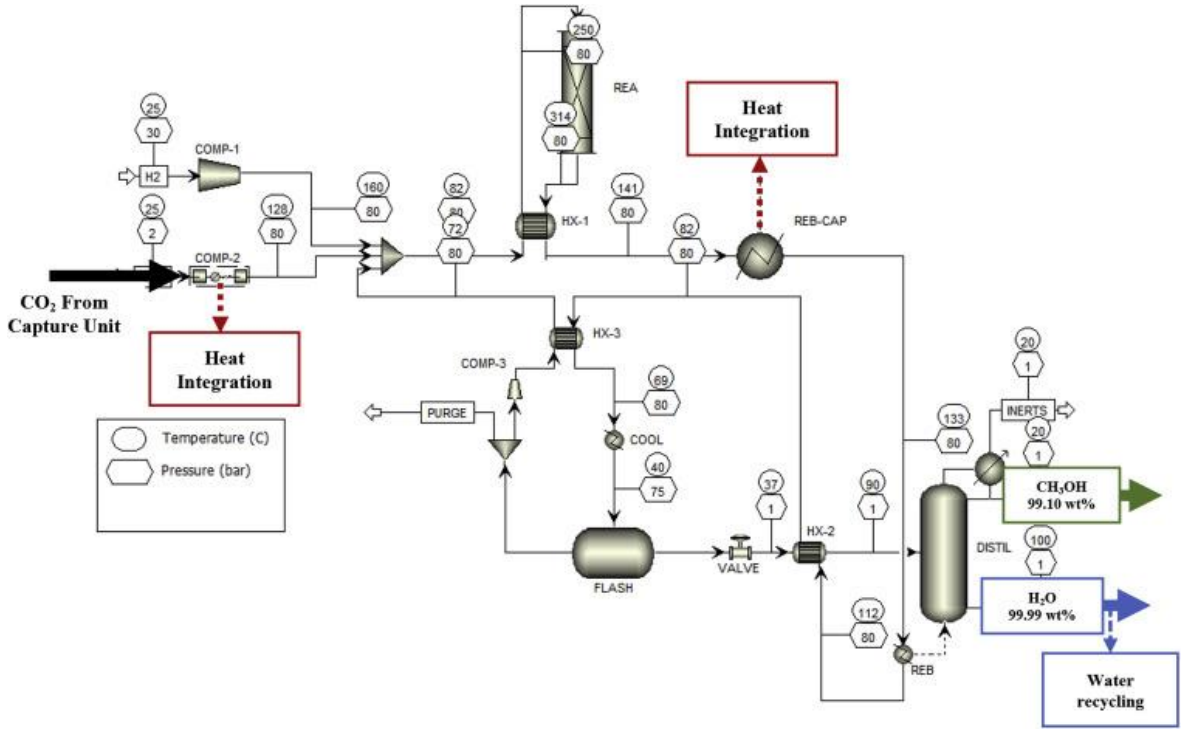

Figure 1.38 CO_2 conversion process flowsheet scheme proposed by Meunier et al., 2020 [40]. *HX, REB-CAP, REB: Heat exchanger; REA: Reactor; DISTIL: Distillation column; COOL: Cooler.*

Leonzio et al., 2019 [271] analysed and simulated the performance of three equilibrium methanol reactors configurations in Aspen Plus®: once-through (without any recirculation) equilibrium reactor (Figure 1.39a), equilibrium reactor with recycle of CO-CO_2-H_2 (R=80%) and separation of CH_3OH-H_2O by condensation (Figure 1.39b) and, membrane reactor with water separation modelled with six stages of equilibrium reactors and water separators (Figure 1.39c). The reactor with recycle was found the most efficient for CO_2 conversion. A major outcome of their study is the verification of the positive effect of adding CO and H to the feed because of the recycling process. The investigators compared their results with those published by Pérez-Fortes et al., 2016 [252] and Kiss et al., 2016 [272] and found them to be in good concordance with their work.

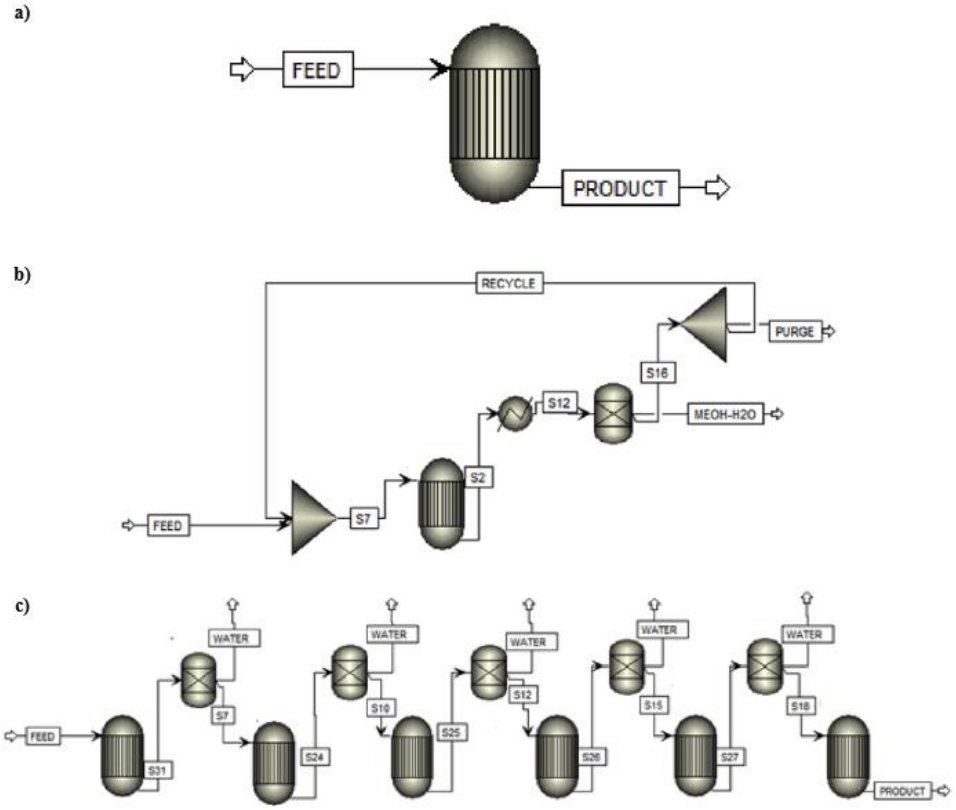

Figure 1.39 Reactor configurations developed by Leonzio et al., 2019 [271]*: a) once-through equilibrium reactor; b) equilibrium reactor with recycle of CO-CO_2-H_2 and separation of CH_3OH-H_2O by condensation; c) membrane reactor with water separation.*

Another comparative work on reactors was conducted by Cui & Kær, 2020 [273]. They evaluated the potential application in the CO_2 to methanol (CTM) process of three reactors used for the conversion of syngas into methanol, including an adiabatic, water-cooled, and gas-cooled reactor (Figure 1.40). Aspen Plus was used for process simulations. Their results demonstrated that adiabatic (without internal cooling) and gas-cooled reactors are suitable for the CTM process if the operating temperature is 220-280°C and the pressure is below 50 bar. Therefore, based on the performance and capital cost results of these two reactors, they have potential for a small-scale CTM process. [273]

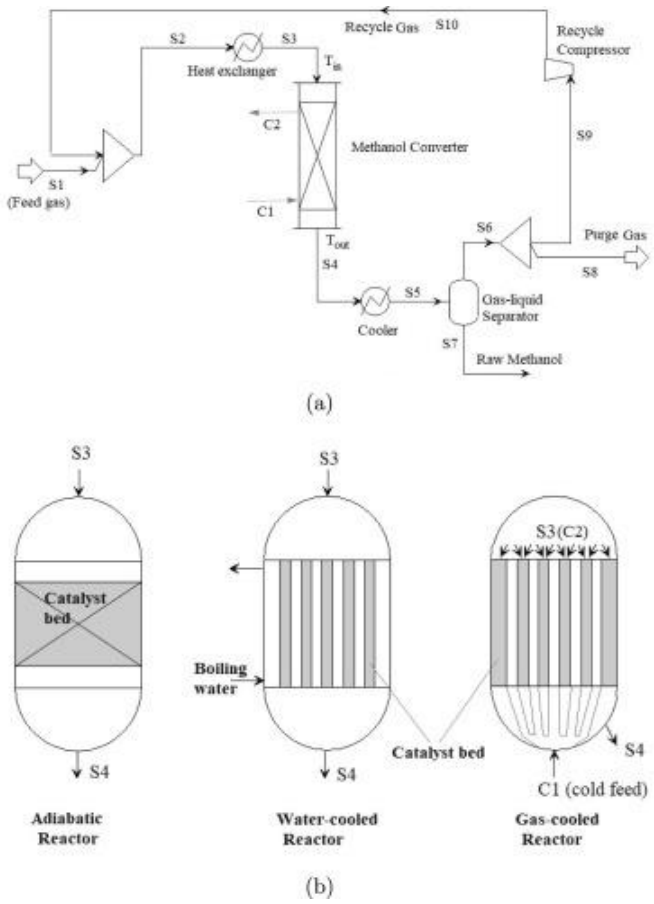

Figure 1.40 Schemes of (a) CTM process and (b) methanol converters [273].

Other authors [274] coupled the design, process simulation and optimisation with techno-economic evaluation for the CTM. According to their analysis, the highest manufacturing and operating cost was generated by water electrolysis stage for hydrogen production. In the research of Sollai et al., 2023 [275], they elucidated that for the optimised and simulated process, the market price of CTM (€960 per ton) is more than double the market price of fossil-derived methanol (€450 per ton) with a net present value (NPV) equal to zero. Nonetheless, they affirmed that the projected technology can be cost-effective in 2030-2035. Likewise, Borisut & Nuchitprasittichai, 2019 [276] performed a sensitivity analysis and simulation for CTM. They noticed that their projected methanol production cost was USD 565.54 per ton with the optimal operating conditions.

Chiou et al., 2023 [186] evaluated six alternative processes of CTM. The researchers conducted a design, optimisation, control, economic, and environmental examination. Their recommendation was the employment of two reactors: a non-adiabatic with co-current cooling reactor, followed by an adiabatic reactor (Figure 1.41), to have a minimum required selling

price for methanol of USD 998 per ton. They put into perspective the need to obtain green hydrogen at lower cost.

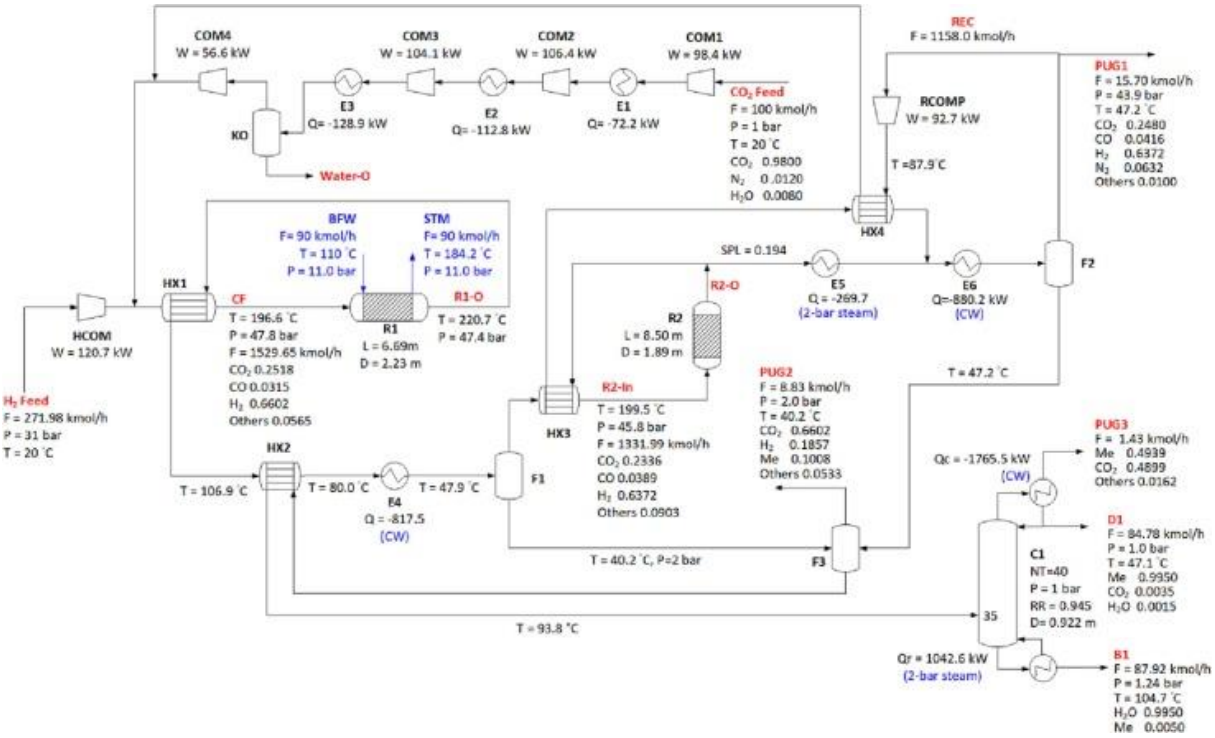

Figure 1.41 The optimised process flowsheet of Chiou et al., 2023 [186].

Techno-economic and environmental assessment have been completed in various publications concerning the CO_2 hydrogenation to methanol [277], [278]. Alsunousi & Kayabasi, 2024 proposed a process which utilized waste heat, and results showed high environmental impact reduction. The study emphasized the significance of flue gas levels in influencing various parameters. With a methanol production capacity of over 43.360 million tons, the total cost of the plant for 30 years is 11.350 billion dollars, making it competitive in clean synthetic fuel manufacturing. The study underscored the importance of renewable energy in controlling production costs and emission rates [278]. In 2016, the Joint Research Centre (JRC) science for policy report presented a techno-economic and environmental assessment of CO_2 utilisation for fuel production. They pointed out that the profitability of a carbon dioxide utilisation (CDU) plant can vary depending on specific factors such as the source of feedstock CO_2, H_2 and/or electricity, electricity requirements and costs, and product prices. The capacity of the CDU plant is determined by the renewable electricity available to power it, rather than by product demand. Under certain conditions, this business model is viable and contributes to reducing CO2 emissions [277].

Most authors agree that the greatest challenge lies in the economic feasibility of the process. Despite recycling gases (CO_2, CO, H_2) and improving process efficiency are considered in the evaluated processes, the viability of this process under certain conditions is still possible, especially depending on the source of feedstock and/or electricity.

1.8.2. DME synthesis

Bîldea et al., 2017 [279] designed and simulated two DME synthesis processes with a reactive distillation (RD), one with a single RD column (Figure 1.42) and another one coupling a gas-phase reactor and a RD column (Figure 1.43) being the most suitable for renovation of existing DME plants based on methanol dehydration. RD is a well-known process technology which combines chemical kinetics and vapour–liquid equilibrium within a single column, intensifying the interaction between reaction and separation [280]. In RD, removing products in situ from equilibrium-limited reactions enhances conversion, selectivity, and minimises recycles [280].

Bîldea et al., 2017 [279] compared the two RD with the conventional fixed bed reactor-separator-recycle (R-S-R) process (at a capacity of 100 kton·year^{-1} of DME, over 99.99% purity). The research group used Aspen Plus for simulations considering Langmuir-Hinshelwood-Hougen-Watson (LHHW) kinetics. Based on the total investment costs (CapEx: capital expenditure), OpEx (operating expenses) and specific energy requirements, they proposed the single step RD column as the most promising for new plants. For their second design option, they recommended a slight additional investment in existing DME plants to have a complete methanol conversion without recycling.

Nikhil et al., 2020 [281] also analysed the intensified RD configurations for DME synthesis. They evaluated the RD and the reactive divided wall column (RDWC) with a dual reaction zone. A RDWC is a single column with a dividing wall, which integrates both reaction and separation within a single unit. The reaction occurs on the feed side, while the light, heavy, and middle components are separated at different points. The use of RD and RDWC configurations represented higher methanol conversion versus classic method. They concurred with the findings of Bîldea et al., 2017 [279] in terms of complete methanol conversion, attenuated total annual cost (TAC) and energy efficiency of RD column. RD column CapEx and OpEx were 12.14% and 8.30% lower, respectively, than those of the RDWC.

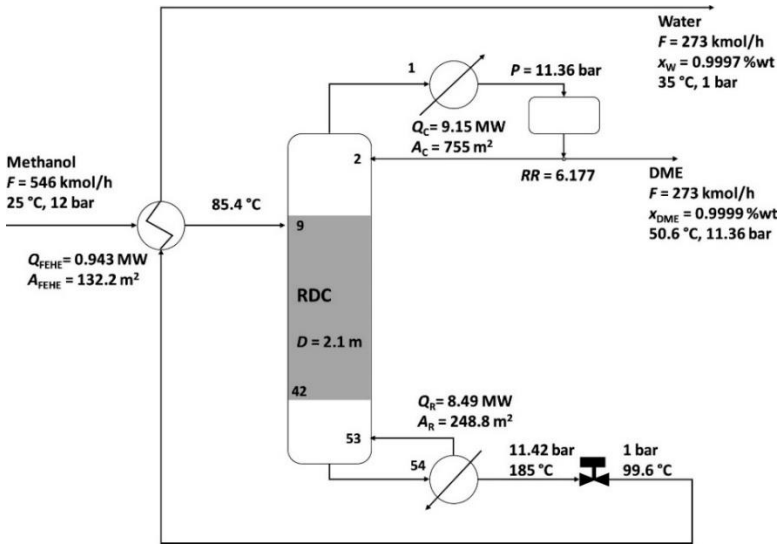

Figure 1.42 Flowsheet diagram of one step methanol dehydration process with a reactive distillation column. Reproduced from [279].

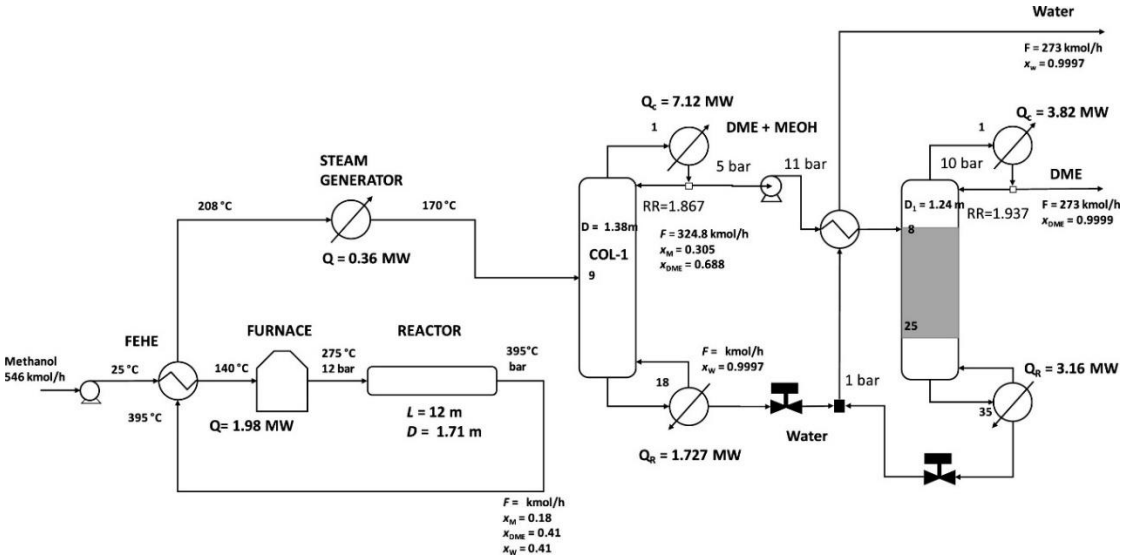

Figure 1.43 Flowsheet diagram of coupled gas-phase reactor and a reactive distillation column for methanol dehydration process. Reproduced from [279].

Polsen et al., 2020 [282] simulated a direct synthesis process of DME from biomass syngas (30% H_2, 25% CO, 29% CO_2, 10% CH_4, 1% C_2H_4 and 5% N_2) in Aspen Plus V8.8 using LHHW kinetic model in a plug flow reactor to design the process. The reactor was tested over a temperature range of 220-300 °C and 20-80 bar. They elucidated that for their model the proper operating conditions were 280 °C and 60 bar with 14.078 mole fraction of DME (%). Similarly, Giuliano et al., 2021 [283] performed a process simulation of DME production from syngas (CO_2/CO/H_2) derived from gasification of an anaerobic digestate in ChemCAD software (Figure 1.44). After evaluating different CO_2/CO/H_2 ratios, they suggested that the syngas valorisation is only possible with specific ratios. They affirmed that high CO_2 content

lessens DME equilibrium yield, though the effect of increasing of the amount of CO_2 is less meaningful for high CO_2/CO molar ratios. The optimal pressure and temperature ranges were 60-80 bar and 200-250 °C, respectively. At 78 bar and 244 °C, they obtained a pure DME flowrate of 7 496 ton·year^{-1} and 30 923 ton·year^{-1} of CO_2 captured and stored. On the other hand, a techno-economic study of direct synthesis of DME from a synthesis gas derived from natural gas reported that the higher production rate of DME favours the net reduction of CO_2 emissions to the atmosphere, natural gas consumption and energy consumption per kg of DME produced, in addition to the higher carbon efficiency and power production from the steam produced [284].

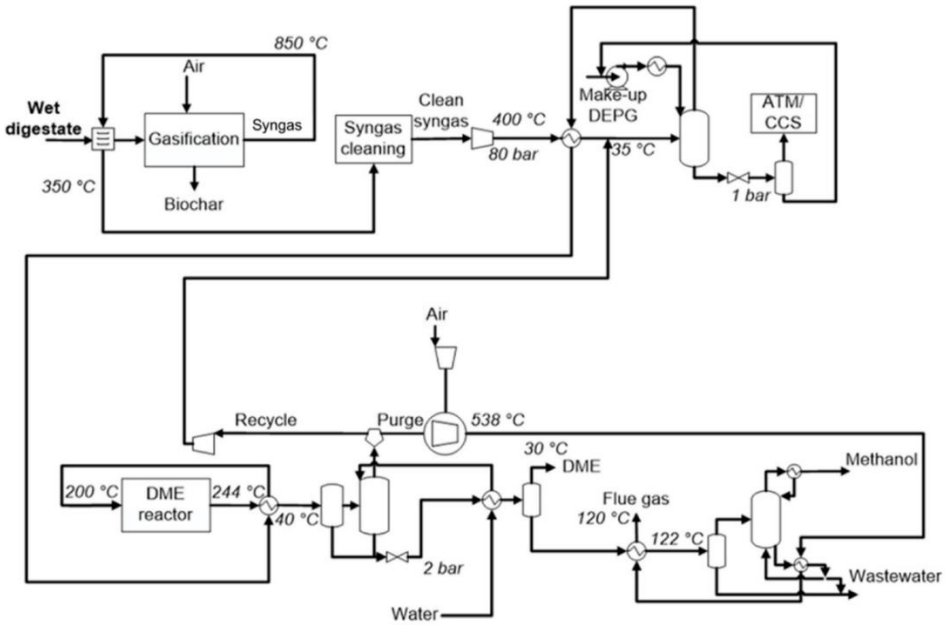

Figure 1.44 Flowsheet diagram for the identified optimal process result by Giuliano et al., 2021 [283].

Wu & Chien, 2022 [285] worked on a techno-economic analysis and carbon emission analysis for the intensification of the two existing DME synthesis processes, direct and indirect, also validating the reaction kinetics. Among the five-scenario proposed in their study, the authors identified the indirect configuration (two-step configuration, methanol synthesis + methanol dehydration) as superior to the direct one (CO_2 to DME synthesis) in CO_2 reduction emission due to the simpler separation after the first methanol synthesis reaction. Further, the simulation result of the two-step synthesis with heat integration (TSHI) exhibited a saving of about 48% of CO_2 emissions and more than 23% of energy in consumption per unit weight of DME with a consumption of 1.704 tons of CO_2 per ton of DME. But, for this process to be viable, a development in electrolysis to produce H_2 is necessary given the high price of renewable H_2. Likewise, Michailos et al., 2019 [286] after designing and performing a techno-economic assessment of a large-scale DME plant from CO_2 hydrogenation and methanol

dehydration, stated that there is a high CO_2 conversion (82.3%). Nonetheless, the electricity price constituted the higher cost with the electrolysis unit being the most affecting factor. However, a more recent techno-economic analysis indicated the feasibility of a DME plant from landfill gas to syngas (dry reforming of methane) and then to DME estimating a revenue of 3.49 million euros per year and an operating profit of €2.317 million euros per year, resulting in a cost-effective and net CO_2 consumption process [287].

Innovative process simulations with membrane reactors for DME synthesis have also been conducted. De Falco et al., 2017 [288] developed an industrial plant simulation and optimisation for direct DME synthesis from CO_2-rich stream with recirculation in a membrane reactor (to selectively remove water steam of reactions (1.2) and (1.4)) using MATLAB and Aspen Plus (Figure 1.45). The system comprised the MR unit, Steam Generation Unit, Separation & Recirculation Unit, and Distillation unit. The recirculation units handle separation, mixing, and recirculation for feedstock (syngas) and sweeping gas preparation in the reaction and permeation zones of the MR. In this configuration, a CO2-rich stream (stream 21) combined with the recirculated stream 20 to remove permeated H_2O/H_2. Stream 13 was cooled to condense and separate the water, and the CO_2/H_2 was separated by PSA. The CO_2 stream (stream 18) was recirculated to the permeation zone of the reactor, and a portion was recirculated to the reaction zone (RZ) via stream 19, maintaining a CO_2 composition higher than that of the syngas. H_2 (stream 15), compressed by CC-1, was recycled to the RZ of the MR. This resulted in 60% CO_2 conversion and 60% DME yield at 532 K, 60 bar, H_2/CO_x=3 and GHSV=6000 h^{-1}.

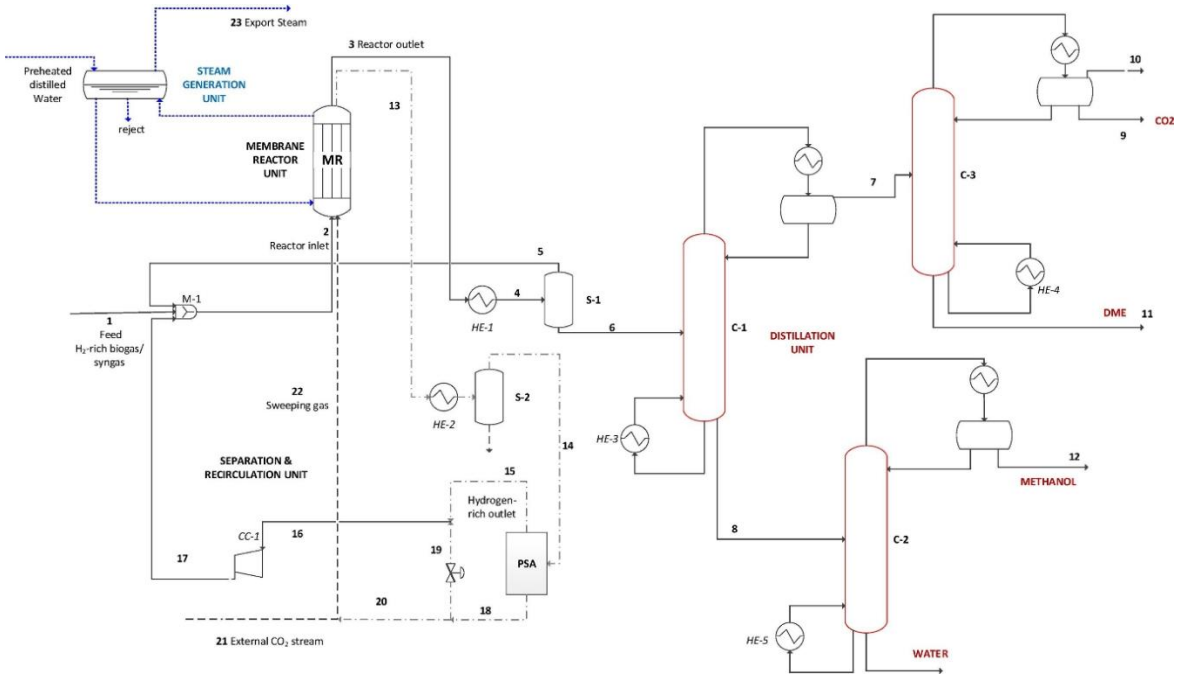

Figure 1.45 Flowsheet diagram of the Double Recycling Loop-DME production plant (solid line = reactants-products, dashed line = membrane reactor sweeping gas line; dotted line = reactor cooling line). Reproduced from [288].

In a previous work [289], the authors compared the performance of a MR with that of a conventional reactor and demonstrated an improvement of 31.5% in DME yield, 15.4% in COx conversion and 30.2% in CO_2 conversion when employing a MR. De Falco et al., 2017 [288] concluded that the process implied low energy footprint, but production costs were impacted by equipment costs additional to operative and capital costs. According to the simulation results of Hamedi & Brinkmann, 2022 [290], the MR-based process reduced the refrigerant, heating and energy consumptions by 69.4%, 44.5% and 1.5%, respectively, at 7.5 MPa. Therefore, the decrease in energy consumption led to a 7.3% and 1.7% improvement in CO_2 utilisation efficiency versus the conventional reactor.

An analysis of the intensification of CO_2 valorisation in one-step DME production established that recirculation of unconverted reactants can ensure high CO_2 conversion and high DME production as well as lower catalyst deactivation in a packed bed membrane reactor (PBMR) [291]. A CO_2 conversion of 70% and a DME yield of 60% were achieved, at 275 °C and 30 bar, with CO_2/CO_x=0.25 and with space time velocity over 5 $g_{cat}\cdot h\cdot(mol_C)^{-1}$. This study supported that the use of a PMBR improved CO_2 conversion in 3.5-4% and a 25% difference in DME yield was possible for pure CO_2+H_2 feed over the PBR. Nevertheless, the design of membranes able to withstand reaction operating conditions in the standard process without deterioration of their properties is still a subject of investigation.

Other technologies for the intensification of the DME process have also been simulated being more focus on reactors design modifications. For instance, one-, two- and three-stage spherical reactor configurations for methanol dehydration were modelled and deemed feasible to boost DME production, diminish pressure drop and manufacturing costs [292]. Behloul et al., 2021 [293] evaluated the coupling of a reactor, a heat exchanger and a membrane separator (R-E-M) to cope with the limitations of catalytic reaction, heat exchange and separation for the direct hydrogenation of CO_2 to DME. They also analysed the development and the performance of the proposed multifunctional reactor by dynamic optimisation, focusing on the methodological aspect [294].

1.9. Conclusions

In this chapter, the products of CO_2 hydrogenation were reviewed. The main focus was on methane, methanol and dimethyl ether syntheses. The synthesis processes and their thermodynamics, used catalysts, reaction pathways and kinetic modelling were exposed to understand the focus of this research. The methane synthesis has been widely studied in the literature and, moreover, is a mature technology proven in operational environments (industrial processes). However, the methanol synthesis is identified as most investigated and, DME synthesis is the least researched, becoming the focal point of this thesis.

Catalyst optimisation, reactor designs, and process innovations are the cornerstones of performance intensification. At catalytic level, CZA is still outstanding compared to other catalysts tested (Pd-, Au-, Rh-, Pt- based catalyst) for methanol synthesis, from an economic and environmental point of view. However, the incorporation of modifiers/promoters into CZA and the catalyst preparation method are still object of investigation to enhance catalytic activity and stability. Regarding DME synthesis, the attention is on the acid sites of catalyst, and subsequently its acid capacity to improve performance and stability, in addition to the measures mentioned earlier for methanol synthesis catalyst. Silica, zeolites and clay are generally used for methanol dehydration.

The fixed bed reactor is generally employed for methanol and DME syntheses. Nevertheless, the need of process optimisation to enhance CO_2 conversion and product yield while preserving catalyst lifetime has prompted the design of new reactors. Thus, laboratory and industrial-scale reactors were studied and simulations of processes to produce methanol and DME from CO_2 hydrogenation were carried out, bearing in mind that methanol is an intermediate product in the synthesis of DME. In both cases, the water generated in the process is the biggest issue, due to the deactivation of the catalyst and equilibrium limitations. Therefore, most of the investigations are centred on the development of membrane reactors. Less attention has been given to heat exchangers and temperature gradient reactors.

The aim of this thesis is to develop or improve a process for converting CO_2 into usable molecule(s), namely, methanol and DME. We are leaning more towards DME, because fewer researches have been carried out on it. Since it is still possible to optimise the DME synthesis process, we aim to improve a heat exchanger reactor to maximise CO_2 conversion or consumption. This is particularly important as heat exchanger reactors have received relatively less attention compared to the other technologies explored in this State-of-the-Art review. For the aim, it is required to study the kinetics and modelling, besides the simulation of the optimised reactor.

1.10. References

[1] P. R. Yaashikaa, P. Senthil Kumar, S. J. Varjani, and A. Saravanan, “A review on photochemical, biochemical and electrochemical transformation of CO2 into value-added products,” *J. CO2 Util.*, vol. 33, pp. 131–147, Oct. 2019, doi: 10.1016/J.JCOU.2019.05.017.

[2] T. Sharma, S. Sharma, H. Kamyab, and A. Kumar, “Energizing the CO2 utilization by chemo-enzymatic approaches and potentiality of carbonic anhydrases: A review,” *J. Clean. Prod.*, vol. 247, p. 119138, Feb. 2020, doi: 10.1016/J.JCLEPRO.2019.119138.

[3] W. Zhang, D. Ma, J. Pérez-Ramírez, and Z. Chen, “Recent Progress in Materials Exploration for Thermocatalytic, Photocatalytic, and Integrated Photothermocatalytic CO2 -to-Fuel Conversion,” *Adv. Energy Sustain. Res.*, vol. 3, no. 2, p. 2100169, Feb. 2022, doi: 10.1002/aesr.202100169.

[4] S. Castro, J. Albo, and A. Irabien, “Photoelectrochemical Reactors for CO2 Utilization,” *ACS Sustain. Chem. Eng.*, vol. 6, no. 12, pp. 15877–15894, Dec. 2018, doi: 10.1021/ACSSUSCHEMENG.8B03706/ASSET/IMAGES/LARGE/SC-2018-03706H_0003.JPEG.

[5] N. Podrojková, V. Sans, A. Oriňak, and R. Oriňaková, “Recent Developments in the Modelling of Heterogeneous Catalysts for CO2 Conversion to Chemicals,” *ChemCatChem*, vol. 12, no. 7, pp. 1802–1825, Apr. 2020, doi: 10.1002/cctc.201901879.

[6] G. Leonzio, “State of art and perspectives about the production of methanol, dimethyl ether and syngas by carbon dioxide hydrogenation,” *J. CO2 Util.*, vol. 27, pp. 326–354, Oct. 2018, doi: 10.1016/j.jcou.2018.08.005.

[7] W. Wu, K. Xie, D. Sun, X. Li, and F. Fang, “CuO/ZnO/Al2O3 Catalyst Prepared by Mechanical-Force-Driven Solid-State Ion Exchange and Its Excellent Catalytic Activity under Internal Cooling Condition,” *Ind. Eng. Chem. Res.*, vol. 56, no. 29, pp. 8216–8223, Jul. 2017, doi: 10.1021/acs.iecr.7b01464.

[8] K. Markandan *et al.*, “A Review on the Progress in Chemo-Enzymatic Processes for CO2 Conversion and Upcycling,” *Catalysts*, vol. 13, no. 3, p. 611, Mar. 2023, doi: 10.3390/CATAL13030611.

[9] R. P. Ye *et al.*, “CO2 hydrogenation to high-value products via heterogeneous catalysis,” *Nat. Commun.*, vol. 10, no. 1, pp. 1–15, Dec. 2019, doi: 10.1038/s41467-019-13638-9.

[10] S. Kar, J. Kothandaraman, A. Goeppert, and G. K. S. Prakash, “Advances in catalytic

homogeneous hydrogenation of carbon dioxide to methanol," *J. CO2 Util.*, vol. 23, pp. 212–218, Jan. 2018, doi: 10.1016/J.JCOU.2017.10.023.

[11] R. Guil-López *et al.*, "Methanol Synthesis from CO2: A Review of the Latest Developments in Heterogeneous Catalysis," *Materials (Basel).*, vol. 12, no. 23, p. 3902, Nov. 2019, doi: 10.3390/ma12233902.

[12] B. Alrafei, "Etude catalytique et cinétique de la méthanation du CO_2 en lit fixe et sous plasma micro-ondes," Normandie Université, Rouen, 2019.

[13] M. J. Quezada, "Hydrogénation catalytique de CO_2 en méthanol en lit fixe sous chauffage conventionnel et sous plasma à DBD," Normandie Université, 2020.

[14] A. M. Bahmanpour, M. Signorile, and O. Kröcher, "Recent progress in syngas production via catalytic CO2 hydrogenation reaction," *Applied Catalysis B: Environmental*, vol. 295. Elsevier B.V., p. 120319, Oct. 15, 2021, doi: 10.1016/j.apcatb.2021.120319.

[15] M. Liu, Y. Yi, L. Wang, H. Guo, and A. Bogaerts, "Hydrogenation of Carbon Dioxide to Value-Added Chemicals by Heterogeneous Catalysis and Plasma Catalysis," *Catalysts*, vol. 9, no. 3, p. 275, Mar. 2019, doi: 10.3390/CATAL9030275.

[16] L. Wei, H. Azad, W. Haije, H. Grenman, and W. de Jong, "Pure methane from CO2 hydrogenation using a sorption enhanced process with catalyst/zeolite bifunctional materials," *Appl. Catal. B Environ.*, vol. 297, p. 120399, Nov. 2021, doi: 10.1016/j.apcatb.2021.120399.

[17] M. Xiang *et al.*, "Boosting CO2 hydrogenation to methane over Ni-based ETS-10 zeolite catalyst," *Front. Chem.*, vol. 10, Oct. 2022, doi: 10.3389/fchem.2022.1041843.

[18] S. N. Bukhari, C. C. Chong, H. D. Setiabudi, Y. W. Cheng, L. P. Teh, and A. A. Jalil, "Ni/Fibrous type SBA-15: Highly active and coke resistant catalyst for CO2 methanation," *Chem. Eng. Sci.*, vol. 229, p. 116141, Jan. 2021, doi: 10.1016/J.CES.2020.116141.

[19] C. H. Tan, S. Nomanbhay, A. H. Shamsuddin, Y. K. Park, H. Hernández-Cocoletzi, and P. L. Show, "Current Developments in Catalytic Methanation of Carbon Dioxide—A Review," *Front. Energy Res.*, vol. 9, p. 1031, Jan. 2022, doi: 10.3389/FENRG.2021.795423/BIBTEX.

[20] M. Bowker, "Methanol Synthesis from CO2 Hydrogenation," *ChemCatChem*, vol. 11, no. 17, pp. 4238–4246, 2019, doi: 10.1002/cctc.201900401.

[21] I. Iliuta and F. Larachi, “Enhanced Methanol Synthesis Process via an Integrated Process Involving CO2 Hydrogenation under Plasma Conditions,” *Ind. Eng. Chem. Res.*, vol. 59, no. 15, pp. 6815–6827, Apr. 2020, doi: 10.1021/ACS.IECR.9B04278/ASSET/IMAGES/LARGE/IE9B04278_0003.JPEG.

[22] V. H. Nguyen *et al.*, “Towards artificial photosynthesis: Sustainable hydrogen utilization for photocatalytic reduction of CO2 to high-value renewable fuels,” *Chem. Eng. J.*, vol. 402, p. 126184, Dec. 2020, doi: 10.1016/J.CEJ.2020.126184.

[23] F. Samimi, N. Hamedi, and M. R. Rahimpour, “Green Methanol Production Process from Indirect CO2 Conversion: RWGS Reactor versus RWGS Membrane Reactor,” *J. Environ. Chem. Eng.*, vol. 7, no. 1, p. 102813, Feb. 2019, doi: 10.1016/J.JECE.2018.102813.

[24] A. Weilhard, M. I. Qadir, V. Sans, and J. Dupont, “Selective CO2 Hydrogenation to Formic Acid with Multifunctional Ionic Liquids,” *ACS Catal.*, vol. 8, no. 3, pp. 1628–1634, Mar. 2018, doi: 10.1021/ACSCATAL.7B03931/ASSET/IMAGES/LARGE/CS-2017-039312_0006.JPEG.

[25] X. Chen, Y. Liu, and J. Wu, “Sustainable production of formic acid from biomass and carbon dioxide,” *Mol. Catal.*, vol. 483, p. 110716, Mar. 2020, doi: 10.1016/J.MCAT.2019.110716.

[26] F. L. Chan, G. Altinkaya, N. Fung, and A. Tanksale, “Low temperature hydrogenation of carbon dioxide into formaldehyde in liquid media,” *Catal. Today*, vol. 309, pp. 242–247, Jul. 2018, doi: 10.1016/J.CATTOD.2017.06.012.

[27] L. Deng *et al.*, “Catalytic aqueous CO2 reduction to formaldehyde at Ru surface on hydroxyl-groups-rich LDH under mild conditions,” *Appl. Catal. B Environ.*, vol. 322, p. 122124, Mar. 2023, doi: 10.1016/J.APCATB.2022.122124.

[28] L. Yao, X. Shen, Y. Pan, and Z. Peng, “Unravelling Proximity-Driven Synergetic Effect within CIZO-SAPO Bifunctional Catalyst for CO2Hydrogenation to DME,” *Energy and Fuels*, vol. 34, no. 7, pp. 8635–8643, Jul. 2020, doi: 10.1021/ACS.ENERGYFUELS.0C01256/ASSET/IMAGES/LARGE/EF0C01256_0006.JPEG.

[29] G. Bonura *et al.*, “Interaction effects between CuO-ZnO-ZrO2 methanol phase and zeolite surface affecting stability of hybrid systems during one-step CO2 hydrogenation to DME,” *Catal. Today*, vol. 345, pp. 175–182, Apr. 2020, doi: 10.1016/J.CATTOD.2019.08.014.

[30] I. I. Maor *et al.*, "Performance of Cu/ZnO Nanosheets on Electrospun Al2O3 Nanofibers in CO2 Catalytic Hydrogenation to Methanol and Dimethyl Ether," *Nanomaterials*, vol. 13, no. 4, p. 635, Feb. 2023, doi: 10.3390/NANO13040635/S1.

[31] K. Krim, A. Sachse, A. Le Valant, Y. Pouilloux, and S. Hocine, "One Step Dimethyl Ether (DME) Synthesis from CO2 Hydrogenation over Hybrid Catalysts Containing Cu/ZnO/Al2O3 and Nano-Sized Hollow ZSM-5 Zeolites," *Catal. Letters*, vol. 153, no. 1, pp. 83–94, Jan. 2023, doi: 10.1007/s10562-022-03949-w.

[32] Z. Ma and M. D. Porosoff, "Development of Tandem Catalysts for CO2 Hydrogenation to Olefins," *ACS Catal.*, vol. 9, no. 3, pp. 2639–2656, Mar. 2019, doi: 10.1021/ACSCATAL.8B05060/ASSET/IMAGES/LARGE/CS-2018-05060D_0010.JPEG.

[33] A. Fedorov, H. Lund, V. A. Kondratenko, E. V. Kondratenko, and D. Linke, "Elucidating reaction pathways occurring in CO2 hydrogenation over Fe-based catalysts," *Appl. Catal. B Environ.*, vol. 328, p. 122505, Jul. 2023, doi: 10.1016/J.APCATB.2023.122505.

[34] P. Sharma, J. Sebastian, S. Ghosh, D. Creaser, and L. Olsson, "Recent advances in hydrogenation of CO2into hydrocarbonsviamethanol intermediate over heterogeneous catalysts," *Catalysis Science and Technology*, vol. 11, no. 5. The Royal Society of Chemistry, pp. 1665–1697, Mar. 15, 2021, doi: 10.1039/d0cy01913e.

[35] L. Brübach, D. Hodonj, and P. Pfeifer, "Kinetic Analysis of CO2 Hydrogenation to Long-Chain Hydrocarbons on a Supported Iron Catalyst," *Ind. Eng. Chem. Res.*, vol. 61, no. 4, pp. 1644–1654, Feb. 2022, doi: 10.1021/ACS.IECR.1C04018/ASSET/IMAGES/MEDIUM/IE1C04018_M030.GIF.

[36] J. Wei *et al.*, "Directly converting CO2 into a gasoline fuel," *Nat. Commun.*, vol. 8, no. 1, pp. 1–9, May 2017, doi: 10.1038/ncomms15174.

[37] C. Vogt, M. Monai, G. J. Kramer, and B. M. Weckhuysen, "The renaissance of the Sabatier reaction and its applications on Earth and in space," *Nat. Catal.*, vol. 2, no. 3, pp. 188–197, Mar. 2019, doi: 10.1038/s41929-019-0244-4.

[38] IEA, "Gas - Fuels & Technologies - IEA," 2021. https://www.iea.org/fuels-and-technologies/gas (accessed May 02, 2023).

[39] S. Roy, A. Cherevotan, and S. C. Peter, "Thermochemical CO2 Hydrogenation to Single Carbon Products: Scientific and Technological Challenges," *ACS Energy Lett.*, vol. 3, no. 8, pp. 1938–1966, Aug. 2018, doi: 10.1021/ACSENERGYLETT.8B00740/ASSET/IMAGES/LARGE/NZ-2018-

00740W_0014.JPEG.

[40] N. Meunier, R. Chauvy, S. Mouhoubi, D. Thomas, and G. De Weireld, “Alternative production of methanol from industrial CO2,” *Renew. Energy*, vol. 146, pp. 1192–1203, 2020, doi: 10.1016/j.renene.2019.07.010.

[41] International Renewable Energy Agency and Methanol Institute, “Innovation Outlook Renewable Methanol,” *IRENA*, 2021, Accessed: May 25, 2023. [Online]. Available: www.irena.org.

[42] G. Bonura *et al.*, “Inside the reaction mechanism of direct CO2 conversion to DME over zeolite-based hybrid catalysts,” *Appl. Catal. B Environ.*, vol. 294, p. 120255, Oct. 2021, doi: 10.1016/J.APCATB.2021.120255.

[43] N. Mota, E. M. Ordoñez, B. Pawelec, J. L. G. Fierro, and R. M. Navarro, “Direct Synthesis of Dimethyl Ether from CO2: Recent Advances in Bifunctional/Hybrid Catalytic Systems,” *Catalysts*, vol. 11, no. 4, p. 411, Mar. 2021, doi: 10.3390/CATAL11040411.

[44] E. Catizzone, G. Bonura, M. Migliori, F. Frusteri, and G. Giordano, “CO2 Recycling to Dimethyl Ether: State-of-the-Art and Perspectives,” *Molecules*, vol. 23, no. 1, p. 31, Dec. 2017, doi: 10.3390/MOLECULES23010031.

[45] W. E. E. L. (WEEL) Committee, O. A. for R. S. (OARS), and T. E. for R. A. (TERA), “Dimethyl ether (DME),” *Toxicol. Ind. Health*, vol. 38, no. 11, pp. 713–716, Nov. 2022, doi: 10.1177/07482337221125071.

[46] E. Catizzone, C. Freda, G. Braccio, F. Frusteri, and G. Bonura, “Dimethyl ether as circular hydrogen carrier: Catalytic aspects of hydrogenation/dehydrogenation steps,” *J. Energy Chem.*, vol. 58, pp. 55–77, Jul. 2021, doi: 10.1016/J.JECHEM.2020.09.040.

[47] U. Mondal and G. D. Yadav, “Perspective of dimethyl ether as fuel: Part I. Catalysis,” *J. CO2 Util.*, vol. 32, pp. 299–320, Jul. 2019, doi: 10.1016/J.JCOU.2019.02.003.

[48] C. Liu and Z. Liu, “Perspective on CO2 Hydrogenation for Dimethyl Ether Economy,” *Catalysts*, vol. 12, no. 11, p. 1375, Nov. 2022, doi: 10.3390/CATAL12111375.

[49] C. Herrera, M. Cortés-Reyes, M. Á. Larrubia, M. V. Domínguez-Barroso, M. R. Díaz-Rey, and L. J. Alemany, “Dimethyl ether synthesis via methanol dehydration over Ta-supported catalysts,” *Appl. Catal. A Gen.*, vol. 582, p. 117088, Jul. 2019, doi: 10.1016/J.APCATA.2019.05.022.

[50] Jean-Alain Taupy, “DME Industry and Association Overview,” *4th International DME*

Conference Stockholm, 2010. https://www.aboutdme.org/aboutdme/files/ccLibraryFiles/Filename/00000000163 3/DME4_IDA_Taupy.pdf (accessed Jun. 23, 2023).

[51] R. R. Roberts, "Part 1-B: Physical & Chemical Properties of Selected Fuels (1)-Methanol Safe Handling Technical Bulletin," *Methanol Inst. Tech. Bull.*, 2020, Accessed: Jun. 22, 2023. [Online]. Available: https://www.methanol.org/wp-content/uploads/2020/04/Part-1-B_-Physical-Chemical-Properties-of-Selected-Fuels-.pdf.

[52] Kosangas, "SAFETY DATA SHEET FOR LPG," 2013. www.kosangas.dk (accessed Jun. 23, 2023).

[53] CAMEO Chemicals, "DIMETHYL ETHER | CAMEO Chemicals | National Oceanic and Atmospheric Administration (NOAA)." https://cameochemicals.noaa.gov/chemical/585 (accessed Jun. 23, 2023).

[54] Advanced Motor Fuels (AMF), "Liquefied petroleum gas, LPG." https://www.iea-amf.org/content/fuel_information/lpg (accessed Jun. 23, 2023).

[55] Methanol Institute, "DME: An Emerging Global Fuel," Jun. 2016. https://www.methanol.org/wp-content/uploads/2016/06/DME-An-Emerging-Global-Guel-FS.pdf (accessed Jun. 23, 2023).

[56] Dimeta, "Liquid Gas Europe: Renewable and Recycled Carbon DME," Mar. 07, 2023. https://dimeta.nl/wp-content/uploads/2023/03/LGE-Renewable-and-Recycled-Carbon-DME-brochure.pdf (accessed Jun. 23, 2023).

[57] Oberon Fuels, "Oberon's rDME fuel." https://www.oberonfuels.com/oberons-rdme (accessed Jun. 23, 2023).

[58] J. Park *et al.*, "Kinetic modeling for direct synthesis of dimethyl ether from syngas over a hybrid Cu/ZnO/Al2O3/ferrierite catalyst," *Catal. Today*, vol. 388–389, pp. 323–328, Apr. 2022, doi: 10.1016/J.CATTOD.2020.06.023.

[59] G. Bonura, M. Cordaro, L. Spadaro, C. Cannilla, F. Arena, and F. Frusteri, "Hybrid Cu-ZnO-ZrO2/H-ZSM5 system for the direct synthesis of DME by CO2 hydrogenation," *Appl. Catal. B Environ.*, vol. 140–141, pp. 16–24, Jan. 2013, doi: 10.1016/J.APCATB.2013.03.048.

[60] K. Stangeland, H. Li, and Z. Yu, "Thermodynamic Analysis of Chemical and Phase Equilibria in CO2 Hydrogenation to Methanol, Dimethyl Ether, and Higher Alcohols," *Ind. Eng. Chem. Res.*, vol. 57, no. 11, pp. 4081–4094, 2018, doi:

10.1021/ACS.IECR.7B04866/ASSET/IMAGES/LARGE/IE-2017-04866G_0013.JPEG.

[61] M. Y. Mohamud *et al.*, "Direct Synthesis of Dimethyl Ether from CO2 Hydrogenation over Core-Shell Nanotube Bi-Functional Catalyst," *Catalysts*, vol. 13, no. 2, p. 408, Feb. 2023, doi: 10.3390/CATAL13020408.

[62] K. P. Brooks, J. Hu, H. Zhu, and R. J. Kee, "Methanation of carbon dioxide by hydrogen reduction using the Sabatier process in microchannel reactors," *Chem. Eng. Sci.*, vol. 62, no. 4, pp. 1161–1170, Feb. 2007, doi: 10.1016/J.CES.2006.11.020.

[63] A. Tripodi, F. Conte, and I. Rossetti, "Carbon Dioxide Methanation: Design of a Fully Integrated Plant," *Energy & Fuels*, vol. 34, no. 6, pp. 7242–7256, Jun. 2020, doi: 10.1021/acs.energyfuels.0c00580.

[64] E. C. Ra, K. Y. Kim, E. H. Kim, H. Lee, K. An, and J. S. Lee, "Recycling Carbon Dioxide through Catalytic Hydrogenation: Recent Key Developments and Perspectives," *ACS Catal.*, vol. 10, no. 19, pp. 11318–11345, Oct. 2020, doi: 10.1021/ACSCATAL.0C02930/ASSET/IMAGES/LARGE/CS0C02930_0015.JPEG.

[65] M. Younas, L. Loong Kong, M. J. K. Bashir, H. Nadeem, A. Shehzad, and S. Sethupathi, "Recent Advancements, Fundamental Challenges, and Opportunities in Catalytic Methanation of CO2," *Energy and Fuels*, vol. 30, no. 11, pp. 8815–8831, Nov. 2016, doi: 10.1021/ACS.ENERGYFUELS.6B01723/ASSET/IMAGES/LARGE/EF-2016-017238_0007.JPEG.

[66] S. Nieß, U. Armbruster, S. Dietrich, and M. Klemm, "Recent Advances in Catalysis for Methanation of CO2 from Biogas," *Catalysts*, vol. 12, no. 4. MDPI, Apr. 01, 2022, doi: 10.3390/catal12040374.

[67] N. D. Mohd Ridzuan, M. S. Shaharun, M. A. Anawar, and I. Ud-Din, "Ni-Based Catalyst for Carbon Dioxide Methanation: A Review on Performance and Progress," *Catalysts*, vol. 12, no. 5, p. 469, Apr. 2022, doi: 10.3390/catal12050469.

[68] "Final Report Summary - HELMETH (Integrated High-Temperature Electrolysis and Methanation for Effective Power to Gas Conversion) | FP7 | CORDIS | European Commission," Jul. 25, 2018. https://cordis.europa.eu/project/id/621210/reporting (accessed May 05, 2023).

[69] K. Stangeland, D. Kalai, H. Li, and Z. Yu, "CO2 Methanation: The Effect of Catalysts and Reaction Conditions," *Energy Procedia*, vol. 105, pp. 2022–2027, May 2017, doi: 10.1016/J.EGYPRO.2017.03.577.

[70] Y. Yang *et al.*, "Nickel Nanoparticles Encapsulated in SSZ-13 Cage for Highly Efficient CO2 Hydrogenation," *Energy and Fuels*, vol. 35, no. 16, pp. 13240–13248, Aug. 2021, doi: 10.1021/ACS.ENERGYFUELS.1C01881/ASSET/IMAGES/LARGE/EF1C01881_0006.JPEG.

[71] W. Li *et al.*, "A short review of recent advances in CO 2 hydrogenation to hydrocarbons over heterogeneous catalysts," *RSC Adv.*, vol. 8, no. 14, pp. 7651–7669, Feb. 2018, doi: 10.1039/C7RA13546G.

[72] B. Alrafei, I. Polaert, A. Ledoux, and F. Azzolina-Jury, "Remarkably stable and efficient Ni and Ni-Co catalysts for CO2 methanation," *Catal. Today*, vol. 346, pp. 23–33, Apr. 2020, doi: 10.1016/J.CATTOD.2019.03.026.

[73] R. Dębek, F. Azzolina-Jury, A. Travert, and F. Maugé, "A review on plasma-catalytic methanation of carbon dioxide – Looking for an efficient catalyst," *Renew. Sustain. Energy Rev.*, vol. 116, p. 109427, Dec. 2019, doi: 10.1016/J.RSER.2019.109427.

[74] H. C. Wu, Y. C. Chang, J. H. Wu, J. H. Lin, I. K. Lin, and C. S. Chen, "Methanation of CO2 and reverse water gas shift reactions on Ni/SiO2 catalysts: the influence of particle size on selectivity and reaction pathway," *Catal. Sci. Technol.*, vol. 5, no. 8, pp. 4154–4163, Aug. 2015, doi: 10.1039/c5cy00667h.

[75] D. Allam, S. Bennici, L. Limousy, and S. Hocine, "Improved Cu- and Zn-based catalysts for CO 2 hydrogenation to methanol," *Comptes Rendus Chim.*, vol. 22, no. 2–3, pp. 227–237, Feb. 2019, doi: 10.1016/j.crci.2019.01.002.

[76] S. Xiong, Y. Lian, H. Xie, and B. Liu, "Hydrogenation of CO2 to methanol over Cu/ZnCr catalyst," *Fuel*, vol. 256, p. 115975, Nov. 2019, doi: 10.1016/j.fuel.2019.115975.

[77] J. Xiao, D. Mao, G. Wang, X. Guo, and J. Yu, "CO2 hydrogenation to methanol over CuOZnOTiO2ZrO2 catalyst prepared by a facile solid-state route: The significant influence of assistant complexing agents," *Int. J. Hydrogen Energy*, vol. 44, no. 29, pp. 14831–14841, Jun. 2019, doi: 10.1016/J.IJHYDENE.2019.04.051.

[78] K. Chen *et al.*, "CO2 hydrogenation to methanol over Cu catalysts supported on La-modified SBA-15: The crucial role of Cu–LaOx interfaces," *Appl. Catal. B Environ.*, vol. 251, pp. 119–129, Aug. 2019, doi: 10.1016/J.APCATB.2019.03.059.

[79] X. Jiang *et al.*, "CO2 hydrogenation to methanol on PdCu bimetallic catalysts with lower metal loadings," *Catal. Commun.*, vol. 118, pp. 10–14, Jan. 2019, doi: 10.1016/J.CATCOM.2018.09.006.

[80] L. Yao, X. Shen, Y. Pan, and Z. Peng, “Synergy between active sites of Cu-In-Zr-O catalyst in CO2 hydrogenation to methanol,” *J. Catal.*, vol. 372, pp. 74–85, Apr. 2019, doi: 10.1016/J.JCAT.2019.02.021.

[81] T. Kamsuwan, C. Krutpijit, S. Praserthdam, S. Phatanasri, B. Jongsomjit, and P. Praserthdam, “Comparative study on the effect of different copper loading on catalytic behaviors and activity of Cu/ZnO/Al2O3 catalysts toward CO and CO2 hydrogenation,” *Heliyon*, vol. 7, no. 7, p. e07682, Jul. 2021, doi: 10.1016/j.heliyon.2021.e07682.

[82] T. Kamsuwan, A. Guntida, P. Praserthdam, and B. Jongsomjit, “Differences in Deterioration Behaviors of Cu/ZnO/Al2O3 Catalysts with Different Cu Contents toward Hydrogenation of CO and CO2,” *ACS Omega*, vol. 7, no. 29, pp. 25783–25797, Jul. 2022, doi: 10.1021/ACSOMEGA.2C03068/ASSET/IMAGES/LARGE/AO2C03068_0008.JPEG.

[83] A. Karelovic and P. Ruiz, “The role of copper particle size in low pressure methanol synthesis via CO2 hydrogenation over Cu/ZnO catalysts,” *Catal. Sci. Technol.*, vol. 5, no. 2, pp. 869–881, Feb. 2015, doi: 10.1039/c4cy00848k.

[84] T. Witoon *et al.*, “Tuning of catalytic CO2 hydrogenation by changing composition of CuO-ZnO-ZrO2 catalysts,” *Energy Convers. Manag.*, vol. 118, pp. 21–31, Jun. 2016, doi: 10.1016/J.ENCONMAN.2016.03.075.

[85] O. Tursunov, L. Kustov, and A. Kustov, “A Brief Review of Carbon Dioxide Hydrogenation to Methanol Over Copper and Iron Based Catalysts,” *Oil Gas Sci. Technol. – Rev. d’IFP Energies Nouv.*, vol. 72, no. 5, p. 30, Sep. 2017, doi: 10.2516/OGST/2017027.

[86] M. Ren, Y. Zhang, X. Wang, and H. Qiu, “Catalytic Hydrogenation of CO2 to Methanol: A Review,” *Catalysts*, vol. 12, no. 4, p. 403, Apr. 2022, doi: 10.3390/CATAL12040403.

[87] J. Zhong, X. Yang, Z. Wu, B. Liang, Y. Huang, and T. Zhang, “State of the art and perspectives in heterogeneous catalysis of CO2 hydrogenation to methanol,” *Chem. Soc. Rev.*, vol. 49, no. 5, pp. 1385–1413, Mar. 2020, doi: 10.1039/C9CS00614A.

[88] C. Liu, X. Guo, Q. Guo, D. Mao, J. Yu, and G. Lu, “Methanol synthesis from CO2 hydrogenation over copper catalysts supported on MgO-modified TiO2,” *J. Mol. Catal. A Chem.*, vol. 425, pp. 86–93, Dec. 2016, doi: 10.1016/J.MOLCATA.2016.09.032.

[89] H. Lei, Z. Hou, and J. Xie, “Hydrogenation of CO2 to CH3OH over CuO/ZnO/Al2O3 catalysts prepared via a solvent-free routine,” *Fuel*, vol. 164, pp. 191–198, Jan. 2016, doi: 10.1016/j.fuel.2015.09.082.

[90] L. Li, D. Mao, J. Yu, and X. Guo, "Highly selective hydrogenation of CO2 to methanol over CuO-ZnO-ZrO2 catalysts prepared by a surfactant-assisted co-precipitation method," *J. Power Sources*, vol. 279, pp. 394–404, Apr. 2015, doi: 10.1016/j.jpowsour.2014.12.142.

[91] V. Deerattrakul, P. Dittanet, M. Sawangphruk, and P. Kongkachuichay, "CO2 hydrogenation to methanol using Cu-Zn catalyst supported on reduced graphene oxide nanosheets," *J. CO2 Util.*, vol. 16, pp. 104–113, Dec. 2016, doi: 10.1016/J.JCOU.2016.07.002.

[92] W. Cai, P. Ramírez De La Piscina, J. Toyir, and N. Homs, "CO2 hydrogenation to methanol over CuZnGa catalysts prepared using microwave-assisted methods," *Catal. Today*, vol. 242, no. Part A, pp. 193–199, Mar. 2015, doi: 10.1016/J.CATTOD.2014.06.012.

[93] Z. Q. Wang *et al.*, "High-Performance and Long-Lived Cu/SiO2 Nanocatalyst for CO2 Hydrogenation," *ACS Catal.*, vol. 5, no. 7, pp. 4255–4259, Jun. 2015, doi: 10.1021/ACSCATAL.5B00682/ASSET/IMAGES/LARGE/CS-2015-006828_0006.JPEG.

[94] Y. H. Wang, W. G. Gao, H. Wang, Y. E. Zheng, W. Na, and K. Z. Li, "Structure–activity relationships of Cu–ZrO2 catalysts for CO2 hydrogenation to methanol: interaction effects and reaction mechanism," *RSC Adv.*, vol. 7, no. 14, pp. 8709–8717, Jan. 2017, doi: 10.1039/C6RA28305E.

[95] W. Wang, Z. Qu, L. Song, and Q. Fu, "Probing into the multifunctional role of copper species and reaction pathway on copper-cerium-zirconium catalysts for CO2 hydrogenation to methanol using high pressure in situ DRIFTS," *J. Catal.*, vol. 382, pp. 129–140, Feb. 2020, doi: 10.1016/J.JCAT.2019.12.022.

[96] Q. Tan, Z. Shi, and D. Wu, "CO2 Hydrogenation to Methanol over a Highly Active Cu-Ni/CeO2-Nanotube Catalyst," *Ind. Eng. Chem. Res.*, vol. 57, no. 31, pp. 10148–10158, Aug. 2018, doi: 10.1021/ACS.IECR.8B01246/ASSET/IMAGES/LARGE/IE-2018-01246T_0009.JPEG.

[97] I. U. Din, M. S. Shaharun, A. Naeem, S. Tasleem, and M. Rafie Johan, "Carbon nanofibers based copper/zirconia catalysts for carbon dioxide hydrogenation to methanol: Effect of copper concentration," *Chem. Eng. J.*, vol. 334, pp. 619–629, Feb. 2018, doi: 10.1016/j.cej.2017.10.087.

[98] G. Wang, L. Chen, Y. Sun, J. Wu, M. Fu, and D. Ye, "Carbon dioxide hydrogenation to methanol over Cu/ZrO2/CNTs: effect of carbon surface chemistry," *RSC Adv.*, vol. 5,

no. 56, pp. 45320–45330, May 2015, doi: 10.1039/C5RA04774A.

[99] S. Chen *et al.*, "Induced high selectivity methanol formation during CO2 hydrogenation over a CuBr2-modified CuZnZr catalyst," *J. Catal.*, vol. 389, pp. 47–59, Sep. 2020, doi: 10.1016/J.JCAT.2020.05.023.

[100] Y. Men *et al.*, "Synthesis of Ni5Ga3 catalyst by Hydrotalcite-like compound (HTlc) precursors for CO2 hydrogenation to methanol," *Appl. Catal. B Environ.*, vol. 275, p. 119067, Oct. 2020, doi: 10.1016/J.APCATB.2020.119067.

[101] X. Jia, K. Sun, J. Wang, C. Shen, and C. jun Liu, "Selective hydrogenation of CO2 to methanol over Ni/In2O3 catalyst," *J. Energy Chem.*, vol. 50, pp. 409–415, Nov. 2020, doi: 10.1016/J.JECHEM.2020.03.083.

[102] A. Cherevotan *et al.*, "Operando Generated Ordered Heterogeneous Catalyst for the Selective Conversion of CO2 to Methanol," *ACS Energy Lett.*, vol. 6, no. 2, pp. 509–516, Feb. 2021, doi: 10.1021/ACSENERGYLETT.0C02614/ASSET/IMAGES/MEDIUM/NZ0C02614_M003.GIF.

[103] J. Wang, K. Sun, X. Jia, and C. jun Liu, "CO2 hydrogenation to methanol over Rh/In2O3 catalyst," *Catal. Today*, vol. 365, pp. 341–347, Apr. 2021, doi: 10.1016/J.CATTOD.2020.05.020.

[104] J. A. Singh *et al.*, "Theoretical and Experimental Studies of CoGa Catalysts for the Hydrogenation of CO2 to Methanol," *Catal. Letters*, vol. 148, no. 12, pp. 3583–3591, Dec. 2018, doi: 10.1007/S10562-018-2542-X/FIGURES/7.

[105] H. Bahruji *et al.*, "Pd/ZnO catalysts for direct CO2 hydrogenation to methanol," *J. Catal.*, vol. 343, pp. 133–146, Nov. 2016, doi: 10.1016/J.JCAT.2016.03.017.

[106] O. Martin *et al.*, "Indium Oxide as a Superior Catalyst for Methanol Synthesis by CO2 Hydrogenation," *Angew. Chemie Int. Ed.*, vol. 55, no. 21, pp. 6261–6265, May 2016, doi: 10.1002/ANIE.201600943.

[107] S. Kiatphuengporn, M. Chareonpanich, and J. Limtrakul, "Effect of unimodal and bimodal MCM-41 mesoporous silica supports on activity of Fe–Cu catalysts for CO2 hydrogenation," *Chem. Eng. J.*, vol. 240, pp. 527–533, Mar. 2014, doi: 10.1016/J.CEJ.2013.10.090.

[108] J. Schittkowski *et al.*, "Methanol Synthesis from Steel Mill Exhaust Gases: Challenges for the Industrial Cu/ZnO/Al2O3 Catalyst," *Chemie Ing. Tech.*, vol. 90, no. 10, pp. 1419–1429, Oct. 2018, doi: 10.1002/CITE.201800017.

[109] J. Toyir, P. Ramírez de la Piscina, J. L. G. Fierro, and N. Homs, "Catalytic performance for CO2 conversion to methanol of gallium-promoted copper-based catalysts: influence of metallic precursors," *Appl. Catal. B Environ.*, vol. 34, no. 4, pp. 255–266, Nov. 2001, doi: 10.1016/S0926-3373(01)00203-X.

[110] J. Schumann *et al.*, "Promoting strong metal support interaction: Doping ZnO for enhanced activity of Cu/ZnO:M (M = Al, Ga, Mg) catalysts," *ACS Catal.*, vol. 5, no. 6, pp. 3260–3270, Jun. 2015, doi: 10.1021/ACSCATAL.5B00188/ASSET/IMAGES/LARGE/CS-2015-001889_0010.JPEG.

[111] C. L. Chiang, K. S. Lin, and H. W. Chuang, "Direct synthesis of formic acid via CO2 hydrogenation over Cu/ZnO/Al2O3 catalyst," *J. Clean. Prod.*, vol. 172, pp. 1957–1977, Jan. 2018, doi: 10.1016/j.jclepro.2017.11.229.

[112] A. Hadipour and M. Sohrabi, "Synthesis of some bifunctional catalysts and determination of kinetic parameters for direct conversion of syngas to dimethyl ether," *Chem. Eng. J.*, vol. 137, no. 2, pp. 294–301, Apr. 2008, doi: 10.1016/j.cej.2007.04.039.

[113] R. Khoshbin and M. Haghighi, "Direct syngas to DME as a clean fuel: The beneficial use of ultrasound for the preparation of CuO-ZnO-Al2O3/HZSM-5 nanocatalyst," *Chem. Eng. Res. Des.*, vol. 91, no. 6, pp. 1111–1122, Jun. 2013, doi: 10.1016/j.cherd.2012.11.017.

[114] S. Kuld *et al.*, "Quantifying the promotion of Cu catalysts by ZnO for methanol synthesis," *Science (80-.).*, vol. 352, no. 6288, pp. 969–974, May 2016, doi: 10.1126/science.aaf0718.

[115] B. E. Koel and J. Kim, "Promoters and Poisons," *Handb. Heterog. Catal.*, pp. 1593–1624, Mar. 2008, doi: 10.1002/9783527610044.HETCAT0087.

[116] M. Behrens *et al.*, "Performance improvement of nanocatalysts by promoter-induced defects in the support material: Methanol synthesis over Cu/ZnO:Al," *J. Am. Chem. Soc.*, vol. 135, no. 16, pp. 6061–6068, Apr. 2013, doi: 10.1021/JA310456F/SUPPL_FILE/JA310456F_SI_001.PDF.

[117] M. Behrens, F. Studt, I. Kasatkin, S. Kühl, M. Hävecker, and F. Abild-, "Methanol Synthesis over Cu/ZnO/Al2O3 The Active Site in Industrial Catalysis," *Science (80-.).*, vol. 336, no. 6083, pp. 893–897, 2012, doi: 10.1126/science.1219831.

[118] D. Previtali *et al.*, "Low pressure conversion of CO2 to methanol over Cu/Zn/Al catalysts. The effect of Mg, Ca and Sr as basic promoters," *Fuel*, vol. 274, Aug. 2020, doi: 10.1016/j.fuel.2020.117804.

[119] F. Zhang *et al.*, "Synthesis of Cu/Zn/Al/Mg catalysts on methanol production by different precipitation methods," *Mol. Catal.*, vol. 441, pp. 190–198, 2017, doi: 10.1016/j.mcat.2017.08.015.

[120] K. Nishida *et al.*, "Effective MgO surface doping of Cu/Zn/Al oxides as water-gas shift catalysts," *Appl. Clay Sci.*, vol. 44, no. 3–4, pp. 211–217, May 2009, doi: 10.1016/j.clay.2009.02.005.

[121] Z. Cheng *et al.*, "High-performance Cu/ZnO/Al2O3 catalysts for methanol steam reforming with enhanced Cu-ZnO synergy effect via magnesium assisted strategy," *J. Energy Chem.*, vol. 63, pp. 550–557, Dec. 2021, doi: 10.1016/j.jechem.2021.08.025.

[122] B. S. Xaba, A. S. Mahomed, and H. B. Friedrich, "The effect of CO2and H2adsorption strength and capacity on the performance of Ga and Zr modified Cu-Zn catalysts for CO2hydrogenation to methanol," *J. Environ. Chem. Eng.*, vol. 9, no. 1, p. 104834, Feb. 2021, doi: 10.1016/j.jece.2020.104834.

[123] M. M. J. Li, Z. Zeng, F. Liao, X. Hong, and S. C. E. Tsang, "Enhanced CO2 hydrogenation to methanol over CuZn nanoalloy in Ga modified Cu/ZnO catalysts," *J. Catal.*, vol. 343, pp. 157–167, Nov. 2016, doi: 10.1016/J.JCAT.2016.03.020.

[124] A. Arandia *et al.*, "Effect of atomic layer deposited zinc promoter on the activity of copper-on-zirconia catalysts in the hydrogenation of carbon dioxide to methanol," *Appl. Catal. B Environ.*, vol. 321, 2022, doi: 10.1016/j.apcatb.2022.122046.

[125] N. Pasupulety, A. A. Al-Zahrani, M. A. Daous, S. Podila, and H. Driss, "A study on highly active Cu-Zn-Al-K catalyst for CO2 hydrogenation to methanol," *Arab. J. Chem.*, vol. 14, no. 2, p. 102951, Feb. 2021, doi: 10.1016/J.ARABJC.2020.102951.

[126] L. Zhang, Y. Zhang, and S. Chen, "Effect of promoter SiO2, TiO2 or SiO2-TiO2 on the performance of CuO-ZnO-Al2O3 catalyst for methanol synthesis from CO2 hydrogenation," *Appl. Catal. A Gen.*, vol. 415–416, pp. 118–123, Feb. 2012, doi: 10.1016/J.APCATA.2011.12.013.

[127] P. Gao *et al.*, "Fluorinated Cu/Zn/Al/Zr hydrotalcites derived nanocatalysts for CO2 hydrogenation to methanol," *J. CO2 Util.*, vol. 16, pp. 32–41, Dec. 2016, doi: 10.1016/J.JCOU.2016.06.001.

[128] J. Díez-Ramírez, F. Dorado, A. R. De La Osa, J. L. Valverde, and P. Sánchez, "Hydrogenation of CO2 to Methanol at Atmospheric Pressure over Cu/ZnO Catalysts: Influence of the Calcination, Reduction, and Metal Loading," *Ind. Eng. Chem. Res.*, vol. 56, no. 8, pp. 1979–1987, Mar. 2017, doi:

10.1021/ACS.IECR.6B04662/ASSET/IMAGES/LARGE/IE-2016-04662K_0009.JPEG.

[129] V. D. B. C. Dasireddy and B. Likozar, "The role of copper oxidation state in Cu/ZnO/Al2O3 catalysts in CO2 hydrogenation and methanol productivity," *Renew. Energy*, vol. 140, pp. 452–460, Sep. 2019, doi: 10.1016/J.RENENE.2019.03.073.

[130] A. M. Hengne, K. D. Bhatte, S. Ould-Chikh, Y. Saih, J. M. Basset, and K. W. Huang, "Selective Production of Oxygenates from Carbon Dioxide Hydrogenation over a Mesoporous-Silica-Supported Copper-Gallium Nanocomposite Catalyst," *ChemCatChem*, vol. 10, no. 6, pp. 1360–1369, Mar. 2018, doi: 10.1002/cctc.201701679.

[131] S. Ren, S. Li, N. Klinghoffer, M. Yu, and X. Liang, "Effects of mixing methods of bifunctional catalysts on catalyst stability of DME synthesis via CO2 hydrogenation," *Carbon Resour. Convers.*, vol. 2, no. 1, pp. 85–94, Apr. 2019, doi: 10.1016/j.crcon.2019.03.002.

[132] S. Xia *et al.*, "Effects of precursor phase distribution on the performance of Cu-based catalysts for direct CO2 conversion to dimethyl ether," *J. Energy Inst.*, vol. 109, p. 101302, Aug. 2023, doi: 10.1016/J.JOEI.2023.101302.

[133] D. F. Carvalho, G. C. Almeida, R. S. Monteiro, and C. J. A. Mota, "Hydrogenation of CO2 to Methanol and Dimethyl Ether over a Bifunctional Cu·ZnO Catalyst Impregnated on Modified γ-Alumina," *Energy and Fuels*, vol. 34, no. 6, pp. 7269–7274, Jun. 2020, doi: 10.1021/ACS.ENERGYFUELS.0C00680/ASSET/IMAGES/LARGE/EF0C00680_0004.JPEG.

[134] H. R. Godini, S. R. Kumar, N. Tadikamalla, and F. Gallucci, "Performance analysis of hybrid catalytic conversion of CO2 to DiMethyl ether," *Int. J. Hydrogen Energy*, vol. 47, no. 21, pp. 11341–11358, Mar. 2022, doi: 10.1016/j.ijhydene.2021.11.073.

[135] G. Bonura *et al.*, "Acidity control of zeolite functionality on activity and stability of hybrid catalysts during DME production via CO2 hydrogenation," *J. CO2 Util.*, vol. 24, pp. 398–406, Mar. 2018, doi: 10.1016/J.JCOU.2018.01.028.

[136] S. Ren *et al.*, "Enhanced catalytic performance of Zr modified CuO/ZnO/Al2O3 catalyst for methanol and DME synthesis via CO2 hydrogenation," *J. CO2 Util.*, vol. 36, pp. 82–95, Feb. 2020, doi: 10.1016/j.jcou.2019.11.013.

[137] A. Kornas, R. Grabowski, M. Śliwa, K. Samson, M. Ruggiero-Mikołajczyk, and A. Żelazny, "Dimethyl ether synthesis from CO2 hydrogenation over hybrid catalysts: effects of preparation methods," *React. Kinet. Mech. Catal.*, vol. 121, no. 1, pp. 317–327,

Jun. 2017, doi: 10.1007/S11144-017-1153-7/TABLES/5.

[138] H. Bahruji, R. D. Armstrong, J. Ruiz Esquius, W. Jones, M. Bowker, and G. J. Hutchings, "Hydrogenation of CO2 to Dimethyl Ether over Brønsted Acidic PdZn Catalysts," *Ind. Eng. Chem. Res.*, vol. 57, no. 20, pp. 6821–6829, May 2018, doi: 10.1021/ACS.IECR.8B00230/ASSET/IMAGES/MEDIUM/IE-2018-00230E_M005.GIF.

[139] W. Li, K. Wang, G. Zhan, J. Huang, and Q. Li, "Hydrogenation of CO2 to Dimethyl Ether over Tandem Catalysts Based on Biotemplated Hierarchical ZSM-5 and Pd/ZnO," *ACS Sustain. Chem. Eng.*, vol. 8, no. 37, pp. 14058–14070, Sep. 2020, doi: 10.1021/ACSSUSCHEMENG.0C04399/ASSET/IMAGES/LARGE/SC0C04399_0012.JPEG.

[140] A. Pechenkin *et al.*, "CO2 hydrogenation to dimethyl ether over In2O3 catalysts supported on aluminosilicate halloysite nanotubes," *Green Process. Synth.*, vol. 10, no. 1, pp. 594–605, Jan. 2021, doi: 10.1515/GPS-2021-0058/ASSET/GRAPHIC/J_GPS-2021-0058_FIG_010.JPG.

[141] A. García-Trenco and A. Martínez, "Direct synthesis of DME from syngas on hybrid CuZnAl/ZSM-5 catalysts: New insights into the role of zeolite acidity," *Appl. Catal. A Gen.*, vol. 411–412, pp. 170–179, Jan. 2012, doi: 10.1016/J.APCATA.2011.10.036.

[142] C. Niamnuy *et al.*, "Synthesis of Dimethyl Ether via CO2 Hydrogenation: Effect of the Drying Technique of Alumina on Properties and Performance of Alumina-Supported Copper Catalysts," *ACS Omega*, vol. 5, no. 5, pp. 2334–2344, Feb. 2020, doi: 10.1021/acsomega.9b03713.

[143] X. Fan, B. Jin, S. Ren, S. Li, M. Yu, and X. Liang, "Roles of interaction between components in CZZA/HZSM-5 catalyst for dimethyl ether synthesis via CO2 hydrogenation," *AIChE J.*, vol. 67, no. 11, p. e17353, Nov. 2021, doi: 10.1002/AIC.17353.

[144] T. Zhao, Z. Yang, Y. Tang, J. Liu, and F. Wang, "Advances and Perspectives of Photopromoted CO2 Hydrogenation for Methane Production: Catalyst Development and Mechanism Investigations," *Energy and Fuels*, vol. 36, no. 13, pp. 6711–6735, Jul. 2022, doi: 10.1021/ACS.ENERGYFUELS.2C01507/ASSET/IMAGES/LARGE/EF2C01507_0016.JPEG.

[145] A. Karelovic and P. Ruiz, "Mechanistic study of low temperature CO2 methanation over Rh/TiO2 catalysts," *J. Catal.*, vol. 301, pp. 141–153, May 2013, doi: 10.1016/J.JCAT.2013.02.009.

[146] C. Vogt *et al.*, "Unravelling structure sensitivity in CO2 hydrogenation over nickel," *Nat. Catal.*, vol. 1, no. 2, pp. 127–134, Jan. 2018, doi: 10.1038/s41929-017-0016-y.

[147] J. Huang, X. Li, X. Wang, X. Fang, H. Wang, and X. Xu, "New insights into CO2 methanation mechanisms on Ni/MgO catalysts by DFT calculations: Elucidating Ni and MgO roles and support effects," *J. CO2 Util.*, vol. 33, pp. 55–63, Oct. 2019, doi: 10.1016/J.JCOU.2019.04.022.

[148] R. P. Ye *et al.*, "High-performance of nanostructured Ni/CeO2 catalyst on CO2 methanation," *Appl. Catal. B Environ.*, vol. 268, p. 118474, Jul. 2020, doi: 10.1016/J.APCATB.2019.118474.

[149] K. Klier, "Methanol Synthesis," *Adv. Catal.*, vol. 31, no. C, pp. 243–313, Jan. 1982, doi: 10.1016/S0360-0564(08)60455-1.

[150] G. C. Chinchen, P. J. Denny, D. G. Parker, M. S. Spencer, and D. A. Whan, "Mechanism of methanol synthesis from CO2/CO/H2 mixtures over copper/zinc oxide/alumina catalysts: use of14C-labelled reactants," *Appl. Catal.*, vol. 30, no. 2, pp. 333–338, Apr. 1987, doi: 10.1016/S0166-9834(00)84123-8.

[151] L. C. Grabow and M. Mavrikakis, "Mechanism of methanol synthesis on Cu through CO2 and CO hydrogenation," *ACS Catal.*, vol. 1, no. 4, pp. 365–384, Apr. 2011, doi: 10.1021/CS200055D/ASSET/IMAGES/LARGE/CS-2011-00055D_0010.JPEG.

[152] R. Gaikwad, H. Reymond, N. Phongprueksathat, P. Rudolf Von Rohr, and A. Urakawa, "From CO or CO2?: space-resolved insights into high-pressure CO2 hydrogenation to methanol over Cu/ZnO/Al2O3," *Catal. Sci. Technol.*, vol. 10, no. 9, pp. 2763–2768, May 2020, doi: 10.1039/D0CY00050G.

[153] E. Furimsky, "CO2 hydrogenation to methanol and methane over carbon-supported catalysts," *Ind. Eng. Chem. Res.*, vol. 59, no. 35, pp. 15393–15423, Sep. 2020, doi: 10.1021/ACS.IECR.0C02250/ASSET/IMAGES/LARGE/IE0C02250_0020.JPEG.

[154] M. D. Porosoff, B. Yan, and J. G. Chen, "Catalytic reduction of CO2 by H2 for synthesis of CO, methanol and hydrocarbons: challenges and opportunities," *Energy Environ. Sci.*, vol. 9, no. 1, pp. 62–73, Jan. 2016, doi: 10.1039/C5EE02657A.

[155] A. Ghorbanpour, J. D. Rimer, and L. C. Grabow, "Computational Assessment of the Dominant Factors Governing the Mechanism of Methanol Dehydration over H-ZSM-5 with Heterogeneous Aluminum Distribution," *ACS Catal.*, vol. 6, no. 4, pp. 2287–2298, Apr. 2016, doi: 10.1021/ACSCATAL.5B02367/ASSET/IMAGES/LARGE/CS-2015-02367C_0008.JPEG.

[156] Q. Sheng *et al.*, "Mechanism and catalytic performance for direct dimethyl ether synthesis by CO2 hydrogenation over CuZnZr/ferrierite hybrid catalyst," *J. Environ. Sci. (China)*, vol. 92, pp. 106–117, Jun. 2020, doi: 10.1016/j.jes.2020.02.015.

[157] K. L. Ng, D. Chadwick, and B. A. Toseland, "Kinetics and modelling of dimethyl ether synthesis from synthesis gas," *Chem. Eng. Sci.*, vol. 54, no. 15–16, pp. 3587–3592, Jul. 1999, doi: 10.1016/S0009-2509(98)00514-4.

[158] W. Z. Lu, L. H. Teng, and W. De Xiao, "Simulation and experiment study of dimethyl ether synthesis from syngas in a fluidized-bed reactor," *Chem. Eng. Sci.*, vol. 59, no. 22–23, pp. 5455–5464, Nov. 2004, doi: 10.1016/J.CES.2004.07.031.

[159] Z. Nie, H. Liu, D. Liu, W. Ying, and D. Fang, "Intrinsic Kinetics of Dimethyl Ether Synthesis from Syngas," *J. Nat. Gas Chem.*, vol. 14, pp. 22–28, 2005.

[160] A. Ateka, J. Ereña, J. Bilbao, and A. T. Aguayo, "Kinetic modeling of the direct synthesis of dimethyl ether over a CuO-ZnO-MnO/SAPO-18 catalyst and assessment of the CO2 conversion," *Fuel Process. Technol.*, vol. 181, pp. 233–243, Dec. 2018, doi: 10.1016/j.fuproc.2018.09.024.

[161] N. Delgado Otalvaro, P. G. Bilir, K. H. Delgado, S. Pitter, and J. Sauer, "Kinetics of the Direct DME Synthesis: State of the Art and Comprehensive Comparison of Semi-Mechanistic, Data-Based and Hybrid Modeling Approaches," *Catalysts*, vol. 12, no. 3, p. 347, Mar. 2022, doi: 10.3390/CATAL12030347/S1.

[162] N. Delgado Otalvaro, G. Sogne, K. H. Delgado, S. Wild, S. Pitter, and J. ¨ Org Sauer, "Kinetics of the direct DME synthesis from CO2 rich syngas under variation of the CZA-to-g-Al2O3 ratio of a mixed catalyst bed," *RSC Adv.*, vol. 11, no. 40, pp. 24556–24569, Jul. 2021, doi: 10.1039/d1ra03452a.

[163] N. Delgado Otalvaro, M. Kaiser, K. Herrera Delgado, S. Wild, J. Sauer, and H. Freund, "Optimization of the direct synthesis of dimethyl ether from CO2 rich synthesis gas: Closing the loop between experimental investigations and model-based reactor design," *React. Chem. Eng.*, vol. 5, no. 5, pp. 949–960, Apr. 2020, doi: 10.1039/dore00041h.

[164] S. Guffanti, C. G. Visconti, J. van Kampen, J. Boon, and G. Groppi, "Reactor modelling and design for sorption enhanced dimethyl ether synthesis," *Chem. Eng. J.*, vol. 404, p. 126573, Jan. 2021, doi: 10.1016/j.cej.2020.126573.

[165] B. C. Gates and L. N. Johanson, "Langmuir-hinshelwood kinetics of the dehydration of methanol catalyzed by cation exchange resin," *AIChE J.*, vol. 17, no. 4, pp. 981–983, 1971, doi: 10.1002/aic.690170435.

[166] K. Klusáček and P. Schneider, "Stationary catalytic kinetics via surface concentrations from transient data. Methanol dehydration," *Chem. Eng. Sci.*, vol. 37, no. 10, pp. 1523–1528, Jan. 1982, doi: 10.1016/0009-2509(82)80010-9.

[167] W. An, K. T. Chuang, and A. R. Sanger, "Dehydration of Methanol to Dimethyl Ether by Catalytic Distillation," *Can. J. Chem. Eng.*, vol. 82, 2004, doi: 10.1002/cjce.5450820510.

[168] M. Mollavali, F. Yaripour, H. Atashi, and S. Sahebdelfar, "Intrinsic kinetics study of dimethyl ether synthesis from methanol on γ-Al2O3 catalysts," *Ind. Eng. Chem. Res.*, vol. 47, no. 9, pp. 3265–3273, May 2008, doi: 10.1021/IE800051H/ASSET/IMAGES/LARGE/IE800051HF00010.JPEG.

[169] K. S. Ha *et al.*, "New reaction pathways and kinetic parameter estimation for methanol dehydration over modified ZSM-5 catalysts," *Appl. Catal. A Gen.*, vol. 395, no. 1–2, pp. 95–106, Mar. 2011, doi: 10.1016/J.APCATA.2011.01.025.

[170] S. Hosseininejad, A. Afacan, and R. E. Hayes, "Catalytic and kinetic study of methanol dehydration to dimethyl ether," *Chem. Eng. Res. Des.*, vol. 90, no. 6, pp. 825–833, Jun. 2012, doi: 10.1016/J.CHERD.2011.10.007.

[171] Y. Tavan, S. H. Hosseini, M. Ghavipour, M. R. K. Nikou, and A. Shariati, "From laboratory experiments to simulation studies of methanol dehydration to produce dimethyl ether - Part I: Reaction kinetic study," *Chem. Eng. Process. Process Intensif.*, vol. 73, pp. 144–150, 2013, doi: 10.1016/j.cep.2013.06.006.

[172] C. Ortega, M. Rezaei, V. Hessel, and G. Kolb, "Methanol to dimethyl ether conversion over a ZSM-5 catalyst: Intrinsic kinetic study on an external recycle reactor," *Chem. Eng. J.*, vol. 347, pp. 741–753, Sep. 2018, doi: 10.1016/j.cej.2018.04.160.

[173] J. Xu and G. F. Froment, "Methane steam reforming, methanation and water-gas shift: I. Intrinsic kinetics," *AIChE J.*, vol. 35, no. 1, pp. 88–96, Jan. 1989, doi: 10.1002/aic.690350109.

[174] G. D. Weatherbee and C. H. Bartholomew, "Hydrogenation of CO2 on group VIII metals. II. Kinetics and mechanism of CO2 hydrogenation on nickel," *J. Catal.*, vol. 77, no. 2, pp. 460–472, Oct. 1982, doi: 10.1016/0021-9517(82)90186-5.

[175] L. Falbo, M. Martinelli, C. G. Visconti, L. Lietti, C. Bassano, and P. Deiana, "Kinetics of CO2 methanation on a Ru-based catalyst at process conditions relevant for Power-to-Gas applications," *Appl. Catal. B Environ.*, vol. 225, pp. 354–363, Jun. 2018, doi: 10.1016/j.apcatb.2017.11.066.

[176] P. LUNDE, “Rates of methane formation from carbon dioxide and hydrogen over a ruthenium catalyst*,” *J. Catal.*, vol. 30, no. 3, pp. 423–429, Sep. 1973, doi: 10.1016/0021-9517(73)90159-0.

[177] D. Schmider, L. Maier, and O. Deutschmann, “Reaction Kinetics of CO and CO2 Methanation over Nickel,” *Ind. Eng. Chem. Res.*, vol. 60, no. 16, pp. 5792–5805, Apr. 2021, doi: 10.1021/acs.iecr.1c00389.

[178] D. W. Green and R. H. Perry, “Perry’s Chemical Engineers’ Handbook,” 2008. doi: 10.1036/0071422943.

[179] G. H. Graaf, E. J. Stamhuis, and A. A. C. M. Beenackers, “Kinetics of low-pressure methanol synthesis,” *Chem. Eng. Sci.*, vol. 43, no. 12, pp. 3185–3195, Jan. 1988, doi: 10.1016/0009-2509(88)85127-3.

[180] P. K. Kiviranta-Pääkkönen, L. K. Struckmann née Rihko, J. A. Linnekoski, and A. O. I. Krause, “Dehydration of the Alcohol in the Etherification of Isoamylenes with Methanol and Ethanol,” *Ind. Eng. Chem. Res.*, vol. 37, no. 1, pp. 18–24, Jan. 1998, doi: 10.1021/ie970454d.

[181] A. Ateka, P. Rodriguez-Vega, J. Ereña, A. T. Aguayo, and J. Bilbao, “Kinetic modeling and reactor design of the direct synthesis of dimethyl ether for CO2 valorization. A review,” *Fuel*, vol. 327, p. 125148, Nov. 2022, doi: 10.1016/j.fuel.2022.125148.

[182] N. Park, M. J. Park, Y. J. Lee, K. S. Ha, and K. W. Jun, “Kinetic modeling of methanol synthesis over commercial catalysts based on three-site adsorption,” *Fuel Process. Technol.*, vol. 125, pp. 139–147, Sep. 2014, doi: 10.1016/J.FUPROC.2014.03.041.

[183] J. Sobczak, I. Wysocka, S. Murgrabia, and A. Rogala, “A Review on Deactivation and Regeneration of Catalysts for Dimethyl Ether Synthesis,” *Energies*, vol. 15, no. 15. Multidisciplinary Digital Publishing Institute, p. 5420, Jul. 27, 2022, doi: 10.3390/en15155420.

[184] J. Worstell, *Adiabatic fixed-bed reactors*. Waltham: Elsevier Inc., 2014.

[185] R. G. Santiago *et al.*, “Synthesis of MeOH and DME From CO2 Hydrogenation Over Commercial and Modified Catalysts,” *Front. Chem.*, vol. 10, Jun. 2022, doi: 10.3389/fchem.2022.903053.

[186] H.-H. Chiou, C.-J. Lee, B.-S. Wen, J.-X. Lin, C.-L. Chen, and B.-Y. Yu, “Evaluation of alternative processes of methanol production from CO2: Design, optimization, control, techno-economic, and environmental analysis,” *Fuel*, vol. 343, p. 127856, Jul. 2023, doi: 10.1016/j.fuel.2023.127856.

[187] K. Ahmad and S. Upadhyayula, "Greenhouse gas CO2 hydrogenation to fuels: A thermodynamic analysis," *Environ. Prog. Sustain. Energy*, vol. 38, no. 1, pp. 98–111, Jan. 2019, doi: 10.1002/ep.13028.

[188] M. Bibi *et al.*, "Catalytic Hydrogenation of Carbon Dioxide over Magnetic Nanoparticles: Modification in Fixed-Bed Reactor," *Catalysts*, vol. 11, no. 5, p. 592, May 2021, doi: 10.3390/catal11050592.

[189] Y. Zhang *et al.*, "Catalytic performance of spray-dried Cu/ZnO/Al2O3/ZrO2 catalysts for slurry methanol synthesis from CO2 hydrogenation," *J. CO2 Util.*, vol. 15, pp. 72–82, Sep. 2016, doi: 10.1016/j.jcou.2016.01.005.

[190] S. Ren *et al.*, "Highly active and selective Cu-ZnO based catalyst for methanol and dimethyl ether synthesis via CO2 hydrogenation," *Fuel*, vol. 239, pp. 1125–1133, Mar. 2019, doi: 10.1016/J.FUEL.2018.11.105.

[191] J. R. Grace, "Fluidized-bed catalytic reactors," in *Multiphase Catalytic Reactors*, Hoboken, NJ, USA: John Wiley & Sons, Inc., 2016, pp. 80–94.

[192] G. Wang, Y. Zuo, M. Han, and J. Wang, "Cu-Zr-Zn catalysts for methanol synthesis in a fluidized bed reactor," *Appl. Catal. A Gen.*, vol. 394, no. 1–2, pp. 281–286, Feb. 2011, doi: 10.1016/j.apcata.2011.01.010.

[193] B. Tabiś, "Methanol synthesis in a fluidized-bed reactor coupled with an external heat exchanger," *Chem. Eng. J.*, vol. 83, no. 3, pp. 191–200, Aug. 2001, doi: 10.1016/S1385-8947(00)00254-0.

[194] M. E. E. Abashar, "Dimethyl ether synthesis in a multi-stage fluidized bed reactor," *Chem. Eng. Process. Process Intensif.*, vol. 122, pp. 172–180, Dec. 2017, doi: 10.1016/j.cep.2017.09.018.

[195] L. H. Teng, "Attrition resistant catalyst for dimethyl ether synthesis in fluidized-bed reactor," *J. Zhejiang Univ. Sci. A*, vol. 9, no. 9, pp. 1288–1295, Sep. 2008, doi: 10.1631/jzus.A0820155.

[196] M. Kumar and V. C. Srivastava, "Simulation of a Fluidized-Bed Reactor for Dimethyl Ether Synthesis," *Chem. Eng. Technol.*, vol. 33, no. 12, pp. 1967–1978, Dec. 2010, doi: 10.1002/ceat.201000158.

[197] G. R. Moradi, J. Ahmadpour, F. Yaripour, and J. Wang, "Equilibrium calculations for direct synthesis of dimethyl ether from syngas," *Can. J. Chem. Eng.*, vol. 89, no. 1, pp. 108–115, Feb. 2011, doi: 10.1002/cjce.20373.

[198] Z. Azizi, M. Rezaeimanesh, T. Tohidian, and M. R. Rahimpour, “Dimethyl ether: A review of technologies and production challenges,” *Chemical Engineering and Processing: Process Intensification*, vol. 82. Elsevier, pp. 150–172, Aug. 01, 2014, doi: 10.1016/j.cep.2014.06.007.

[199] I. U. Din, A. I. Alharthi, M. A. Alotaibi, A. Naeem, T. Saeed, and A. A. Nassar, “Deciphering the role of CNT for methanol fuel synthesis by CO2 hydrogenation over Cu/CNT catalysts,” *Chem. Eng. Res. Des.*, vol. 194, pp. 115–120, Jun. 2023, doi: 10.1016/j.cherd.2023.04.034.

[200] Y. Jiang *et al.*, “Slurry methanol synthesis from CO2 hydrogenation over micro-spherical SiO2 support Cu/ZnO catalysts,” *J. CO2 Util.*, vol. 26, pp. 642–651, Jul. 2018, doi: 10.1016/j.jcou.2018.06.023.

[201] K. Lau, P. Schühle, S. X. Liang, F. De Kock, J. Albert, and S. Reichenberger, “Laser-Generated InOx/ZrO2Catalysts for CO2Hydrogenation: Role of in Situ Fragmentation and Ripening Control,” *ACS Appl. Energy Mater.*, vol. 4, no. 9, pp. 9206–9215, Sep. 2021, doi: 10.1021/acsaem.1c01465.

[202] P. Schühle, S. Reichenberger, G. Marzun, and J. Albert, “Slurry Phase Hydrogenation of CO2 to Methanol Using Supported In2O3 Catalysts as Promising Approach for Chemical Energy Storage,” *Chemie Ing. Tech.*, vol. 93, no. 4, pp. 585–593, Apr. 2021, doi: 10.1002/cite.202000109.

[203] H. Yagi, Y. Ohno, N. Inoue, K. Okuyama, and S. Aoki, “Slurry phase reactor technology for DME direct synthesis,” *Int. J. Chem. React. Eng.*, vol. 8, no. 1, Jul. 2010, doi: 10.2202/1542-6580.2267.

[204] S. P. Naik, T. Ryu, V. Bui, J. D. Miller, N. B. Drinnan, and W. Zmierczak, “Synthesis of DME from CO2/H2 gas mixture,” *Chem. Eng. J.*, vol. 167, no. 1, pp. 362–368, Feb. 2011, doi: 10.1016/j.cej.2010.12.087.

[205] S. N. Khadzhiev, N. N. Ezhova, and O. V. Yashina, “Catalysis in the dispersed phase: Slurry technology in the synthesis of dimethyl ether (Review),” *Pet. Chem.*, vol. 57, no. 7, pp. 553–570, Jul. 2017, doi: 10.1134/S0965544117070040.

[206] U. Mondal and G. D. Yadav, “Perspective of dimethyl ether as fuel: Part II- analysis of reactor systems and industrial processes,” *Journal of CO2 Utilization*, vol. 32. Elsevier Ltd, pp. 321–338, Jul. 01, 2019, doi: 10.1016/j.jcou.2019.02.006.

[207] K. Li, X. An, K. H. Park, M. Khraisheh, and J. Tang, “A critical review of CO2 photoconversion: Catalysts and reactors,” *Catal. Today*, vol. 224, pp. 3–12, Apr. 2014,

doi: 10.1016/j.cattod.2013.12.006.

[208] Z. H. He *et al.*, "Photothermal CO2 hydrogenation to methanol over a CoO/Co/TiO2 catalyst in aqueous media under atmospheric pressure," *Catal. Today*, vol. 356, pp. 579–588, Oct. 2020, doi: 10.1016/J.CATTOD.2020.01.007.

[209] K. Tripathi, R. Singh, S. Singh, S. Asthana, and K. K. Pant, "Perspectives in carbon oxides conversion to methanol/dimethyl ether: Distinctive contribution of heterogeneous and photocatalysis," in *Catalysis for Clean Energy and Environmental Sustainability: Petrochemicals and Refining Processes - Volume 2*, Springer International Publishing, 2021, pp. 557–597.

[210] Q. Zhang, S. Wang, M. Dong, and W. Fan, "CO2 Hydrogenation on Metal-Organic Frameworks-Based Catalysts: A Mini Review," *Front. Chem.*, vol. 10, p. 802, Jul. 2022, doi: 10.3389/FCHEM.2022.956223.

[211] A. George *et al.*, "A Review of Non-Thermal Plasma Technology: A novel solution for CO2 conversion and utilization," *Renew. Sustain. Energy Rev.*, vol. 135, p. 109702, Jan. 2021, doi: 10.1016/J.RSER.2020.109702.

[212] L. Wang, Y. Yi, H. Guo, and X. Tu, "Atmospheric Pressure and Room Temperature Synthesis of Methanol through Plasma-Catalytic Hydrogenation of CO2," *ACS Catal.*, vol. 8, no. 1, pp. 90–100, Jan. 2018, doi: 10.1021/ACSCATAL.7B02733/ASSET/IMAGES/LARGE/CS-2017-027335_0015.JPEG.

[213] T. Su, X. Zhou, Z. Qin, and H. Ji, "Intrinsic Kinetics of Dimethyl Ether Synthesis from Plasma Activation of CO2 Hydrogenation over Cu-Fe-Ce/HZSM-5," *ChemPhysChem*, vol. 18, no. 3, pp. 299–309, Feb. 2017, doi: 10.1002/cphc.201601283.

[214] W. Donphai, N. Piriyawate, T. Witoon, P. Jantaratana, V. Varabuntoonvit, and M. Chareonpanich, "Effect of magnetic field on CO2 conversion over Cu-ZnO/ZrO2 catalyst in hydrogenation reaction," *J. CO2 Util.*, vol. 16, pp. 204–211, Dec. 2016, doi: 10.1016/j.jcou.2016.07.007.

[215] C. Sriakkarin, W. Umchoo, W. Donphai, Y. Poo-arporn, and M. Chareonpanich, "Sustainable production of methanol from CO2 over 10Cu-10Fe/ZSM-5 catalyst in a magnetic field-assisted packed bed reactor," *Catal. Today*, vol. 314, pp. 114–121, Sep. 2018, doi: 10.1016/j.cattod.2017.12.037.

[216] F. Gallucci, L. Paturzo, and A. Basile, "An experimental study of CO2 hydrogenation into methanol involving a zeolite membrane reactor," *Chem. Eng. Process. Process*

Intensif., vol. 43, no. 8, pp. 1029–1036, Aug. 2004, doi: 10.1016/j.cep.2003.10.005.

[217] R. Raso *et al.*, "Zeolite membranes: Comparison in the separation of H2O/H2/CO2 mixtures and test of a reactor for CO2 hydrogenation to methanol," *Catal. Today*, Mar. 2020, doi: 10.1016/j.cattod.2020.03.014.

[218] Z. Dehghani, M. R. Rahimpour, and A. Shariati, "Simulation and multi-objective optimization of a radial flow gas-cooled membrane reactor, considering reduction of CO2 emissions in methanol synthesis," *J. Environ. Chem. Eng.*, vol. 9, no. 2, p. 104910, Apr. 2021, doi: 10.1016/j.jece.2020.104910.

[219] Z. Li and T. T. Tsotsis, "Methanol synthesis in a high-pressure membrane reactor with liquid sweep," *J. Memb. Sci.*, vol. 570–571, pp. 103–111, Jan. 2019, doi: 10.1016/j.memsci.2018.09.071.

[220] F. S. Zebarjad, J. Gong, Z. Li, K. Jessen, and T. Tsotsis, "Simulation of methanol synthesis in a membrane-contactor reactor," *J. Memb. Sci.*, vol. 661, p. 120677, Nov. 2022, doi: 10.1016/j.memsci.2022.120677.

[221] F. S. Zebarjad, Z. Wang, H. Li, S. Hu, Y. Tang, and T. T. Tsotsis, "Investigation of CO2 and methanol solubility at high pressure and temperature in the ionic liquid [EMIM][BF4] employed during methanol synthesis in a membrane-contactor reactor," *Chem. Eng. Sci.*, vol. 242, p. 116722, Oct. 2021, doi: 10.1016/j.ces.2021.116722.

[222] F. S. Zebarjad, S. Hu, Z. Li, and T. T. Tsotsis, "Experimental Investigation of the Application of Ionic Liquids to Methanol Synthesis in Membrane Reactors," *Ind. Eng. Chem. Res.*, vol. 58, no. 27, pp. 11811–11820, Jul. 2019, doi: 10.1021/acs.iecr.9b01178.

[223] J. Gong, F. Sadat-Zebarjad, K. Jessen, and T. Tsotsis, "An experimental and modeling study of the application of membrane contactor reactors to methanol synthesis using pure CO2 feeds," *Chem. Eng. Process. - Process Intensif.*, vol. 183, p. 109241, Jan. 2023, doi: 10.1016/j.cep.2022.109241.

[224] M. R. Rahimpour, M. Bayat, and F. Rahmani, "Dynamic simulation of a cascade fluidized-bed membrane reactor in the presence of long-term catalyst deactivation for methanol synthesis," *Chem. Eng. Sci.*, vol. 65, no. 14, pp. 4239–4249, Jul. 2010, doi: 10.1016/j.ces.2010.04.018.

[225] S. Saeidi, N. A. S. Amin, and M. R. Rahimpour, "Hydrogenation of CO2 to value-added products - A review and potential future developments," *Journal of CO2 Utilization*, vol. 5. Elsevier Ltd, pp. 66–81, Mar. 01, 2014, doi: 10.1016/j.jcou.2013.12.005.

[226] D. A. Fedosov, A. V. Smirnov, V. V. Shkirskiy, T. Voskoboynikov, and I. I. Ivanova,

"Methanol dehydration in NaA zeolite membrane reactor," *J. Memb. Sci.*, vol. 486, pp. 189–194, Jul. 2015, doi: 10.1016/j.memsci.2015.03.047.

[227] C. Zhou, N. Wang, Y. Qian, X. Liu, J. Caro, and A. Huang, "Efficient Synthesis of Dimethyl Ether from Methanol in a Bifunctional Zeolite Membrane Reactor," *Angew. Chemie - Int. Ed.*, vol. 55, no. 41, pp. 12678–12682, Oct. 2016, doi: 10.1002/anie.201604753.

[228] M. Farsi, A. Hallaji Sani, and P. Riasatian, "Modeling and operability of DME production from syngas in a dual membrane reactor," *Chem. Eng. Res. Des.*, vol. 112, pp. 190–198, Aug. 2016, doi: 10.1016/j.cherd.2016.06.019.

[229] A. Ateka, P. Rodriguez-Vega, T. Cordero-Lanzac, J. Bilbao, and A. T. Aguayo, "Model validation of a packed bed LTA membrane reactor for the direct synthesis of DME from CO/CO2," *Chem. Eng. J.*, vol. 408, p. 127356, Mar. 2021, doi: 10.1016/j.cej.2020.127356.

[230] S. Poto, F. Gallucci, and M. Fernanda Neira d'Angelo, "Direct conversion of CO2 to dimethyl ether in a fixed bed membrane reactor: Influence of membrane properties and process conditions," *Fuel*, vol. 302, p. 121080, Oct. 2021, doi: 10.1016/j.fuel.2021.121080.

[231] N. Beltermann *et al.*, "An evaluation of direct dimethyl ether (DME) synthesis from hydrogen and carbon dioxide based on CFD reactor simulations," *Int. J. Hydrogen Energy*, Jun. 2023, doi: 10.1016/j.ijhydene.2023.05.260.

[232] M. M. Mardanpour, R. Sadeghi, M. R. Ehsani, and M. Nasr Esfahany, "Enhancement of dimethyl ether production with application of hydrogen-permselective Pd-based membrane in fluidized bed reactor," *J. Ind. Eng. Chem.*, vol. 18, no. 3, pp. 1157–1165, May 2012, doi: 10.1016/j.jiec.2012.01.012.

[233] R. Sadeghi and M. Karimi, "New configuration gas-cooled fluidized bed membrane reactor to reduce the thermodynamic limitations of dimethyl ether production," *Chem. Eng. Process. - Process Intensif.*, vol. 183, p. 109223, Jan. 2023, doi: 10.1016/j.cep.2022.109223.

[234] M. R. Rahimpour, E. Pourazadi, D. Iranshahi, and A. M. Bahmanpour, "Methanol synthesis in a novel axial-flow, spherical packed bed reactor in the presence of catalyst deactivation," *Chem. Eng. Res. Des.*, vol. 89, no. 11, pp. 2457–2469, Nov. 2011, doi: 10.1016/j.cherd.2011.02.030.

[235] F. Samimi, M. Bayat, D. Karimipourfard, M. R. Rahimpour, and P. Keshavarz, "A novel

axial-flow spherical packed-bed membrane reactor for dimethyl ether synthesis: Simulation and optimization," *J. Nat. Gas Sci. Eng.*, vol. 13, pp. 42–51, Jul. 2013, doi: 10.1016/j.jngse.2013.03.001.

[236] M. R. Rahimpour, P. Parvasi, and P. Setoodeh, "Dynamic optimization of a novel radial-flow, spherical-bed methanol synthesis reactor in the presence of catalyst deactivation using Differential Evolution (DE) algorithm," *Int. J. Hydrogen Energy*, vol. 34, no. 15, pp. 6221–6230, Aug. 2009, doi: 10.1016/j.ijhydene.2009.05.068.

[237] M. Farsi, "DME production in multi-stage radial flow spherical membrane reactors: Reactor design and modeling," *J. Nat. Gas Sci. Eng.*, vol. 20, pp. 366–372, Sep. 2014, doi: 10.1016/j.jngse.2014.07.009.

[238] M. J. Bos, Y. Slotboom, S. R. A. Kersten, and D. W. F. Brilman, "110th Anniversary: Characterization of a Condensing CO2 to Methanol Reactor," *Ind. Eng. Chem. Res.*, vol. 58, no. 31, pp. 13987–13999, Aug. 2019, doi: 10.1021/acs.iecr.9b02576.

[239] X. K. Phan *et al.*, "Pd/CeO2 catalysts as powder in a fixed-bed reactor and as coating in a stacked foil microreactor for the methanol synthesis," *Catal. Today*, vol. 273, pp. 25–33, Sep. 2016, doi: 10.1016/j.cattod.2016.02.047.

[240] S. Allahyari, M. Haghighi, and A. Ebadi, "Direct synthesis of DME over nanostructured CuO-ZnO-Al2O3/HZSM-5 catalyst washcoated on high pressure microreactor: Effect of catalyst loading and process condition on reactor performance," *Chem. Eng. J.*, vol. 262, pp. 1175–1186, Feb. 2015, doi: 10.1016/j.cej.2014.10.062.

[241] S. Allahyari, M. Haghighi, and A. Ebadi, "Direct conversion of syngas to DME as a green fuel in a high pressure microreactor: Influence of slurry solid content on characteristics and reactivity of washcoated CuO-ZnO-Al2O3/HZSM-5 nanocatalyst," *Chem. Eng. Process. - Process Intensif.*, vol. 86, pp. 53–63, Dec. 2014, doi: 10.1016/j.cep.2014.10.001.

[242] F. Hayer, H. Bakhtiary-Davijany, R. Myrstad, A. Holmen, P. Pfeifer, and H. J. Venvik, "Characteristics of integrated micro packed bed reactor-heat exchanger configurations in the direct synthesis of dimethyl ether," *Chem. Eng. Process. Process Intensif.*, vol. 70, pp. 77–85, Aug. 2013, doi: 10.1016/j.cep.2013.03.021.

[243] D. Li, T. Maloney, N. Mannan, and S. Niknam, "Design of additively manufactured methanol conversion reactor for high throughput production," *Mater. Des. Process. Commun.*, vol. 3, no. 1, p. e143, Feb. 2021, doi: 10.1002/mdp2.143.

[244] W. Ding *et al.*, "Simulation of One-Stage Dimethyl Ether Synthesis over a Core-Shell

Catalyst," *Chemie Ing. Tech.*, vol. 87, no. 6, pp. 702–712, Jun. 2015, doi: 10.1002/cite.201400157.

[245] K. Omata, Y. Watanabe, T. Umegaki, G. Ishiguro, and M. Yamada, "Low-pressure DME synthesis with Cu-based hybrid catalysts using temperature-gradient reactor," *Fuel*, vol. 81, no. 11–12, pp. 1605–1609, Jul. 2002, doi: 10.1016/S0016-2361(02)00080-7.

[246] K. Omata, T. Ozaki, T. Umegaki, Y. Watanabe, N. Nukui, and M. Yamada, "Optimization of the Temperature Profile of a Temperature Gradient Reactor for DME Synthesis Using a Simple Genetic Algorithm Assisted by a Neural Network," *Energy & Fuels*, vol. 17, no. 4, pp. 836–841, Jul. 2003, doi: 10.1021/ef0202438.

[247] K. Omata and M. Yamada, "Artificial Neural Network and Grid Search Aided Optimization of Temperature Profile of Temperature Gradient Reactor for Dimethyl Ether Synthesis from Syngas," *Ind. Eng. Chem. Res.*, vol. 48, no. 2, pp. 844–849, Jan. 2009, doi: 10.1021/ie8008633.

[248] S. Masoudi, M. Farsi, and M. R. Rahimpour, "Dynamic optimization of methanol synthesis section in the dual type configuration to increase methanol production," *Oil Gas Sci. Technol. – Rev. d'IFP Energies Nouv.*, vol. 74, p. 90, 2019, doi: 10.2516/OGST/2019062.

[249] S. Lee, *Methanol synthesis technology*. CRC Press, 1990.

[250] Casale SA, "Methanol synthesis reactor - Casale SA." https://www.casale.ch/technologies/methanol-synthesis-reactor (accessed May 25, 2023).

[251] V. Dieterich, A. Buttler, A. Hanel, H. Spliethoff, and S. Fendt, "Power-to-liquid via synthesis of methanol, DME or Fischer–Tropsch-fuels: a review," *Energy and Environmental Science*, vol. 13, no. 10. Royal Society of Chemistry, pp. 3207–3252, Oct. 01, 2020, doi: 10.1039/d0ee01187h.

[252] M. Pérez-Fortes, J. C. Schöneberger, A. Boulamanti, and E. Tzimas, "Methanol synthesis using captured CO2 as raw material: Techno-economic and environmental assessment," *Appl. Energy*, vol. 161, pp. 718–732, 2016, doi: 10.1016/j.apenergy.2015.07.067.

[253] C. Hobson and Carlos Márquez (editor), "Renewable Methanol Report," *Methanol Inst.*, 2018, Accessed: May 25, 2023. [Online]. Available: www.methanol.orgwww.methanol.org.

[254] L. ENN Ecological Holdings Co., "Production - What we do." https://www.enn-

ng.com/en/business/index54.html (accessed Aug. 18, 2023).

[255] S. Ningxia, "Typical Plant Performance TOYO DME TECHNOLOGY Substitute for LPG and Diesel," *Toyo Eng. Corp.*, pp. 1–2, 2006, Accessed: Aug. 15, 2023. [Online]. Available: https://toyo-eng.com/wordpress/wp-content/uploads/2022/12/TOYO_DME.pdf.

[256] TOYO Engineering Corporation, "DME (Dimethyl Ether)." https://www.toyo-eng.com/jp/en/solution/dme/ (accessed Aug. 16, 2023).

[257] Japan DME Association, "Production of DME." https://www.japan-dme.or.jp/english/dme/production.html (accessed Aug. 18, 2023).

[258] Mitsubishi Corporation, "Press Room - 2021 - Commercial Operations Commence at Methanol / Dimethyl Ether Plant in Trinidad and Tobago," *Mitsubishi Corporation*, 2021. https://www.mitsubishicorp.com/jp/en/pr/archive/2021/html/0000046481.html (accessed Aug. 18, 2023).

[259] F. Pontzen, W. Liebner, V. Gronemann, M. Rothaemel, and B. Ahlers, "CO2-based methanol and DME - Efficient technologies for industrial scale production," in *Catalysis Today*, Aug. 2011, vol. 171, no. 1, pp. 242–250, doi: 10.1016/j.cattod.2011.04.049.

[260] Uhde, "Olefins & Solvents," *Thyssenkrupp Uhde GmbH*. https://www.thyssenkrupp-uhde.com/en/products-and-technologies/refining-and-petrochemicals/olefins-and-solvents (accessed Aug. 18, 2023).

[261] Y. Ohno, M. Yoshida, T. Shikada, O. Inokoshi, T. Ogawa, and N. Inoue, "New direct synthesis technology for DME (dimethyl ether) and its application technology," *JFE Tech. Rep.*, vol. 8, no. 8, pp. 34–40, 2006.

[262] M. I. Afokin and M. V. Magomedova, "Process Solutions for Recovery of Dimethyl Ether Produced Through One-Step Synthesis and Their Assessment," *Petroleum Chemistry*, vol. 61, no. 2. Pleiades journals, pp. 115–122, Feb. 01, 2021, doi: 10.1134/S0965544121020109.

[263] I. Air Products and Chemicals, "Development of alternative fuels and chemicals from synthesis gas," 2003.

[264] S. Ravn, "Air Products and Haldor Topsoe Sign Global Alliance Agreement for Collaboration on Large-Scale Ammonia, Methanol, and/or Dimethyl Ether Projects Around the World," *Air Products*, 2020.

https://www.airproducts.com/company/news-center/2020/05/0515-air-products-and-haldor-topsoe-sign-global-alliance (accessed Aug. 16, 2023).

[265] S. Ravn, "Air Products and Topsoe sign global alliance agreement for collaboration on large-scale ammonia, methanol, and/or dimethyl ether projects around the world," *Topsoe*, 2020. https://www.topsoe.com/blog/air-products-and-topsoe-sign-global-alliance-agreement-for-collaboration-on-large-scale-ammonia-methanol-and/or-dimethyl-ether-projects-around-the-world (accessed Aug. 16, 2023).

[266] BASF, "BASF and Lutianhua plan to pilot a new production process that significantly reduces CO2 emissions," *BASF*, 2019. https://www.basf.com/global/en/media/news-releases/2019/06/p-19-249.html (accessed Aug. 16, 2023).

[267] Sichuan Lutianhua Co. Ltd., "Sichuan Lutianhua Luyuanchun Industrial Corp." http://en.sclth.com/group.asp?cid=13 (accessed Aug. 16, 2023).

[268] Johnson Matthey, "Dimethyl ether process," *Johnson Matthey*. https://matthey.com/products-and-markets/chemicals/process-licensing/dimethyl-ether-process (accessed Aug. 18, 2023).

[269] F. Lonis, V. Tola, and G. Cau, "Renewable methanol production and use through reversible solid oxide cells and recycled CO2 hydrogenation," *Fuel*, vol. 246, no. February, pp. 500–515, 2019, doi: 10.1016/j.fuel.2019.02.108.

[270] É. S. Van-Dal and C. Bouallou, "Design and simulation of a methanol production plant from CO2 hydrogenation," *J. Clean. Prod.*, vol. 57, pp. 38–45, 2013, doi: 10.1016/j.jclepro.2013.06.008.

[271] G. Leonzio, E. Zondervan, and P. U. Foscolo, "Methanol production by CO2 hydrogenation: Analysis and simulation of reactor performance," *Int. J. Hydrogen Energy*, vol. 44, no. 16, pp. 7915–7933, Mar. 2019, doi: 10.1016/j.ijhydene.2019.02.056.

[272] A. A. Kiss, J. J. Pragt, H. J. Vos, G. Bargeman, and M. T. de Groot, "Novel efficient process for methanol synthesis by CO2 hydrogenation," *Chem. Eng. J.*, vol. 284, pp. 260–269, Jan. 2016, doi: 10.1016/j.cej.2015.08.101.

[273] X. Cui and S. K. Kær, "A comparative study on three reactor types for methanol synthesis from syngas and CO2," *Chem. Eng. J.*, vol. 393, p. 124632, Aug. 2020, doi: 10.1016/j.cej.2020.124632.

[274] S. Emebu *et al.*, "Design, techno-economic evaluation, and optimisation of renewable methanol plant model: Finland case study," *Chem. Eng. Sci.*, vol. 278, p. 118888, Aug.

2023, doi: 10.1016/J.CES.2023.118888.

[275] S. Sollai, A. Porcu, V. Tola, F. Ferrara, and A. Pettinau, “Renewable methanol production from green hydrogen and captured CO2: A techno-economic assessment,” *J. CO2 Util.*, vol. 68, p. 102345, Feb. 2023, doi: 10.1016/J.JCOU.2022.102345.

[276] P. Borisut and A. Nuchitprasittichai, “Methanol Production via CO2 Hydrogenation: Sensitivity Analysis and Simulation—Based Optimization,” *Front. Energy Res.*, vol. 7, p. 81, Sep. 2019, doi: 10.3389/FENRG.2019.00081/BIBTEX.

[277] Pérez-Fortes Mar and Tzimas Evangelos, “Techno-economic and environmental evaluation of CO2 utilisation for fuel production - Publications Office of the EU,” 2016. Accessed: Jan. 26, 2024. [Online]. Available: https://op.europa.eu/en/publication-detail/-/publication/080a6950-2c73-11e6-b497-01aa75ed71a1/language-en/format-PDF/source-303231907.

[278] M. Alsunousi and E. Kayabasi, “Techno-economic assessment of a floating photovoltaic power plant assisted methanol production by hydrogenation of CO2 captured from Zawiya oil refinery,” *Int. J. Hydrogen Energy*, vol. 57, pp. 589–600, Feb. 2024, doi: 10.1016/j.ijhydene.2024.01.055.

[279] C. S. Bîldea, R. Győrgy, C. C. Brunchi, and A. A. Kiss, “Optimal design of intensified processes for DME synthesis,” *Comput. Chem. Eng.*, vol. 105, pp. 142–151, Oct. 2017, doi: 10.1016/j.compchemeng.2017.01.004.

[280] G. Krishna, T. H. Min, and G. P. Rangaiah, “Modeling and Analysis of Novel Reactive HiGee Distillation,” *Comput. Aided Chem. Eng.*, vol. 31, pp. 1201–1205, Jan. 2012, doi: 10.1016/B978-0-444-59506-5.50071-7.

[281] N. K. Gor, N. A. Mali, and S. S. Joshi, “Intensified reactive distillation configurations for production of dimethyl ether,” *Chem. Eng. Process. - Process Intensif.*, vol. 149, p. 107824, Mar. 2020, doi: 10.1016/j.cep.2020.107824.

[282] C. Polsen, P. Narataruksa, P. Hunpinyo, and C. Prapainainar, “Simulation of single-step dimethyl ether synthesis from syngas,” *Energy Reports*, vol. 6, pp. 516–520, Feb. 2020, doi: 10.1016/j.egyr.2019.11.112.

[283] A. Giuliano, E. Catizzone, and C. Freda, “Process Simulation and Environmental Aspects of Dimethyl Ether Production from Digestate-Derived Syngas,” *Int. J. Environ. Res. Public Health*, vol. 18, no. 2, p. 807, Jan. 2021, doi: 10.3390/ijerph18020807.

[284] E. Yasari, M. Panahi, and A. Rafiee, “Multi-objective optimization and techno-economic analysis of CO2 utilization through direct synthesis of di-methyl ether plant,” *Int. J.*

Energy Res., vol. 45, no. 12, pp. 18103–18120, Oct. 2021, doi: 10.1002/ER.6961.

[285] T.-W. Wu and I.-L. Chien, "A novel energy-efficient process of converting CO2 to dimethyl ether with techno-economic and environmental evaluation," *Chem. Eng. Res. Des.*, vol. 177, pp. 1–12, Jan. 2022, doi: 10.1016/j.cherd.2021.10.013.

[286] S. Michailos, S. McCord, V. Sick, G. Stokes, and P. Styring, "Dimethyl ether synthesis via captured CO2 hydrogenation within the power to liquids concept: A techno-economic assessment," *Energy Convers. Manag.*, vol. 184, pp. 262–276, Mar. 2019, doi: 10.1016/j.enconman.2019.01.046.

[287] L. P. Merkouri, H. Ahmet, T. Ramirez Reina, and M. S. Duyar, "The direct synthesis of dimethyl ether (DME) from landfill gas: A techno-economic investigation," *Fuel*, vol. 319, p. 123741, Jul. 2022, doi: 10.1016/j.fuel.2022.123741.

[288] M. De Falco, M. Capocelli, and A. Giannattasio, "Membrane Reactor for one-step DME synthesis process: Industrial plant simulation and optimization," *J. CO2 Util.*, vol. 22, pp. 33–43, Dec. 2017, doi: 10.1016/j.jcou.2017.09.008.

[289] M. De Falco, M. Capocelli, and A. Basile, "Selective membrane application for the industrial one-step DME production process fed by CO2 rich streams: Modeling and simulation," *Int. J. Hydrogen Energy*, vol. 42, no. 10, pp. 6771–6786, Mar. 2017, doi: 10.1016/J.IJHYDENE.2017.02.047.

[290] H. Hamedi and T. Brinkmann, "Valorization of CO2 to DME using a membrane reactor: A theoretical comparative assessment from the equipment to flowsheet level," *Chem. Eng. J. Adv.*, vol. 10, p. 100249, May 2022, doi: 10.1016/j.ceja.2022.100249.

[291] A. Ateka, J. Ereña, J. Bilbao, and A. T. Aguayo, "Strategies for the Intensification of CO2 Valorization in the One-Step Dimethyl Ether Synthesis Process," *Ind. Eng. Chem. Res.*, vol. 59, no. 2, pp. 713–722, Jan. 2020, doi: 10.1021/acs.iecr.9b05749.

[292] M. Farsi, M. Asemani, and M. R. Rahimpour, "Mathematical modeling and optimization of multi-stage spherical reactor configurations for large scale dimethyl ether production," *Fuel Process. Technol.*, vol. 126, pp. 207–214, Oct. 2014, doi: 10.1016/j.fuproc.2014.04.029.

[293] C. R. Behloul, J. M. Commenge, and C. Castel, "Influence of the synergy between reaction, heat exchange and membrane separation on the process intensification of the dimethyl ether direct synthesis from carbon dioxide and hydrogen," *Chem. Eng. Process. - Process Intensif.*, vol. 167, p. 108513, Oct. 2021, doi: 10.1016/j.cep.2021.108513.

[294] C. R. Behloul, J.-M. Commenge, and C. Castel, “Modeling and Optimization of Mass and Heat Flux Profiles in a Multifunctional Reactor for CO2 and H2 Valorization to Dimethyl Ether,” *Ind. Eng. Chem. Res.*, vol. 61, no. 41, pp. 15301–15315, Oct. 2022, doi: 10.1021/acs.iecr.2c02713.

Chapter 2

2. Experimental DME synthesis

2.1. Materials

As we assumed that DME is synthesized by two consecutive reactions, hydrogenation of CO_2 into methanol followed by methanol dehydration into DME, some catalysts were selected to be active for each of the two steps and were physically mixed. Two catalysts were used to hydrogenate CO_2 to methanol. One was supplied by Alfa Aesar, the $CuO/ZnO/Al_2O_3/MgO$ (CZA-C), and another, $CuO/ZnO/Al_2O_3$ (CZA-D), was developed by Quezada, 2020 [1] during his PhD work (Table 2.1). For methanol dehydration, two types of zeolites were used: HY purchased from Sigma-Aldrich and HZSM-5 purchased from ACS Material, LLC (Table 2.2).

Table 2.1 Structural composition of the CZA catalysts.

	Loading (wt%)			
Catalyst	**CuO**	**ZnO**	**Al_2O_3**	**MgO**
CZA-D	7.8	7.1	85.1	–
CZA-C	63.8	24.6	9.9	1.4

Table 2.2 Zeolites properties.

Zeolite	$\boldsymbol{SiO_2/Al_2O_3}$	$\boldsymbol{BET}$ $(\boldsymbol{m^2.g^{-1}})$	$\boldsymbol{Pore\ volume}$ $(\boldsymbol{cm^3.g^{-1}})$	$\boldsymbol{Bulk\ density}$ $(\boldsymbol{kg.L^{-1}})$	$\boldsymbol{Brønsted}$ $(\boldsymbol{\mu molPy.mg_{cat}^{-1}})$	$\boldsymbol{Lewis}$ $(\boldsymbol{\mu molPy.mg_{cat}^{-1}})$
HY	2.5^a	605^a	–	–	0.2862^a	0.0233^a
HZSM-5	38	≥ 250	≥ 0.25	~0.72	–	–

[a] [2]

The CZA and zeolites were separately crushed with a mortar and pestle. The desired particle diameter (d_p) was guaranteed by sieving them in a digital electromagnetic screening machine (CISA Cedaceria Industrial, RP200N). In the case of CZA for methanol synthesis, the particle diameter was within the range of 0-200 μm. As for DME synthesis, the CZA diameter was within the range of 90-200 μm and zeolite diameter was within the range of 0-200 μm. The particle size was chosen on the basis of the experimental study of transfer limitations conducted by Quezada, 2020 [1] for 5 different diameters ($< 90\ ; 90 - 200\ ; 500 - 700\ ;\ 700 - 900\ ;\ extruded$). According to this study, CO_2 conversions into methanol as a function of temperature were unchanged whatever the catalyst diameter used below 900 μm, but there

were heat and/or mass transfer limitations for extruded materials. At this stage, we assume that, below 200 µm, the catalyst and reaction behaviours will be the same in our study as those observed by Quezada, 2020 [1], i.e. inducing no transfer limitation. They will however be checked a posteriori in Chapter 3.

The gas in the feed were H_2 (Linde Detector 5.0, 99.999% purity by volume), CO_2 (Linde 4.5, 99.995% purity by volume) and N_2 (Linde 4.5, 99.995% purity by volume).

Three other bottles were used for calibration. A standard cylinder containing CO (10.0% purity by volume), CO_2 (20.0% purity by volume), CH_4 (20.0% purity by volume) and H_2 (50.0% purity by volume) was purchased from Linde France S.A. A methanol standard cylinder with CH_3OH (1.5% purity by volume) and N_2 (98.5% purity by volume) was also purchased from Linde France S.A. A DME standard cylinder (99.9% purity by GC) was acquired from Sigma Aldrich – Merck.

2.2. Installation

2.2.1. Experimental set-up

The scheme of the experimental set-up is depicted in Figure 2.1.

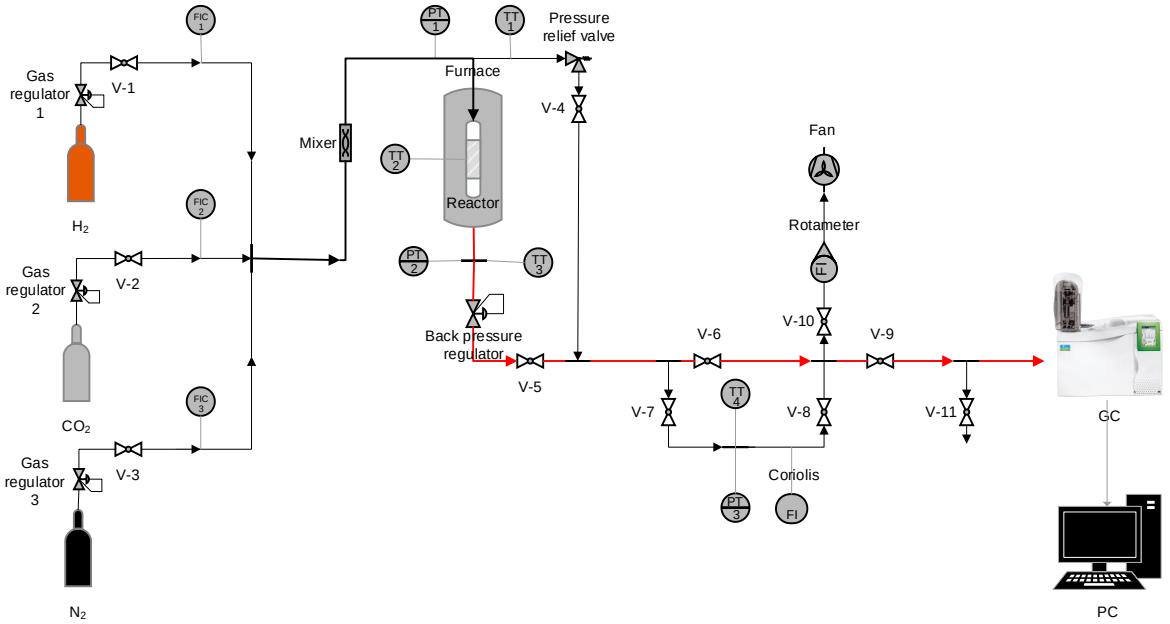

Figure 2.1 Schematic representation of the experimental setup for DME and methanol synthesis from CO_2 hydrogenation over CZA+HZSM-5 and CZA alone.

Gases were regulated with Brooks Instruments mass flowmeters/mass flow controllers before passing through a gas mixer and feeding the reactor. The mass flow controllers used for CO_2 and H_2 flow regulations worked in a range of $0-8\ g.h^{-1}$ and $0-2\ g.h^{-1}$, respectively. The N_2 gas, flowed through a thermal mass flow, dispensed up at $0.4\ ml.min^{-1}$. They were controlled by a Brooks microprocessor control & read out unit (Model series 0154).

The vertical fixed bed reactor was tubular, made of stainless steel with an internal diameter of 0.004 m, an outside diameter of 0.006 m and a length of 0.2 m. The reactor was placed in the core of an electrical tubular furnace including a temperature controller which guaranteed the heating of the reactor. There were three K-type thermocouples to monitor the reaction: one was located inside the furnace to check the furnace temperature, in addition to the one devoted to the PID control; the second one was in the centre of the catalyst bed to measure the reaction temperature and the third thermocouple was located at the reactor outlet. Thanks to the backpressure regulator at the reactor outlet, the reactor could be easily operated up to 36 bar

(the maximum operating pressure of the regulator is 150 bar). A safety relief valve was fitted upstream of the reactor to prevent an overpressure event. Similarly, pressure sensors were located at the inlet and outlet of the reactor. These were connected to a recorder/controller. From the reactor output to the entry of the Gas Chromatography (GC), a heating cord with a fixed temperature of 363.15 K was installed to prevent condensation.

2.2.2. Analytic device

Gas composition of the products was analysed on-line by means of a PerkinElmer Clarus 590 GC equipped with a flame ionization detector (FID) and a thermal conductivity detector (TCD). It has three columns: two Hayesep Q 100/120 (1.0 m x 1.00 mm μPkd), aimed at the TCD and a Molesieve 5A 80/100 (2.0 m x 1.00 mm μPkd), for ignition. The hydrogen for flame ignition was provided by a hydrogen generator PGH2-100 plus which was periodically filled, as required, with ultra-pure water. Argon was the carrier gas used. The software TotalChrom Workstation from PerkinElmer recorded the data to be analysed. Once a week, at the end of the experiments, a column regeneration program was run.

2.3. Procedure for one experiment

2.3.1. Reactor preparation

A mass of 0.4 g of CZA catalyst was used in methanol synthesis experiments. Concerning the DME synthesis, 0.4 g of CZA (-C or -D) and 0.4 g of zeolite (either HY or HZSM-5), were physically mixed for the experiments, having a total mass of 0.8 g. Firstly, glass wool was added to the reactor, followed by the catalyst and finally, another amount of glass wool was added. This was done to ensure that the catalyst remained in the centre of the reactor. The amount of glass wool inserted depended on the volume of catalyst in the reactor, due to the difference in catalyst mass for methanol and DME synthesis.

2.3.2. Leak test

With the aim of testing the catalyst, it was necessary to verify that there were no leaks between the reactor fittings and the installation.

The reactor was connected to the fittings on top of the furnace; however, the third part (see Figure 2.2) was not connected to the installation, but a fitting was screwed to this part to perform the leak test on the reactor only. Then, the pressure was gradually increased with hydrogen, by 5 bar at a time, until it reached 36 bar, thanks to the backpressure regulator at the reactor outlet. At this point, the hydrogen flow rate was stopped and the ball valves were closed to ensure gas stagnation in both the pipeline and reactor. Using a portable gas leak detector (Restek, serial number 118142), the fittings were inspected, and when no leaks were found, the reactor was screwed in as for experiments. Nonetheless, a final verification was required. This time, the top and bottom fittings were inspected, following the same steps to increase the pressure. However, in this case, the backpressure regulator was also closed to maintain the pressure at 36 bars.

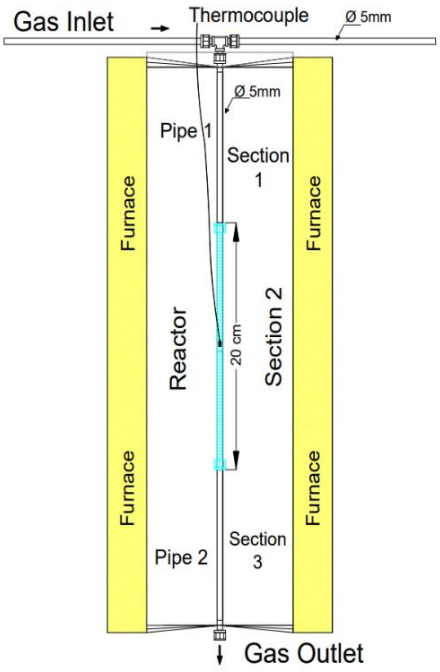

Figure 2.2 Schematic representation of the fixed bed reactor.

2.3.3. Gas chromatography calibration

Three GC calibrations were performed before experiments, one per day, taking into consideration that there were three standard cylinders for calibration. At this stage, the feed passed directly through a bypass valve and did not enter the reactor. This was done at atmospheric pressure and room temperature.

For methanol and DME calibrations, GC injections were conducted every 35 minutes because of the specifications in the method programming: an injection time of 1 minute at 50 °C, an oven hold for 18.5 minutes at 50 °C followed by a ramp of 28 °C/min to 120 °C, and a final oven hold for 9 minutes, so the total run time was 31 minutes. At the end, 5 minutes of cooling and stabilization were needed prior to the subsequent injection.

As for CO_2, CO, H_2 and N_2 analyses, the method was shortened since the retention time of CO, which was the longest of all compounds, was 10.6 minutes. Then, the oven temperature was programmed at 50 °C and maintained for 16 min. H_2 and N_2 were analysed in the GC-TCD detector and CO, CO_2, CH_3OH and CH_3OCH_3 in the GC-FID detector. An overview of the chromatograms for both detectors, TCD and FID, are given in Figure 2.3 and Figure 2.4, respectively.

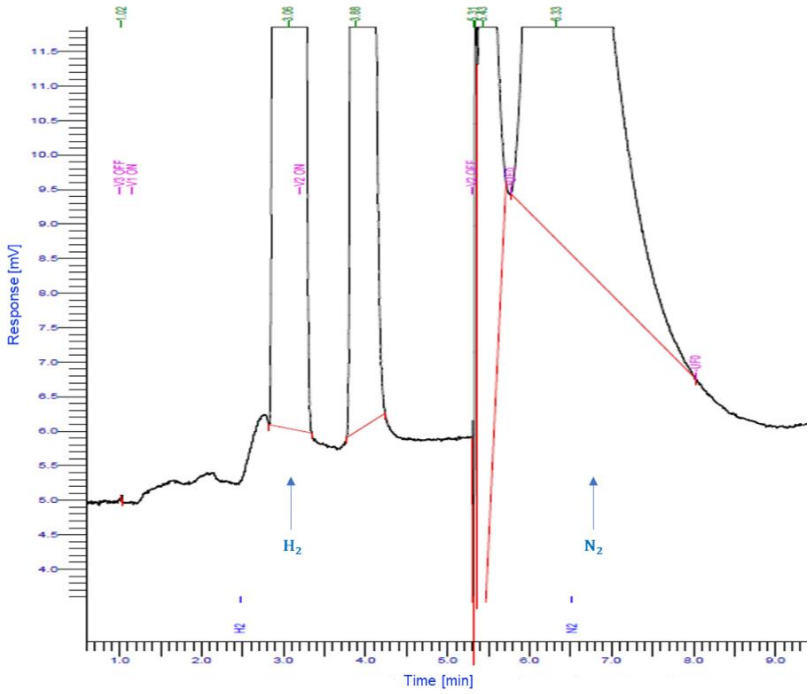

Figure 2.3 Chromatogram from GC-TCD for H_2 and N_2 analyses.

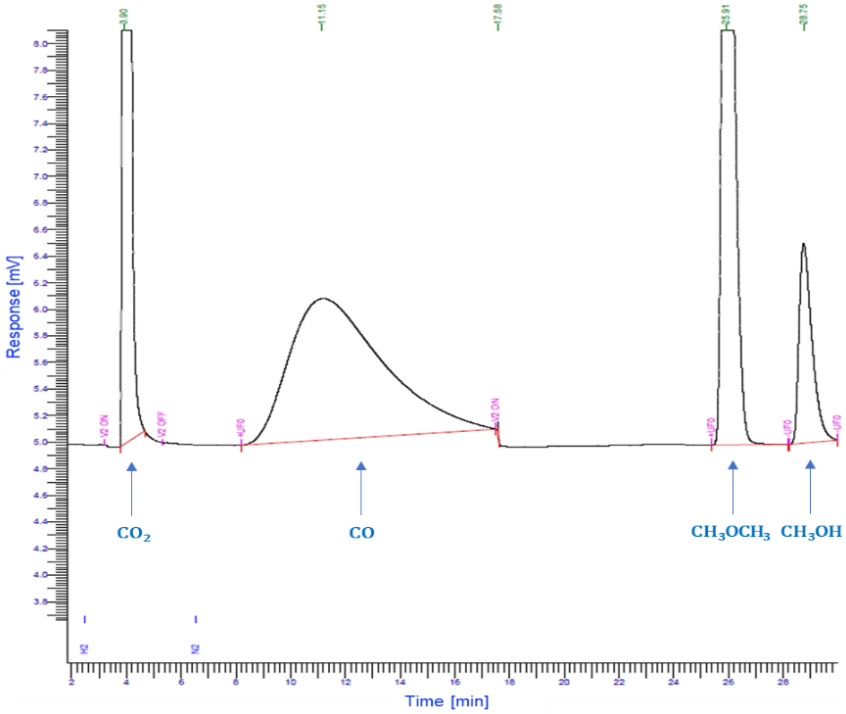

Figure 2.4 Chromatogram from GC-FID for CO, CO_2, CH_3OH and CH_3OCH_3 analyses.

At least two measurements per flow rate were performed for repeatability. In the default report of the runs, the peak area ($\mu V \cdot s$) of species was copied, bearing in mind their retention time.

The linear regression was plotted with the molar fraction of the components as a function of peak area.

2.3.3.1. CO_2, CO, H_2, N_2 calibrations

Several measurements were carried out, at least three per set flow rate, with the gas from the standard cylinder but also with its dilutions in N_2 or H_2 and in a mixture of the two (see Table 2.3).

Table 2.3 CO_2, CO, H_2, N_2 calibration parameters.

Component	**Flow rate** ($g.h^{-1}$)							
Standard	5	5	5	5	5	5	0	0
H_2	0	0.15	0.15	0.15	0.15	0.15	0.78	0.80
N_2	0	0	0.72	10.73	14.31	28.62	1.27	1.14

2.3.3.2. CH_3OH calibration

This calibration was carried out by using the standard gas bottle purchased and described in section 2.1 or by diluting this standard gas with N_2 from a connected N_2 gas cylinder. The gases were mixed at varying N_2 flow rates in the gas mixer before entering the reactor (as shown in Figure 2.1). In these cases, the methanol mass flow rates were varied from $1.2 - 4.5\ g.h^{-1}$ to obtain a dilution between 0.2-1.5%.

2.3.3.3. CH_3OCH_3 calibration

All measurements were done with mixtures of N_2 and DME standard gas cylinder purchased and described in 2.1. The N_2 flow rate was fixed ($28.16\ g.h^{-1}$) and the DME flow rate was varied. For these calibrations, the Brooks mass flowmeter was not used, as it was unsuitable. Instead, the Coriolis mass flowmeter was used to connect the standard cylinder to prevent joint damage (material-gas compatibility). A dilution of DME was sought between 0.2-6.0%.

2.3.4. Catalyst reduction

The last step before performing catalytic experiments was the reduction of the catalyst. The reduction was guaranteed by passing a mixture of 95% N_2 and 5% H_2, i.e. a flow rate of $22.03\ g.h^{-1}$ N_2 and $0.09\ g.h^{-1}$ H_2, at 673.15 K and atmospheric pressure for about 90 minutes. The completion of this step was determined by the stop of H_2 consumption and the

repeatability of the gas analyses reached when the percentages of the components in the chromatogram was the same as at the beginning, i.e. 95% N_2 and 5% H_2, for at least three successive injections. Subsequently, the H_2 flow rate was stopped, the furnace switched off to cool the catalyst and the system purged with N_2 for about 5 minutes.

As for gas analysis, the GC oven was set to 50 °C for 8 minutes, since H_2 and N_2 retention times are 3.0 and 6.4 minutes, respectively.

2.3.5. Operating conditions

A series of laboratory experiments were carried out to screen the catalysts. CO_2 flow rate was set to 3.30 $g.h^{-1}$ (22.5%), H_2 flow rate to 0.39 $g.h^{-1}$ (67.5%) and N_2 flow rate to 0.70 $g.h^{-1}$ (10%). N_2 was added as inert gas to monitor the molar fractions of reagents. In order to compare the performance of the CZA catalysts, commercial and developed, for methanol production and of the mixtures of one CZA and one zeolite for DME synthesis, these flow rates were kept constant, independently on the catalyst natures, the target products and catalyst amounts (Table 2.4). The operating temperature range was 453-623 K. The set pressure was 36 bars.

Table 2.4 Main target product depending on catalysts.

Catalyst	**Product**
CZA+HZSM-5	DME
CZA+HY	DME
CZA	MeOH

For the kinetic study, a plan of experiments was done with the commercial CZA catalyst (CZA-C), which is the best performing catalyst, and the mixture of CZA-C and HZSM-5 zeolite. The feed molar fractions of the components were varied for three tested pressures (26, 31 & 36 bar) (see Table 2.5). It was therefore necessary to change the partial pressures of the reactants and their molar ratios, followed by the total pressure variation. The same temperature range (453-623 K) was kept.

Table 2.5 Plan of experiments: operating conditions.

H_2/CO_2	H_2 $(g.h^{-1})$	CO_2 $(g.h^{-1})$	N_2 $(g.h^{-1})$	P (bar)	GHSV inlet $(L.g_{cat}^{-1}.h^{-1})$
1	0.13	3.10	0.28	36	3.5
1	0.13	3.10	0.21	26	3.5
3	0.39	3.30	0.70	36	7.0
3	0.39	3.30	0.70	31	7.0

3	0.39	3.00	0.70	26	7.0
3	0.13	1.00	5.48	26	7.0
3	0.18	1.50	0.21	36	3.5
9	0.78	2.08	1.05	36	12.0
9	0.44	1.26	0.49	26	7.0

2.3.6. Experimental procedure

The experiments were carried out as follows:

1. The maximum flow rate was set on the N_2 mass flow controller at 5 bar to gradually increase the pressure as planned. Subsequently, the pressure was increased in the other two cylinders, CO_2 and H_2, to have a pressure equal to the final pressure of the nitrogen cylinder.
2. The reagent flow rates were set as desired on the Brooks microprocessor control & read out unit.
3. When the flow rate was confirmed to be stable at Coriolis, a series of GC analyses were performed. These analyses were performed to verify the gas composition and, hence, the material balance of the species. Up to this step, Coriolis flowmeter was used to measure the total mass flow.
4. As soon as repeatability was confirmed, the Coriolis valves were closed to avoid condensation. To begin the reaction stage, the furnace was turned on at 473 K for at least 30 minutes for stabilization. The consistency of temperature was verified in LabVIEW software.
5. During the reaction stage, for the first temperature point, the furnace usually remained at the same temperature for around 70 minutes and two outlet gas analyses were performed. The average result was used as a point for each fixed temperature. For the following temperature points, the temperature was then increased by steps of 25 K and a stabilisation of 35 minutes was respected before GC analysis. Two outlet gas analyses were performed before a new increment of temperature was done.

This protocol was followed for all experiments. This is explained in section 2.3.5. The pressure and flow rates remained the same throughout an experiment, only the temperature varied.

2.4. Component mass balance

The Figure 2.5 represents the path followed by the gas, as in the laboratory set-up.

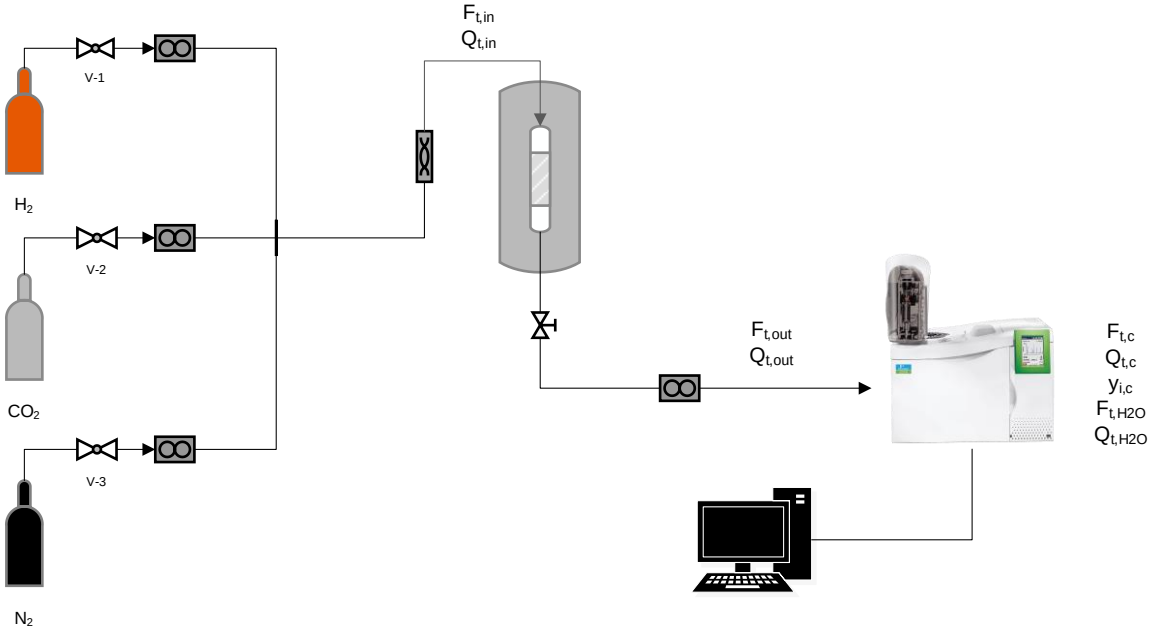

Figure 2.5 Simplified scheme of the experimental setup of molar and mass flow rates. F, Q and y are respectively molar flow rate, mass flow rate and molar fraction. The indexes t, i, H_2O, in and out are respectively total, specie i, water, input and ouput.

The input molar flow rate is calculated based on the input mass flow rate, the molar fractions of the input components read from the GC results and their respective molar masses (Eq. (2.1)).

$$F_{t,\,in} = \frac{\dot{m}_{t,in}}{M_{t,\,in}} = \frac{\dot{m}_{t,in}}{y_{N_2,\,in} \cdot M_{N_2} + y_{CO_2,\,in} \cdot M_{CO_2} + y_{H_2,\,in} \cdot M_{H_2}} \tag{2.1}$$

$M_{t,\,in}$ is the mean molar mass weighted by the molar fractions, y_i, and $\dot{m}_{t,in}$ is the total input mass flow rate read on the Coriolis mass flow rate.

The component mass balance is done taking into consideration the output molar fractions read in the chromatogram. Since N_2 is a vector gas, its molar flow rates do not vary between the reactor input and output and in the GC. They are used to calculate the total output gas flow rate ($F_{t,\,out}$) from the chromatogram analysis as follows:

$$F_{N_2,\,in} = F_{N_2,\,out} = F_{N_2,\,c} \tag{2.2}$$

$$y_{N_2,in} \cdot F_{t,\,in} = y_{N_2,c} \cdot F_{t,\,c} = y_{N_2,out} \cdot F_{t,\,out} \tag{2.3}$$

Thus,

$$F_{t,\,out} = \frac{y_{N_2,in}}{y_{N_2,out}} F_{t,\,in} \tag{2.4}$$

$$F_{t,\,c} = \frac{y_{N_2,in}}{y_{N_2,c}} F_{t,\,in} \tag{2.5}$$

For each specie, except for water, the molar flow rates do not vary between the reactor output and the GC input.

$$F_{i,\,out} = F_{t,\,out} \cdot y_{i,\,out} = F_{t,\,c} \cdot y_{i,\,c} = F_{i,\,c} \tag{2.6}$$

$y_{N_2,in}, y_{N_2,out}$ and $y_{N_2,c}$ are the nitrogen molar fraction of input, output, and chromatogram, respectively. $F_{t,\,in}$ $(mol.h^{-1})$ is the total input molar flow rate, $F_{i,\,out}$ $(mol.h^{-1})$ is the output molar flow rate of each component i. $y_{i,c}$ and $y_{i,out}$ are the molar fractions of components from the chromatogram and from the output, respectively.

The total output molar flow rate $(F_{t,\,out})$ is calculated based on the carbon balance. The molar flow rate of water (F_{t,H_2O}) is deduced from the stoichiometry of the reactions. Eq. (2.5) gives $F_{t,c}$ and Eq. (2.8) allows the calculation of $F_{t,\,out}$.

$$F_{t,H_2O} = F_{CH_3OH,\,c} + F_{CO,\,c} + 3 \cdot F_{CH_3OCH_3,\,c} \tag{2.7}$$

$$F_{t,\,out} = F_{t,\,c} + F_{H_2O,\,out} = F_{t,\,c} + F_{CH_3OH,\,c} + F_{CO,\,c} + 3 \cdot F_{CH_3OCH_3,\,c} \tag{2.8}$$

Substituting (2.7) on (2.8),

$$y_{i,\,out} = \frac{F_{j,\,out}}{F_{t,\,out}} = \frac{y_{i,c} \cdot F_{t,\,c}}{F_{t,\,c} + F_{H_2O,\,out}} = \frac{y_{i,c} \cdot F_{t,\,c}}{\left(1 + y_{CH_3OH,\,c} + y_{CO,\,c} + 3 \cdot y_{CH_3OCH_3,c}\right) \cdot F_{t,\,c}} \tag{2.9}$$

$$y_{i,\,out} = \frac{y_{i,c}}{1 + y_{CH_3OH,\,c} + y_{CO,\,c} + 3 \cdot y_{CH_3OCH_3,\,c}} \tag{2.10}$$

The gas hourly space velocity (GHSV) is calculated according to:

$$GHSV = \frac{F_{t,\,in} \cdot T \cdot R}{P \cdot m_{cat}} \tag{2.11}$$

R is the gas ideal constant, T is the room temperature, P is the room pressure and m_{cat} the mass of the catalyst.

For methanol synthesis, the carbon dioxide conversion $X_{CO_2,\,MeOH}$ is determined based on converted carbon products, knowing that the carbon dioxide conversions X_{CO_2} for all the syntheses are defined by:

$$X_{CO_2,\,MeOH} = \frac{y_{CH_3OH,\,c} + y_{CO,c}}{y_{CO_2,\,c} + y_{CH_3OH,\,c} + y_{CO,\,c}} \cdot 100 \tag{2.12}$$

CO and MeOH yields are computed as:

$$Y_{MeOH,MeOH} = \frac{y_{CH_3OH,c}}{y_{CO_2,c} + y_{CH_3OH,c} + y_{CO,\,c}} \cdot 100 \tag{2.13}$$

$$Y_{CO,MeOH} = \frac{y_{CO,c}}{y_{CO_2,c} + y_{CH_3OH,c} + y_{CO,\,c}} \cdot 100 \tag{2.14}$$

Likewise, for DME synthesis, the CO_2 conversion (Eq. (2.15)) and yield of CO, MeOH and DME are defined based on the ratio of molar fraction of component and the sum of carbon products (Eq. (2.16)-(2.18)) at the GC stream.

$$X_{CO_2,DME} = \frac{y_{CH_3OH,\,c} + y_{CO,\,c} + 2 \cdot y_{CH_3OCH_3,c}}{y_{CO_2,c} + y_{CH_3OH,c} + y_{CO,\,c} + 2 \cdot y_{CH_3OCH_3,c}} \cdot 100 \tag{2.15}$$

$$Y_{MeOH,DME} = \frac{y_{CH_3OH,c}}{y_{CO_2,c} + y_{CH_3OH,c} + y_{CO,c} + 2 \cdot y_{CH_3OCH_3,c}} \cdot 100 \tag{2.16}$$

$$Y_{CO,DME} = \frac{y_{CO,c}}{y_{CO_2,c} + y_{CH_3OH,c} + y_{CO,\,c} + 2 \cdot y_{CH_3OCH_3,c}} \cdot 100 \tag{2.17}$$

$$Y_{DME,DME} = \frac{2 \cdot y_{CH_3OCH_3,c}}{y_{CO_2,c} + y_{CH_3OH,c} + y_{CO,\,c} + 2 \cdot y_{CH_3OCH_3,c}} \cdot 100 \tag{2.18}$$

2.5. Catalyst screening

A series of experiments was performed to screen the catalysts to find the best catalyst for the CO_2 hydrogenation and the best catalytic mixture for the DME synthesis. Firstly, for CO_2 hydrogenation to methanol, two different catalysts (CZA-C and CZA-D) were tested and then, for DME synthesis, four mixtures were tested: 0.4 g of a zeolite (HY or HZSM-5) plus 0.4 g of a CZA catalyst (CZA-C or CZA-D). An assessment of CO_2 conversion, DME, methanol and CO yields is done in this section using the mentioned catalysts. The succession of catalyst tests is displayed in Table 2.6. For each experimental point, the total number of moles of CO2 converted were calculated by integrating over the whole experiment duration, from the early beginning of the catalyst life, the CO_2 converted flow rate calculated from X_{CO_2}. This parameter will be useful later for evaluating the "working time" of the catalyst.

Table 2.6 Chronology of catalyst screening.

Exp. series number	**Catalyst**	**H_2/CO_2**	**P** (bar)	**GHSV** $(L.g_{cat}^{-1}.h^{-1})$	**n_{CO_2} (moles) converted**
1	CZA-D	3	36	15.7	$1.30 \cdot 10^{-2}$
2	CZA-D + HY	3	36	7.6	$4.23 \cdot 10^{-2}$
3	CZA-D + HZSM5	3	36	7.8	$2.87 \cdot 10^{-2}$
4	CZA-C	3	36	15.3	$2.55 \cdot 10^{-2}$
5	CZA-C+HZSM5	3	36	7.3	$6.17 \cdot 10^{-2}$
6	CZA-C+HY	3	36	7.3	$6.05 \cdot 10^{-2}$

2.5.1. Performance of CZA on methanol synthesis

The obtained results of CO2 conversion (X_{CO_2}) and product yield (Y_i) over CZA-D and CZA-C for methanol synthesis are shown in Figure 2.6. The reaction temperatures evaluated for these experiments were in the range of 453-593 K at 36 bars of pressure with a molar ratio of $H_2/CO_2/N_2$= 67.5/22.5/10.

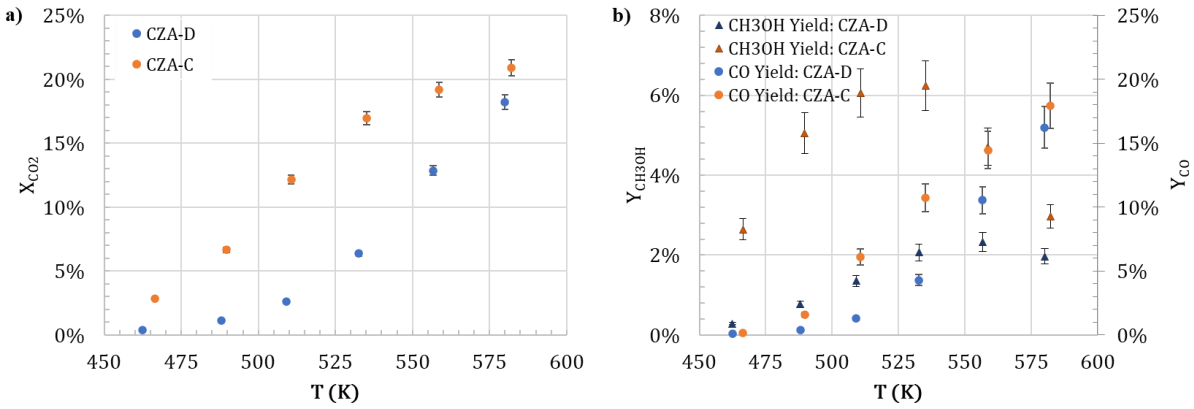

Figure 2.6 a) CO_2 conversion and b) methanol and CO yields for CZA-C and CZA-D. Operating conditions: P=36 bars, $H_2/CO_2/N_2$= 67.5/22.5/10, GHSV= 15.3-15.7 L. g_{cat}^{-1}. h^{-1}.

A marked difference can be noticed between both catalysts, especially at temperatures between 498-543 K. The commercial catalyst exhibits a superior conversion. As well, it can be observed that methanol yields are approximately three or more times greater than those for the developed catalyst. For higher temperatures (>553 K), the difference starts to decrease due to the thermodynamic equilibrium that tends to be reached. As far as CO yield is concerned, no significant differences are observed between the catalysts, although the developed catalyst shows lower results.

As is well known, high copper content improves CO_2 conversion. Though, zinc oxide, as a main promoter for enhancement of catalyst activity, has a direct influence on the performance of the catalyst. Catalyst activity and stability are boosted by Al_2O_3. Among its characteristics, CZA-C contains magnesium, which improves CO_2 conversion as well as the stability and activity of the catalyst. In Chapter 1, this topic was discussed (refer to page 39).

In conclusion, the high performance of CZA-C may be ascribed to its components high loading and its preparation method.

2.5.2. Performance of catalyst mixtures, CZA-zeolite

Further experiments were performed with both CZA catalysts (commercial and developed), following the experimental protocol as explained in section 2.3.6. But, in these cases, the catalyst tests were done with a powder mixture ($d_p = 90 - 200\,\mu m$) of CZA and zeolite (HZSM-5 or HY). These experiments were carried out at a temperature range of 453-613 K under 36 bars of pressure with a feed molar ratio of $H_2/CO_2/N_2$=67.5/22.5/10.

a) Tests on CZA + HZSM5 mixtures

On Figure 2.7, the catalytic tests show significantly higher CO_2 conversions for CZA-C+HZSM-5 than for CZA-D+HZSM-5 (38.6% respect to 22%). The maximum conversions are 38.6% at 562 K for CZA-C+HZSM-5 and 24.6% at 604 K for CZA-D+HZSM-5 and even the DME yield for CZA-C+HZSM-5 is more than triple that of CZA-D+HZSM-5 (Figure 2.8a). CO_2 conversion increase is evident with the temperature increase, as expected. The typical volcano-shapes, observed for the CO_2 conversions and DME yields, are due to thermodynamic reaction equilibrium limitation.

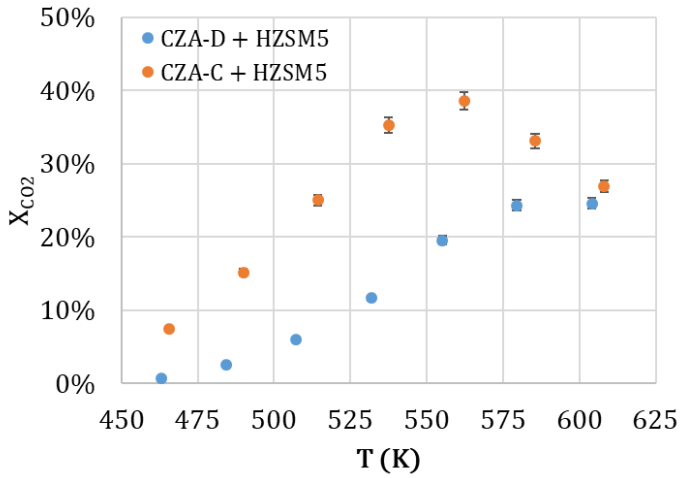

Figure 2.7 CO_2 conversion as a function of temperature for the mixture of CZA and HZSM5. Operating conditions: P=36 bars, $H_2/CO_2/N_2$= 67.5/22.5/10, GHSV= 7.3-7.8 L. g_{cat}^{-1}. h^{-1}.

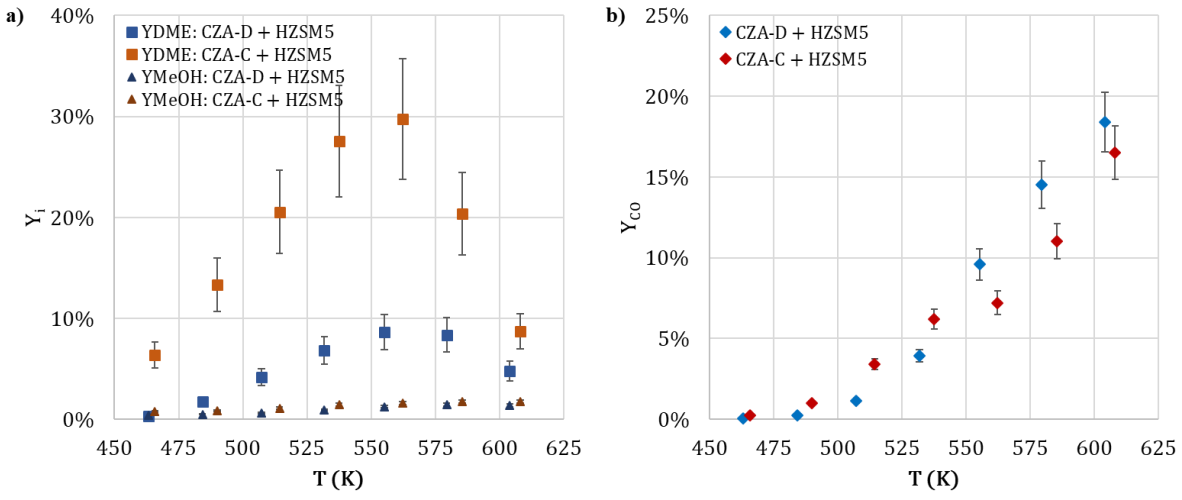

Figure 2.8 a) DME and methanol yields, and b) CO yield for CZA-D and CZA-C mixed with zeolite HZSM5. Operating conditions: P=36 bars, $H_2/CO_2/N_2$= 67.5/22.5/10, GHSV= 7.3-7.8 L. g_{cat}^{-1}. h^{-1}.

The CO yields are fairly similar for both catalysts (Figure 2.8b). The CO yield curve for CZA-D+HZSM-5 catalyst shows a monotone behaviour, whereas a monotony break in the curve is noticed for the commercial catalyst at about 553K, mismatching the common shape. The same uncommon behaviour in the CO yield was observed in the other experiences with CZA-C at temperatures above 553 K.

Ren et al., 2019 [3] illustrates analogous lag from about 513 K for alike catalysts (CZA) and operating conditions ($P = 28\,bar,\ T = 200 - 260\,°C,\ GHSV = 3050.h^{-1}$), but for methanol synthesis, without zeolite. Three of the four CZA catalysts studied by the authors showed a shift in the CO yield curve. The difference in catalysts evaluated was associated with the catalyst surface area (BET) and precursor concentrations. However, as the temperatures in their experiments did not exceed 280 °C for DME synthesis, it was not possible to determine whether there was an offset in CO yield.

On the other hand, Santiago et al., 2022 [4] synthesized and analysed different CZA catalysts. They determined that after reaction tests there was a modification in catalyst composition. A reduction of copper and zinc percentages was identified. Likewise, Kamsuwan et al., 2021 [5] reported a decrease of weight percentages of catalyst elements after catalysts test.

By seeing Figure 2.8b, it seems like there were two CO production reactions: one favoured at $T < 550\,K$ with the maximum yield reached around 520 K, and the other which starts exponentially around $520\,K$.

From these outcomes, it is suggested that the lag in CO yield could be related to a structure change of catalyst.

b) Tests on CZA + HY mixtures

Figure 2.9 displays the CO_2 conversions of CZA-D+HY and CZA-C+HY as function of temperature. Even though the CO_2 conversion curves are closer to each other in this case, CZA-C+HY still achieves better performance than CZA-D+HY. The highest CO_2 conversion obtained, 38.3%, at 560.55 K was also with the commercial catalyst CZA-C.

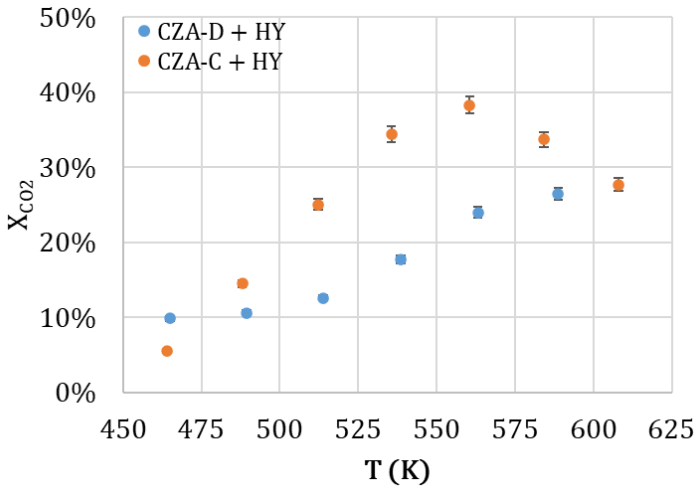

Figure 2.9 CO_2 conversion as a function of temperature for the mixture of CZA and HY. Operating conditions: P=36 bars, $H_2/CO_2/N_2$= 67.5/22.5/10, GHSV= 7.3-7.6 L. $g_{cat}^{-1}.h^{-1}$.

For the CZA-D+HY catalyst, the DME yield is almost the same for the different temperatures (Figure 2.10a). A greater activity of CZA-C+HY is noticeable, as evidenced by its DME yield. In Figure 2.10b, small differences can be observed in the CO yield of these catalysts. The closeness of the CO yields at the first four points, and the break in slope for CZA-C+HY at subsequent temperatures, remains the same as that observed with CZA-C+HZSM-5.

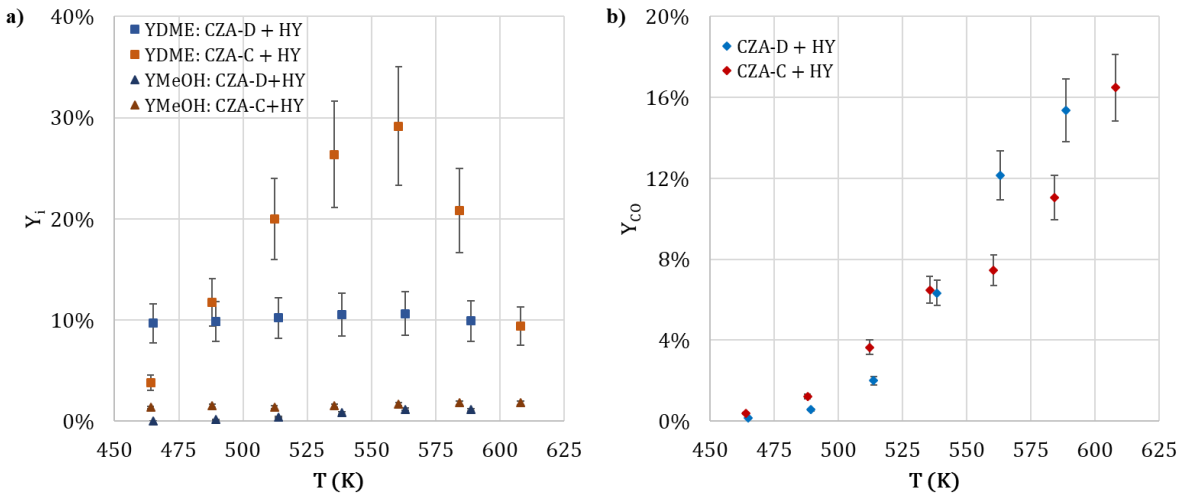

Figure 2.10 a) DME and methanol, and b) CO yield of CZA-D and CZA-C mixed with zeolite HY. Operating conditions: P=36 bars, $H_2/CO_2/N_2$= 67.5/22.5/10, GHSV= 7.3-7.6 L. $g_{cat}^{-1}.h^{-1}$.

c) Comparison of CZA-C+HY and CZA-C+HZSM5 mixtures

The comparison of the performances of the CZA-C+HY and CZA-C+HZSM5 catalysts shows that their CO_2 conversions are identical, only a slight difference can be perceived at ~463 K

(Figure 2.11). With the HZSM-5 zeolite, the maximum CO_2 conversion of 38.6% was achieved at ~563 K like the 38.3% obtained with the HY zeolite.

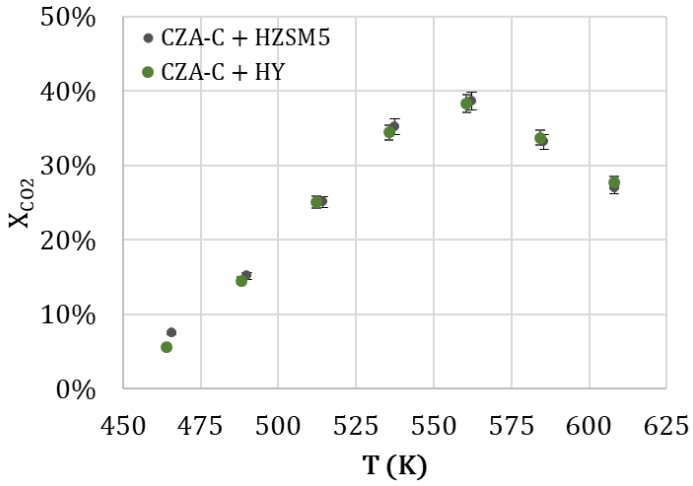

Figure 2.11 Comparison between the CO_2 conversion for CZA-C + HZSM5 and CZA-C + HY. Operating conditions: P=36 bars, $H_2/CO_2/N_2$= 67.5/22.5/10, GHSV= 7.3 $L.g_{cat}^{-1}.h^{-1}$.

An analogous performance can be observed for both the zeolites by assessing the yields of the products (Figure 2.12).

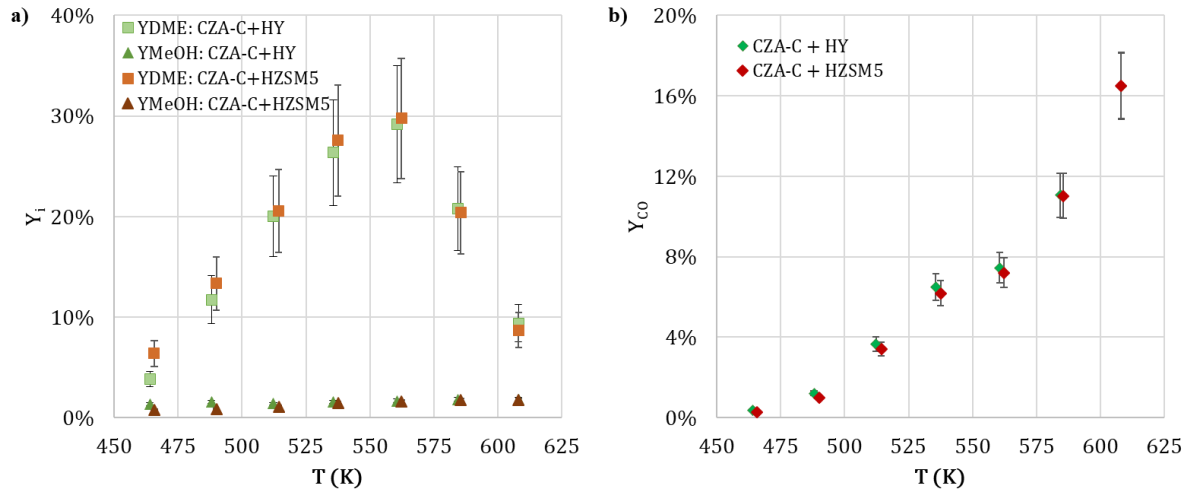

Figure 2.12 Comparison between the a) DME and methanol, and b) CO yields of the CZA-C + HZSM5 and of the CZA-C + HY. Operating conditions: P=36 bars, $H_2/CO_2/N_2$= 67.5/22.5/10, GHSV= 7.3 $L.g_{cat}^{-1}.h^{-1}$.

A slight difference can be detected in DME yield (Figure 2.12a). At ~463 K, the DME yields for the two catalytic mixtures differ from those obtained at higher temperatures in the sense that the error bars do not coincide. Regarding the maximum DME yields, CZA-C+HZSM-5 and CZA-C+HY were extremely close at 29.8% and 29.2%, respectively. This was achieved at ~563

K, which was the temperature at which the conversion of CO_2 is the greatest. At this point, the CO yields for CZA-C+HZSM-5 and CZA-C+HY were below 8%, 7.2%, and 7.5%, respectively (Figure 2.12b). After 563 K, a more pronounced increase in the percentage of CO yield starts to be seen, about 4% more, being double at 608.15 K. This proves that at high temperatures the RWGS reaction is favoured. Besides, there is a decline in CO_2 conversion and in the yield of DME, the desired product. Methanol production is almost the same at all the temperatures. The variations are so small, about 0.2%, that they are barely noticeable.

To understand these results, the influence of the Si/Al mole ratio has been investigated, considering the composition of zeolites evaluated. The Si/Al mole ratios of HY and HZSM-5 are 2.5 and 38, respectively. Catuzo et al., 2021 [6] tested zeolites with various Si/Al mole ratios to verify their influence on the adsorption of water in the ketalization reaction of glycerol with acetone. They identified a relationship between the Si/Al ratio and the water adsorption. As the Si/Al mole ratio increases, the hydrophobicity of the zeolite is intensified. Thus, there is less water adsorption at a higher Si/Al ratio [6]–[8]. Notwithstanding, the evaluation results of Halasz & Agarwal of two zeolites, H-Y (Si/Al ~40) and ZSM-5 (Si/Al ~4330), indicate that despite the remarkable difference in the Si/Al ratio, they were able to obtain close water adsorption [9]. Only the post-treatment conditions and their synthesis are referred to as modifications. Water adsorption differed even when studying two H-Y, CBV 901 and CBV 780, with an equal Si/Al ratio. This was associated with mesoporous defects on the surface. Besides, Bowen et al., 2004 [8] said that the hydrophilicity decreases as the pore diameter increases.

Furthermore, the Brønsted acidity needs to be studied [7], [9]–[11]. Azzolina Jury et al., 2013 [2] explains that a lower Si/Al ratio implies an increase quantity of acid sites. Equally, Bonura et al., 2018 [12] while elucidating the effects of acidity capacity of ferrierite-type zeolite identified that acidity diminished with the increase of Si/Al ratio. As well, they explained that the acid capacity is similarly dependent on the particle size of zeolite, being higher when the grains are smaller. In conclusion, they correlated their observed differences in CO_2 conversion to surface Brønsted acidity density. The lower the Si/Al ratio is, the higher the acidity and the water adsorption are, leading to a lower CO_2 conversion and implying the CO_2 conversion is more driven by the water adsorption than by the acidity.

As a result of the data available on the zeolites screened in this thesis, the explanation for the results cannot be attributed to the Si/Al ratio only. Other parameters, such as the amount of adsorbed water, should also be analysed to understand the vicinity of the results. However, estimating water adsorption on the zeolites during the experiments and the "lifetime" of the catalyst is impossible, as the water produced by the reactions must be balanced with the reactor outlet water, which is unrealistic in the absence of water analysis and a perfectly heated set-up. As the HZSM-5 zeolite had a higher Si/Al and is therefore less prone to water

adsorption, it was decided to carry out the kinetic study with the commercial CZA-C and the HZSM-5.

2.6. Catalytic tests for kinetics

2.6.1. Thermodynamics of reaction

To determine the kinetics of direct DME synthesis, it is first necessary to study the thermodynamics of reactions and calculate the equilibrium constants for all the reactions. Four reactions were considered here as part of the process:

$$CO_2 + 3H_2 \rightleftharpoons CH_3OH + H_2O \qquad \Delta H_{298K} = -49.25\ kJ.mol^{-1} \tag{2.19}$$

$$CO_2 + H_2 \rightleftharpoons CO + H_2O \qquad \Delta H_{298K} = 41.16\ kJ.mol^{-1} \tag{2.20}$$

$$CO + 2H_2 \rightleftharpoons CH_3OH \qquad \Delta H_{298K} = -90.41\ kJ.mol^{-1} \tag{2.21}$$

$$2CH_3OH \rightleftharpoons CH_3OCH_3 + H_2O \qquad \Delta H_{298K} = -24.04\ kJ.mol^{-1} \tag{2.22}$$

Two methods were used to calculate the thermodynamic equilibria of the reactions:

1. Using the equilibrium reactor (REQUIL) on Aspen Plus V12.
2. Working with the Gibbs reactor (RGIBBS) on Aspen Plus V12.

Table 2.7 Enthalpies and Gibbs energies of formation at 298.15 K and 1 bar.

Formula	H_2	N_2	CO_2	CH_3OH	CO	CH_3OCH_3	H_2O
$\Delta_f H_i^o\ (kJ.mol^{-1})$	0	0	−393.51	−200.94	−110.53	−184.10	−241.82
$\Delta_f G_i^o\ (kJ.mol^{-1})$	0	0	−394.37	−162.32	−137.15	−112.80	−228.57

Using the standard Gibbs energy change of reaction ($\Delta_r G°$), it was possible to accurately determine the equilibrium composition of the reaction system. The data of the standard heat change of reaction ($\Delta_r H°$), as well as those of the standard Gibbs energy change of reaction ($\Delta_r G°$), were retrieved from Aspen Plus V12 (Table 2.7). The equilibrium constant of the chemical reaction j (K_j) was calculated with the standard heat change of reaction, as function of temperature and using the chemical reaction equilibrium constants (K_{j0}) at 298.15 K (= T_0) (Van't Hoff relation):

$$K_j = K_{j0}\ exp\left[\frac{\Delta_r H_j^o}{R}\left(\frac{1}{T_0} - \frac{1}{T}\right)\right] \tag{2.23}$$

knowing that the standard heat change of reaction j is:

$$\Delta_r H_j^o = \sum_i \nu_i \Delta_f H_i^o \tag{2.24}$$

and the standard Gibbs energy change of reaction *j* is:

$$\Delta_r G_j^o = \sum_i \nu_i \Delta_f G_i^o \tag{2.25}$$

and as, by definition,

$$K_{j0} = \frac{\prod_{i:products} a_i^{\nu_{ij}}}{\prod_{i:reactants} a_i^{\nu_{ij}}} \equiv exp\left(\frac{-\Delta_r G_j^o}{RT_0}\right) \tag{2.26}$$

where,

$$a_i = f_i/f_i^o = p_i/P^o \tag{2.27}$$

and

$$p_i = y_i P \tag{2.28}$$

where a_i is the activity, p_i is the partial pressure of species i in reaction j and P is the total system pressure.

REQUIL block calculates chemical and phase equilibrium constants for the stated reactions defined by the activity coefficients as a function of their fugacity (Eq. (2.26)-(2.28)). The reactions of CO_2 hydrogenation (2.19), Reverse Water Gas Shift (RWGS) (2.20), CO hydrogenation (2.21) and methanol dehydration (2.22) were considered. They were further assumed to approach the chemical equilibrium. The Soave-Redlich-Kwong (SRK) equation of state was chosen as thermodynamic model. In properties, STEAMNBS was chosen as free-water method because this steam table is recommended for use with the SRK for pure water and steam with the temperature and pressure ranges being explored in this thesis. The feed was adjusted according to the stoichiometry of the reactions, i.e., a molar fraction ratio of $H_2/CO_2/N_2 = 3/1/1$. A pressure of 36 bar was established. The range of temperature evaluated was from 423.15 – 673.15 K with an increment of 5 K. The simulations were computed under isothermal conditions. The equilibrium constants and the molar flows and fractions are taken from block and stream results.

In a similar way, RGIBBS block was also used to calculate equilibrium constants. RGIBBS computes equilibrium by means of Gibbs free energy minimisation, specifying only the implicated components, but not the reactions involved. This estimates the phase composition at equilibrium at the set pressure and temperature. Through the Model Analysis Tool in Aspen Plus, the results of component mole fractions and inlet mole flow rates were used to compute the partial pressure of components (Eq. (2.28)), CO_2 conversions, yields of DME, CH_3OH and CO (in accordance with the Eq. (2.12)-(2.14)) and finally, the equilibrium constants (according to the Eq. (2.29)-(2.32)). The properties and operating conditions were the same as for the REQUIL block.

$$K_1 = \frac{p_{CH_3OH} p_{H_2O}}{p_{CO_2} p_{H_2}^3} \tag{2.29}$$

$$K_2 = \frac{p_{CO} p_{H_2O}}{p_{CO_2} p_{H_2}} \tag{2.30}$$

$$K_3 = \frac{p_{CH_3OH}}{P_{CO} P_{H_2}^2} \tag{2.31}$$

$$K_4 = \frac{p_{CH_3OCH_3} p_{H_2O}}{p_{CH_3OH}^2} \tag{2.32}$$

For both cases, REQUIL and RGIBBS blocks, the logarithms of each equilibrium constant K versus the inverse temperature were drawn to obtain linear equations that allow easily calculating the equilibrium constants for each experiment as functions of temperature (Figure 2.13-Figure 2.14). Following these steps, similar results were obtained for REQUIL and RGIBBS blocks.

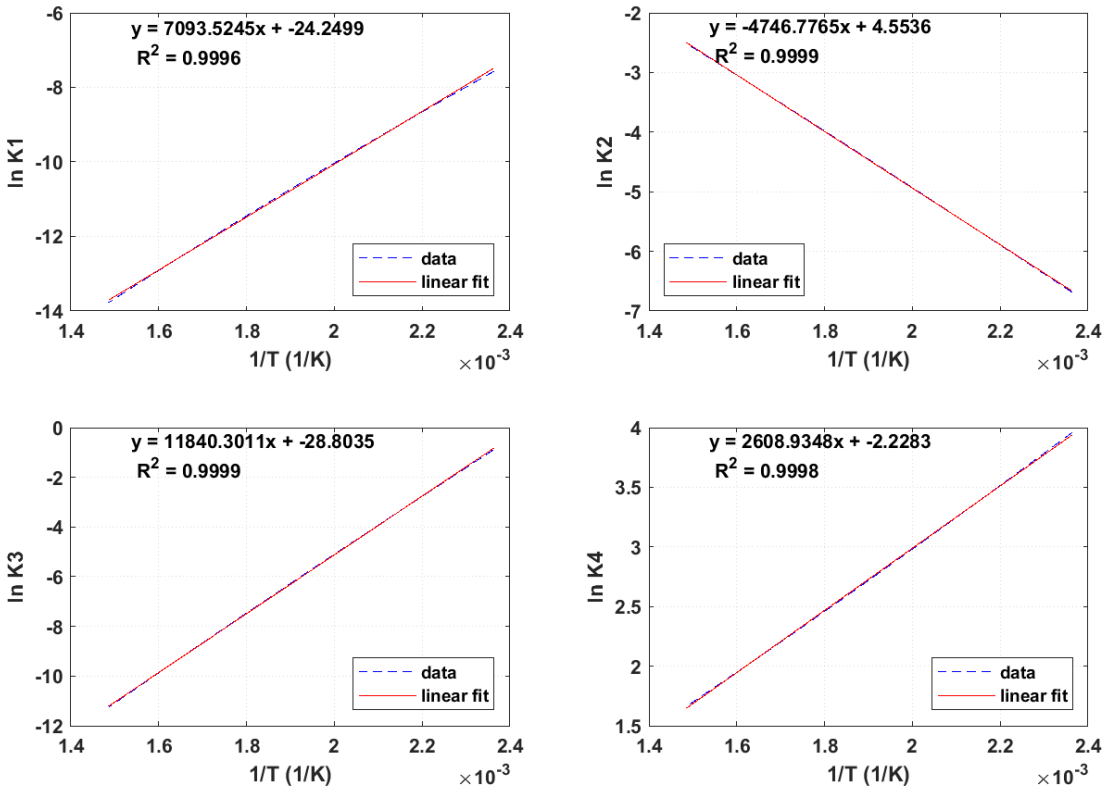

Figure 2.13 Linear equation of ln (Kj) vs 1/T obtained with REQUIL block results.

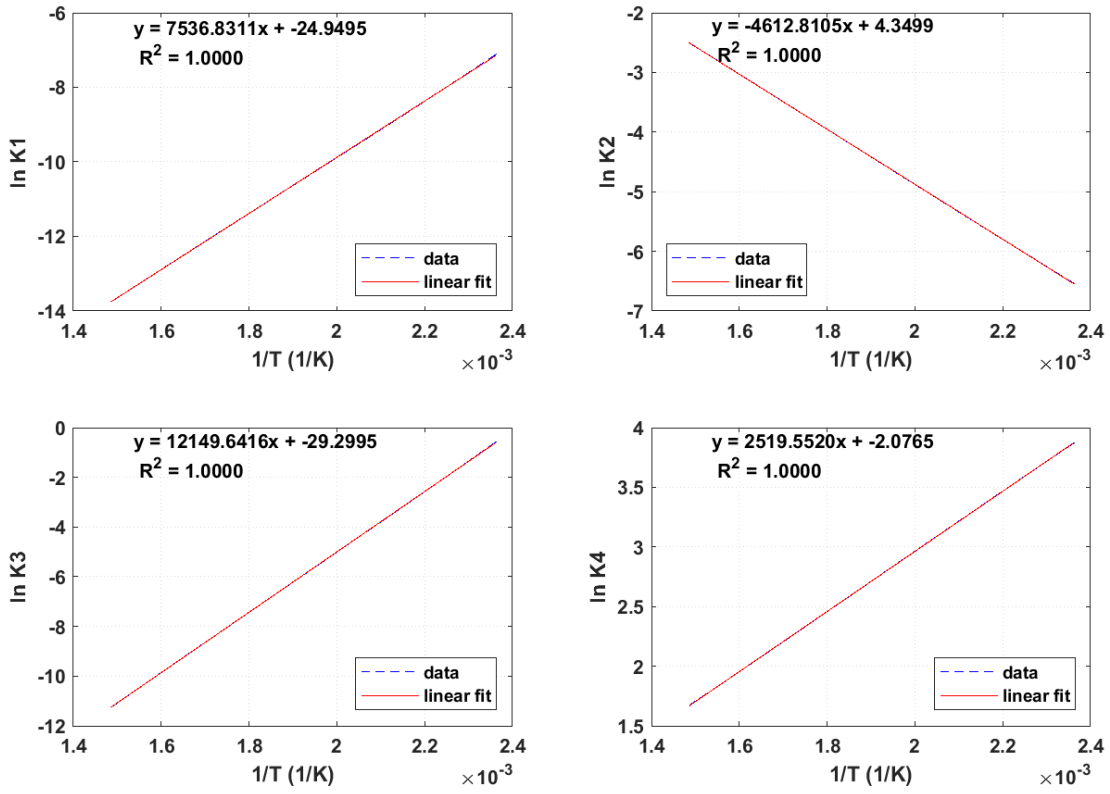

Figure 2.14 Linear equation of ln (Kj) vs 1/T obtained with RGIBBS block results.

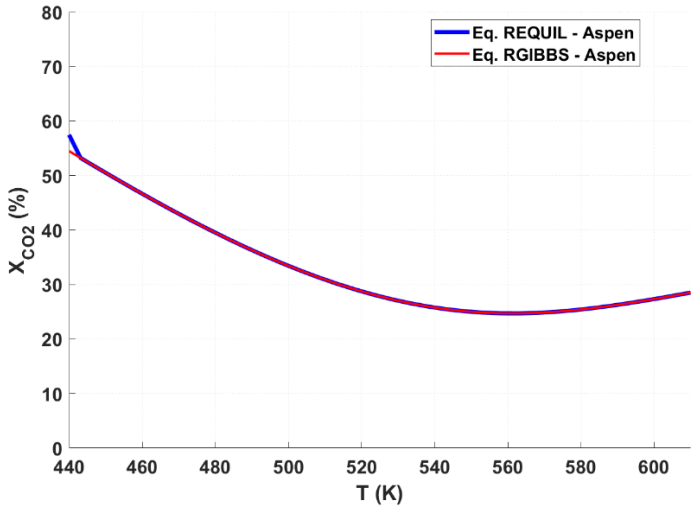

Figure 2.15 CO_2 conversion at equilibrium by two calculation methods of equilibrium constant: equilibrium reactor (REQUIL) and Gibbs reactor (RGIBBS). P=36 bars, $H_2/CO_2/N_2$=3/1/1, EoS: SRK.

The CO_2 conversions calculated with both Aspen blocks (REQUIL and RGIBBS) were drawn versus the temperature in Figure 2.15. An overlap can be noticed in the curves of both Aspen reactors. These results indicate that both Aspen methods are agreeing and can be employed for determining equilibrium constants. In the following figures showing the experimental results devoted to kinetics study and in our analysis of the results, thermodynamic calculations with the RGIBBS block will be applied. The decision was made to use the RGIBBS block, because the coefficient of determination (R-Squared) shows a better prediction than with REQUIL block and since it is possible to get compositions, CO_2 conversion, and product yields for the specified temperature range and increment in one-step from Aspen by using Sensitivity as a Model Analysis Tool. This was done by programming the Eq. (2.12)-(2.18), as applicable, directly in the Fortran of the Sensitivity Model Analysis Tool. Thus, in a single run, it was possible to retrieve the compositions for a set pressure and feed mole fraction with a temperature range of 423.15 – 773.15 K with a 5 K increment. Otherwise, REQUIL block can only give equilibrium constants (K_j) for one temperature set, as the Sensitivity Model Analysis Tool cannot be used, requiring a manual process to calculate the rest of the variables (X_{CO_2}, Y_i).

2.6.2. Experimental results and discussion

An analysis of the experimental results for the kinetic study is presented in this section. The quantification of CO_2 conversion, DME, methanol and CO yields resulting from CO_2 hydrogenation to DME by using CZA-C+HZSM5 are discussed. The list of the performed

experiments is shown in Table 2.8. All the experiments were performed with the same catalytic bed. They are sorted out in the chronological order. These tests were meant to help develop the kinetics of DME synthesis. For achieving this goal, the effects of some experimental conditions were assessed:

- Temperature
- Pressure
- Feed molar ratio: H_2/CO_2
- Gas hourly space velocity (GHSV).

Table 2.8 Experiments of DME synthesis with CZA-C+HZSM-5 in chronological order.

Exp. series number	**H_2/CO_2**	**N_2 (%)**	**P (bar)**	**GHSV ($L.g_{cat}^{-1}.h^{-1}$)**	**n_{CO_2} (moles) converted[1]**
1	3	10	36	7.3	6.17E-02
2	3	10	26	7.4	3.88E-02
3	3	73	26	7.4	9.40E-03
4	3	10	31	7.7	2.78E-02
5	1	10	36	3.6	1.35E-02
6	9.7	10	36	12.2	3.25E-02
7	1	10	26	3.6	1.29E-02
8	9	10	26	7	1.93E-02
9	3	10	36	3.6	7.01E-03
10	3	10	36	3.4	1.45E-02

[1]moles of CO_2 converted by experiments carried out.

The effect of catalyst deactivation was also evaluated, knowing that catalytic activity endurance remains a challenge for catalytic processes. Quezada, 2020 [1] identified the catalyst deactivation of CZA-D as a direct effect of CO_2 conversion. After repeating an experiment at the end of all the experiments he had performed on the same sample, he observed a significant lessening of CO_2 conversion and a slight variation in the reactor bed core temperature. The selectivity lasted equal, indicating homogenous deactivation. Therefore, the number of moles of converted CO_2 was taken as the parameter controlling deactivation [1]. Due to this, we conducted the deactivation analysis for CZA-C through the results of experiments carried out in this investigation.

The catalyst powder mixture previously selected by the catalyst screening is CZA-C+HZSM5. 0.4 g of CZA-C were mixed with 0.4 g of HZSM-5 to simultaneoulsly synthesize and dehydrate methanol. Figure 2.16 displays the results obtained with CZA-C+HZSM5 at a pressure of 36 bars and different temperatures in the laboratory fixed-bed reactor. The molar ratio of the feed was $H_2/CO_2/N_2$= 67.5/22.5/10. GHSV was 3.4-3.6 L. g_{cat}^{-1}. h^{-1}. Two series of experiments were repeated one day after the other: experiments series 9 and 10.

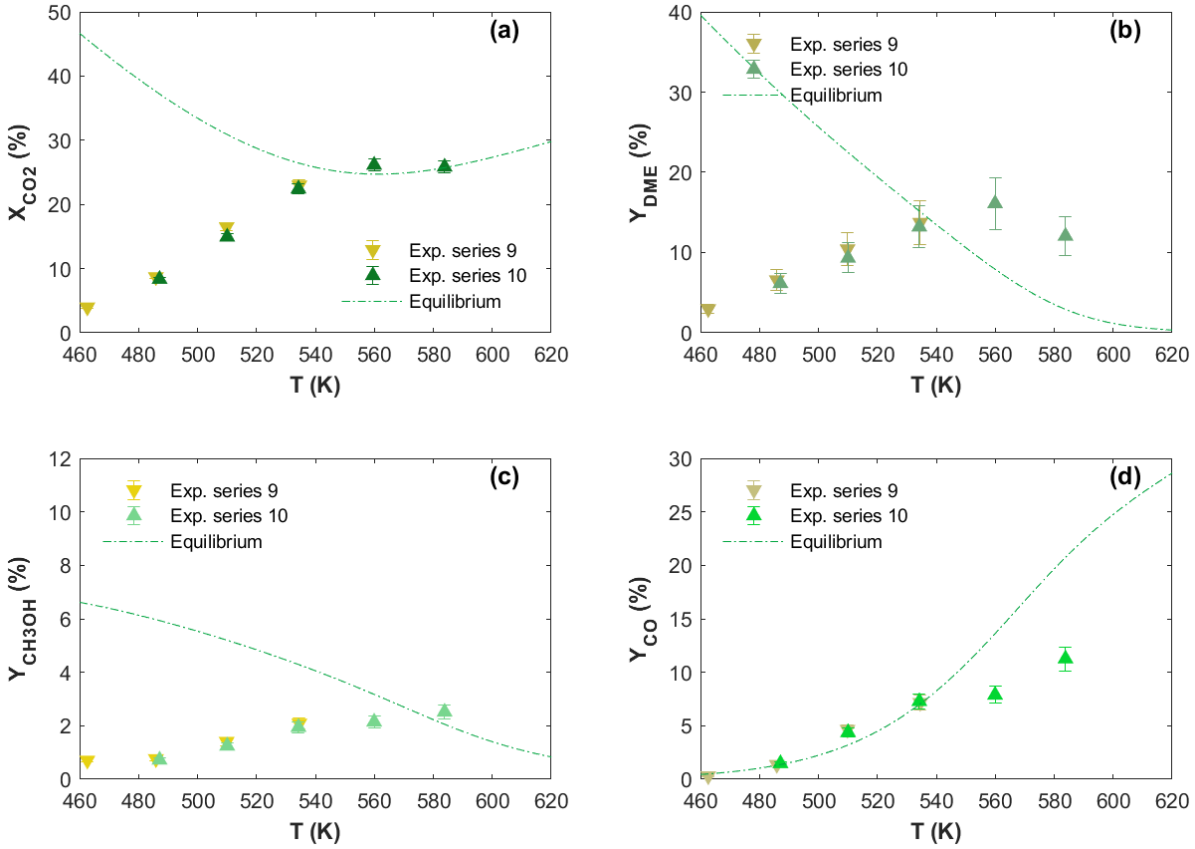

Figure 2.16 (a) CO_2 conversion, (b) DME yield, (c) methanol yield and (d) CO yield as a function of temperature. Operating conditions: P=36 bars, $H_2/CO_2/N_2$=67.5/22.5/10, GHSV=3.4-3.6 L. g_{cat}^{-1}. h^{-1}. Dashes lines represent the chemical equilibrium. Refer to Table 2.8: Experiments 9-10.

Figure 2.16 presents the results of the last two experiments performed. Figure 2.16a illustrates the evolution of CO_2 conversion as the furnace temperature rises. Figure 2.16(b-d) shows the yields of products, DME, methanol and CO, respectively, as a function of temperature. These tests were conducted consecutively, one per day. The same setup and operating conditions were applied to both tests. The same results can be confirmed on each of these graphs; therefore, it is safe to assume that Exp. series 9 is a repeatable experiment. Deactivation, if any, is weak and not very visible in a single repeated series.

2.6.2.1. Effect of temperature

The effect of temperature on CO_2 conversion and DME, methanol and CO yield was investigated.

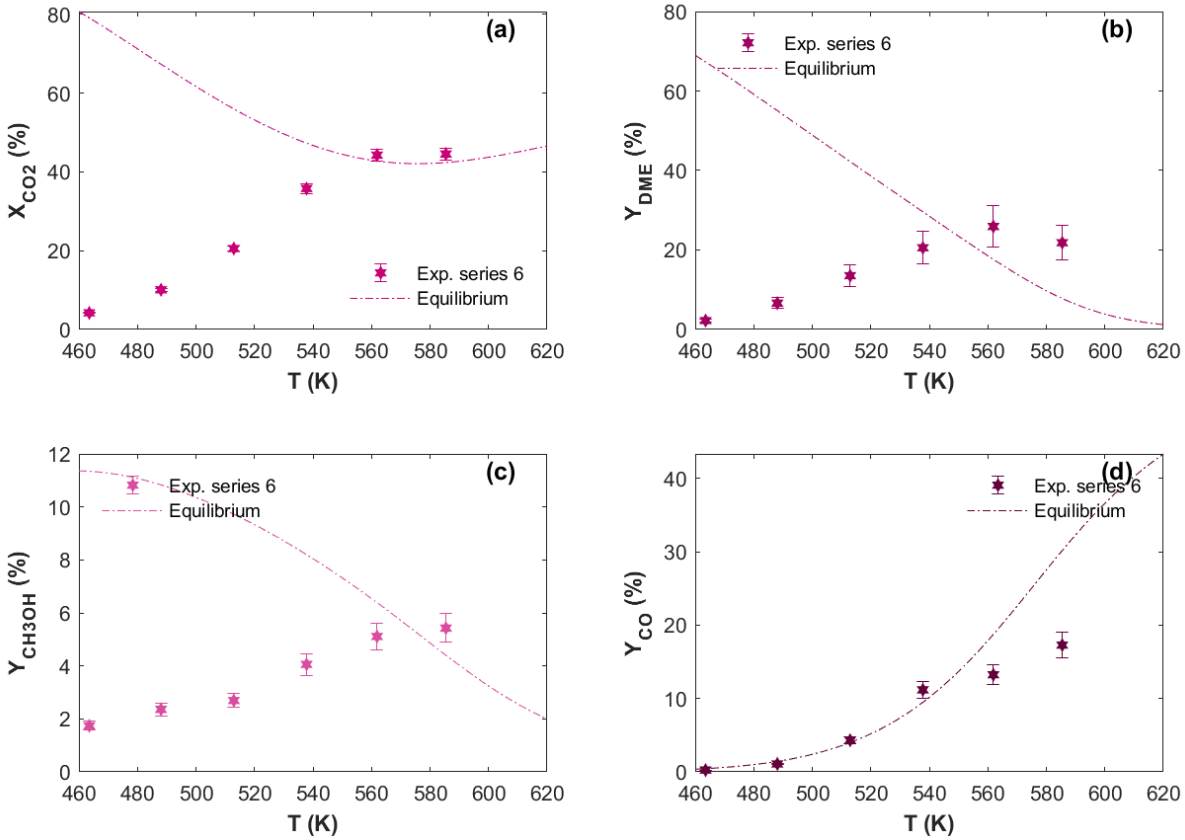

Figure 2.17 Effect of temperature on (a) CO_2 conversion, (b) DME, (c) methanol and (d) CO yield. Dashes lines represent the chemical equilibrium. Operating conditions: P=36 bars, $H_2/CO_2/N_2$= 81/9/10, GHSV=12.2 L. $g_{cat}^{-1}.h^{-1}$. Refer to Table 2.8: Experiment 6.

Figure 2.16 and Figure 2.17 depict the results. Figure 2.16a and Figure 2.17a illustrate how CO_2 conversion is favoured by temperature increases. It approaches equilibrium (dash lines) between 560-585 K and, for DME yield, even surpasses it. Although this is the case, the CO yield follows chemical equilibrium from the moment the process starts until it reaches 540 K. Only at the highest temperature, methanol yield exceeds thermodynamics, where DME yield decays. Temperature rise favours X_{CO_2}, CH_3OH and CO yields, and DME yield until ~560 K.

Respecting methanol dehydration, for the three experiments, the maximum DME yield is obtained at ~560 K. Methanol yield is weak, not even 6.0%, compared with other products. After all, since DME synthesis is done from methanol, the results are logical. RWGS dominates

at high temperatures due to its endothermic nature. This still explains the increase in CO yield and the decline in DME yield after 563 K, because this latter is an exothermic reaction.

At high temperatures, methanol is formed less because it is thermally limited. Therefore, less DME is formed, which explains the decrease in DME in all experiments. Results are consistent with the observed experiences, despite distinct operating conditions.

A trend has been identified for points exceeding 540 K in the experiments shown. DME yields clearly show that thermodynamic equilibrium is exceeded at higher temperatures (> 540 K). Methanol yields are striking above 560 K. Even the last two points of CO_2 conversion are borderline. On the other hand, CO yields are well below the equilibrium curve. It seems like there is a non-equilibrium shift in the reaction at high temperatures, in favour of DME formation.

Godini et al., 2022 [13] tested a similar Cu-Zn-Al commercial catalyst in mixture with a HZSM-5 zeolite to convert CO_2 to dimethyl ether in a packed bed-reactor with 100-250 μm particle size powders. At 533 K, they identified a surpass of thermodynamic values when analysing the CO_2 hydrogenation to methanol. They attributed their findings to the thermal characteristics of their reactor. Their inference was that local reaction temperatures may differ meaningfully from those measured at another location of the catalytic bed. In this thesis, we found the same results for DME synthesis using different thermocouples and reactors.

The hypotheses identified in this work that could explain these results are:

1- The evolution of the catalyst over time: water is adsorbed and accumulated by the zeolite during runs.
2- Concerning the equilibrium of reaction Eq. (2.22): DME does not seem to be limited by thermodynamic equilibrium whereas methanol is. Hence, as soon as DME is formed, it continues to accumulate because the reverse reaction of DME in methanol seems kinetically unfavourable.

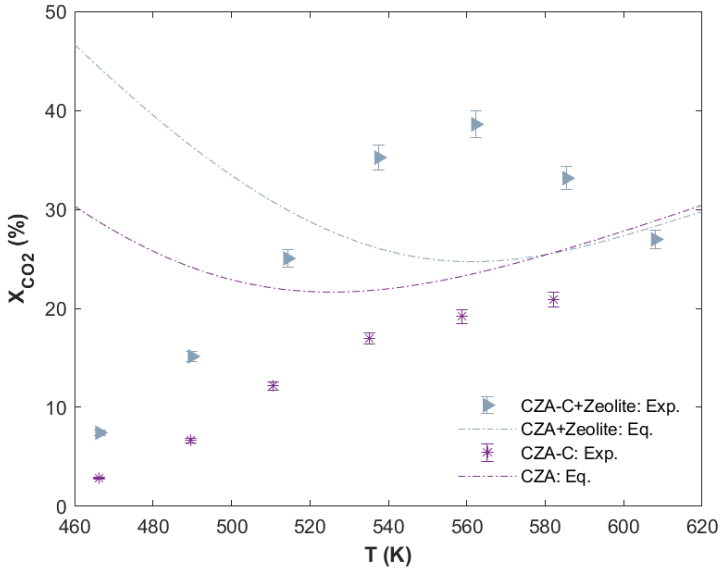

Figure 2.18 Effect of zeolite on CO_2 conversion. Operating conditions: P=36 bars, $H_2/CO_2/N_2$= 67.5/22.5/10, $GHSV_{CZA\text{-}C}$ =15.3 $L.g_{cat}^{-1}.h^{-1}$, $GHSV_{CZA\text{-}C+HZSM_5}$ =7.3 $L.g_{cat}^{-1}.h^{-1}$. Refer to Table 2.6: Experiments 4-5.

Moreover, Figure 2.18 illustrates the effect of zeolite on the reaction. The vivid violet curve displays the catalytic performance of fresh CZA-C and the clear blue of fresh CZA-C but with fresh HZSM-5. It is observed that the violet curve (CZA-C: Exp) is below thermodynamic equilibrium values. Even though running of CZA-C+HZSM-5 was carried out at the same operating conditions (P=36 bars, $H_2/CO_2/N_2$=67.5/22.5/10), the CZA-C+HZSM-5 mixture overcomes the thermodynamic equilibrium curve of DME synthesis from CO_2 hydrogenation. The overall GHSV are different ($GHSV_{CZA-C}$ = 15.3 $L.g_{cat}^{-1}.h^{-1}$, $GHSV_{CZA-c+HZSM5}$ = 7.3 $L.g_{cat}^{-1}.h^{-1}$), owing to the addition of zeolite (0.4 g) which implies a higher total mass of catalyst.

Consequently, this overshooting of thermodynamic equilibrium can certainly be related to the presence of zeolite, hence to reaction Eq. (2.22). Accordingly, the most plausible hypothesis is that water is retained in the zeolite pores and equilibrium is shifted towards DME formation. Due to the water content of the zeolite is not measurable, this assumption is to verify.

2.6.2.2. Effect of pressure

Pressure influences methanol synthesis, following Le Chatelier's principle. In this reaction, one mole of methanol is formed for every four moles of reactants. Thus, the increase in pressure benefits CO_2 conversion, methanol and DME yields. But CO production (RWGS

reaction) is favoured by low pressure. This is evident in Figure 2.19a-d, where, especially with chemical equilibrium dash lines highlight the disparity by changing the pressure.

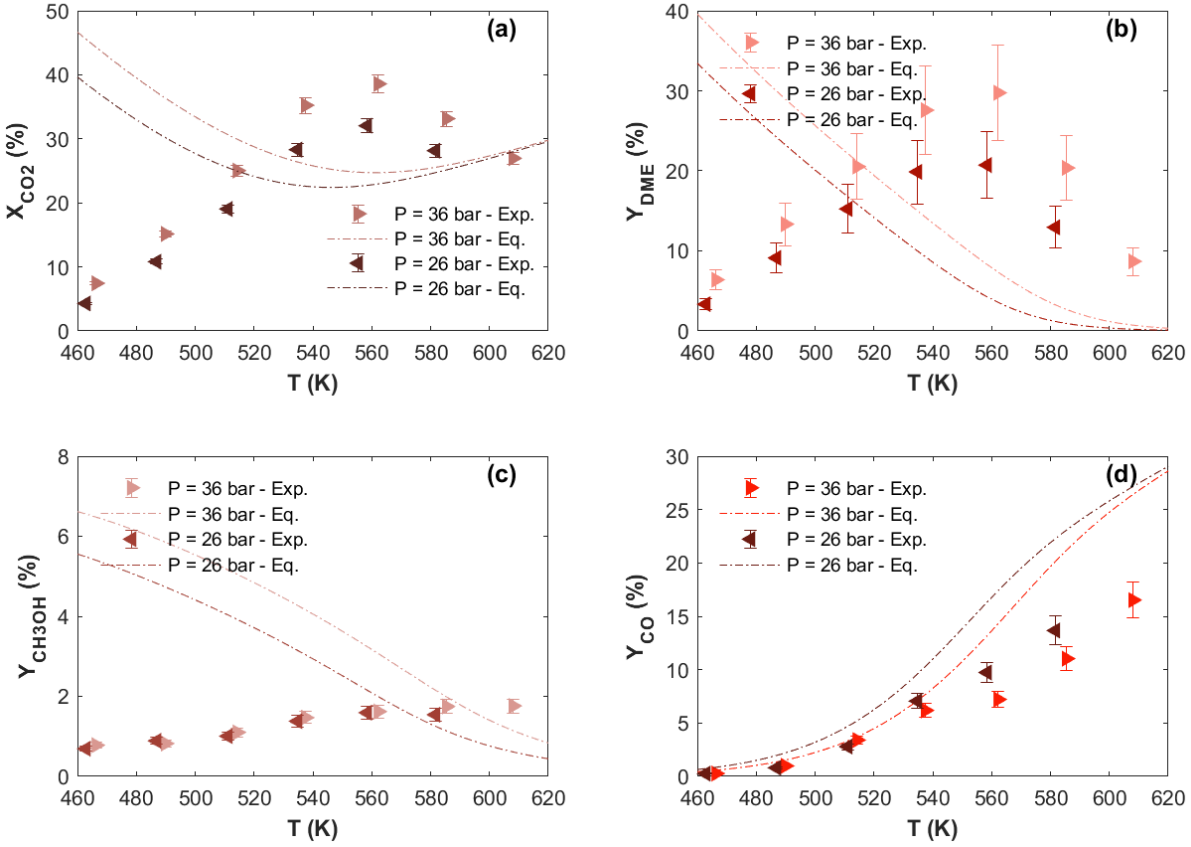

Figure 2.19 Effect of pressure on (a) CO_2 conversion, (b) DME, (c) methanol and (d) CO yield. Dashes lines represent the chemical equilibrium. Operating conditions: $H_2/CO_2/N_2$=67.5/22.5/10, GHSV= 7.3-7.4 L. $g_{cat}^{-1}.h^{-1}$. Refer to Table 2.8: Experiments 1-2.

CO_2 conversion predominates at 36 bars (Figure 2.19a). Regarding DME yield, one can draw a more striking distinction between the pressures and identify the advantage of rising pressure in the system (Figure 2.19b). Methanol production remains low and matches (Figure 2.19c). Figure 2.19d depicts that CO yield is adversely affected by pressure rise. It is necessary to use high pressure to optimise CO_2 conversion and DME production as has been demonstrated.

Again, thermodynamic equilibrium is exceeded. Even CO_2 conversion is higher than predicted by thermodynamic equilibrium at temperatures between 520 and 600 K (Figure 2.19). It is pertinent to note that these are the first two experiences in the series with CZA-C+HZSM5. It is hypothesised that, since the catalyst deactivation (CZA-C) is zero at the beginning of the reaction and zeolite should be able to adsorb more water in its pores, this could be the reason for the outstanding thermodynamic equilibrium shifts towards DME formation.

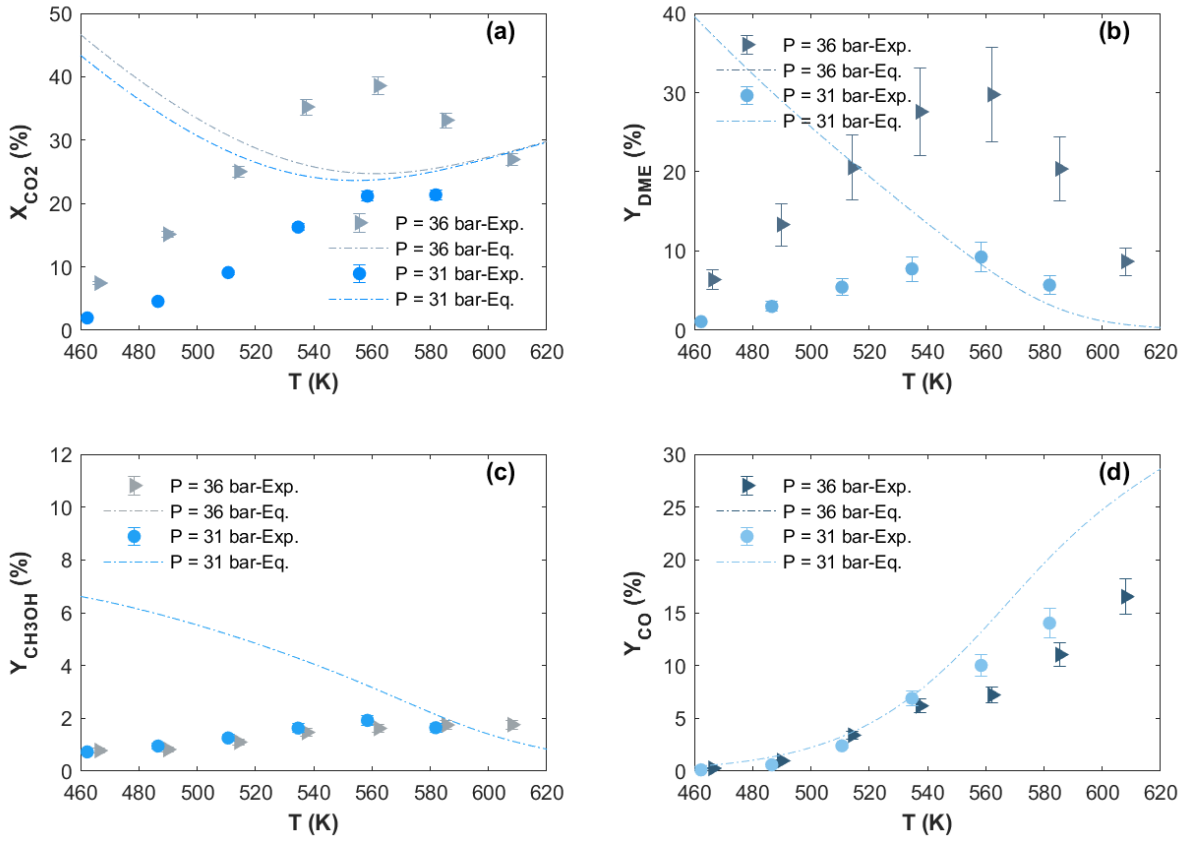

Figure 2.20 Effect of pressure on (a) CO_2 conversion, (b) DME, (c) methanol and (d) CO yield. Dashes lines represent the chemical equilibrium. Operating conditions: $H_2/CO_2/N_2$=67.5/22.5/10, GHSV= 7.3-7.7 $L.g_{cat}^{-1}.h^{-1}$. Refer to Table 2.8: Experiments 1 and 4.

Figure 2.20 displays the first and fourth experiments of the series (Table 2.8). The same molar ratio was established, $H_2/CO_2/N_2$=67.5/22.5/10. The GHSV was about 7.5 $L.g_{cat}^{-1}.h^{-1}$. They differed by 5 bars in pressure: 36 and 31 bars. On the other hand, the first experiment was run by increasing the temperature (473.15-623.15 K), while the fourth experiment was run by reducing the temperature (598.15-473.15 K). It is evident that equilibrium curves are similar for DME, methanol and carbon monoxide yields, as well as for CO_2 conversion from 568 K and on. There are, however, substantial differences in experimental results for CO_2 conversion and DME yield. These differences are less significant for methanol and carbon monoxide yields. Comparing the results from experiments in the range of 581-585 K, where CO_2 conversion equilibrium curves are closest, there is a clear gap between the results of about 12%. Still, there is a tenuous excess of equilibrium depicted in Figure 2.20b at 31 bars, not seen in Figure 2.20a, c and d.

In the same way, it can be noted that the overshoot of equilibrium is more noticeable at the beginning of the experiment series than at the end. In the first experiment, at 36 bars, equilibrium displacement is shown after 520 K for X_{CO_2} and Y_{DME}. This is not seen at 31 bars

(4th experiment), but above 558 K for DME yields. These findings support the hypotheses previously discussed. There should be adsorption of water by the catalyst in the furnace as the experiments progress to saturation. This is in addition to the effect of CZA-C deactivation deduced from CO_2 conversion decline perceived in Figure 2.20a.

2.6.2.3. Effect of feed molar ratio: $H_2/CO_2/N_2$

Feed molar ratios of H_2, CO_2 and N_2 have a huge effect on CO_2 conversion and product yields because it varies partial pressures of the inlet compounds. The influence of H_2/CO_2 ratio at fixed N_2 (10%) is illustrated in Figure 2.21a-d and the influence of N_2 percentage at fixed H_2/CO_2 (3/1) in Figure 2.22a-d.

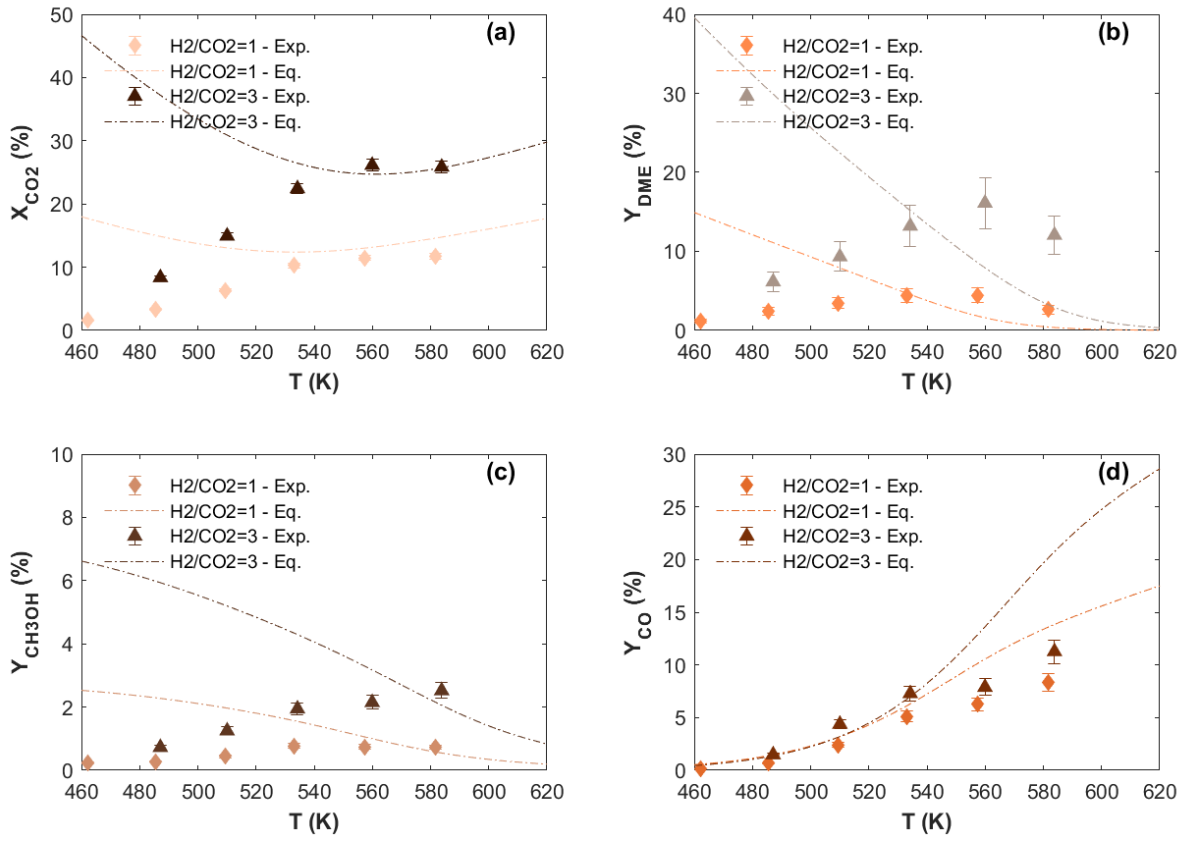

Figure 2.21 Effect of feed molar ratio on (a) CO_2 conversion, (b) DME, (c) methanol and (d) CO yield. Dashes lines represent the chemical equilibrium. Operating conditions: P=36 bars, GHSV=3.6 L.g_{cat}^{-1}.h^{-1}, N_2=10%. Refer to Table 2.8: Experiments 5 and 10.

Since H_2 acts as the limiting reagent, CO_2 conversion and DME yield increase along with the H_2/CO_2 molar ratio. Even by observing the chemical equilibrium curves, it is evident there is a vast divergence.

In Figure 2.21a-d, two H_2/CO_2 feed molar ratios of one and three, in the presence of 10% nitrogen are shown. It can be acknowledged that the highest CO_2 conversion and DME yield were at 560 K for both H_2/CO_2 feed ratios. In contrast to previous operating parameters evaluated in this section, the H_2/CO_2 ratio affected the methanol yield (Figure 2.21c). The higher the ratio was, the higher the methanol yield was. Figure 2.21 d shows that enhancing the feed molar ratio slightly improves the RWGS reaction. Maximum CO yield values were reached at ~583K.

In addition, the effect of increasing nitrogen in the feed was assessed. Figure 2.22 displays the outcomes. Dehydration of methanol is negatively affected by increased nitrogen mole flow. There is a reduction in CO_2 conversion as depicted in Figure 2.22a while having 63% more nitrogen in the system. Correspondingly, DME and methanol yields are reduced as well with 73% nitrogen. It is even beneficial for CO yield to have more nitrogen in the feed. As evidenced by the data, nitrogen in the system reduces the partial pressures of the reactants, leading to a decrease in reaction rates.

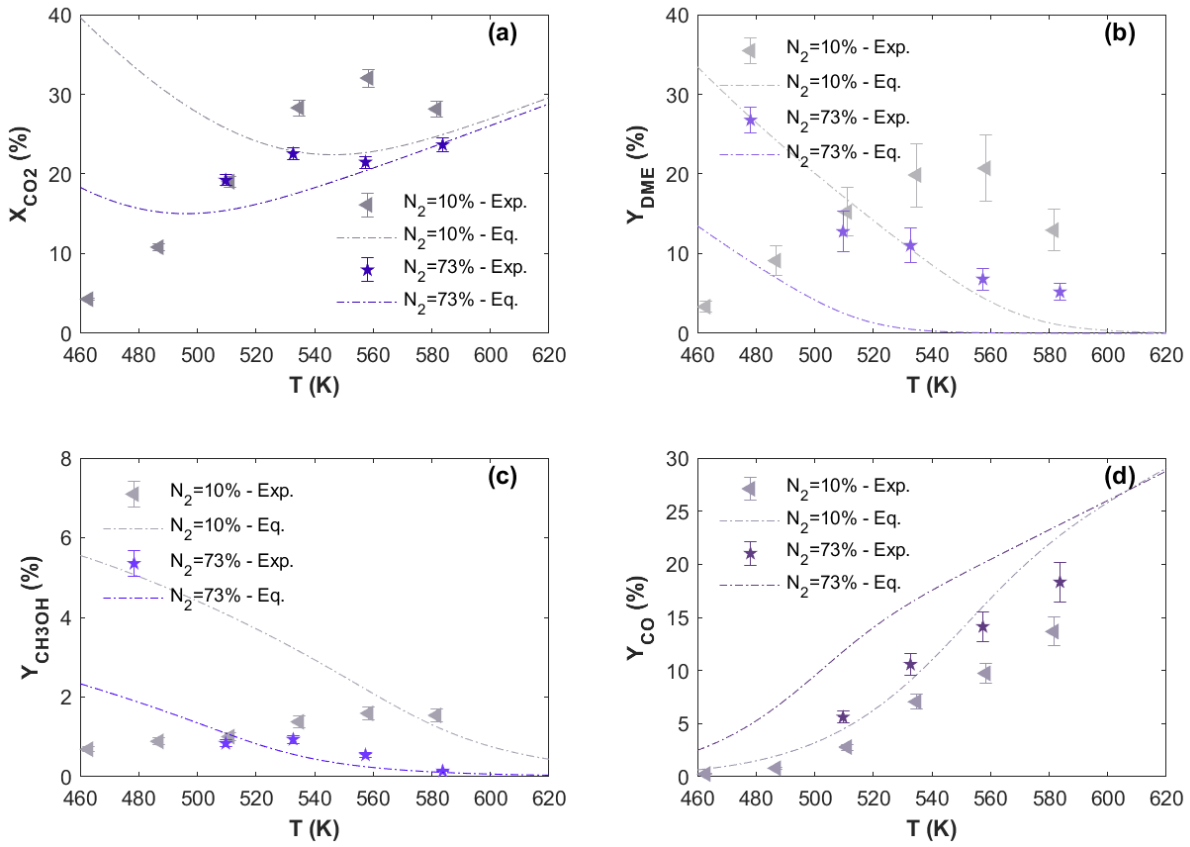

Figure 2.22 Effect of feed molar ratio on (a) CO_2 conversion, (b) DME, (c) methanol and (d) CO yield. Dashes lines represent the chemical equilibrium. Operating conditions: P=26 bar, H_2/CO_2=3/1, GHSV=7.4 $L.g_{cat}^{-1}.h^{-1}$. Refer to Table 2.8: Experiments 2-3.

2.6.2.4. Effect of gas hourly space velocity (GHSV)

At a pressure of 36 bars, reaction performance was evaluated for a GHSV between 7.3 and 3.6 $L.g_{cat}^{-1}.h^{-1}$. Figure 2.23 shows the effect of the mentioned change on CO_2 conversion, DME, methanol and carbon monoxide yields as a function of temperature at 36 bar, over a catalyst mass of 0.8 g and a feed molar ratio of $H_2/CO_2/N_2$=67.5/22.5/10 and varying the temperature from 460 to 610 K.

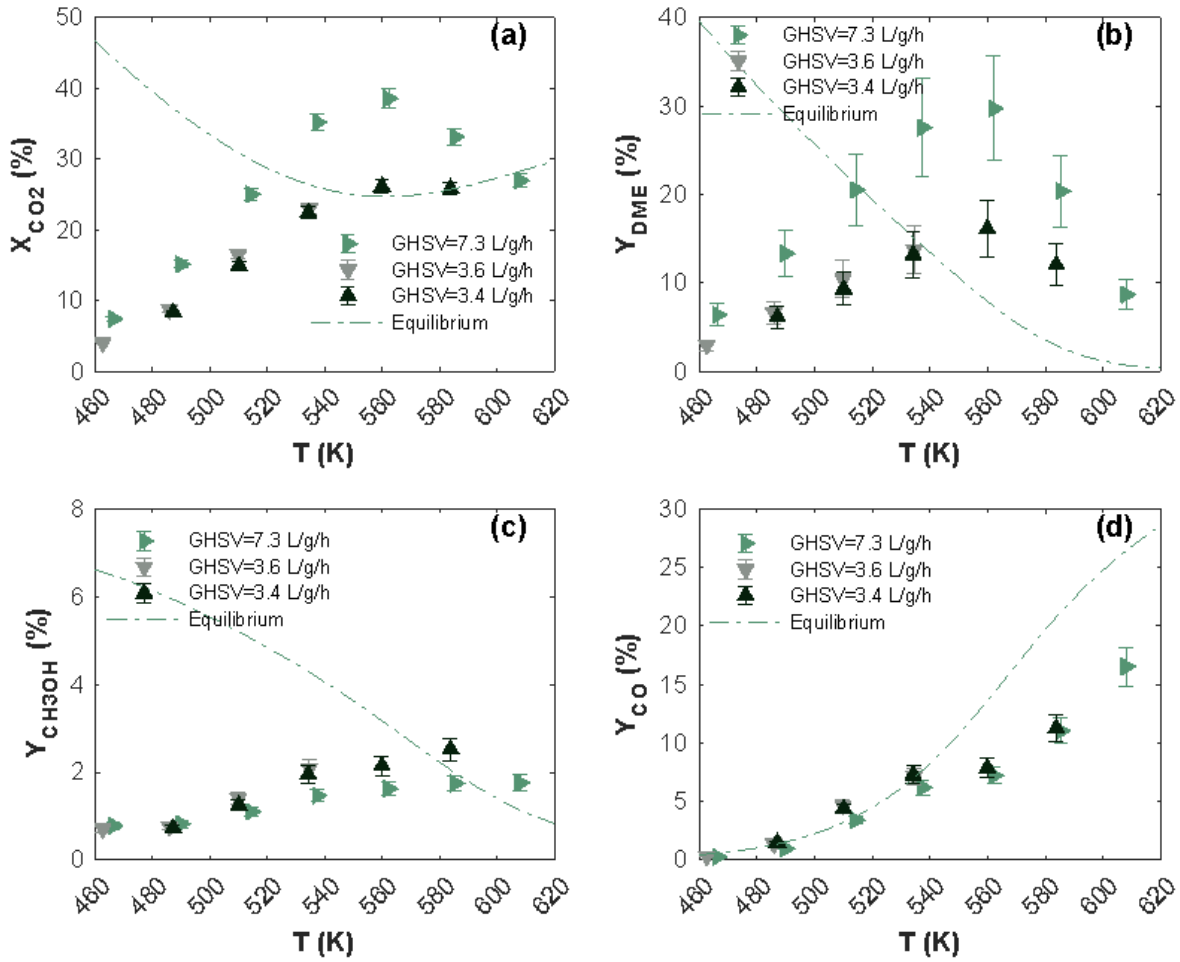

Figure 2.23 Effect of GHSV on (a) CO_2 conversion, (b) DME, (c) methanol and (d) CO yields. Dashes lines represent the chemical equilibrium. Operating conditions: P=36 bars, $H_2/CO_2/N_2$= 67.5/22.5/10. Refer to Table 2.8: Experiments 1, 9 and 10.

Unexpected results were gathered. Experimental data indicate that catalytic performance rises with the GHSV; the lower the GHSV, the lower the catalytic performance. However, theoretically, this would be the reverse. As has been widely observed, CO_2 conversion decreases with higher flow rate and GHSV and shorter residence time when increasing the flow rate. Similarly, Figure 2.23c shows that lowering GHSV increases methanol yield (a bit) and DME yield [13], [14].

Finally, experimental data do not support this statement, making these results incoherent. Consequently, two hypotheses have been inferred:

1. There is a catalyst deactivation of CZA-C.
2. Water adsorption on HZSM-5 modifies reaction behaviour.

In Table 2.8, it can be confirmed that the catalyst tests exhibited in Figure 2.23 are the first (green curve, $GHSV = 7.3\ L.g_{cat}^{-1}.h^{-1}$), ninth (grey curve, $GHSV = 3.6\ L.g_{cat}^{-1}.h^{-1}$) and tenth

(black curve, $GHSV = 3.4\ L.g_{cat}^{-1}.h^{-1}$). In this regard, we believe that catalyst modification is responsible for the contrary effect observed. Fresh catalysts are not deactivated and have full water adsorption capacity. Since the copper zinc aluminium catalyst was used from the first to the tenth experiment, there was either a deactivation of the catalyst or a reduction in water adsorption on the zeolite or both.

Consistency of results is not obvious at this stage, although this induces us to integrate deactivation into the kinetic model. It will be explained in more detail in Chapter 3.

2.7. Conclusions

This chapter presented the materials used for methanol and DME synthesis from CO_2 hydrogenation. The characteristics of two copper zinc aluminium catalysts, one commercial (CZA-C) and another developed (CZA-D) were presented for methanol synthesis and two commercial zeolites, HY and HZSM-5, for DME synthesis. The experimental set-up and detailed methodology are described, allowing us to proceed to catalytic screening.

The catalysts were tested to compare their performances. The importance of catalyst composition, and the possible adjustment of additive compounds for the CZA catalysts to obtain the highest catalytic performance for methanol synthesis was tested and analysed. CZA-C was identified as the most performant catalyst. Considering its composition and preparation method, this result is consistent with the literature.

The powder mixture of two catalysts Cu-Zn-Al and zeolite is a suitable combination to promote the conversion of CO_2 by hydrogenation to DME. There were similar results with both zeolites. HZSM-5 had slightly higher performance than HY. It could be interesting to carry out other experiments with HY to evaluate its performance over time.

Four parameters for DME synthesis were evaluated for a kinetic model: temperature, pressure, feed molar ratio ($H_2/CO_2/N_2$) and GHSV. An identified optimum temperature for this process is close to 560 K (287°C), considering CO_2 conversion, DME, methanol and CO yield, regardless of operating conditions.

Thermodynamic equilibrium is drastically exceeded for the first three experimental runs carried out. In the literature, there is not much information related to the comparison of experiments with thermodynamic equilibrium and catalytic performance. In this work, it was hypothesised that this could be related to catalyst deactivation and to water retention in the zeolite pores. In experimental series 4-10 in contrast to experimental series 1-3, CO_2 conversion reached the equilibrium values, but did not overshoot them significantly, i.e., it was very close to the limit, especially at high temperatures (>545 K). Several coupled phenomena were observed at the same temperature. As for DME and less so for methanol, the yields are still above the thermodynamic values. Meanwhile, in all experiments conducted, a shift in the CO yield curve was evident at the same temperature. However, it cannot be linked to a CZA crystallography change, since it is recurrent for all the experiments, unless we consider that this change is not permanent and disappears when the temperature drops at the shutdown of the furnace every experiment day. For the development of the kinetic model, it is necessary to consider deactivation considering these results. GHSV results have also shown

inconsistent results, suggesting that some simulations are necessary to evaluate the effect of incorporating or excluding deactivation.

Based solely on the results of these experiments, a simple kinetic model cannot be established. To provide a detailed description of the presented results, a complete kinetic model must be developed, and the aim of Chapter 3 is to do this.

2.8. References

[1] M. J. Quezada, "Hydrogénation catalytique de CO_2 en méthanol en lit fixe sous chauffage conventionnel et sous plasma à DBD," Normandie Université, 2020.

[2] F. Azzolina Jury, "Préparation et caractérisation de zéolithes dopées par des métaux de transition : Mesure de propriétés diélectriques et magnétiques et leur application à la synthèse de composés chimiques sous irradiation microondes," *http://www.theses.fr*, Dec. 2013, Accessed: Aug. 25, 2022. [Online]. Available: http://www.theses.fr/2013ISAM0025.

[3] S. Ren *et al.*, "Highly active and selective Cu-ZnO based catalyst for methanol and dimethyl ether synthesis via CO_2 hydrogenation," *Fuel*, vol. 239, pp. 1125–1133, Mar. 2019, doi: 10.1016/J.FUEL.2018.11.105.

[4] R. G. Santiago *et al.*, "Synthesis of MeOH and DME From CO_2 Hydrogenation Over Commercial and Modified Catalysts," *Front. Chem.*, vol. 10, Jun. 2022, doi: 10.3389/fchem.2022.903053.

[5] T. Kamsuwan, C. Krutpijit, S. Praserthdam, S. Phatanasri, B. Jongsomjit, and P. Praserthdam, "Comparative study on the effect of different copper loading on catalytic behaviors and activity of Cu/ZnO/Al2O3 catalysts toward CO and CO_2 hydrogenation," *Heliyon*, vol. 7, no. 7, p. e07682, Jul. 2021, doi: 10.1016/j.heliyon.2021.e07682.

[6] G. L. Catuzo, C. V. Santilli, and L. Martins, "Hydrophobic-hydrophilic balance of ZSM-5 zeolites on the two-phase ketalization of glycerol with acetone," *Catal. Today*, vol. 381, pp. 215–223, Dec. 2021, doi: 10.1016/J.CATTOD.2020.07.008.

[7] T. A. Semelsberger, K. C. Ott, R. L. Borup, and H. L. Greene, "Role of acidity on the hydrolysis of dimethyl ether (DME) to methanol," *Appl. Catal. B Environ.*, vol. 61, no. 3–4, pp. 281–287, Nov. 2005, doi: 10.1016/J.APCATB.2005.05.014.

[8] T. C. Bowen, R. D. Noble, and J. L. Falconer, "Fundamentals and applications of pervaporation through zeolite membranes," *J. Memb. Sci.*, vol. 245, no. 1–2, pp. 1–33, Dec. 2004, doi: 10.1016/J.MEMSCI.2004.06.059.

[9] I. Halasz and M. Agarwal, "Hydrophobic nano-layer on surface prevents H2O adsorption in moderately aluminum deficient Y zeolite crystals," *Microporous Mesoporous Mater.*, vol. 310, Jan. 2021, doi: 10.1016/J.MICROMESO.2020.110621.

[10] J. Fei, Z. Hou, B. Zhu, H. Lou, and X. Zheng, "Synthesis of dimethyl ether (DME) on modified HY zeolite and modified HY zeolite-supported Cu–Mn–Zn catalysts," *Appl.*

Catal. A Gen., vol. 304, no. 1–2, pp. 49–54, May 2006, doi: 10.1016/J.APCATA.2006.02.019.

[11] P. Salvador and W. Kladnic, "Surface Reactivity of Zeolites Type H-Y and Na-Y with Methanol," *J. Chem. Soc. Faraday Trans. 1*, vol. 73, pp. 1153–1168, 1977, doi: 10.1039/F19777301153.

[12] G. Bonura *et al.*, "Acidity control of zeolite functionality on activity and stability of hybrid catalysts during DME production via CO_2 hydrogenation," *J. CO_2 Util.*, vol. 24, pp. 398–406, Mar. 2018, doi: 10.1016/J.JCOU.2018.01.028.

[13] H. R. Godini, S. R. Kumar, N. Tadikamalla, and F. Gallucci, "Performance analysis of hybrid catalytic conversion of CO_2 to DiMethyl ether," *Int. J. Hydrogen Energy*, vol. 47, no. 21, pp. 11341–11358, Mar. 2022, doi: 10.1016/j.ijhydene.2021.11.073.

[14] H. Hamedi and T. Brinkmann, "Valorization of CO_2 to DME using a membrane reactor: A theoretical comparative assessment from the equipment to flowsheet level," *Chem. Eng. J. Adv.*, vol. 10, p. 100249, May 2022, doi: 10.1016/j.ceja.2022.100249.

Chapter 3

3. Kinetic Model

3.1. Reactions and reaction rates

The experimental results of CO_2 hydrogenation over the Cu-Zn-Al + HZSM-5 mixture in a fixed-bed reactor have been presented in Chapter 2. The computation steps to develop a kinetic model, where catalyst deactivation is considered, are explained in this chapter. The main objective is to describe the experiments carried out in the laboratory by the parametrization of the reactions kinetic model.

Four reactions, (3.1)-(3.4), are considered in the synthesis of dimethyl ether from CO_2 hydrogenation.

$$CO_2 + 3H_2 \rightleftharpoons CH_3OH + H_2O \qquad \Delta H_{298K} = -49.25\ kJ.mol^{-1} \qquad (3.1)$$

$$CO_2 + H_2 \rightleftharpoons CO + H_2O \qquad \Delta H_{298K} = 41.16\ kJ.mol^{-1} \qquad (3.2)$$

$$CO + 2H_2 \rightleftharpoons CH_3OH \qquad \Delta H_{298K} = -90.41\ kJ.mol^{-1} \qquad (3.3)$$

$$2CH_3OH \rightleftharpoons CH_3OCH_3 + H_2O \qquad \Delta H_{298K} = -24.04\ kJ.mol^{-1} \qquad (3.4)$$

Based on these reactions, several kinetic models have been recommended for this process. Reactions (3.1)-(3.3) occur over the CZA-C for methanol synthesis and, to produce DME, the reaction (3.4) takes place over the zeolite HZSM-5.

For methanol synthesis, the first three reactions are involved. Quezada, 2020 [1] proposed a kinetic model for methanol synthesis from CO_2 hydrogenation over the CZA-D catalyst in a fixed bed reactor. He was assessing two models to develop numerical resolution for kinetics: a Power Law model and a Langmuir–Hinshelwood model. After their evaluation, the researcher found that the Power Law model was not accurate on modelling the experiments results, probably some phenomena are not accounted for by this model. Nonetheless, the Langmuir–Hinshelwood model described satisfactorily the experiments carried out. This has been attributed to the presence of adsorption constants in the last model. On this evaluation, the author also compared the possibility of having one (Cu^0 for CO_2) or two (Cu^0 for CO_2 and ZnO for H_2) types of active sites. The modelling

results demonstrated a proper prediction with only one type of active site. Therefore, here, the model for the methanol synthesis reactions to be considered is Langmuir–Hinshelwood models with one type of active sites. Thence, the reaction rates of reactions (3.1)-(3.3) were defined as:

$$r_1 = \frac{k_1 e^{-\frac{E_1}{RT}}\left(p_{CO_2} p_{H_2}^3 - p_{CH_3OH} p_{H_2O}/K_1\right)}{p_{H_2}^{(3-\nu_1/2)} \cdot \left(1 + K_{CO_2} p_{CO_2} + \sqrt{K_{H_2} p_{H_2}} + K_{CH_3OH} p_{CH_3OH} + K_{H_2O} p_{H_2O} + K_{CO} p_{CO}\right)^3} \quad (3.5)$$

$$r_2 = \frac{k_2 e^{-\frac{E_2}{RT}}\left(p_{CO_2} p_{H_2} - p_{CO} p_{H_2O}/K_2\right)}{p_{H_2}^{(1-\nu_2/2)} \cdot \left(1 + K_{CO_2} p_{CO_2} + \sqrt{K_{H_2} p_{H_2}} + K_{CH_3OH} p_{CH_3OH} + K_{H_2O} p_{H_2O} + K_{CO} p_{CO}\right)^2} \quad (3.6)$$

$$r_3 = \frac{k_3 e^{-\frac{E_3}{RT}}\left(p_{CO} p_{H_2}^2 - p_{CH_3OH}/K_3\right)}{p_{H_2}^{(2-\nu_3/2)} \cdot \left(1 + K_{CO_2} p_{CO_2} + \sqrt{K_{H_2} p_{H_2}} + K_{CH_3OH} p_{CH_3OH} + K_{H_2O} p_{H_2O} + K_{CO} p_{CO}\right)^2} \quad (3.7)$$

where r_j is the reaction rate of the reaction j, k_j is the pre-exponential factor, E_j is the activation energy, K_j the reaction equilibrium constant, p_i the partial pressure of the component i and K_i the adsorption equilibrium constant.

The values of $\nu_1 = 2$; $\nu_2 = 1$; $\nu_3 = 4$, expressed by Seidel et al., 2018 [2], were taken into consideration on the basis on the rate determining steps (RDS) in the reaction mechanism of CO_2 hydrogenation, RWGS and CO hydrogenation for the Langmuir-Hinshelwood kinetic model.

In view of the dependency of reactions in the methanol synthesis and that Quezada, 2020 [1] found the conversion of the third reaction (CO hydrogenation to methanol) negligible in the modelling, in this work, the third reaction was not considered. Thus, reactions Eq. (3.1), (3.2) and (3.4) are treated for the presented kinetic model. The evaluated reactions are:

$$\frac{1}{3}CO_2 + H_2 \rightleftharpoons \frac{1}{3}CH_3OH + \frac{1}{3}H_2O \quad (3.8)$$

$$CO_2 + H_2 \rightleftharpoons CO + H_2O \quad (3.9)$$

$$2CH_3OH \rightleftharpoons CH_3OCH_3 + H_2O \quad (3.10)$$

There are also various kinetic models for the dehydration of methanol to DME over the zeolite ZSM-5. According to the research, like the methanol synthesis, there are two

different reaction mechanisms by which this can occur, the associative (direct) route and the dissociative (indirect) route. Park et al., 2021 [3] performed microkinetic modelling using a theoretical computational chemistry approach and experimental data from the literature and concluded that the dissociative pathway was dominant. On this basis, the following reaction rate expression is presented, assuming dissociation of methanol during adsorption:

$$r_4 = \frac{k_4 e^{-\frac{E_4}{RT}} \left(p_{CH_3OH}^2 - \frac{p_{CH_3OCH_3} p_{H_2O}}{K_4} \right)}{\left(1 + 2\sqrt{K_{CH_3OH,ZSM5} p_{CH_3OH}} + K_{CH_3OCH_3} p_{CH_3OCH_3} + K_{H_2O,ZSM5} p_{H_2O} \right)^2} \quad (3.11)$$

3.2. Transport phenomena

In a heterogenous catalytic reaction sequence, mass and heat transfers have a crucial influence over the measured (or observed) reaction rate. Firstly, external mass transfer from the bulk fluid to the external catalyst surface and then, internal mass transfer from external surface into and through the catalyst pores need to be studied to develop the reaction kinetics. For the aim, the computations of internal and external diffusions are done. Like manner, the external heat transfer limitation is evaluated.

3.2.1. External transfer limitations

3.2.1.1. External mass transfer limitation

External diffusion of reactants from the bulk fluid to the catalyst surface was verified according to Eq. (3.12) [4].

$$f_{ext} = \frac{C_{i,b} - C_{i,s}}{C_{i,b}} = \frac{r_{obs,i} L}{k_{D,i} C_{i,b}} \tag{3.12}$$

where f_{ext}: is the external resistance fraction. When the external resistance fraction tends towards one, it means severe external diffusion and as far as $f_{ext} \ll 1$, external limitation can be neglected. $C_{i,b}$ is the concentration of i component in the bulk fluid. $C_{i,s}$ is the concentration of i component in the surface. $r_{obs,i}$ is the observed or measured reaction rate of component i per volume of catalyst. In a first approach, $r_{obs,i}$ was calculated by the relation $r_{obs,i} = \left(F_{CO_2,in} - F_{CO_2,out}\right)/V_r(1-\varepsilon)$, considering the reactor behaved as a CSTR (Continuous-flow Stirred-Tank Reactor). L_p is the characteristic length of catalytic particle. It is the ratio of the external surface and the volume of the particle, thus $L_p = V_p/A_p$. For spherical particles, $L_p = d_p/6$ with d_p as the particle diameter. $k_{D,i}$ is the external mass transfer coefficient of component i, calculated from the Sherwood number Sh definition and the correlation of Kunii & Levenspiel [5], [6] suitable for packed bed:

$$Sh = \frac{k_D d_p}{D_{m,i}} = 2.0 + 1.8 Re^{\frac{1}{2}} Sc^{\frac{1}{3}} \tag{3.13}$$

where Reynolds, Re, and Schmidt, Sc, numbers are defined as:

$$Re = \frac{u\rho d_p}{\mu_m};\ Sc = \frac{\mu_m}{\rho D_{m,i}} \tag{3.14}$$

$D_{m,i}$ is the mixture molar diffusivity of the component i, u is the superficial velocity in the porosity of the particle bed, ρ is the gas density and μ_m is the mixture fluid dynamic viscosity. The computations performed to obtain μ_m, ρ and $D_{m,i}$ are explained in the Appendix A (Eq. (A.1)-(A.10)).

All the experimental reaction rates obtained for CO_2 were calculated and the assessment of the mass and heat transfer limitation was performed on the worst case, that is the experiment where the maximum CO_2 consumption was reached. This point corresponds to the following conditions: $P = 35\ bar, T = 585.43\ K, H_2/CO_2 = 9$ and $GHSV = 12\ L \cdot g_{cat}^{-1} h^{-1}$. Using this case, the input values for the calculations performed for CO_2 and H_2 is given in Table 3.1.

Table 3.1 Parameters to estimate the external resistance fraction.

Parameter	**Value**	**Unit**	**Parameter**	**Value**	**Unit**
P	35	bar	T	585.43	K
H_2/CO_2	9	–	C_{in}	695.45	$mol.m^{-3}$
d_p	$2.00 \cdot 10^{-4}$	m	$u\rho$	$6.69 \cdot 10^{-2}$	$kg.m^{-2}.s^{-1}$
r_{obs,CO_2}	21.33	$mol.s^{-1}.m^{-3}$	r_{obs,H_2}	72.71	$mol.s^{-1}.m^{-3}$
$C_{CO_2,in}$	34.91	$mol.m^{-3}$	$C_{H_2,in}$	507.71	$mol.m^{-3}$
μ_m	$2.28 \cdot 10^{-5}$	$Pa.s$	Re	$5.86 \cdot 10^{-1}$	–
D_{e,CO_2}	$2.69 \cdot 10^{-7}$	$m^2.s^{-1}$	D_{e,H_2}	$9.53 \cdot 10^{-7}$	$m^2.s^{-1}$
Sh_{CO_2}	3.49	–	Sh_{H_2}	3.08	–
Sc_{CO_2}	1.28	–	Sc_{H_2}	0.48	–
k_{D,CO_2}	0.05	$m.s^{-1}$	k_{D,H_2}	0.14	$m.s^{-1}$
$\boldsymbol{f_{ext,CO_2}}$	$\mathbf{1.61 \cdot 10^{-3}}$	–	$\boldsymbol{f_{ext,H_2}}$	$\mathbf{3.75 \cdot 10^{-5}}$	–

As the external resistance fractions, f_{ext}, obtained for CO_2 and H_2 were less than 0.05 ($1.61 \cdot 10^{-3}$ for CO_2 and $3.75 \cdot 10^{-5}$ for H_2), it can be stated that there is not external limitation diffusion in the film.

3.2.1.2. External heat transfer limitation

The Mears criterion (C_M), Eq. (3.15), also uses the observed reaction rate to understand the presence of heat transfer limitation between the particle surface and the bulk fluid.

$$\frac{|-\Delta H_{rx}|r_{obs}}{hT}\frac{d_p}{6} < 0.15\frac{RT}{E_{obs}} \tag{3.15}$$

where ΔH_{rx} is the heat of reaction, E_{obs} is the activation energy, h is the heat transfer coefficient between gas and pellet and R is the gas constant ($8.314\ J.mol^{-1}.K^{-1}$).

The computation of heat transfer coefficient, h, is explained in Appendix A (Eq. (A.11)-(*A.17*)). The heat of reactions of methanol synthesis and RWGS reactions are $-49.25\ kJ.mol^{-1}$ and $41.16\ kJ.mol^{-1}$, respectively. Delgado Otalvaro et al., 2021 [7] proposed $E_{a,CH_3OH} = 32.70\ kJ.mol^{-1}$ and $E_{a,RWGS} = 175.40\ kJ.mol^{-1}$ for CO_2 hydrogenation to methanol and RWGS, respectively, with a CZA catalyst from Alfa Aesar. Table 3.2 contains the data and parameters to estimate the external heat transfer limitation and Table 3.3 the computation results. The two criteria were compared with the lowest value obtained with right term of the Eq. (3.15). Hence, the heat of reaction and the activation energy of RWGS were used.

Table 3.2 Parameters to estimate the external heat transfer limitation.

Parameter	Value	Unit	Parameter	Value	Unit
λ_m	0.19	$W.m^{-1}.K^{-1}$	Cp_m	32.10	$J.mol^{-1}.K^{-1}$
Nu	3.01	$-$	Pr	0.40	$-$
E_{a,CH_3OH}	32.70	$kJ.mol^{-1}$	$E_{a,RWGS}$	175.40	$kJ.mol^{-1}$
$\Delta H_{rx,CH_3OH}$	-49.25	$kJ.mol^{-1}$	$\Delta H_{rx,RWGS}$	41.16	$kJ.mol^{-1}$
h	2.88	$kW.m^{-2}.K^{-1}$			

Table 3.3 Mears Criterion for CO_2 and H_2.

Criterion			
C_{M,CO_2}	$7.37 \cdot 10^{-5}$	$<$	$4.16 \cdot 10^{-3}$
C_{M,H_2}	$5.87 \cdot 10^{-5}$	$<$	$4.16 \cdot 10^{-3}$

The obtained results demonstrate no external heat limitations. Equally, the external diffusion and heat transfer limitations are negligible.

According to these calculations, we concluded that there was no external heat limitation. For mass and heat transfers, the calculations were performed with RWGS reaction data and CO_2 and H_2 properties; in theory, therefore, this conclusion could be correct only for the CZA catalyst. However, the synthesis of DME is softer than the RWGS (lower heat of reaction), the diffusivities and thermal conductivities are quite the same for CO2 and DME and the DME measured reaction rate could not be greater than that of CO2. Thus, we could assume that the external mass and heat transfer limitations were negligible both for HZSM-5 zeolite and CZA catalyst.

3.2.2. Internal transfer limitation

It is necessary to review the laws of Fick and Fourier for mass and heat flow gradients across the pore surface, respectively, to evaluate the mass and heat diffusion in a porous catalyst. From Fick's law, the diffusional fluid flux per unit of cross-sectional area of pore is given by:

$$N = -D_e \frac{dC_i}{dz} \tag{3.16}$$

where D_e is the effective diffusivity:

$$D_e = \frac{\varepsilon_p D_i}{\tau_p} \tag{3.17}$$

where D_i is the diffusivity inside the pores, ε_p is the internal (pellet) porosity (pore volume/total volume=0.74) and τ_p is tortuosity (assumed as 3).

The diffusivity inside the pores is calculated according to Eq. (3.18):

$$\frac{1}{D_i} = \frac{1}{D_{K,i}} + \frac{1}{D_{m,i}} \tag{3.18}$$

where $D_{K,i}$ is the Knudsen's diffusivity. In our case, $D_{K,i}$ was calculated using the mean pore diameter measured by BET for CZA catalyst ($\delta = 1.237 \cdot 10^{-8}\ m$) and we assumed a pore diameter of 10 Å for the HZSM-5.

The internal mass transfer limitation is characterized by the internal effectiveness factor (η), which is the ratio of the measured rate of reaction to the intrinsic reaction rate, that is when there is no internal transfer limitation and is calculated considering the concentration inside the pores is isotropic and equal to the concentration at the external

catalyst surface. The internal diffusion limitation is negligible if η is close to one [9]. For spherical particles, the internal effectiveness factor is:

$$\eta = \frac{3}{\phi}(\phi coth\phi - 1) \tag{3.19}$$

where ϕ is the Thiele modulus, which is the ratio of the maximal intrinsic reaction rate of a component in particle surface conditions to its maximal diffusion rate. Internal diffusion typically limits the overall reaction rate, while Thiele modulus is large; but when this is small then the surface reaction is rate-limiting. Its expression is:

$$\phi^2 = \frac{r_s}{D_e C_s}\left(\frac{d_p}{6}\right)^2 \tag{3.20}$$

C_s and r_s are concentration and intrinsic reaction rate in particle surface conditions. As r_s was the information we searched, we used the Weisz-Prater criterion (ϕ') that needed the observed rather than the intrinsic reaction rate to estimate the internal mass transfer limitation. Thiele modulus and internal effectiveness factor are correlated in Weisz-Prater criterion. Then, it was possible to define the pore diffusion rate by:

$$\phi' = \phi^2\eta = \frac{r_{obs,i}}{D_{e,i}C_{i,s}}\left(\frac{d_p}{6}\right)^2 \tag{3.21}$$

For the CZA catalyst, by means of Eq. (3.12), the concentration of i component on the surface was calculated. Their values and those of ϕ' are given in Table 3.4.

Table 3.4 Parameters to estimate the internal mass transfer limitation for the CZA catalyst.

Parameter	Value	Unit	Parameter	Value	Unit
$C_{CO_2,s}$	34.91	$mol.m^{-3}$	$C_{H_2,s}$	507.71	$mol.m^{-3}$
ϕ'_{CO_2}	$\mathbf{9.43 \cdot 10^{-3}}$	–	ϕ'_{H_2}	$\mathbf{1.83 \cdot 10^{-4}}$	–

Computation results indicate $\phi' \ll 1$, thus no internal diffusion limitations were present in CZA catalyst. For the HZSM-5 zeolite, we used the same logic as for the external transfer limitation, that was: the effective diffusivities were quite the same for CO_2 and DME in both catalysts, the effective diffusivity was about 7 times lower in HZSM-5 than in CZA catalyst and the DME measured reaction rate could not be greater than that of CO_2. Thus, we concluded, both in CZA and in HZSM-5, there were neither internal mass transfer limitations, nor internal heat transfer limitations insofar as the two are directly correlated and the thermal conductivity is much higher in solid phase than in gas phase.

3.3. Reactor modelling

3.3.1. Preliminary considerations

3.3.1.1. Reactor model, pressure drop and thermal profile

Villermaux, 1993 [4] explains that for a reactor to be of the plug flow type, it is necessary to consider the height of the reactor and the diameter of the particles, consequently the following criteria must be met:

$$H_r/d_p \geq 50 \tag{3.22}$$

In our case, H_r/d_p was equal to 150, far above 50, as $H_r = 0.03\,m$ and $d_p = 2 \cdot 10^{-4} m$. The relation of Eq. (3.22) was thus confirmed.

During the experiments, the pressure difference between the input and output of reactor was identified to be equal to or less than 1 bar, which supports the assumption that the reactor is isobaric.

Besides, to verify the isothermicity of reactor, the temperature of reactor core and wall (the temperature of the furnace) were recorded while carrying out the experiments. As a result, it was observed a relative radial gradient of 5.0% between the furnace temperature and the fixed bed core temperature (see Figure 3.1). In Figure 3.1, all experiments are shown, regardless of the conditions. The observed ΔT ranges from 7.46 to 16.50 degrees. However, this does not necessarily imply the existence of such a gradient within the bed, as the reactor wall and the external furnace (stationary air) provide resistance to heat transfer. With regard to the axial gradient, Quezada, 2020 [1] proved that the axial temperature gradient in the core bed can be neglected for methanol synthesis. In the case of DME synthesis, the CO_2 conversion was higher than that of methanol synthesis, but this excess heat produced can be removed by twice the wall surface area, as the total mass of catalyst was 0.8 g for the DME synthesis experiments and 0.4 g for the methanol synthesis experiments. Thus, we considered in this work that the reactor was isothermal.

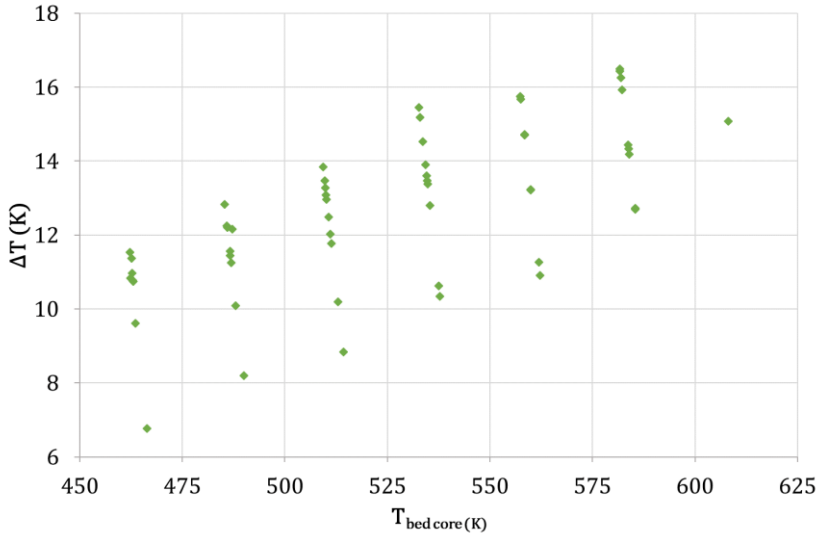

Figure 3.1 Temperature gradient of the furnace and fixed bed core as a function of the fixed bed core temperature. Operating conditions: P=26, 31 and 36 bars, T=473.15 – 623.15 K, GHSV=3.6 – 12.2 L. $g_{cat}^{-1}.h^{-1}$.

3.3.1.2. Deactivation kinetics

Two similar experiments were carried out to assess deactivation at same feed molar ratio $H_2/CO_2/N_2$= 67.5/22.5/10 and GHSV=7.3-7.7 $L.g_{cat}^{-1}.h^{-1}$. Even though, they were not at the same pressure, 31 and 36 bars; it was confirmed by thermodynamics by means of RGIBBS in Aspen Plus, that their CO_2 conversions should be very close, as shown in Figure 3.2a. For DME, methanol and CO yields, the differences seemed to be even smaller (Figure 3.2b-d). Firstly, an experiment at 36 bars and T=200-350 °C was performed after two other experiments at different operating conditions were performed and then, after about 19 hours 23 minutes of operation, a fourth experiment at 31 bars and T=325-200 °C was carried out (as presented in Chapter 2, Table 2.8).

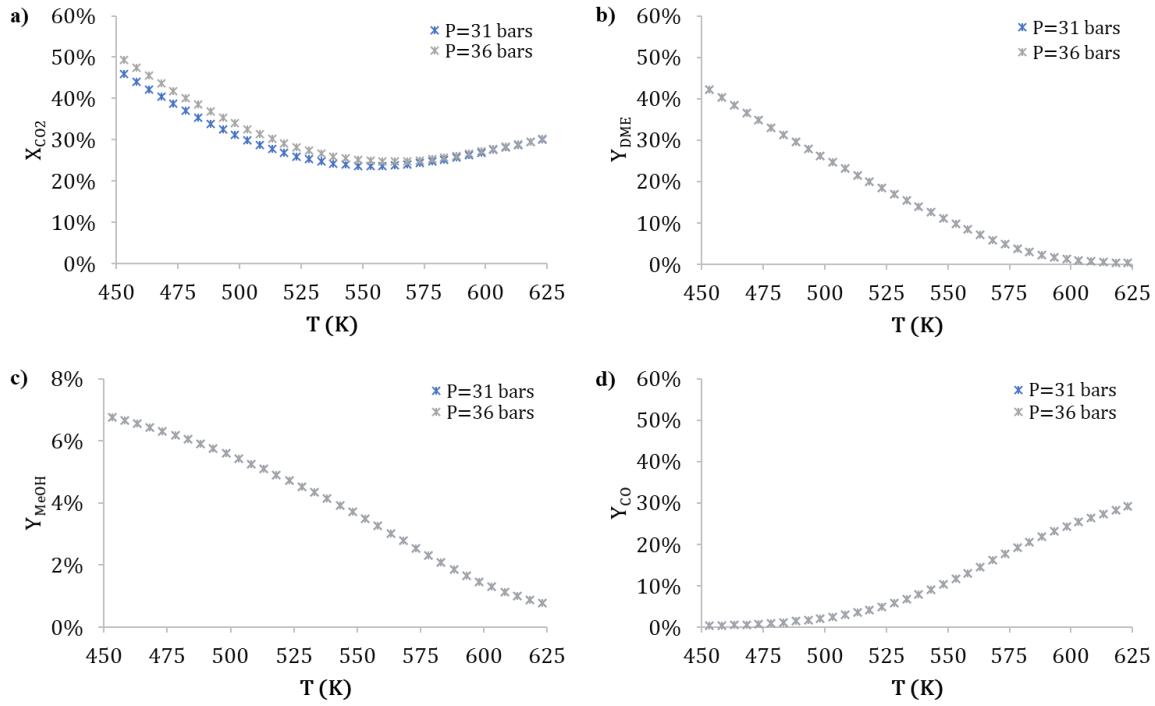

Figure 3.2 a) CO_2 conversion, b) DME, c) methanol and) CO yields as a function of temperature in chemical equilibrium calculated by means of RGIBBS in Aspen Plus. Operating conditions: P=31 and 36 bars, $H_2/CO_2/N_2$=67.5/22.5/10.

For the experiments, there was a significant difference between CO_2 conversion and DME yield at 31 and 36 bars that should be thermodynamically similar, especially at high temperatures where thermodynamic equilibrium is reached. Less significant discrepancies were observed in methanol and CO yields (Figure 3.3). The inequality cannot be interpreted only through the difference in pressure. Despite the fact that a minor temperature mismatch was observed, this same behaviour was found by other authors in the literature [1], [10], [11]. Thus, following the results of Quezada, 2020 [1] obtained for a similar CZA catalyst, the deactivation is introduced in this model by multiplying the reaction rates by a deactivation function, directly proportional to the moles of CO_2 converted.

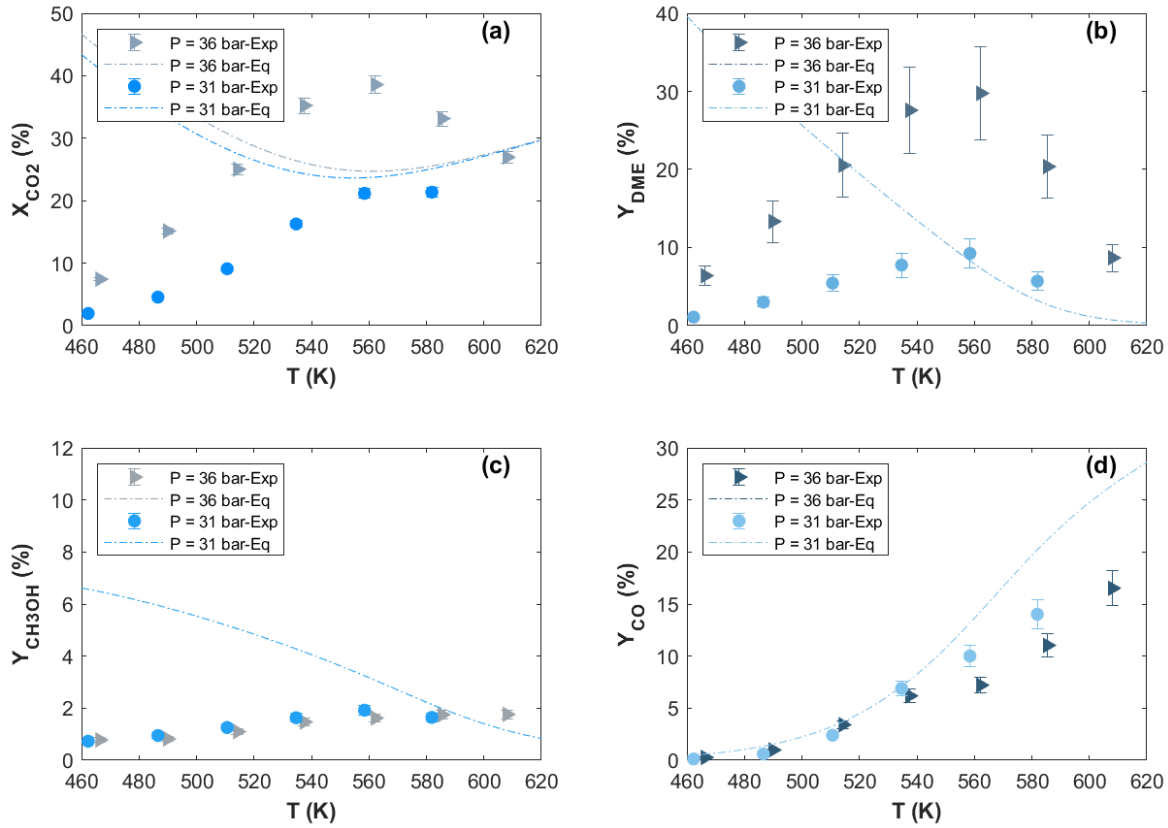

Figure 3.3 Comparison of experiments to demonstrate catalyst deactivation. (a) CO_2 conversion, (b) DME, (c) methanol and (d) CO yield. Dashes lines represent the chemical equilibrium. Operating conditions: $H_2/CO_2/N_2$=67.5/22.5/10, GHSV= 7.3-7.7 8 L. $g_{cat}^{-1}.h^{-1}$.

In Figure 3.4, it is observed the accumulated moles of CO_2 converted while carrying out the fifty-six (56) experimental points with a total of 0.24 moles of CO_2 converted. The last point (56,0.24) in the graphic represents the 56 experiments and the sum of CO_2 converted of all experimental points $\left(\sum_{n=1}^{56} n_{CO2,n}\right)$. Consequently, a deactivation function for the CZA catalyst (Eq. (*3.23*)) has been established based on the amount of cumulative moles of CO_2 converted by all experiments and the full activity of the catalyst at the very start of the first experiment:

$$df = 1 - \alpha \cdot n_{CO2,converted} \tag{3.23}$$

where df is the deactivation function, α is a variable for deactivation. The reaction rates of reactions (3.1) and (3.2) are multiplied by Eq. (3.23) as ensuing:

$$r_1 = \frac{df \cdot k_1 e^{-\frac{E_1}{RT}}\left(p_{CO_2} p_{H_2}^3 - p_{CH_3OH} p_{H_2O}/K_1\right)}{p_{H_2}^{(3-\nu_1/2)} \cdot \left(1 + K_{CO_2} p_{CO_2} + \sqrt{K_{H_2} p_{H_2}} + K_{CH_3OH} p_{CH_3OH} + K_{H_2O} p_{H_2O} + K_{CO} p_{CO}\right)^3} \tag{3.24}$$

$$r_2 = \frac{df \cdot k_2 e^{-\frac{E_2}{RT}}\left(p_{CO_2}p_{H_2} - p_{CO}p_{H_2O}/K_2\right)}{p_{H_2}^{(1-\nu_2/2)} \cdot \left(1 + K_{CO_2}p_{CO_2} + \sqrt{K_{H_2}p_{H_2}} + K_{CH_3OH}p_{CH_3OH} + K_{H_2O}p_{H_2O} + K_{CO}p_{CO}\right)^2} \quad (3.25)$$

The variable α for deactivation is part of the parameters to be optimised.

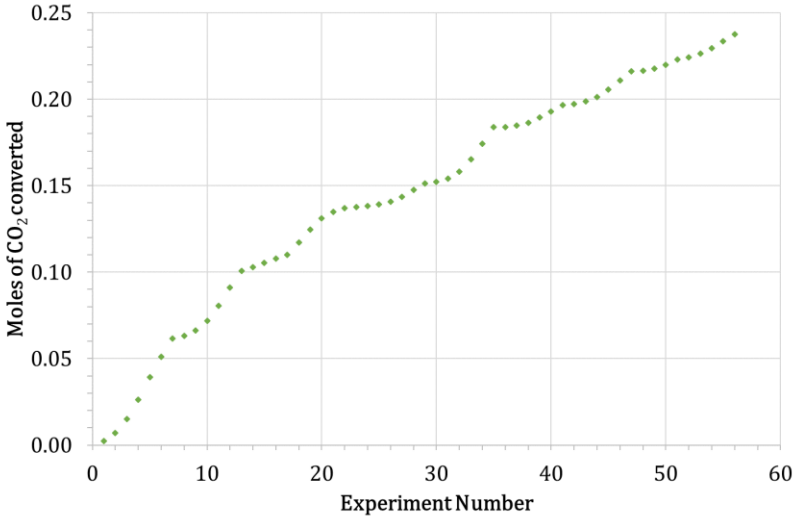

Figure 3.4 Moles of CO_2 converted accumulated during all the carried-out experiments as a function of experiment number.

3.3.2. Model equations

The reactor model is described by material balance equations with the mole fractions of all the involved components in the reactions as state variables. The assumptions for the reactor modelling are:

- reactor behaves as a plug flow reactor with no axial and radial dispersion,
- operation is of steady-state nature,
- the reactor is isobaric and isothermal,
- CZA-C catalyst deactivation occurs and is considered in the reaction rate formulations,
- there is no deactivation of zeolite (HZSM-5).

Figure 3.5 shows a representation of the plug flow reactor (PFR). The input and output molar flows are $F_{t,in}$ and $F_{t,out}$, respectively; z is the axial position in the catalyst bed, and L is the length of the reactor.

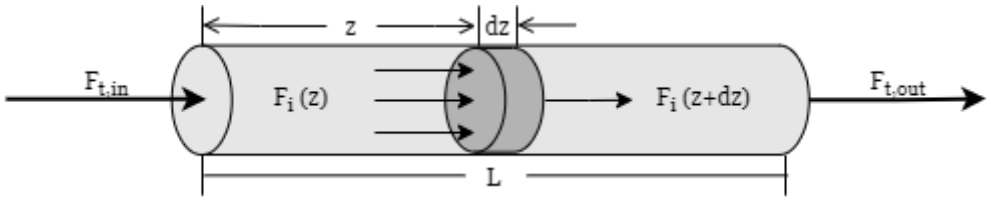

Figure 3.5 Illustration of a plug-flow reactor.

As the steady state is supposed, the variation in the molar flow rate of each component i as it flows through the catalyst bed corresponds to its respective production rate R_i:

$$\frac{dF_i}{dz} = \Omega \rho_{bed} R_i \tag{3.26}$$

$$R_i = \sum_i \nu_{ij} r_j \ (p_i, T) \tag{3.27}$$

where Ω and ρ_{bed} are the cross-sectional area and density of the catalyst bed, respectively. ν_{ij} is the stoichiometric number of each specie i on j reaction and, r_j is the reaction rate.

The total molar balance is expressed:

$$F_t = \sum_i F_i \tag{3.28}$$

$$\frac{dF_t}{dz} = \sum_i \frac{dF_i}{dz} = \Omega \rho_{bed} \sum_i R_i \tag{3.29}$$

The kinetics are done as a function of the molar fractions of concerned species y_i.

$$R_{CO_2} = -\left(\frac{1}{3} r_1 + r_2\right) \tag{3.30}$$

$$R_{H_2} = -(r_1 + r_2) \tag{3.31}$$

$$R_{CH_3OH} = \frac{1}{3} r_1 - 2r_4 \tag{3.32}$$

$$R_{H_2O} = \frac{1}{3} r_1 + r_2 + r_4 \tag{3.33}$$

$$R_{CO} = r_2 \tag{3.34}$$

$$R_{CH_3OCH_3} = r_4 \tag{3.35}$$

For all the species, the global material balances (between the reactor input and output) can be written as in Table 3.5.

Table 3.5 Global material balances of the species.

Species	$F_{i,out}$		
N_2	$F_{N_2,\,out}$	=	$F_{N_2,\,in}$
CO_2	$F_{CO_2,\,out}$	=	$F_{CO_2,\,in} - (1/3\,X_1 + X_2)F_{t,in}$
H_2	$F_{H_2,\,out}$	=	$F_{H_2,\,in} - (X_1 + X_2)F_{t,in}$
CH_3OH	$F_{CH_3OH,\,out}$	=	$F_{CH_3OH,\,in} + (1/3\,X_1 - 2X_4)F_{t,in}$
H_2O	$F_{H_2O,\,out}$	=	$F_{H_2O,\,in} + (1/3\,X_1 + X_2 + X_4)F_{t,in}$
CO	$F_{CO,\,out}$	=	$F_{CO,\,in} + X_2F_{t,in}$
CH_3OCH_3	$F_{CH_3OCH_3,\,out}$	=	$F_{CH_3OCH_3,\,in} + X_4F_{t,in}$
Total	$F_{t,\,out}$	=	$F_{t,\,in}(1 - 2/3\,X_1)$

Bearing in mind expressions (3.26) and (3.30) – (3.35), the mole fractions of each component i are obtained as:

$$\frac{dF_i}{dz} = \frac{d(F_t \cdot y_i)}{dz} = F_t\frac{dy_i}{dz} + y_i\frac{dF_t}{dz} = \Omega\rho_{bed}R_i \tag{3.36}$$

Substituting (3.29) into (3.36), we obtain:

$$\frac{dy_i}{dz} = \frac{1}{F_t}\left(\Omega\rho_{bed}R_i - y_i\frac{dF_t}{dz}\right) = \frac{\Omega\rho_{bed}}{F_t}\left(R_i - y_i\sum_i R_i\right) \tag{3.37}$$

As $\sum_i R_i = -\frac{2}{3}r_1$,

$$\frac{dy_i}{dz} = \frac{\Omega\rho_{bed}}{F_t}\left(R_i + \frac{2}{3}y_i r_1\right) \tag{3.38}$$

Then,

$$\frac{dy_{CO_2}}{dz} = -\frac{\Omega\rho_{bed}}{F_t}\left(\frac{1}{3}r_1 + r_2 - \frac{2}{3}y_{CO_2}r_1\right) \tag{3.39}$$

$$\frac{dy_{H_2}}{dz} = -\frac{\Omega\rho_{bed}}{F_t}\left(r_1 + r_2 - \frac{2}{3}y_{H_2}r_1\right) \tag{3.40}$$

$$\frac{dy_{H_2O}}{dz} = \frac{\Omega\rho_{bed}}{F_t}\left(\frac{1}{3}r_1 + r_2 + r_4 + \frac{2}{3}y_{H_2O}r_1\right) \tag{3.41}$$

$$\frac{dy_{CO}}{dz} = \frac{\Omega\rho_{bed}}{F_t}\left(r_2 + \frac{2}{3}y_{CO}r_1\right) \tag{3.42}$$

$$\frac{dy_{CH_3OH}}{dz} = \frac{\Omega\rho_{bed}}{F_t}\left(\frac{1}{3}r_1 - 2r_4 + \frac{2}{3}y_{CH_3OH}r_1\right) \tag{3.43}$$

$$\frac{dy_{CH_3OCH_3}}{dz} = \frac{\Omega\rho_{bed}}{F_t}\left(r_4 + \frac{2}{3}y_{CH_3OCH_3}r_1\right) \tag{3.44}$$

Finally, the expressions for the reaction rates expressed as functions of the partial pressures can be written using the mole fractions due to the relation:

$$p_i = y_i P_t \tag{3.45}$$

knowing that reaction rates of reactions (3.1), (3.2) and (3.4) are:

$$r_1 = \frac{df \cdot k_1 e^{-\frac{E_1}{RT}}\left(p_{CO_2}p_{H_2}^3 - p_{CH_3OH}p_{H_2O}/K_1\right)}{p_{H_2}^2 \cdot \left(1 + K_{CO_2}p_{CO_2} + \sqrt{K_{H_2}p_{H_2}} + K_{CH_3OH}p_{CH_3OH} + K_{H_2O}p_{H_2O} + K_{CO}p_{CO}\right)^3} \tag{3.46}$$

$$r_2 = \frac{df \cdot k_2 e^{-\frac{E_2}{RT}}\left(p_{CO_2}p_{H_2} - p_{CO}p_{H_2O}/K_2\right)}{p_{H_2}^{0.5} \cdot \left(1 + K_{CO_2}p_{CO_2} + \sqrt{K_{H_2}p_{H_2}} + K_{CH_3OH}p_{CH_3OH} + K_{H_2O}p_{H_2O} + K_{CO}p_{CO}\right)^2} \tag{3.47}$$

$$r_4 = \frac{k_4 e^{-\frac{E_4}{RT}}\left(p_{CH_3OH}^2 - \frac{p_{CH_3OCH_3}p_{H_2O}}{K_4}\right)}{\left(1 + 2\sqrt{K_{CH_3OH,ZSM5}p_{CH_3OH}} + K_{CH_3OCH_3}p_{CH_3OCH_3} + K_{H_2O,ZSM5}p_{H_2O}\right)^2} \tag{3.48}$$

and substituting Eq. (3.46)-(3.48) into Eq. (3.39)-(3.44), as applicable, to obtain the respective component molar fraction.

3.3.3. Parameter estimation algorithm

The computation algorithm for the parameter estimate is described in Figure 3.6. The "parameters initialization" module initializes the operating variables and reactor characteristics, and initializes the parameters to be estimated, which were the activation energy (E_a), pre-exponential factor (k_j) and adsorption constants (K_i), and deactivation factor (α). The first two were calculated by Arrhenius law.

Table 3.6 lists the operating variables used for reactor modelling. Likewise, the input and output molar flows and moles of converted CO_2 of each experiment are part of the program inputs.

Table 3.6 Reactor configuration and operating conditions

Parameters	Value	Unit
Catalyst mass	0.4	g
Bed diameter	0.004	m
Bed length	0.059	m
Pressure	$26, 31, 36$	bar
Temperature	$473.15 - 623.15$	K
R	8.3145	$J.mol^{-1}.K^{-1}$

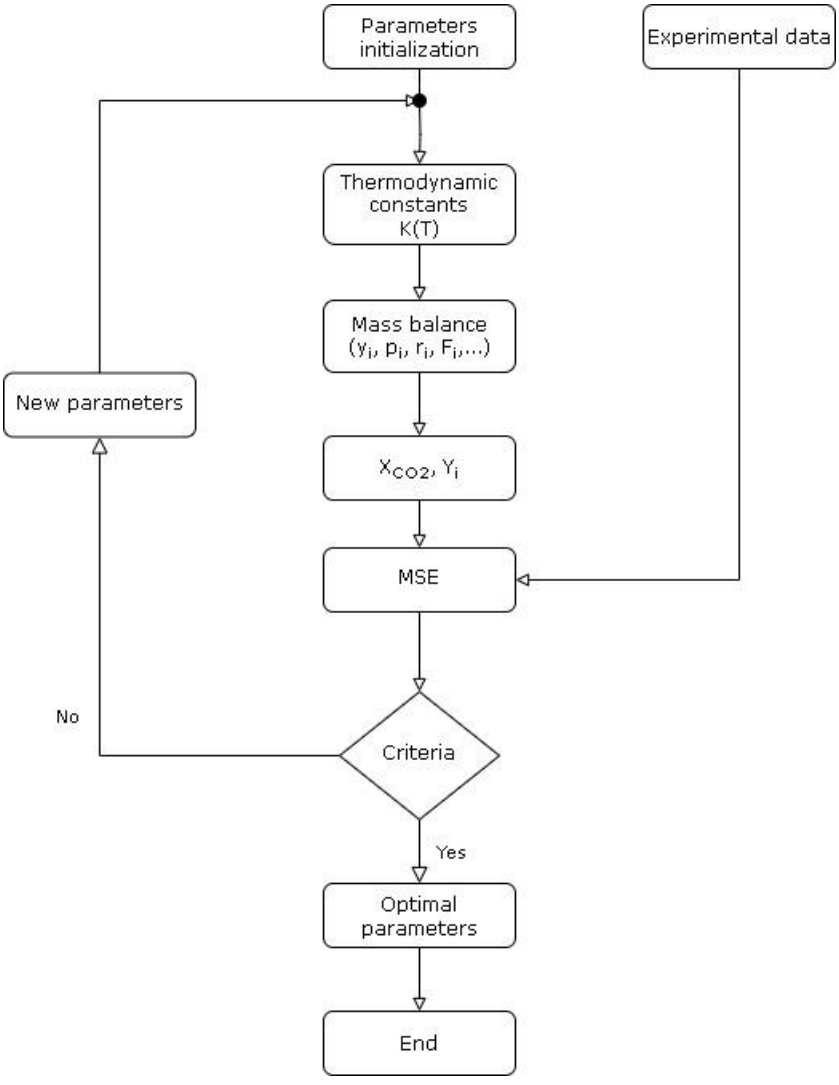

Figure 3.6 Representation of program modelling in MATLAB. MSE is the mean squared error.

The equilibrium thermodynamic constants of each reaction (K_j) are calculated by means of RGIBBS on Aspen Plus. CO_2, H_2 and N_2 were considered as reactants and as main

products in combination with H_2O, CO, CH_3OH and CH_3OCH_3. Soave-Redlich-Kwong (SRK) was chosen as the equation of state. Equilibrium partial pressures are computed based on the molar fractions stream results. Equilibrium constants are derived as a function of these partial pressures (Eq. (3.45), (3.49)-(3.52)). Calculations were performed by adjusting operating conditions based on experiments using the Sensitivity Model Analysis Tool, enabling systematic calculation of equilibrium partial pressures and equilibrium constants over a temperature range of 300.15–800.15 K for specific inlet conditions.

$$K_{1,T} = \frac{p_{CH_3OH} p_{H_2O}}{p_{CO_2} p_{H_2}^3} \tag{3.49}$$

$$K_{2,T} = \frac{p_{CO} p_{H_2O}}{P_{CO_2} P_{H_2}} \tag{3.50}$$

$$K_{3,T} = \frac{p_{CH_3OH}}{p_{CO} p_{H_2}^2} \tag{3.51}$$

$$K_{4,T} = \frac{p_{CH_3OCH_3} p_{H_2O}}{p_{CH_3OH}^2} \tag{3.52}$$

CO_2 conversion and CO, CH_3OH and CH_3OCH_3 yield equilibrium curves were calculated using Eq. (3.53)-(3.56). Hence, it was possible to plot them under the different conditions assessed.

$$X_{CO_2,DME} = \frac{y_{CH_3OH} + y_{CO} + 2 \cdot y_{CH_3OCH_3}}{y_{CO_2} + y_{CH_3OH} + y_{CO} + 2 \cdot y_{CH_3OCH_3}} \cdot 100 \tag{3.53}$$

$$Y_{MeOH,DME} = \frac{y_{CH_3OH}}{y_{CO_2} + y_{CH_3OH} + y_{CO} + 2 \cdot y_{CH_3OCH_3}} \cdot 100 \tag{3.54}$$

$$Y_{CO,DME} = \frac{y_{CO}}{y_{CO_2} + y_{CH_3OH} + y_{CO} + 2 \cdot y_{CH_3OCH_3}} \cdot 100 \tag{3.55}$$

$$Y_{DME,DME} = \frac{2 \cdot y_{CH_3OCH_3}}{y_{CO_2} + y_{CH_3OH} + y_{CO} + 2 \cdot y_{CH_3OCH_3}} \cdot 100 \tag{3.56}$$

To solve the balance equation system, MATLAB® uses ordinary differential equations (ODE). ODE45 was chosen, based on Runge-Kutta of fourth- and fifth-order formula, the Dormand-Prince pair.

The adjustable model parameters of reactions are estimated by means of global optimisation using *MultiStart* to search for the global minimum and using nonlinear least-squares (*lsqnonlin*) as local minimum solver in MATLAB®. This solves curve fitting

problem by global localization minimisation of the followed criteria, OF, where the experimental inlet molar flows were the source of comparison:

$$OF = \sum_{i=1}^{n} \left[\left(\frac{F_{CH_3OCH_3,exp} - F_{CH_3OCH_3,cal}}{F_{CH_3OCH_3,exp}} \right)^2 + \left(\frac{F_{CH_3OH,exp} - F_{CH_3OH,cal}}{F_{CH_3OH,exp}} \right)^2 + \left(\frac{F_{CO,exp} - F_{CO,cal}}{F_{CO,exp}} \right)^2 \right] \quad (3.57)$$

where n is the number of experimental points, $F_{i,exp}$ and $F_{i,cal}$ represent the experimental and calculated molar flow rates at the reactor outlet of species i, respectively. The algorithm method chosen to work with was the Levenberg-Marquardt.

3.3.4. Numerical solution approach

The first model was based on model developed by Quezada, 2020 [1] and assuming dissociation of methanol during adsorption for DME synthesis. For methanol and DME synthesis, the parameters were initialized, but not limited to, with the values of Quezada, 2020 [1] and of Ortega et al., 2018 [12], respectively. In the first trial, all kinetic parameters were optimised at the same time. But, as it was not working, it was decided to optimise by set of parameters; in first place, the pre-exponential factors (k_1, k_2, k_4) and activation energies (E_1, E_2, E_4) of reactions and then, the adsorptions constants ($K_{H_2}, K_{CO_2}, K_{CH_3OH}, K_{CO}, K_{CH_3OH,DME}, K_{H_2O,DME}$) with the deactivation factor (α).

Several initiations were tried considering the proposals found in literature. As part of the model fitting, a discrimination and estimate of the parameter values was done. Quezada, 2020 [1] remained in kinetic model for methanol synthesis. Nonetheless, for DME synthesis, it was required to change the reaction rate, as explained later in this chapter, due to the experiments results distant from thermodynamic equilibrium.

3.4. Results of kinetic parameter estimate

3.4.1. Initial values

The initial kinetic parameters used to optimise methanol synthesis are those obtained by Quezada, 2020 [1] and given in Table 3.7. Parameters will be re-optimised according to the results of our new experiments carried out with the commercial Alfa Aesar "copper-based methanol synthesis catalyst" CZA-C.

Table 3.7 Initial parameters for methanol synthesis.

Parameter	Value	Unit	Parameter	Value	Unit
k_1	$1.96 \cdot 10^5$	$mol.g^{-1}.h^{-1}.bar^{-2}$	E_1	58.19	$kJ.mol^{-1}$
k_2	$2.09 \cdot 10^8$	$mol.g^{-1}.h^{-1}.bar^{-1.5}$	E_2	94.76	$kJ.mol^{-1}$
k_3	0	$mol.g^{-1}.h^{-1}.bar^{-2}$	E_3	0	$kJ.mol^{-1}$
$\left(K_{H_2}\right)^{0.5}$	2.12	$bar^{-0.5}$	K_{CO}	0.58	bar^{-1}
K_{CO_2}	1.5	bar^{-1}	K_{CH_3OH}	7.16	bar^{-1}

Regarding the synthesis of DME, Ortega et al., 2018 [12] compared different models, but they concluded that the modified Klusáček & Schneider model was the most robust at the kinetic level and it provides excellent performance in describing the conversion of methanol to DME on ZSM-5. These kinetic parameters are therefore the ones taken into consideration as initial values (Table 3.8).

In relation to the adsorption constants of methanol and water for reaction Eq. (3.4), they were expressed as a function of the entropy $\left(\Delta S^0_{ad,i}\right)$ and enthalpy $\left(\Delta H^0_{ad,i}\right)$ of adsorption in ZSM-5 as follows:

$$K_i = exp\left[\frac{\Delta S^0_{ad,i}}{R}\right] exp\left[-\frac{\Delta H^0_{ad,i}}{RT}\right] \tag{3.58}$$

with K_i as the adsorption constant of specie i.

Table 3.8 Initial parameters for DME synthesis.

Parameter	Value	Unit	Parameter	Value	Unit
k_4	6.61	$mol \cdot g^{-1} \cdot h^{-1}$	E_4	109.3	$kJ.mol^{-1}$
K_{DME}	0	bar^{-1}			
$\Delta H^0_{ad,H_2O}$	−73.1	$kJ.mol^{-1}$	$\Delta S^0_{ad,H_2O}$	−0.153	$kJ.mol^{-1}.K^{-1}$
$\Delta H^0_{ad,CH_3OH}$	−70.3	$kJ.mol^{-1}$	$\Delta S^0_{ad,CH_3OH}$	−0.137	$kJ.mol^{-1}.K^{-1}$

DME adsorption is negligible [13]. This is also supported by the work of Ortega et al., 2018 [12].

3.4.2. Kinetics of methanol synthesis

A first optimisation was made, using the results of the experiment with CZA-C without zeolite. This was initialized with the parameters of Table 3.7. The program was executed by means of *lsqnonlin*. As we have considered only reactions (3.1) and (3.2) present in CO_2 hydrogenation to methanol, Eq. (3.57) and Eq. (*3.46*)-(3.47) are used for this optimisation. Therefore, in all the equations such as Eq. (3.53)-(3.55), (3.57), variables related to DME were fixed equal to zero.

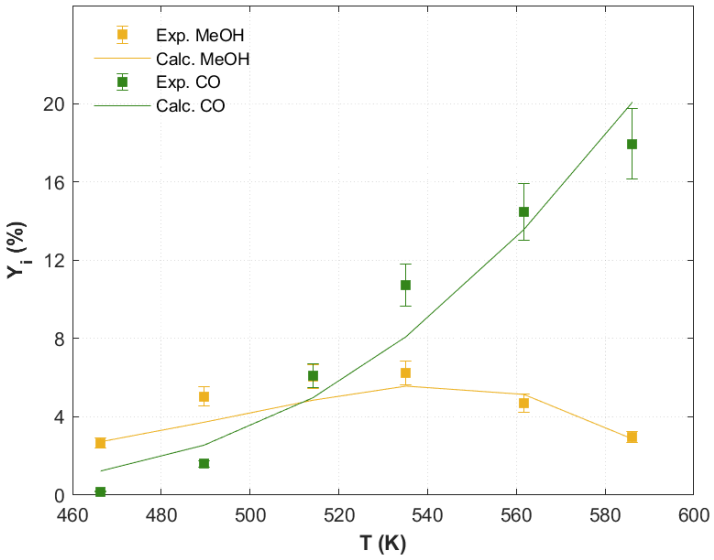

Figure 3.7 Comparison of experimental and calculated data for methanol synthesis. Operating conditions: H_2/CO_2=3, P = 36 bar, GHSV=15.3 $L.g_{cat}^{-1}.h^{-1}$ and N_2=10%. Refer to Table 2.6, Experiment 4.

Figure 3.7 displays the fitting outcome plotted with the optimised parameters given in Table 3.9. Error bars are set at 3.5%, based on the values reported by Quezada, 2020 [1], who used the same experimental setup. Simulated values are satisfactorily aligned with experimental findings. After estimate, adsorption parameters remained unchanged, but activation energies and pre-exponential factors changed significantly. Since there were only six experiments carried out for methanol synthesis, the estimated values could have been not totally significant. Moreover, as there were more experiments performed for DME synthesis, we assumed that the precision could have improved during the estimate

for the DME synthesis. Thus, it was decided to use these values as the feed for the next optimisation step: DME synthesis (CZA-C+HZSM-5). Table 3.9 is then the initiation data used for DME optimisation.

Table 3.9 Optimised parameters for methanol synthesis.

Parameter	Value	Unit	Parameter	Value	Unit
k_1	$1.94 \cdot 10^3$	$mol.g^{-1}.h^{-1}.bar^{-2}$	E_1	29.5	$kJ.mol^{-1}$
k_2	$4.10 \cdot 10^5$	$mol.g^{-1}.h^{-1}.bar^{-1.5}$	E_2	63.8	$kJ.mol^{-1}$
$\left(K_{H_2}\right)^{0.5}$	2.12	$bar^{-0.5}$	K_{CO}	0.58	bar^{-1}
K_{CO_2}	1.5	bar^{-1}	K_{CH_3OH}	7.16	bar^{-1}

3.4.3. Kinetics of dimethyl-ether synthesis

At this stage, the optimisation was done with experiments 4-10 of Table 2.8. Because experiments 1-3 were found to be far above equilibrium, they were excluded from the set of data for parameters optimisation. It could be related to the fact that the catalyst was unlikely to be stable. This is even though there was a catalyst reduction for about 90 minutes at 400 °C before the tests. Moreover, it was confirmed that the sum of moles of water converted from experiments 1-3 $\left(\sum_1^3 n_{H_2O} = 1.25 \cdot 10^{-1}\ moles\right)$ was very close to the sum of the rest of catalytic tests $\left(\sum_4^{10} n_{H_2O} = 1.26 \cdot 10^{-1}\ moles\right)$. Consequently, it was assumed that the adsorption of water by fresh zeolite was more critical at the beginning of the runs. This was supposed to lead to the displacement of equilibrium in the process. According to everything explained, experiments 1-3 are not part of the optimisation model, even though they will be later included in the simulations.

Chapter 2 illustrates that experiments performed with CZA-C+HZSM-5 exceeded thermodynamic equilibrium at temperatures above 530 K, in most cases. Consequently, optimisation was not able to simulate this behaviour with Eq. (3.48). As an example, refer to Figure 3.8, DME yield is slightly superior to equilibrium above 560 K, but not enough to approach experimental values.

Table 3.10 gives the values of kinetic parameters after optimisation. After consecutive trials, the adsorption constant of water in DME reaction was identified to be negligible. Therefore, it is not present in Table 3.10. Despite numerous attempts, it was not possible to get closer to the experimental results at high temperatures.

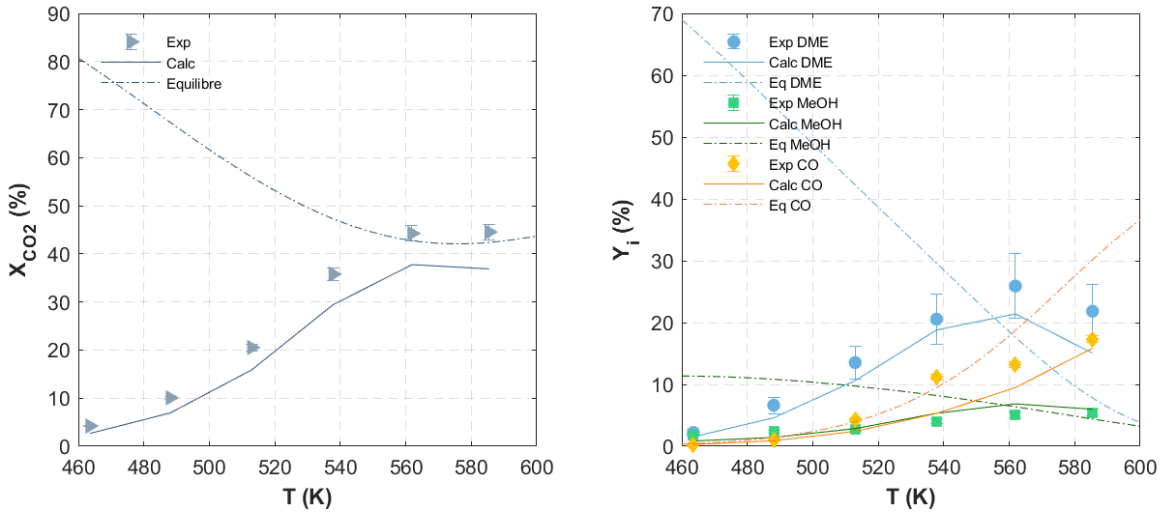

Figure 3.8 Comparison of experimental and calculated conversion and yields for DME synthesis considering chemical equilibrium. Experiment 6. P=36.1 bar, H_2/CO_2=9.7, GHSV=12.2 $L.g_{cat}^{-1}.h^{-1}$ and N_2=10%.

Table 3.10 Optimised parameters values considering equilibrium.

Parameter	Value	Unit	Parameter	Value	Unit
k_1	$3.41 \cdot 10^7$	$mol.g^{-1}.h^{-1}.bar^{-2}$	E_1	73.5	$kJ.mol^{-1}$
k_2	$4.44 \cdot 10^7$	$mol.g^{-1}.h^{-1}.bar^{-1.5}$	E_2	89.8	$kJ.mol^{-1}$
k_4	$7.02 \cdot 10^2$	$mol.g^{-1}.h^{-1}.bar^{-2}$	E_4	23.3	$kJ.mol^{-1}$
$(K_{H_2})^{0.5}$	1.30	$bar^{-0.5}$	K_{CO}	6.47	bar^{-1}
K_{CO_2}	1.09	bar^{-1}	K_{CH_3OH}	$1.33 \cdot 10^2$	bar^{-1}
$K_{CH_3OH,ZSM5}$	$1.89 \cdot 10^{-13}$	bar^{-1}	α	2.53	mol^{-1}

Other kinetic models were also tested such as the ones proposed by Ateka et al., 2018 [14]; De Falco et al., 2016 [15]; Delgado Otalvaro et al., 2020 [16]; Guffanti et al., 2021 [17]; Ortega et al., 2018 [12]. Equally, various initialisation parameters were tested by changing E_j, k_j, adsorption constants, and deactivation factor (α). However, all trials failed.

It was necessary to adjust Eq. (3.48) to evaluate whether the experiments could be adequately simulated, since reaction (3.4) cannot be considered balanced. Several optimisations with updated parameter initialization consistently indicated a decreasing curve from 530-560 K, as thermodynamically predicted, but not as observed. Thus, these outcomes do not describe at all what was happening in our experiments. Consequently, it was decided to use Eq. (3.59) which considers the backward reaction (k_5, E_5). Methanol

dehydration reaction is not yet an equilibrated reaction. It is thus necessary to optimise these two supplementary parameters (k_5, E_5). Associative pathway is applied.

$$r_4 = \frac{k_4 e^{-\frac{E_4}{RT}} p_{CH_3OH}^2 - k_5 e^{-\frac{E_5}{RT}} p_{CH_3OCH_3} p_{H_2O}}{\left(1 + 2\sqrt{K_{CH_3OH,ZSM5} p_{CH_3OH}} + K_{CH_3OCH_3} p_{CH_3OCH_3} + K_{H_2O,ZSM5} p_{H_2O}\right)^2} \quad (3.59)$$

Bearing this in mind, the values of Table 3.10 were employed for another optimisation not taking into account equilibrium. For the newly introduced parameters, k_5 and E_5, initial values that were lower than the ones for reaction (3.4) were settled and given in Table 3.11.

Table 3.11 Initial parameters values with backward reaction (k_5, E_5) not considering equilibrium.

Parameter	Value	Unit	Parameter	Value	Unit
k_5	1.55	$mol.g^{-1}.h^{-1}.bar^{-2}$	E_5	12.3	$kJ.mol^{-1}$

Figure 3.9 illustrates that DME yield was better simulated. No drop exists from 560 K onwards, in contrast to observation in Figure 3.8. Improved fitting is also depicted for CO_2 conversion. Notwithstanding, optimisation enhancement is still necessary in view of CO yield.

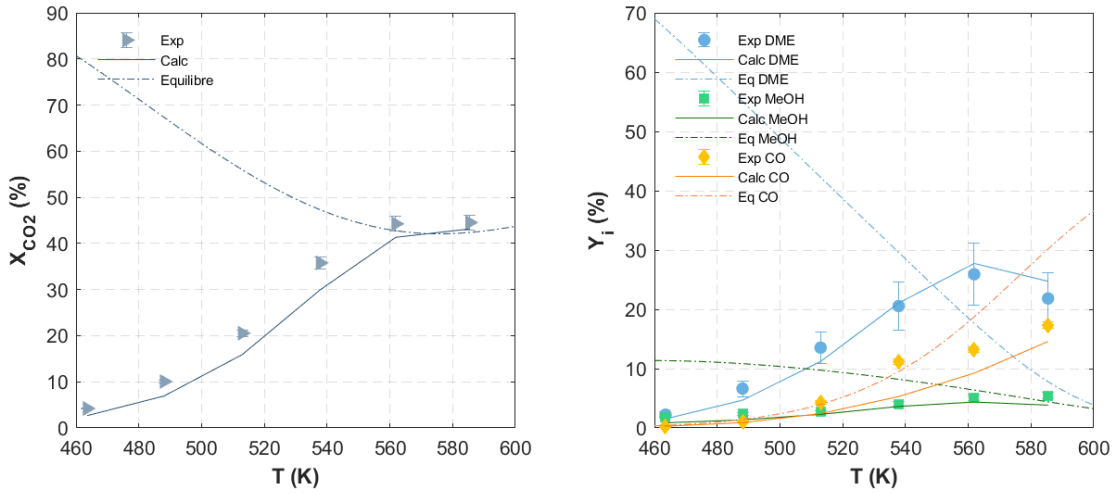

Figure 3.9 Comparison of experimental and calculated for DME synthesis not considering chemical equilibrium. Experiment 6. P=36.1 bar, H_2/CO_2=9.7, GHSV=12.2 L. $g_{cat}^{-1}.h^{-1}$, N_2=10%.

Water and methanol adsorption constants on zeolite for DME synthesis $(K_{H_2O,ZSM5}, K_{CH_3OH,ZSM5})$ were insignificant which is coherent with the kinetics equation for methanol dehydration to DME proposed by Aguayo et al., 2007 [18]; Ateka et al.,

2018, 2020, 2022 [14], [19], [20]; De Falco et al., 2016 [15]; Delgado Otalvaro et al., 2020, 2021, 2022 [7], [16], [21]; Guffanti et al., 2021 [17]; Ortega et al., 2018 [12]. This led to the formulation of Eq. (3.60).

$$r_4 = k_4 e^{-\frac{E_4}{RT}} p_{CH_3OH}^2 - k_5 e^{-\frac{E_5}{RT}} p_{CH_3OCH_3} p_{H_2O} \quad (3.60)$$

Eq. (3.60) enabled the most accurate fit of the experimental data of conditions evaluated in this PhD thesis for methanol dehydration to DME. New kinetic parameters were computed (see Table 3.12). The objective function (OF) was equal to 6.38.

Table 3.12 Optimised final kinetic parameters.

Parameter	Value	Unit	Parameter	Value	Unit
k_1	$3.70 \cdot 10^7$	$mol.g^{-1}.h^{-1}.bar^{-2}$	E_1	73.8	$kJ.mol^{-1}$
k_2	$4.37 \cdot 10^8$	$mol.g^{-1}.h^{-1}.bar^{-1,5}$	E_2	99.1	$kJ.mol^{-1}$
k_4	82.7	$mol.g^{-1}.h^{-1}.bar^{-2}$	E_4	16.5	$kJ.mol^{-1}$
k_5	1.83	$mol.g^{-1}.h^{-1}.bar^{-2}$	E_5	16.1	$kJ.mol^{-1}$
$\left(K_{H_2}\right)^{0.5}$	1.25	$bar^{-0.5}$	K_{CO}	10.1	bar^{-1}
K_{CO_2}	1.03	bar^{-1}	K_{CH_3OH}	4.45	bar^{-1}
α	2.16	mol^{-1}			

Despite the differences in operating conditions, catalysts, and kinetic equations compared, the final calculated kinetic parameters were within the range of those computed by other authors (see Table 3.13).

Table 3.13 Summary of kinetic parameters from literature.

Reference	P (bar)	E_1 ($kJ \cdot mol^{-1}$)	E_2 ($kJ \cdot mol^{-1}$)	E_4 ($kJ \cdot mol^{-1}$)
Aguayo et al., 2007 [18]	$10-40$	–	–	84.1 ± 1.88
Tavan et al., 2013 [22]	10	–	–	69.4
N. Park et al., 2014 [23]	$50-80$	68.25	126.6	123.8
De Falco et al., 2016 [15]	$20-70$	17.1	20.5	52.9
Ortega et al., 2018 [12]	1	–	–	$80-130$
Ainara Ateka et al., 2018 [14]	30	–	91.0 ± 0.35	17.2 ± 0.35
Quezada, 2020 [1]	$26-36$	58.2	94.8	–
Delgado Otalvaro et al., 2021 [7]	50	32.7 ± 2.20	175.4 ± 4.96	105.6 ± 3.22

The fit between simulated and experimental results for CO_2, DME, CH_3OH and CO are represented in Figure 3.10-Figure 3.12. The model parameters were estimated based on 39 experimental data points.

In Figure 3.10-Figure 3.13, the simulated evolution with temperature of CO_2 conversion and DME, CH_3OH and CO yields are compared with the experimental data and the conversion and yields at the thermodynamical equilibrium. It is pertinent to note that the experimental data in Figure 3.13 were not part of the optimisation (experiments 1-3), and are given here to compare with a model simulation. Although experiments 1-3 have been removed from optimisation, the calculated curves of CO_2 conversion and yields in Figure 3.13 a), b), c), d) and f) appear to be similar in shape to experimental data. Only the methanol yield (green lines) appears to be more precisely simulated. Figure 3.10-Figure 3.12 show satisfactory fitting for CO_2 conversion, DME and CH_3OH yields, but CO yield is less accurate, due to the change in shape of the CO yield curve after 530 K, phenomena that we failed to take into account in our model.

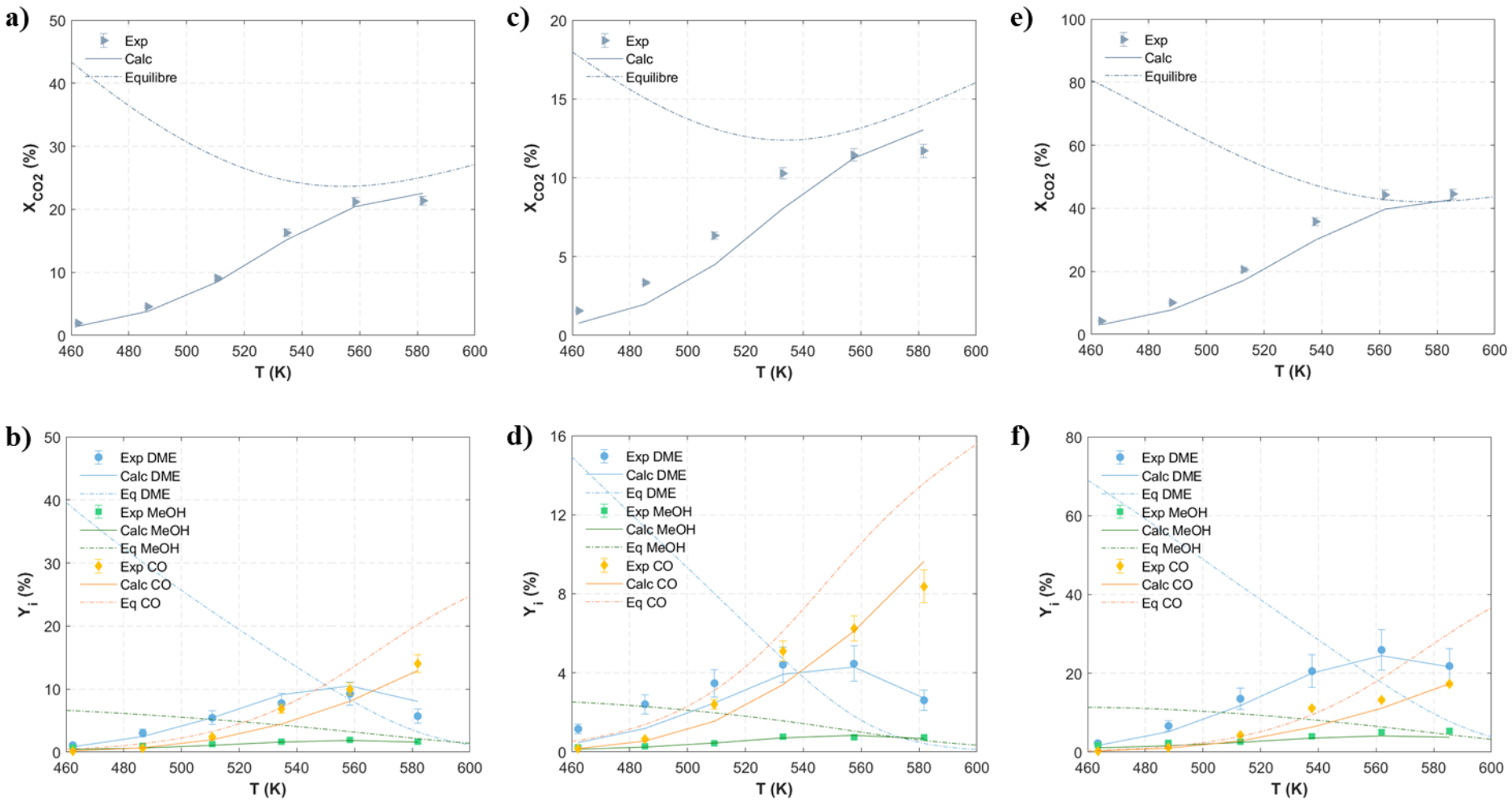

Figure 3.10 Fitting responses of experimental data for CO_2 conversion and DME, methanol and CO yields: a)- b) H_2/CO_2=3, P=31 bar, GSHV=7.7 $L.g_{cat}^{-1}.h^{-1}$; c)- d) H_2/CO_2=1, P=36 bar, GSHV=3.6 $L.g_{cat}^{-1}.h^{-1}$; e)-f) H_2/CO_2=9.7, P=36 bar, GSHV=12.2 $L.g_{cat}^{-1}.h^{-1}$. See Table 2.8: Experiments 4-6.

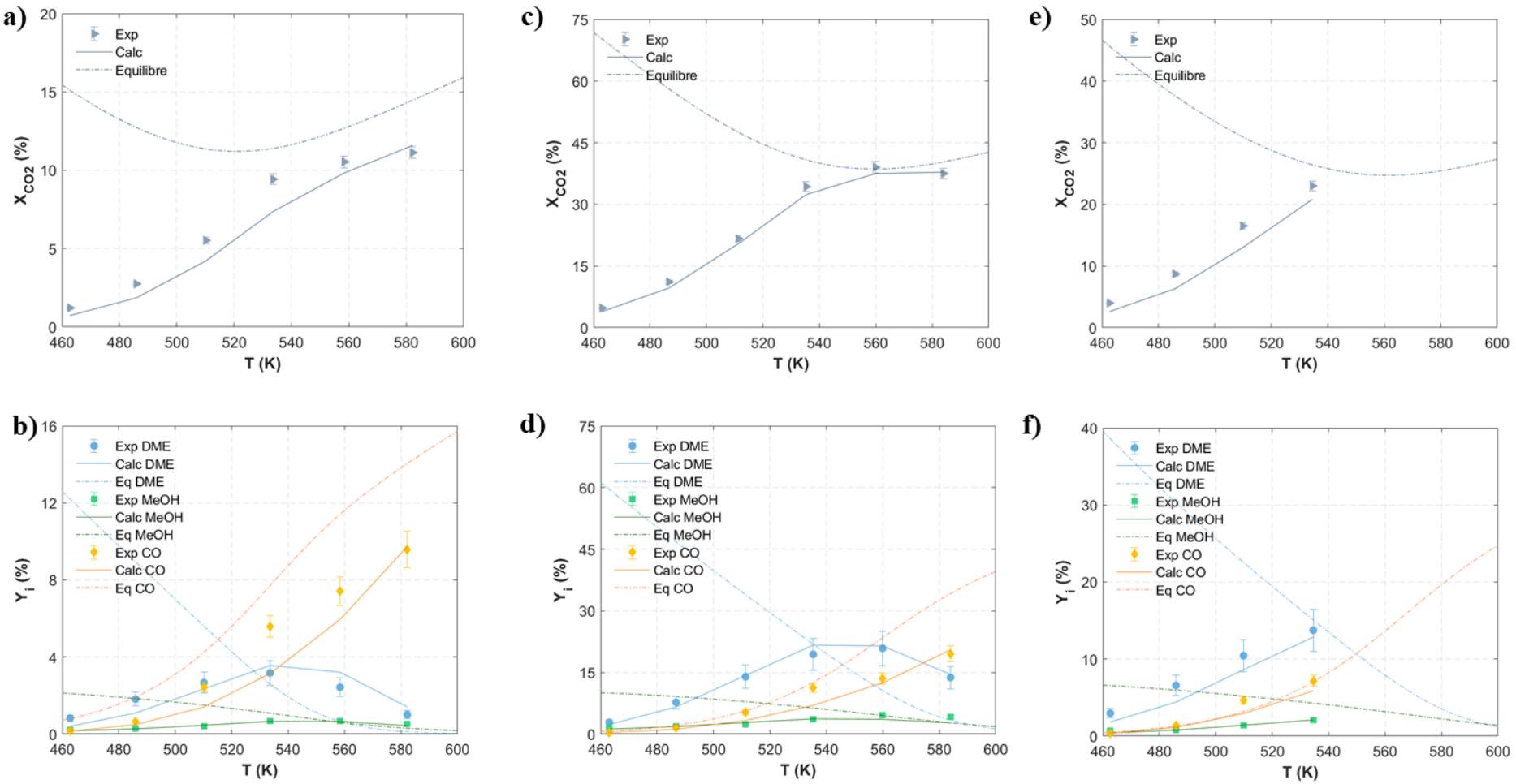

Figure 3.11 Fitting responses of experimental data for CO_2 conversion and DME, methanol and CO yields: a)- b) H_2/CO_2=1, P=26 bar, GSHV=3.6 L. g_{cat}^{-1}. h^{-1}; c)- d) H_2/CO_2=9, P=26 bar, GSHV=7 L. g_{cat}^{-1}. h^{-1}; e)-f) H_2/CO_2=3, P=36 bar, GSHV=3.6 L. g_{cat}^{-1}. h^{-1}. See Table 2.8: Experiments 7-9

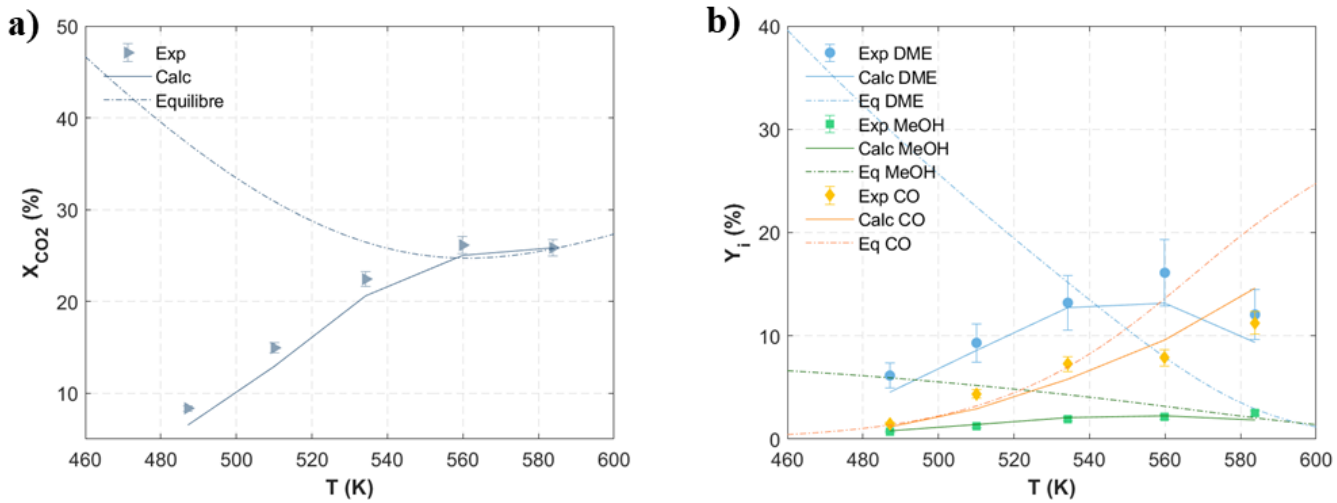

Figure 3.12 Fitting responses of experimental data for CO_2 conversion and DME, methanol and CO yields: a)- b) H_2/CO_2=3, P=36 bar, GSHV=3.4 $L.g_{cat}^{-1}.h^{-1}$. See Table 2.8: Experiment 10.

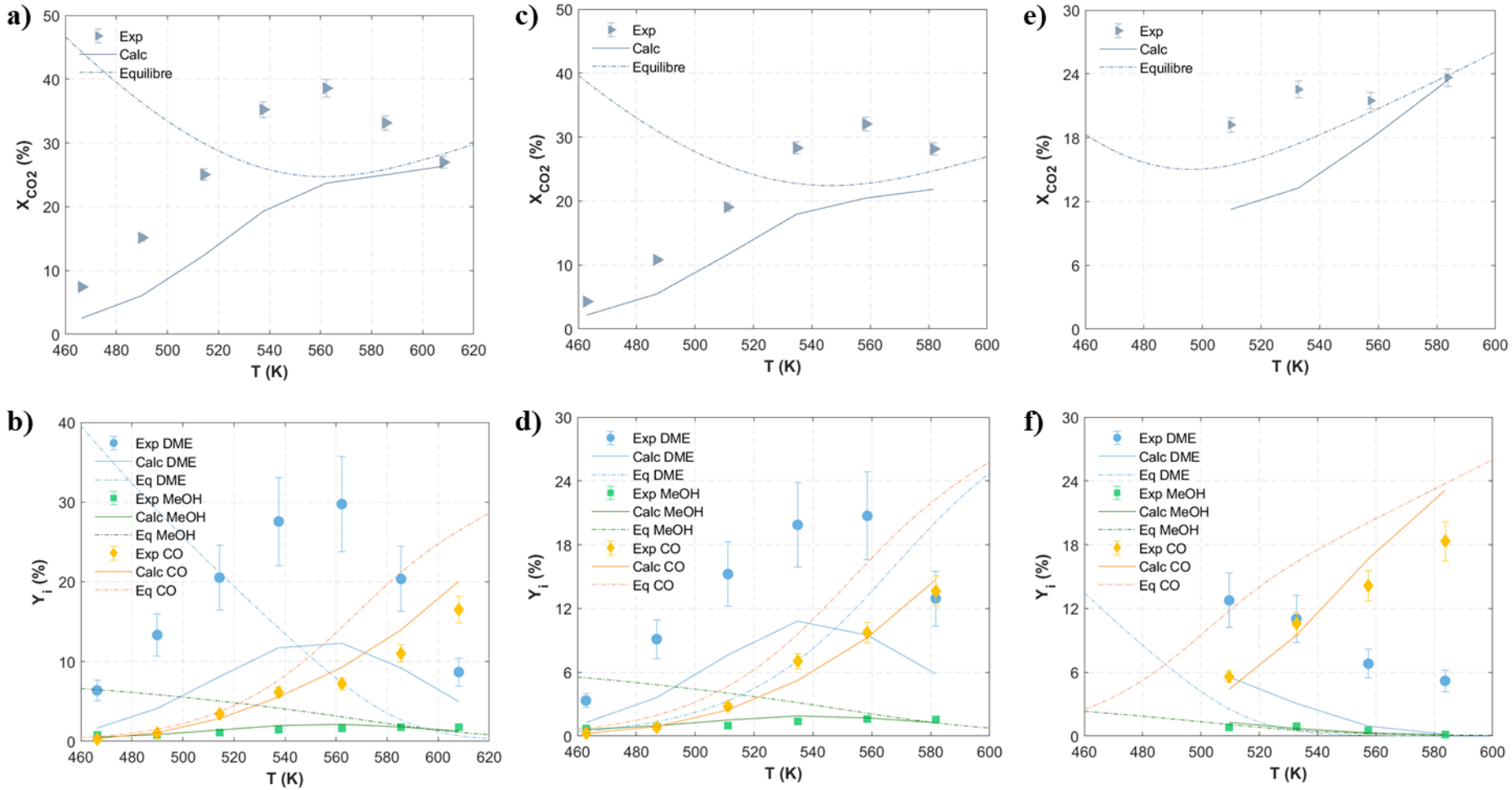

Figure 3.13 Fitting responses of experimental data for CO_2 conversion and DME, methanol and CO yields: a)- b) H_2/CO_2=3, P=36 bar, GSHV=7.3 L. g_{cat}^{-1}. h^{-1}; c)- d) H_2/CO_2=3, P=26 bar, GSHV=7.4 L. g_{cat}^{-1}. h^{-1}; e)-f) H_2/CO_2=3, P=26 bar, GSHV=7.4 L. g_{cat}^{-1}. h^{-1}. See Table 2.8: Experiments 1-3.

3.4.4. Evaluation of model accuracy

Using Minitab® Statistical Software, the accuracy of the kinetic model was evaluated by means of a regression analysis including: parity plots and residual plots (histogram of residuals, normal plot of residuals and residuals versus order of experiments). The experimental and calculated outcomes of the 39 data points were employed to perform the corresponding appraisal (see Figure 3.14). On Figure 3.14, the dotted lines represent the experimental percentage errors. They are estimated at ±3.5% for CO_2 conversion, ±20% for DME yield and ±10% for CH_3OH and CO yields.

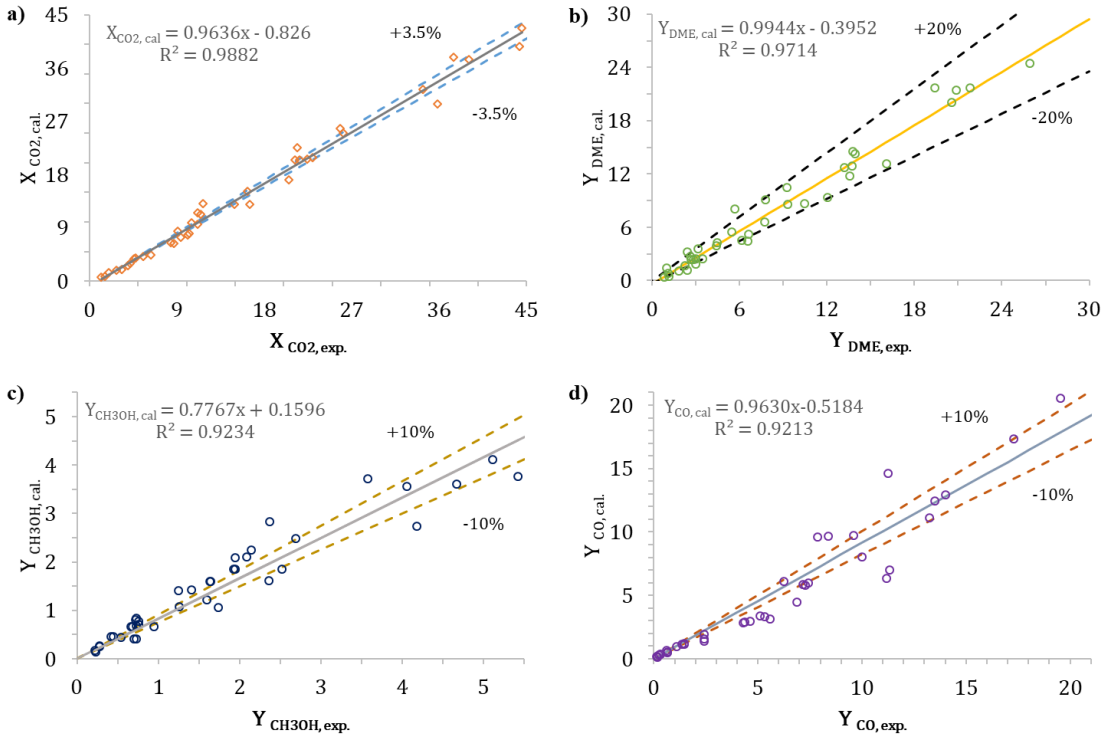

Figure 3.14 Parity plots of experimental vs. calculated a) CO_2 conversion, b) DME, c) CH_3OH and d) CO yields.

Figure 3.14 illustrates that the model fits very well for DME yield and CO_2 conversion but is less precise for CH_3OH and CO yields. In the case of methanol, random scattering could be associated with measurement limitations. Yields are very low and chromatographic errors can lead to high methanol yield errors. CO yield predictions are relatively close to experimental measurements. However, one can notice that 26 points (out of 32) are beyond the lines and the highest relative errors are between 505K and 540K. A change in CO formation mechanism or a more complex mechanism than the simple reaction (3.2) has also been observed experimentally around 530-540 K, indicating that the model probably does not adequately describe it effectively. Nevertheless, the coefficient of determination (R-Squared) for CO and

methanol yields are greater than 0.9. This indicates a good prediction of dependent variables, since about 92% of variations in the calculations are explained by the experiments results.

A residual analysis was done to check whether the model is well-fitted. This analysis aims to know the difference between the computed and predicted values, the latter estimated by the regression equation. Firstly, we analyse the normal probability plot. This supports the assumption of a normal distribution of residuals. The plot of response (calculated values) versus residuals should form a straight line. Afterwards, while identifying bell-shaped curves (common patterns) in the histogram of residuals, it is evident that there is a normal distribution; therefore, it is possible to determine the existence of points far away from the rest of the data group (outliers) and/or skewness in the data. It also helps to see the frequency distribution. Finally, the residuals as a function of the number of each experiment are displayed. This is done to validate the independence of residuals from one another by identifying random distributions on either side of 0. These distributions have no discernible patterns.

Figure 3.15 to Figure 3.17 display residual plots for CO_2 conversion, DME, CH_3OH and CO yields. In Figure 3.15a, the normal probability plot of CO_2 conversion shows a normal distribution, with the points lining up correctly along the diagonal. Nevertheless, the histogram of residuals is heavy-tailed and with one extreme outlier (value lower than one), suggesting a slightly left-skewed distribution (Figure 3.15b). A normal distribution is represented by a bell-shaped curve. Therefore, this is a suitable model for this data set.

The histogram of DME yield suggests that residuals are slightly right-skewed distributed (Figure 3.15d). The normal probability plot looks justly straight, at least when two large values are ignored (Figure 3.15c). This is also the case for CH_3OH yield (Figure 3.16a). CH_3OH yield histogram (Figure 3.16b) shows that the residuals are normally distributed, though negatively tailed and with one extreme outlier (value larger than 0.4). Nevertheless, the distribution is roughly linear, therefore normal. Regarding CO yield, it exhibits the widest variation in data and spreads from -4.5 to 4.5, but it seems to be unimodal and symmetric (bell-shaped) distribution (Figure 3.16d). Its normal probability plot displays an irregular pattern (Figure 3.16c). However, in all cases (conversion and yields), the plot of residuals versus order reveals serial non-correlation (Figure 3.17) as non-systematic behaviour is noticed and the residuals bounce randomly around the residual equal to zero line. This is indicative of the accuracy of this model for CO_2 hydrogenation to DME.

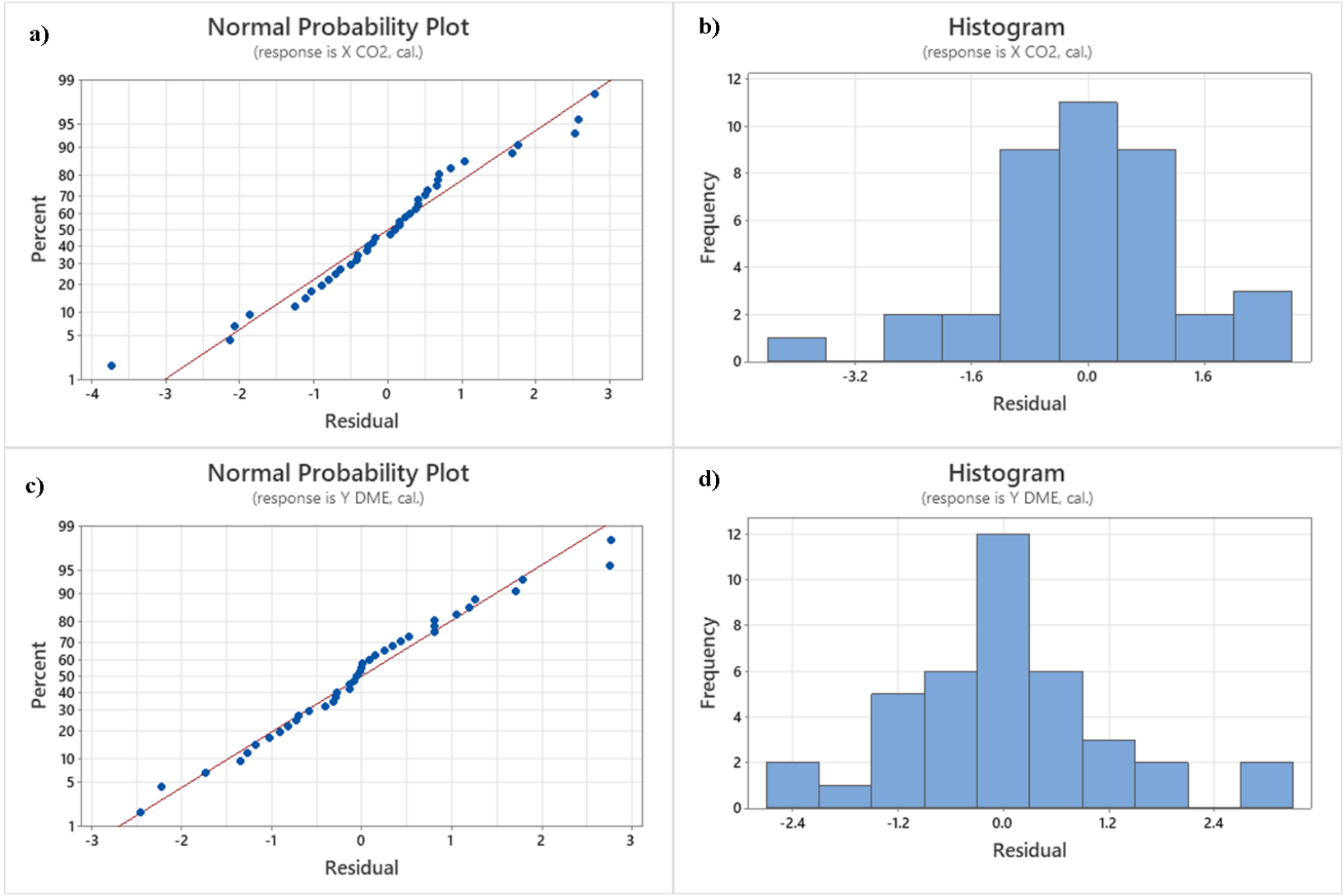

Figure 3.15 Normal and histogram plots of residuals for a) and b) CO_2 conversion, c) and d) DME yield, respectively.

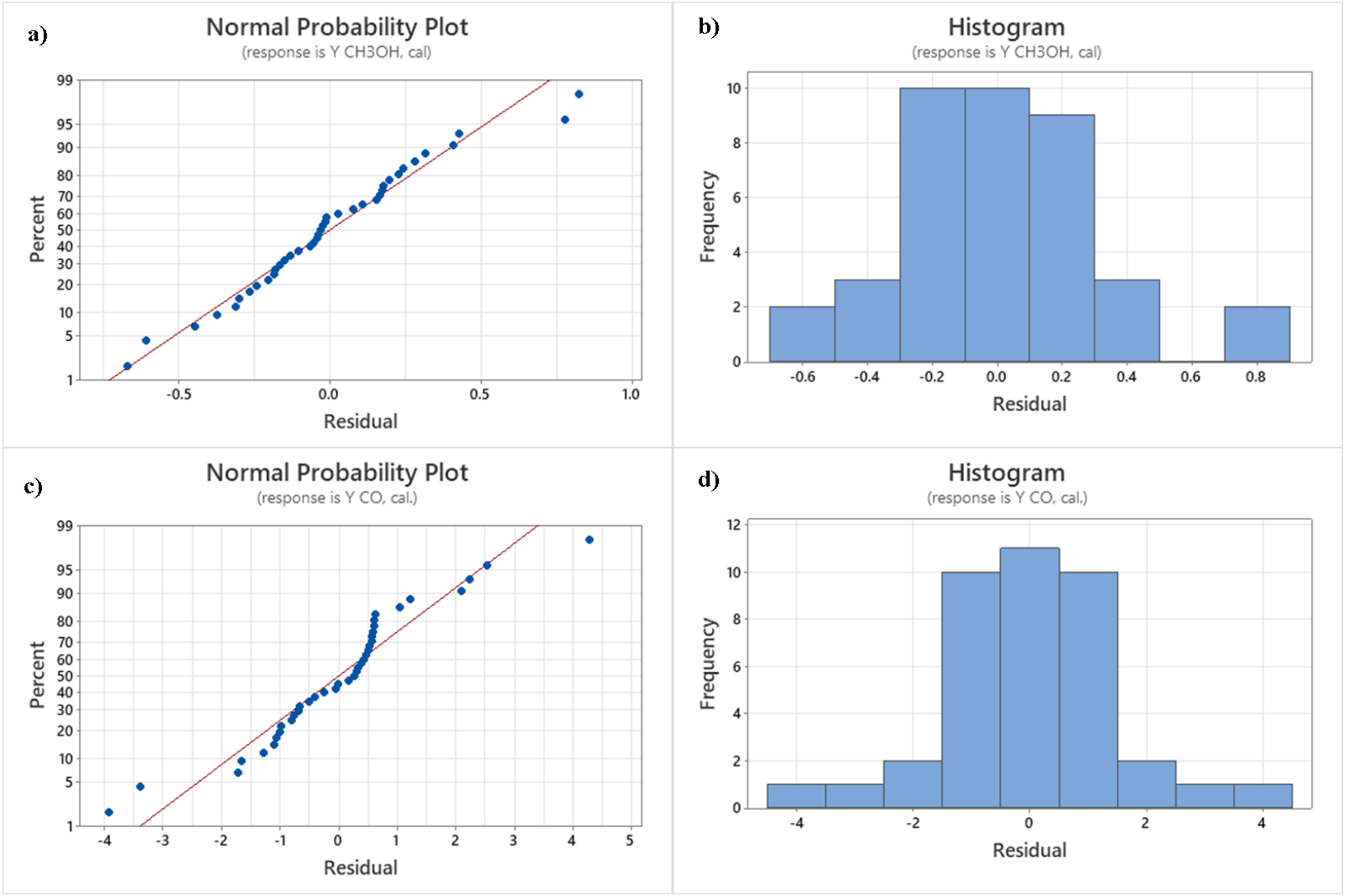

Figure 3.16 Normal and histogram plots of residuals for a) and b) CH_3OH, c) and d) CO yields, respectively.

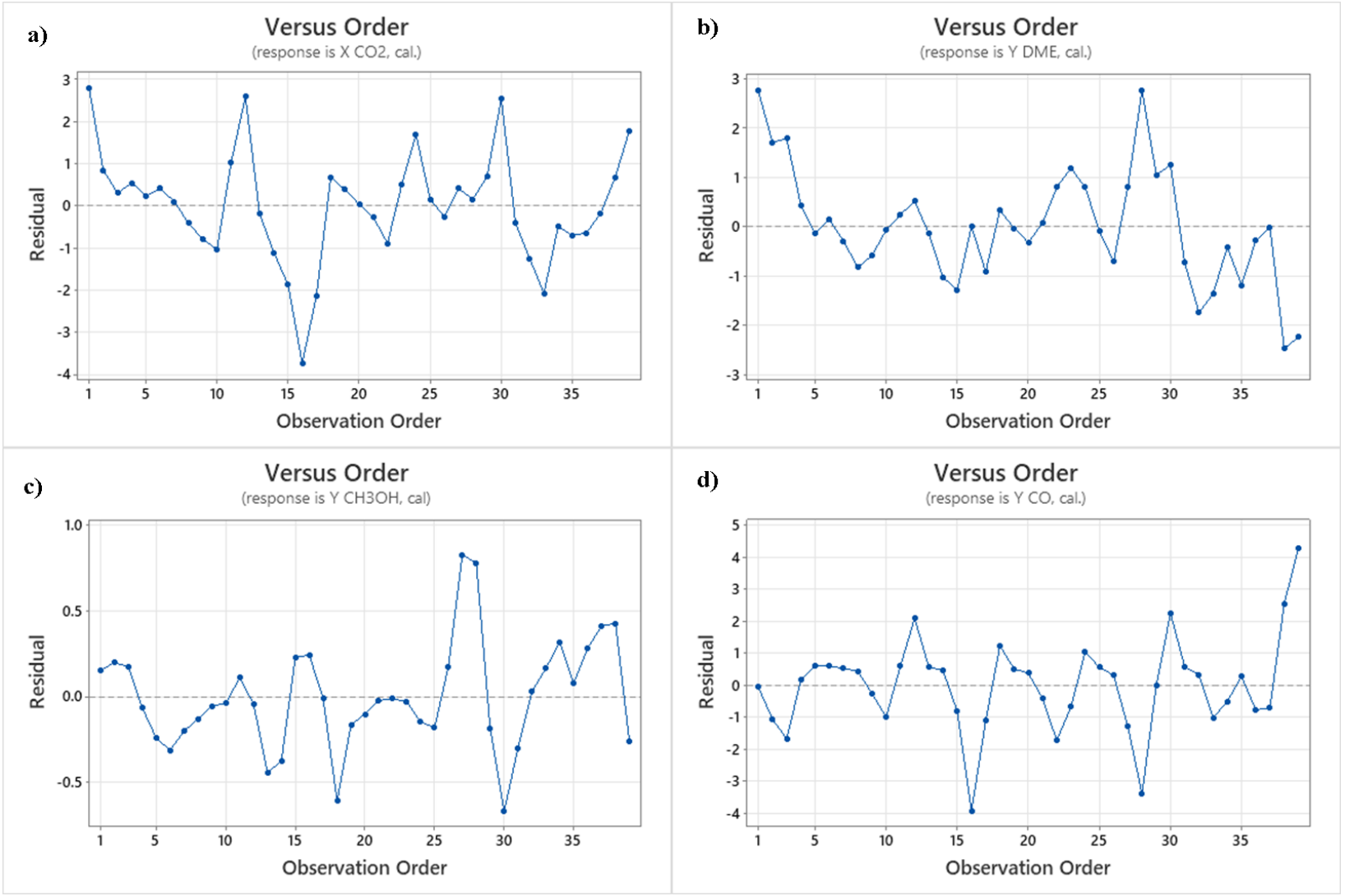

Figure 3.17 Residuals versus order plots for a) CO_2 conversion, b) DME, c) CH_3OH and d) CO yields.

3.5. Conclusions

In this chapter, the steps followed to develop a kinetic model for CO_2 hydrogenation to DME over CZA-C + HZSM-5 in a fixed bed reactor have been presented.

The first step was to assess transport phenomena to determine the possible restrictions related to the external and internal diffusion. Experimental data and computations revealed no limitations to internal and external mass transfer, as well as no external heat transfer limitations.

A reactor model was then performed. Based on the results of the previous chapter, the deactivation of commercial CZA catalyst was analysed. This deactivation was described by a simple equation based on the number of moles of CO_2 converted, which was then incorporated into the kinetic model. Plug-flow reactor was assumed. Kinetics were determined as a function of the molar fractions of the concerned species.

Afterwards, an adapted method was proposed to establish reaction rate equations. The Langmuir-Hinshelwood kinetic model with a single type of active site for adsorption of all species was used for reactions Eq. (3.1) and Eq. (3.2) of methanol synthesis.

Regarding methanol dehydration to DME, our study suggests that the HZSM5 zeolite adsorbs the produced water, driving the final reaction towards the production of DME, which exceeds the expected equilibrium (as well as CO_2 conversion). However, this effect diminishes once the zeolite reaches a certain saturation level. The experimental results indicate that the methanol dehydration reaction to DME is not at equilibrium, contrary to previous claims by other authors. To account for this non-equilibrium behaviour, a novel relation was proposed, incorporating two additional terms, k_5 and E_5, in the reaction rate of DME to better represent the catalyst tests carried out.

Finally, a regression analysis of the model was conducted for its validation. For the aim, the 39 points used to develop the kinetic model were employed. As a result, the developed kinetic model accurately predicts CO_2 conversion and DME yield. Even though the CH_3OH and CO yields are not as well predicted, the fitting of the curves remains acceptable for reactor calculations.

3.6. References

[1] M. J. Quezada, “Hydrogénation catalytique de CO_2 en méthanol en lit fixe sous chauffage conventionnel et sous plasma à DBD,” Normandie Université, 2020.

[2] C. Seidel, A. Jörke, B. Vollbrecht, A. Seidel-Morgenstern, and A. Kienle, “Kinetic modeling of methanol synthesis from renewable resources,” *Chem. Eng. Sci.*, vol. 175, pp. 130–138, Jan. 2018, doi: 10.1016/J.CES.2017.09.043.

[3] J. Park, J. Cho, M. J. Park, and W. B. Lee, “Microkinetic modeling of DME synthesis from methanol over H-zeolite catalyst: Associative vs. dissociative pathways,” *Catal. Today*, vol. 375, pp. 314–323, Sep. 2021, doi: 10.1016/j.cattod.2020.02.011.

[4] J. Villermaux, *Génie de la réaction chimique: conception et fonctionnement des réacteurs*, 2nd ed. Paris, 1993.

[5] D. Kunii and O. Levenspiel, *Fluidization Engineering*, 2nd ed. Butterworth-Heinemann, 1991.

[6] W. E. Ranz, “ Friction and transfer coefficients for single panicles and packed beds.,” *Chem. Eng. Progr.*, vol. 48, pp. 247–253, 1952.

[7] N. Delgado Otalvaro, G. Sogne, K. H. Delgado, S. Wild, S. Pitter, and J. ¨ Org Sauer, “Kinetics of the direct DME synthesis from CO2 rich syngas under variation of the CZA-to-g-Al2O3 ratio of a mixed catalyst bed,” *RSC Adv.*, vol. 11, no. 40, pp. 24556–24569, Jul. 2021, doi: 10.1039/d1ra03452a.

[8] H. S. Fogler, “Elements of chemical reaction engineering,” *Chem. Eng. Sci.*, vol. 42, no. 10, p. 2493, 1987, doi: 10.1016/0009-2509(87)80130-6.

[9] B. Alrafei, “Etude catalytique et cinétique de la méthanation du CO_2 en lit fixe et sous plasma micro-ondes,” Normandie Université, Rouen, 2019.

[10] R. Try, “Étude expérimentale et modélisation dynamique d’un réacteur catalytique modulaire pour l’hydrogénation du CO2 en méthane,” Mar. 2018, Accessed: Mar. 03, 2023. [Online]. Available: https://theses.hal.science/tel-01807801.

[11] C. Ortega, M. Rezaei, V. Hessel, and G. Kolb, “Methanol to dimethyl ether conversion over a ZSM-5 catalyst: Intrinsic kinetic study on an external recycle reactor,” *Chem. Eng. J.*, vol. 347, pp. 741–753, Sep. 2018, doi: 10.1016/j.cej.2018.04.160.

[12] K. Klusáček and P. Schneider, “Stationary catalytic kinetics via surface concentrations from transient data: Methanol dehydration,” *Chem. Eng. Sci.*, vol. 37, no. 10, pp. 1523–1528, Jan. 1982, doi: 10.1016/0009-2509(82)80010-9.

[13] A. Ateka, J. Ereña, J. Bilbao, and A. T. Aguayo, “Kinetic modeling of the direct synthesis of dimethyl ether over a CuO-ZnO-MnO/SAPO-18 catalyst and assessment of the CO2 conversion,” *Fuel Process. Technol.*, vol. 181, pp. 233–243, Dec. 2018, doi: 10.1016/j.fuproc.2018.09.024.

[14] M. De Falco, M. Capocelli, and G. Centi, “Dimethyl ether production from CO2 rich feedstocks in a one-step process: Thermodynamic evaluation and reactor simulation,” *Chem. Eng. J.*, 2016, doi: 10.1016/j.cej.2016.03.009.

[15] N. Delgado Otalvaro, M. Kaiser, K. Herrera Delgado, S. Wild, J. Sauer, and H. Freund, “Optimization of the direct synthesis of dimethyl ether from CO2 rich synthesis gas: Closing the loop between experimental investigations and model-based reactor design,” *React. Chem. Eng.*, vol. 5, no. 5, pp. 949–960, Apr. 2020, doi: 10.1039/d0re00041h.

[16] S. Guffanti, C. G. Visconti, J. van Kampen, J. Boon, and G. Groppi, “Reactor modelling and design for sorption enhanced dimethyl ether synthesis,” *Chem. Eng. J.*, vol. 404, p. 126573, Jan. 2021, doi: 10.1016/j.cej.2020.126573.

[17] A. T. Aguayo, J. Ereña, D. Mier, J. M. Arandes, M. Olazar, and J. Bilbao, “Kinetic modeling of dimethyl ether synthesis in a single step on a CuO-ZnO-Al2O3/γ-Al2O3 catalyst,” *Ind. Eng. Chem. Res.*, vol. 46, no. 17, pp. 5522–5530, Aug. 2007, doi: 10.1021/ie070269s.

[18] A. Ateka, P. Rodriguez-Vega, J. Ereña, A. T. Aguayo, and J. Bilbao, “Kinetic modeling and reactor design of the direct synthesis of dimethyl ether for CO2 valorization. A review,” *Fuel*, vol. 327, p. 125148, Nov. 2022, doi: 10.1016/j.fuel.2022.125148.

[19] A. Ateka, P. Rodriguez-Vega, T. Cordero-Lanzac, J. Bilbao, and A. T. Aguayo, “Model validation of a packed bed LTA membrane reactor for the direct synthesis of DME from CO/CO2,” *Chem. Eng. J.*, vol. 408, p. 127356, Mar. 2021, doi: 10.1016/j.cej.2020.127356.

[20] N. Delgado Otalvaro, P. G. Bilir, K. H. Delgado, S. Pitter, and J. Sauer, “Kinetics of the Direct DME Synthesis: State of the Art and Comprehensive Comparison of Semi-Mechanistic, Data-Based and Hybrid Modeling Approaches,” *Catalysts*, vol. 12, no. 3, p. 347, Mar. 2022, doi: 10.3390/CATAL12030347/S1.

[21] Y. Tavan, S. H. Hosseini, M. Ghavipour, M. R. K. Nikou, and A. Shariati, “From laboratory experiments to simulation studies of methanol dehydration to produce dimethyl ether - Part I: Reaction kinetic study,” *Chem. Eng. Process. Process Intensif.*, vol. 73, pp. 144–150, 2013, doi: 10.1016/j.cep.2013.06.006.

[22] N. Park, M. J. Park, Y. J. Lee, K. S. Ha, and K. W. Jun, “Kinetic modeling of methanol synthesis over commercial catalysts based on three-site adsorption,” *Fuel Process. Technol.*, vol. 125, pp. 139–147, Sep. 2014, doi: 10.1016/J.FUPROC.2014.03.041.

Chapter 4

4. Optimal Temperature Profile

4.1. Introduction

The writing of a kinetic model including thermodynamic equilibria allowed for the estimation of kinetic parameters for the hydrogenation of CO_2 into Methanol and DME. We now have a mathematical tool to calculate reaction rates and advancements for a given reactor. Since the reactions are exothermic and balanced, there is an optimal temperature for isothermal or a changing temperature reactor operation, for a given operating condition. Indeed, the compromise lies between a high temperature favourable to kinetics and a lower temperature thermodynamically favourable to product formation. According to Froment et al., 2011 [1], Levenspiel, 2008 [2]; Villermaux, 1993 [3], it is possible to vary the temperature along the reactor to achieve maximum conversion at each point: this is the optimum temperature progression (OTP). Finding this optimal progression and studying its feasibility is the subject of this chapter.

4.2. Reminder of the OTP principle on one reversible first-order reaction

To illustrate the concept, we assume a reversible reaction $A \rightleftharpoons B$ in a plug flow reactor (uniform velocity of fluid elements in a cross section). The reaction rate is defined as:

$$r = k_1 C_A - k_2 C_B \tag{4.1}$$

and the mass balance of the specie A may be written as:

$$dF_A = -r_A dV \tag{4.2}$$

By conversion definition,

$$F_A = F_{A0}(1 - X) \tag{4.3}$$

Hence,

$$\frac{dX}{d\left(\frac{V}{F_{A0}}\right)} = r_A \tag{4.4}$$

Thus

$$\int_0^V \frac{dV}{F_{A0}} = \int_0^{X_A} \frac{dX}{r_A} \tag{4.5}$$

$$\frac{V}{F_{A0}} = \int_0^{X_A} \frac{dX}{r_A} \tag{4.6}$$

The ratio V/F_{A0}, the space-time, is an appropriate performance metric for flow reactors. It accurately reflects the residence time only under conditions where there is no expansion or contraction resulting from changes in the number of moles or other factors [1]. Space-time refers to the duration needed to process one volume of feed within a reactor at specified conditions. It is given by [2],

$$\tau = \frac{\left(\frac{moles\ A\ entering}{volume\ feed}\right)(volume\ of\ reactor)}{\left(\frac{moles\ A\ entering}{time}\right)} = \frac{C_{A0}V}{F_{A0}} \tag{4.7}$$

Eq. (4.4) relates the reaction progress to the residence time through the reaction rate.

Assuming there is no volume expansion along the reactor, the concentrations of species A and B can be written as:

$$C_A = C_{A0}(1 - X) \tag{4.8}$$

$$C_B = C_{A0}X \tag{4.9}$$

Considering $k_1 = A_1 e^{-\frac{E_1}{RT}}$ and $k_2 = A_2 e^{-\frac{E_2}{RT}}$, iso-reaction rates curves are thus given by Eq. (4.1). Thus, iso-reaction rates curves are given by,

$$r = A_1 e^{-\frac{E_1}{RT}} C_{A0}(1 - X_A) - A_2 e^{-\frac{E_2}{RT}} C_{A0} X_A \tag{4.10}$$

At equilibrium, $r = 0$ and $K = C_B/C_A = k_1/k_2$. Then, we find the equilibrium conversion, X_e,

$$X_e = \frac{k_1(T)}{k_1(T) + k_2(T)} = \frac{K(T)}{1 + K(T)} \tag{4.11}$$

After integration of Eq. (4.6) with Eq. (4.10) and Eq. (4.11), we obtain the equilibrium conversion rate:

$$X = X_e\left(1 - e^{-k_1 \tau / X_e}\right) \tag{4.12}$$

With a fixed space time (τ) and a variable temperature, Eq. (4.12) allows the plotting of a sequence of iso-τ curves in an isothermal plug flow reactor, where a decline in temperature produces an upsurge in thermodynamic conversion for exothermic reactions and a drop for endothermic reactions. On these reversible exothermic reaction plots (Figure 4.1), at a given space time τ, there is an optimal operating temperature T_{opt} that aligns with the peak of the curve $X(T)$. The kinetics slows down significantly when the temperature is lower than T_{opt}; while if the temperature is greater than T_{opt}, the effect of thermodynamic constraints dominates, limiting progress towards equilibrium [3]. Therefore, there is an optimal intermediate temperature that allows for both reasonably rapid reaction rates and a sufficiently high equilibrium conversion [1]. In the case of endothermic reactions, the objective is to operate at very high temperature to maximise conversion [3]. Optimal temperatures do not exist in endothermic reactions, as in irreversible reactions, because the equilibrium conversion and rate of reaction continuously increases with temperature [2]. In non-isothermal operation, the optimal temperature progression is applicable to exothermic reversible reactions.

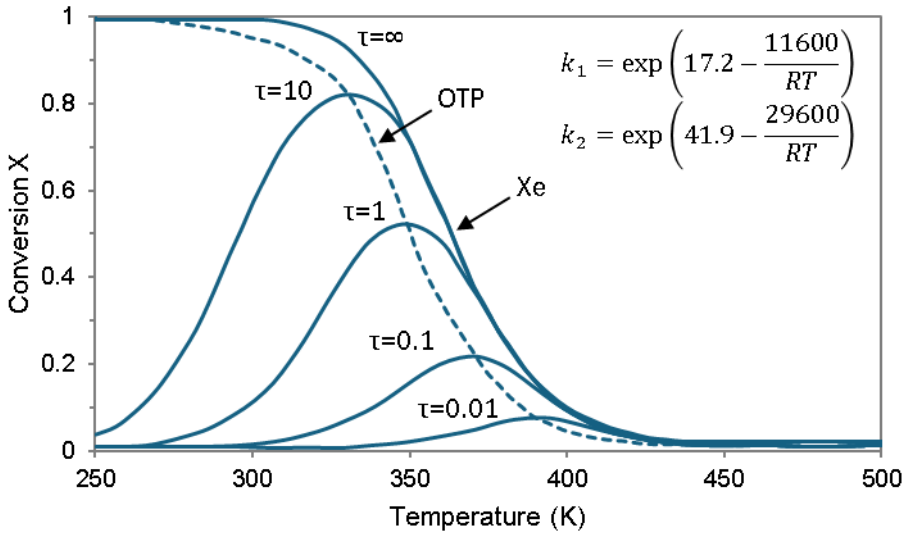

Figure 4.1 Conversion versus temperature curves iso-τ for an exothermic reversible first-order reaction A ⇋ R in an isothermal plug flow reactor. Modified from [4].

The second way of addressing the problem is to find the OTP and to work with an iso-rates diagram:

Figure 4.2 depicts iso-rates of reactions for a stated feed, using the conversion of a key component as an indicator of the composition and extent of reaction. Each curve has a maximum point determining the OTP. At high temperatures, they are asymptotic to the equilibrium curve [3]. Villermaux elucidates that a horizontal line at a constant conversion intersects iso-rate curves, with the curve at maximum rate being tangent to the line at its peak point [3]. This point represents the OTP, ensuring a relative maximum reaction rate, resulting in minimal space-time (or residence time). The importance of knowing this progression resides on the fact that it allows us to represent the ideal that we aim to approximate in a real system. It also provides a mean of estimating how far any real system deviates from this ideal [2].

Using the example of the first-order reversible reaction described above, combining the Eq. (4.10) and Eq. (4.11), the rate of reaction can be expressed as:

$$\frac{r(X,T)}{C_{A0}} = k_1(T)\left[1 - \frac{X}{X_e(T)}\right] \tag{4.13}$$

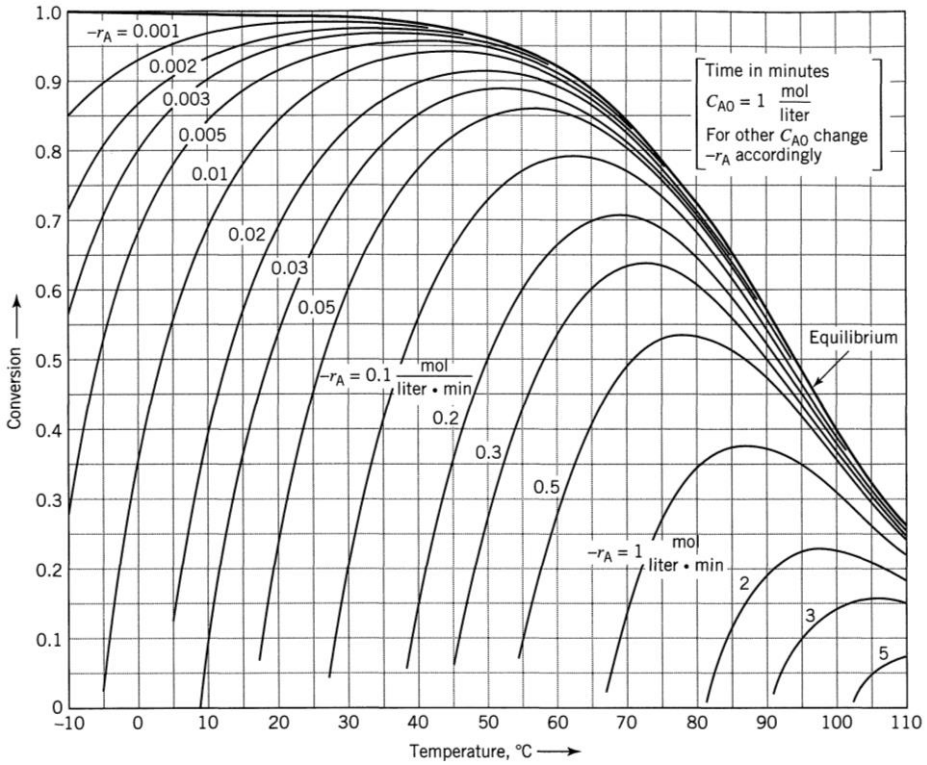

Figure 4.2 Conversion versus temperature curves iso-r for a reversible first-order reaction $A \leftrightharpoons R$: $k_1 = exp\left(17.34 - \frac{48900}{RT}\right)$; $k_2 = exp\left(42.04 - \frac{124200}{RT}\right)$ for $C_{A0} = 1\ mol.liter^{-1}$ and $C_{R0} = 0$. Reproduced from [2].

Consequently, considering Arrhenius' law, at the reactor input the temperatures should be high to increase rate constant, $k_1(T)$, and conversion. But, by the thermodynamic limitations (Le Chatelier's law), as the flow progresses along the reactor, it is necessary to decrease the temperature to maximise the conversion. Thus, there is an optimum temperature to identify to attain a maximum conversion (as close as possible to the equilibrium) with a minimum volume (V/F_{A0}) by changing temperature as a function of a given reactant (A) conversion (X) [1]–[3].

In our case, the OTP is calculated from the space time (τ) in the entire volume of the reactor (see Eq. (4.6)-(4.7)):

$$\frac{\tau}{C_{A0}} = \frac{V}{F_{A0}} = \int_0^X \frac{dX}{r(X,T)} \tag{4.14}$$

This integration can be performed consistently, allowing the determination of the optimal temperature corresponding to a desired conversion, X [1]. Hence, there exists a trajectory $X_{opt}\,(T)$ within the (X,T) plane where the reaction rate consistently reaches a relative maximum.

The quantitative aspect for multiple reactions must usually be determined by methods of mathematical optimisations [1]. Thus, by means of equations proposed in our kinetic model for DME synthesis from CO_2 hydrogenation, we search to define the OTP.

Senthil & Sundaramoorthy, 2018 [5] presented an optimal control policy to track the OTP and maximise the conversion of an exothermic reversible reaction in a batch reactor. They used control vector iteration to solve the optimal control problem. Their development allowed to track the optimal progression of temperature and succeed maximum conversion. Iranshahi et al., 2017 [6] worked with maximising the synthesis of DME from syngas by means of optimum temperature profile and water removal. They discretized a reactor into twenty zones and performed an OTP, combined with a computation of the maximum amount of water removal of each segment, all this by applying differential evolution (DE) algorithm. The researchers concluded that DME production increased by up to 1.5% by optimising only the reactor temperature profile, up to 55% by removing water alone, and up to 70% combining both strategies.

Kiewidt & Thöming, 2015 [7] employed the Semenov number as optimisation method to estimate optimal axial temperature profiles for CO_2 methanation in an externally cooled, single stage fixed bed reactor. The study revealed that Semenov number optimisation enables optimal temperature profiles that balance kinetic and thermodynamic constraints, leading to high methane yields (>90%).

The case examined by Omata et al., 2009 [8] discretized a fixed bed temperature gradient reactor (TGR) into five segments to optimise the temperature settings by combining artificial neural network (ANN) and grid search for DME synthesis from syngas. In their process, methanol is synthesised from syngas ($CO + H_2 \rightleftharpoons CH_3OH$) and DME is produced through methanol dehydration ($CH_3OH \rightleftharpoons CH_3OCH_3 + H_2O$). The water gas shift reaction was also considered, and an overall DME synthesis reaction was expressed as $3CO + 3H_2 \rightleftharpoons CH_3OCH_3 + CO_2$. Both the challenge of overcoming the equilibrium limit of DME synthesis from synthesis gas at elevated temperatures and the issue of low catalyst activity at lower temperatures were successfully addressed. In a previous publication, Omata et al., 2003 [9] demonstrated the effectiveness of a TGR for overcoming the equilibrium limit at high temperature and the low activity of the catalyst at low temperature. Likewise, they combined genetic algorithm and neural network to optimise the temperature profile.

Logist et al., 2008 [10] dealt with the determination of generic optimal temperature profiles for a dispersive plug flow reactor model in which took place an exothermic irreversible first-order reaction. The investigators performed their analytical derivation based on indirect optimal control techniques and the optimisations were completed implementing multiple

shooting approach using the software MUSCOD-II. In another study, the same investigation team derived optimal temperature profiles for a tubular reactor with a fixed number of exothermic jackets of equal length [11]. They employed control vector parameterization in a finite-dimensional nonlinear program to solve the optimisation. Based on their results, it is critical to favour conversion by maintaining high temperature in the first part of the reactor, following a cooling section to reduce the heat loss. It generated an improved performance.

In summary, research shows that OTP grant maximisation of conversion and improved product yields.

4.3. Adopted approach

4.3.1. Study of a single reversible reaction

Continuing with the study of a reversible reaction, $A \rightleftharpoons B$, we can write from the reaction rate presented in Eq. (4.1):

$$r = k_1(C_A - C_B/K) \tag{4.15}$$

Since

$$K = \frac{k_1}{k_2} = \left(\frac{C_B}{C_A}\right)_{eq} = \frac{C_{A0}X_e}{C_{A0}(1 - X_e)} \tag{4.16}$$

Eq. (4.15) may be written

$$r = k_1(C_{A0}(1 - X) - C_{A0}X/K) \tag{4.17}$$

Bearing in mind that it is possible to define the equilibrium constant on the basis of a linear equation such as $K = exp\left(\frac{a_1}{T} + a_2\right)$ and the rate constant by the Arrhenius law, Eq. (4.17) can be given by:

$$r = k_1 e^{-\frac{E_1}{RT}} C_{A0}\left[(1 - X) - \frac{X}{exp\left(\frac{a_1}{T} + a_2\right)}\right] \tag{4.18}$$

Assuming this reaction happens in a plug flow reactor (Figure 3.5), the reaction rate is expressed as:

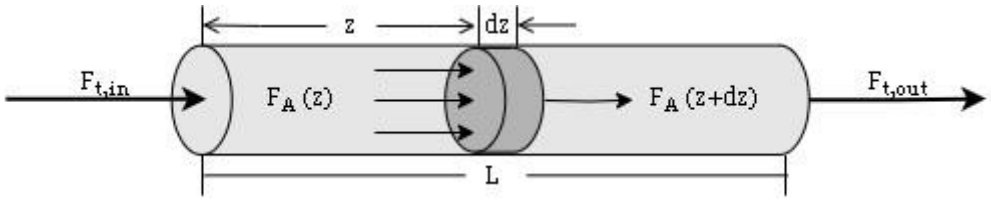

Figure 4.3 Representation of a plug-flow reactor (PFR).

$$r = \frac{F_{AO}}{V}\frac{dX}{dz} = k_1 C_{A0}\left((1 - X) - \frac{X}{K}\right) \tag{4.19}$$

where dX_A/dz is defined as a differential advancement in the reactor, which behaves like a continuous stirred tank reactor (CSRT). Then, we obtain:

$$\frac{dX}{dz} = k_1 \frac{C_{A0} V}{F_{A0}} \left[1 - X\left(1 + \frac{1}{K}\right)\right] \tag{4.20}$$

can also be written

$$\frac{dX}{dz} = k_1 \tau \left[1 - X\left(1 + \frac{1}{K}\right)\right] \tag{4.21}$$

rearranging and integrating, the conversion along the length of reactor with evenly spaced distance (from z_1 to z_2) gives

$$\int_{X_1}^{X_2} \frac{dX}{1 - X\left(1 + \frac{1}{K}\right)} = \int_{z_1}^{z_2} k_1 \tau dz \tag{4.22}$$

or

$$\left. \frac{K\, ln\left(1 - X\left(1 + \frac{1}{K}\right)\right)}{-(K+1)} \right|_{X_1}^{X_2} = k_1 \tau z|_{z_1}^{z_2} \tag{4.23}$$

thus,

$$ln\left(1 - X_2\left(1 + \frac{1}{K}\right)\right) = ln\left(1 - X_1\left(1 + \frac{1}{K}\right)\right) - \left(1 + \frac{1}{K}\right) k_1 \tau (z_2 - z_1) \tag{4.24}$$

In terms of conversion, after rearrangement the result of this equation becomes

$$X_2 = \frac{1 - \left(1 - X_1\left(1 + \frac{1}{K}\right)\right) exp\left[-\left(1 + \frac{1}{K}\right) k_1 \tau (z_2 - z_1)\right]}{1 + 1/K} \tag{4.25}$$

This equation is the objective function of an optimisation programmed in MATLAB for a constant space time and a chosen range of temperature. For a reactor of a given length and fixed inlet conditions, X_2 is calculated for each inlet temperature $\left(X_2(T)\right)$. Two numerical methods were examined to solve this problem: a *while loop* method to find the temperature maximising the reaction rates of interest for a given $(z_2 - z_1)$ element (we will detail our method for the DME synthesis in the section 4.3.2) and a MATLAB optimisation function minimising negative of Eq. (4.25) to maximise X_2 (the optimisation functions programmed in MATLAB only allow criteria minimisations).

Both methods were assessed and are presented below. The two consisted in discretising the catalytic bed into segments in which the concentrations and the temperature were uniform. Knowing the kinetic and equilibrium parameter functions, the temperature and the conversion

in the previous segment and the space time, the temperature in the current segment was varied to find the maximum X_2 value. Then the number of segments was incremented. For the *while loop* method, from a segment to its following segment, the temperatures were not allowed for increasing, as only the temperatures lesser than that of the previous segment were checked. However, in the second optimisation method, a minimisation of unconstrained multivariable function '*fminunc*' was used. It based on the minimisation of the function $-X_2$ exploring the whole temperature range. In this case, the optimal temperature in a segment could be higher than that of the previous segment.

The outcomes of the optimisations are presented in Figure 4.4. The two optimisation methods were assessed for 12 entrance temperatures T_0. For reference, based on the kinetic results for methanol synthesis in this thesis, the inlet fixed conditions used are listed in Table 4.1.

Table 4.1 Inlet parameters for optimisation of a first order reversible reaction $A \rightleftharpoons B$ in a PFR.

Parameters	**Value**	**Unit**	**Parameters**	**Value**	**Unit**
a_1	$7.54 \cdot 10^3$	K	V	$5.03 \cdot 10^{-2}$	m^3
a_2	-24.95	$-$	F_{A0}	$1.72 \cdot 10^{-1}$	$mol.h^{-1}$
k_0	$3.70 \cdot 10^{11}$	h^{-1}	C_{A0}	1.00	$mol.m^{-3}$
E_0	$6.00 \cdot 10^4$	$J.mol^{-1}$	τ	$2.92 \cdot 10^{-1}$	h
$stepT$	$1.00 \cdot 10^{-1}$	K	$z = L$	1.00	m

Figure 4.4(a, b) exhibits the results obtained using the *while loop* method. The Figure 4.4a illustrates how the conversion (X) changes in 12 iterations with $T_0 = 284 - 328\,K$. Curves initiated at 324 and 328 K (Figures a and b) display the greatest similarity and exhibit the closest proximity to the equilibrium line, indicating a near-maximal conversion. Figure 4.4b emphasizes this observation by depicting the superposition of the final conversion for $T_0 = 324\,K$ and $T_0 = 328\,K$ is evident. Besides, the curve initiated at the lowest temperature ($T_0 = 284\,K$, Figure 4.4a and b) is an isotherm, which led to the minimum conversion.

Figure 4.4(c, d) depict the outcomes when applying the nonlinear programming solver '*fminunc*'. In contrast to the findings from the *while* loop simulations, the present analysis reveals a consistent upward trend in temperature in the first section (with the exception observed at 328K) as a requirement to achieve maximum conversion. Figure 4.4e displays that the final conversion presents minimal differences regardless of the inlet temperature, where $T_0 = 300\,K$ and $T_0 = 308\,K$ were the furthest out of the rest. This numerical method does not identify an isotherm, but searches for the best inlet temperature, increasing and then

decreasing it to find the maximum conversion. However, even if this leads to faster reaction rates, it is important to remember that increasing temperature can also indirectly affect heat release in exothermic reactions. Additionally, there are heating costs associated with reaching the desired temperature and then reduce it.

Bearing in mind that each iteration is performed along the uniformly spaced reactor segments, in the second segment of the reactor, the solver consistently identified analogous optimal temperature ($T = 323.38\,K$) for all inlet conditions. This resulted in a final conversion of approximately 0.71 in each case (Figure 4.4e). Furthermore, the behaviour highlights the ability of the solver to converge on a unique optimal solution regardless of the starting point. It suggests that the method prioritizes locating the optimal temperature for initiating the OTP, even if it necessitates an inlet temperature increase to ultimately reduce the temperature and enhance conversion.

A noteworthy finding is that in both optimisation methods (*fminunc* and *while loop*), with an optimal temperature progression, the function determines similar maximum conversion of 0.71 (Table 4.2). In both numerical method, higher entrance temperatures yielded higher conversions. The higher the entrance temperature, the greater the conversion. However, when $T_0 > 312\,K$, further increases in temperature yielded only marginal improvements. All the points converge at a final temperature of 284 K with a conversion of 70.7%. The difference in optimal final conversion between the numerical methods was approximately $8 \cdot 10^{-5}$%.

Table 4.2 Final outputs of both methods: while loop and fminunc.

	while loop		***fminunc***	
$\boldsymbol{T_0}$	T_f	X_f	T_f	X_f
284	284.00	0.58	283.97	0.71
288	286.90	0.65	283.97	0.71
292	285.40	0.68	283.97	0.71
296	284.70	0.69	283.97	0.71
300	284.30	0.70	283.97	0.71
304	284.20	0.70	283.97	0.71
308	284.10	0.70	283.97	0.71
312	284.00	0.71	283.97	0.71
316	284.00	0.71	283.97	0.71
320	284.00	0.71	283.97	0.71
324	284.00	0.71	283.97	0.71
328	284.00	0.71	283.97	0.71

The crucial distinction between the two approaches lies in how they handle the temperatures. The *while loop* method allows for isothermal behaviour, where the temperature remains constant along a section of the reactor. It permits for simpler control, even if it might lead to slower reaction rates, but the same maximum conversion is reached. Additionally, it offers an advantage in terms of managing heat release. In contrast, the non-linear programming approach involves varying the temperature throughout the process. Consequently, it might miss potential operational advantages of isothermal operation. This can achieve faster reaction rates in the first part of the reactor by sharply increasing the temperature, but it also requires more complex temperature control. In essence, the *while loop* method prioritizes simplicity and heat control, while the minimisation function "*fminunc"* prioritizes speed.

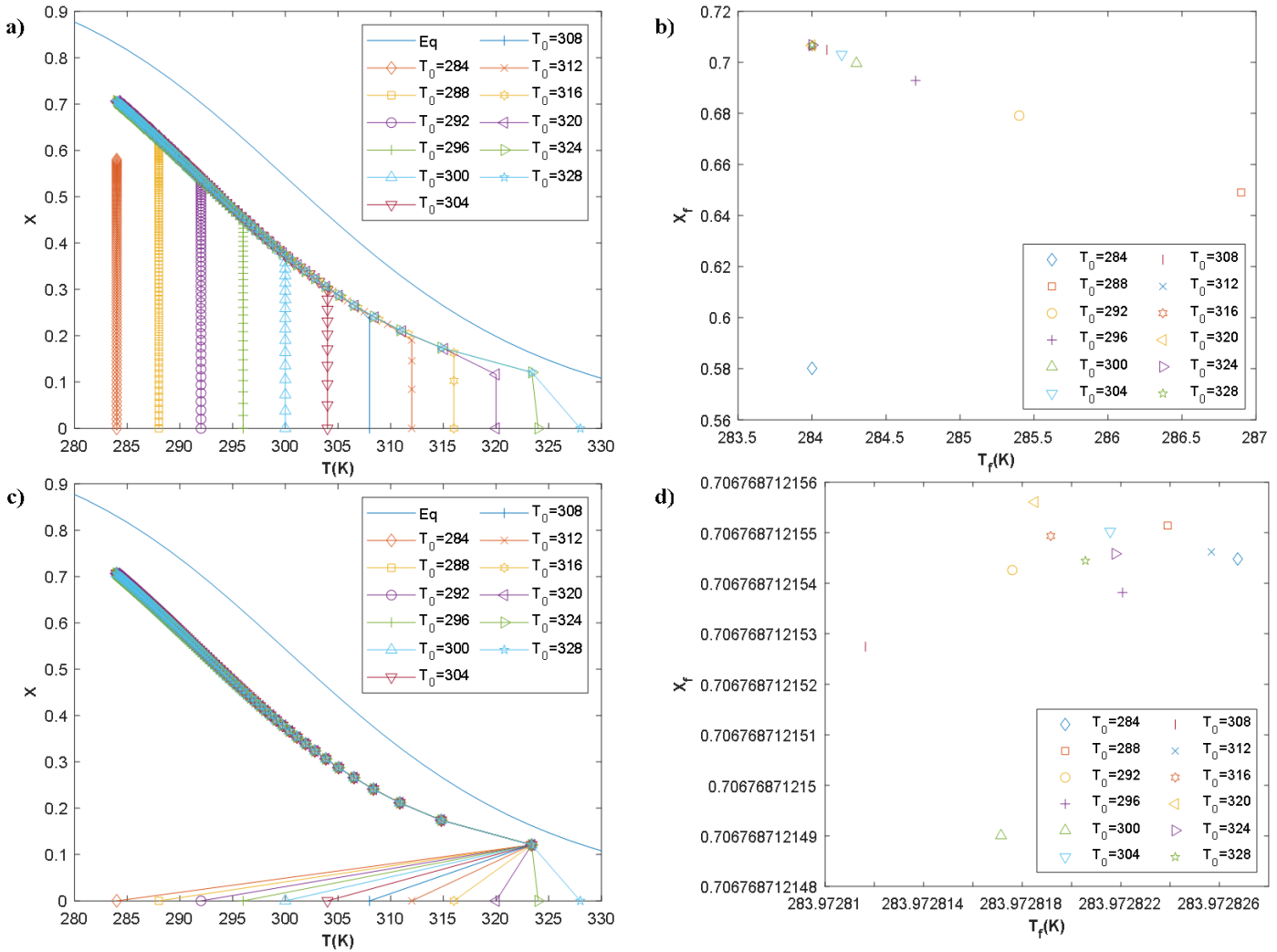

Figure 4.4 Optimisation outcomes for a reversible reaction $A \rightleftharpoons B$, where a) and b) resulted from a while loop method, whereas c) and d) were derived from the nonlinear programming solver 'fminunc'. The graphics represents the conversion, X, vs temperature, T (K) of: a), c) all resulted points and b), d) the final conversion at different inlet temperatures T_o. Refer to Table 4.1 for operating conditions.

4.3.2. Study of the CO_2 to DME reactions

The synthesis of DME differs from the previous section by the coexistence of three reactions, two of which are exothermic, and one is endothermic. The aim of this chapter is to assess the contribution of the OTP in the case of a more complex reaction system compared to a single reversible reaction.

In previous chapter, a kinetic model was proposed for the DME synthesis from CO_2 hydrogenation. Based on the results of Chapter 3, this study focuses solely on three reactions (CO_2 hydrogenation to methanol, reverse water gas shift and methanol dehydration), as described below:

$$CO_2 + 3H_2 \rightleftharpoons CH_3OH + H_2O \qquad \Delta H_{rx,298K} = -49.25\ kJ.mol^{-1} \qquad (4.26)$$

$$CO_2 + H_2 \rightleftharpoons CO + H_2O \qquad \Delta H_{rx,298K} = 41.16\ kJ.mol^{-1} \qquad (4.27)$$

$$2CH_3OH \rightleftharpoons CH_3OCH_3 + H_2O \qquad \Delta H_{rx,298K} = -24.04\ kJ.mol^{-1} \qquad (4.28)$$

The reaction rate expressions used here are those discussed in Chapter 3:

$$r_{MeOH} = \frac{df \cdot k_1 e^{-\frac{E_1}{RT}}\left(p_{CO_2} p_{H_2}^3 - p_{CH_3OH} p_{H_2O}/K_1\right)}{p_{H_2}^2 \cdot \left(1 + K_{CO_2} p_{CO_2} + \sqrt{K_{H_2} p_{H_2}} + K_{CH_3OH} p_{CH_3OH} + K_{H_2O} p_{H_2O} + K_{CO} p_{CO}\right)^3} \qquad (4.29)$$

$$r_{RWGS} = \frac{df \cdot k_2 e^{-\frac{E_2}{RT}}\left(p_{CO_2} p_{H_2} - p_{CO} p_{H_2O}/K_2\right)}{p_{H_2}^{0.5} \cdot \left(1 + K_{CO_2} p_{CO_2} + \sqrt{K_{H_2} p_{H_2}} + K_{CH_3OH} p_{CH_3OH} + K_{H_2O} p_{H_2O} + K_{CO} p_{CO}\right)^2} \qquad (4.30)$$

$$r_{DME} = k_4 e^{-\frac{E_4}{RT}} p_{CH_3OH}^2 - k_5 e^{-\frac{E_5}{RT}} p_{CH_3OCH_3} p_{H_2O} \qquad (4.31)$$

where df is a deactivation function defined as

$$df = 1 - \alpha \cdot n_{CO2,converted} \qquad (4.32)$$

α is a variable for deactivation and $n_{CO2,converted}$ is the amount of cumulative moles of CO_2 converted. The reaction rate constants are given in Table 4.3, from the results of Chapter 3.

Table 4.3 Reaction rates constants.

Parameter	Value	Unit	Parameter	Value	Unit
k_1	$3.70 \cdot 10^7$	$mol.g^{-1}.h^{-1}.bar^{-2}$	E_1	73.8	$kJ.mol^{-1}$
k_2	$4.37 \cdot 10^8$	$mol.g^{-1}.h^{-1}.bar^{-1.5}$	E_2	99.1	$kJ.mol^{-1}$
k_4	82.7	$mol.g^{-1}.h^{-1}$	E_4	16.5	$kJ.mol^{-1}$

k_5	1.83	$mol.g^{-1}.h^{-1}$	E_5	16.1	$kJ.mol^{-1}$
$(K_{H_2})^{0.5}$	1.25	$bar^{-0.5}$	K_{CO}	10.1	bar^{-1}
K_{CO_2}	1.03	bar^{-1}	K_{CH_3OH}	4.45	bar^{-1}
α	2.16	-			

Five variables, X_{CO_2}, X_1, X_2, X_4, and F_{MD}, are evaluated. F_{MD} is the production rate of methanol plus twice that of DME, measured in $mol.h^{-1}$. It corresponds to the molar flow rate of CO_2 converted into molecules of interest (methanol and DME). These are independently evaluated to derive optimal profiles. Based on the global material balances of the species (Table 4.4), X_1, X_2 and X_4 are determined (Eq. (4.33)-(4.35)).

Table 4.4 Global material balances of the species

Species	$F_{i,out}$		
N_2	$F_{N_2,\,out}$	=	$F_{N_2,\,in}$
CO_2	$F_{CO_2,\,out}$	=	$F_{CO_2,\,in} - (1/3\,X_1 + X_2)F_{t,in}$
H_2	$F_{H_2,\,out}$	=	$F_{H_2,\,in} - (X_1 + X_2)F_{t,in}$
CH_3OH	$F_{CH_3OH,\,out}$	=	$F_{CH_3OH,\,in} + (1/3\,X_1 - 2X_4)F_{t,in}$
H_2O	$F_{H_2O,\,out}$	=	$F_{H_2O,\,in} + (1/3\,X_1 + X_2 + X_4)F_{t,in}$
CO	$F_{CO,\,out}$	=	$F_{CO,\,in} + X_2F_{t,in}$
CH_3OCH_3	$F_{CH_3OCH_3,\,out}$	=	$F_{CH_3OCH_3,\,in} + X_4F_{t,in}$
Total	$F_{t,\,out}$	=	$F_{t,\,in}(1 - 2/3\,X_1)$

$$X_1 = \frac{3}{2}\left(\frac{F_{t,\,in} - F_{t,out}}{F_{t,\,in}}\right) \tag{4.33}$$

$$X_2 = \frac{F_{CO,out} - F_{CO,in}}{F_{t,in}} \tag{4.34}$$

$$X_4 = \frac{F_{CH_3OCH_3,out} - F_{CH_3OCH_3,in}}{F_{t,in}} \tag{4.35}$$

$$F_{MD} = F_{CH_3OH,out} + 2F_{CH_3OCH_3,out} \tag{4.36}$$

At each optimisation step, that means, in each fixed bed segment, the heat q_k to be exchanged at the wall reactor is calculated by:

$$\begin{pmatrix} rate\ of\ input \\ heat\ flow \end{pmatrix} - \begin{pmatrix} rate\ of\ output \\ heat\ flow \end{pmatrix} + \begin{pmatrix} rate\ of\ accumulation \\ of heat\ in\ the\ volume \end{pmatrix} + \begin{pmatrix} power\ exchanged \\ with\ outside \end{pmatrix} = \begin{pmatrix} rate\ of\ variation \\ of heat\ by\ reaction \end{pmatrix} \quad (4.37)$$

$$\sum_i F_{i,0} Cp_i \Delta T + \sum_j F_0 \Delta H_{rx,j} \Delta X_j = -q_k \quad (4.38)$$

where Cp_i is the heat capacity ($J.mol^{-1}.K^{-1}$) of species i, $\Delta H_{\mathrm{rx},j}$ is the enthalpy ($J.mol^{-1}$) of j reaction and q_k ($Watt$) is the power to apply at the segment wall for any addition or removal of heat for the current segment.

Summing the power at the segment wall q_k for all the segments leads to the global power involved in the process (Q) and dividing the latter by S_W (the reactor wall surface) leads to the global heat flux through the reactor wall. The same definition can be applied for the local heat flux through the reactor wall, $\dot{q_k}$ where S_k is the segment wall area k.

$$\sum_k q_k = Q \quad (4.39)$$

$$\dot{Q} = \frac{Q}{S_w} \quad (4.40)$$

$$\dot{q_k} = \frac{q_k}{S_k} \quad (4.41)$$

Secondly, we set up the optimisation program *while loop* to plot the OTP for a given reactor. Figure 4.5 depicts a flowchart outlining the process steps. To evaluate the optimisation process, specific inlet conditions were chosen and fixed. These conditions mirrored an experimental point, including inlet pressure, inlet molar flow rate ($F_0 = F$), and inlet temperature ($T_0 = T$). Additionally, the reactor diameter, length, and catalyst mass were held constant. The reactor was discretised into evenly spaced segments.

Thus, our program uses a decision-making process (*if-else*) within a repeating loop (*while*) to calculate the best temperature at each point in the reactor, ultimately leading to the highest possible value for X_{CO_2}, F_{MD}, X_1 or X_4. We proceed like the process explained in section 4.3.1. The *while* loop continued iterating until the condition of maximisation was satisfied throughout the uniformly spaced reactor. Figure 4.5 depicts a flowchart that details the optimisation procedure used to identify the optimal temperature profile applicable to our CO_2 hydrogenation process to DME.

For instance, we initialise the program with an experimental data and assume that the preliminary variable to be optimised is equal to zero at the entrance. Let us consider X_{CO_2} as the variable to be maximised. Then, the algorithm iterates through each segment (k) along the

length of the reactor. The loop starts at $j = 2$ and continues as long as the conversion in the previous segment $\left(X_{CO_2}(j-1)\right)$ is greater than or equal to the maximum conversion achieved so far (X_{max}). During each iteration, the temperature is adjusted by a fixed step size $(stepT)$. Within the *while* loop, the kinetic model is used for the computation of molar fractions and subsequently, the conversion for the current segment $\left(X_{CO_2}(j)\right)$.

Afterwards, depending on the outcome of the conversion, the temperature is then adjusted. If the conversion in the current segment $\left(X_{CO_2}(j)\right)$ is greater than the conversion at the previous segment $\left(X_{CO_2}(j-1)\right)$, then $X_{max} = X_{CO_2}(j)$. In this case, the loop counter (j) is incremented and the temperature is decreased by the fixed step size $(stepT)$ to move to the next segment. Otherwise, only the loop counter (j) is incremented. Equally, the temperature is increased by $stepT$.

Ultimately, the output of each reactor segment $(X_{CO_2,z+1} = X_{max}; T_0 = T;\ Y_0 = Y)$ becomes the input for the next $(k = 2)$, and this process is repeated for all segments $(k = 1{:}\,1000)$ and variables.

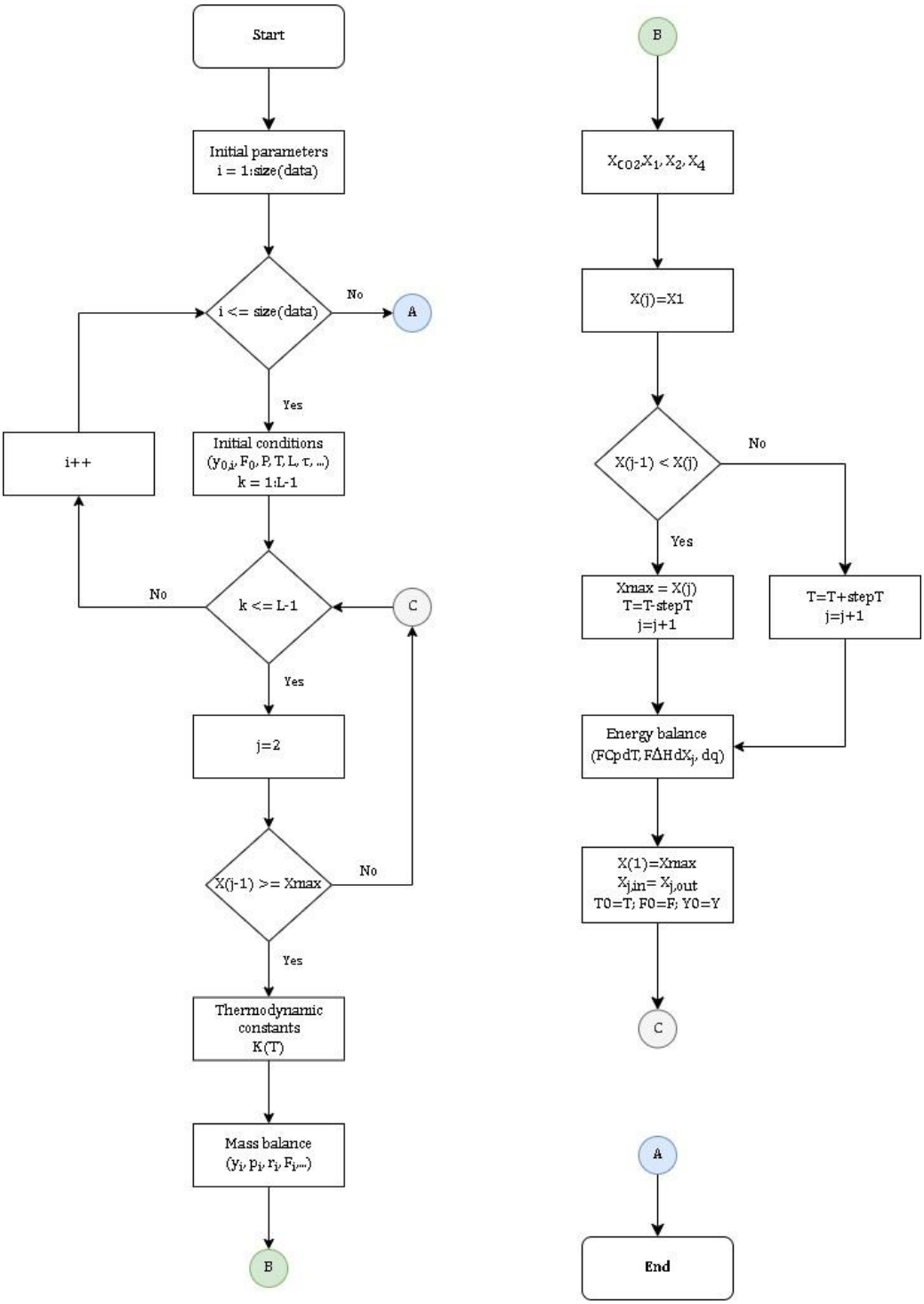

Figure 4.5 Flowchart of optimal temperature progression optimisation program "while loop" in MATLAB for the DME synthesis from CO_2 hydrogenation. L represents the catalyst bed division.

4.4. Simulation of isothermal reactors: Variation of space time (τ)

Prior to optimisation, a series of simulations were conducted to ensure the results were consistent with those presented in Figure 4.1. This preliminary step also served to assess the response of our OTP program when it integrates both our kinetic model and an experimental data point.

We conducted simulations to explore the impact of space time (τ) on conversions in isothermal reactors. τ can be varied either by the flow rate or by the length of the bed. We have done both. By changing these factors, we aimed to analyse the extent of reactions (X_1, X_2, X_4), the CO_2 conversion (X_{CO_2}), and the combined production of DME and methanol ($F_{MD} = F_{CH_3OH} + 2F_{DME}$). Table 4.5 presents the conditions for simulations with a fixed catalyst bed length but varying feed flow rates. Conversely, Table 4.6 shows the settings for simulations with different catalyst bed lengths but the same feed flow rate. All simulations assumed an isothermal fixed-bed reactor with a diameter of 4 mm, a pressure of 36 bar, and temperatures ranging from 453.15 K to 553.15 K in increments of 5 K, since these conditions are similar to those of our kinetic study.

Table 4.5 Inlet conditions set to simulate an isothermal reactor for different set space times (τ) by changing the total feed flow rate at a pressure of 36 bar.

Exp.	F_{N2} ($mol.h^{-1}$)	F_{H2} ($mol.h^{-1}$)	F_{CO2} ($mol.h^{-1}$)	F_{total} ($mol.h^{-1}$)	H_2/CO_2	H_{bed} (cm)	τ (s)
1	0.002	0.015	0.005	0.022	3	6.15	100
2	0.003	0.020	0.007	0.029	3	6.15	75
3	0.004	0.029	0.010	0.044	3	6.15	50
4	0.009	0.059	0.020	0.087	3	6.15	25
5	0.022	0.147	0.049	0.218	3	6.15	10
6	0.031	0.210	0.070	0.311	3	6.15	7
7	0.044	0.294	0.098	0.436	3	6.15	5
8	0.073	0.490	0.163	0.726	3	6.15	3
9	0.218	1.470	0.490	2.178	3	6.15	1

Table 4.6 Inlet conditions set to simulate an isothermal reactor for different set space times (τ) by varying the length of catalyst bed at pressure of 36 bar.

Exp.	F_{N2} ($mol.h^{-1}$)	F_{H2} ($mol.h^{-1}$)	F_{CO2} ($mol.h^{-1}$)	F_{total} ($mol.h^{-1}$)	H_2/CO_2	H_{bed} (cm)	τ (s)
1	0.031	0.21	0.07	0.311	3	87.86	100
2	0.031	0.21	0.07	0.311	3	65.89	75
3	0.031	0.21	0.07	0.311	3	43.93	50
4	0.031	0.21	0.07	0.311	3	21.96	25

5	0.031	0.21	0.07	0.311	3	8.79	10
6	0.031	0.21	0.07	0.311	3	6.15	7
7	0.031	0.21	0.07	0.311	3	4.39	5
8	0.031	0.21	0.07	0.311	3	2.64	3
9	0.031	0.21	0.07	0.311	3	0.88	1

Figure 4.6 displays the simulation of an isothermal reactor for different set space times (τ) by changing the feed flow rate. For X_1, X_4 and CO_2 conversion, the shapes of curves are alike and an evolution with space time (τ) is evident, higher the space time, the higher the conversion of CO_2. The differentiation between them lies in the magnitude of the variables, being higher for CO_2 conversion, followed by X_1, X_4 and X_2. Recalling that in the described DME synthesis process, the conversion of CO_2 to methanol is denoted by X_1 (Eq. (4.26)), and of CO_2 to CO (RWGS) by X_2 (Eq. (4.28)) and the conversion of methanol to DME by X_4 (Eq. (4.27)), the CO_2 conversion means the overall CO_2 conversion, while the extent of reactions are individual for each reaction progress.

On the other hand, the curves iso-τ as a function of the temperature shows a maximum close to the thermodynamic limit for $\tau = 5 - 7\ s$ or exceeding it for $\tau \geq 10\ s$ (Equilibrium: dashed line). The observed proximity or overshoot of the equilibrium curve aligns with the kinetic model described in Chapter 3. This model considers both forward and backward reactions for reaction Eq. (4.28) in the rate expression (Eq. (4.31)). However, it is important to remember that while the kinetic model allows the system to surpass equilibrium due to reaction irreversibility (Eq. (4.28)), the equilibrium curve itself remains unaffected. These deviations are related to the experimental data used to develop the kinetic model.

Figure 4.6e shows that F_{MD} increases as τ decreases. In other words, the lowest space time resulted in the highest productivity F_{MD}. It can be associated with maintaining the same catalyst bed while increasing the feed flow rate. Subsequently, there are more molecules to react in the same amount of catalyst within the same timeframe.

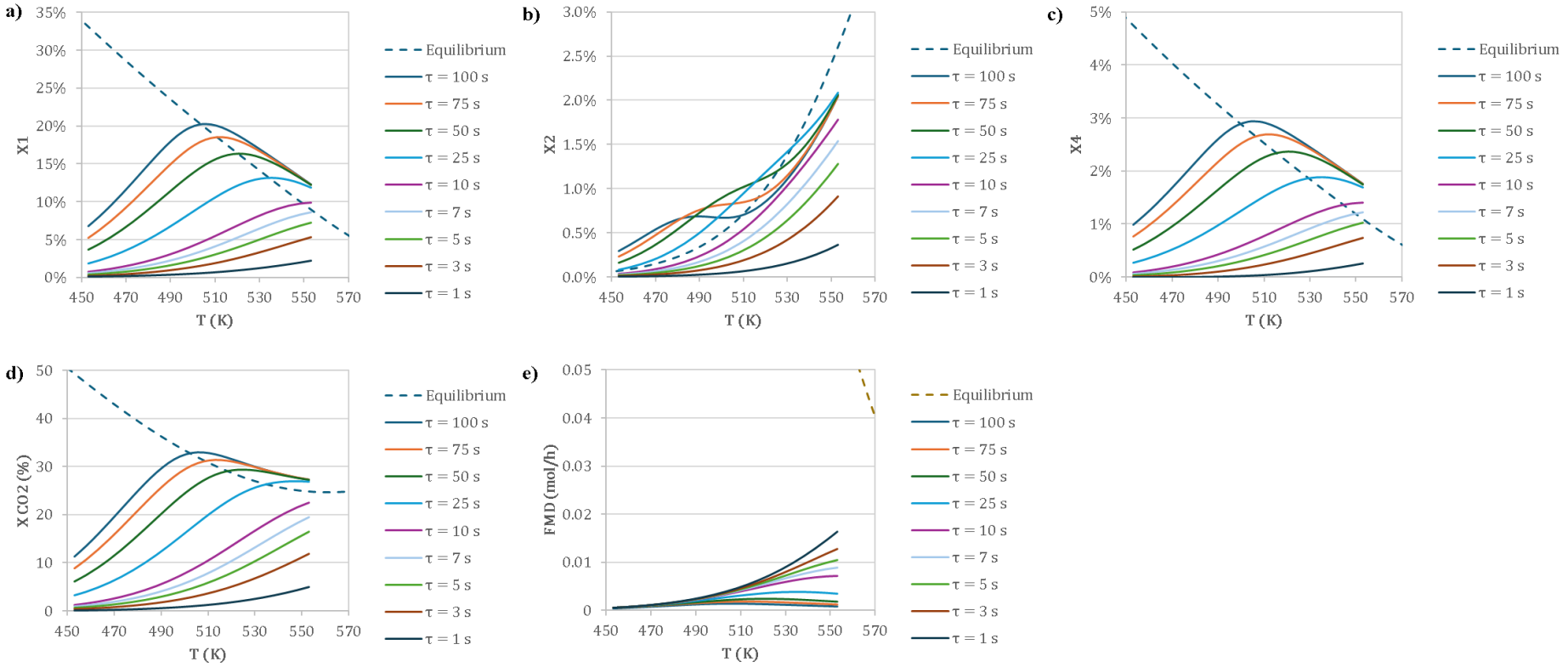

Figure 4.6 Simulation of an isothermal reactor for different set space times (τ) by changing the feed flow rate (F_{total}=0.022-2.178 mol.h^{-1}) for a) X_1, b) X_2, c) X_4, d) X_{CO_2} and e) F_{MD}versus temperature. Operating conditions: P=36 bar, T=453.15-553.15 K, $H_2/CO_2 = 3$, $N_2$2=10%. Refer to Table 4.5.

Figure 4.7 explore the effect of space time by changing the catalyst bed mass (height) at fixed feed flow rate. The resulting simulations, excluding curves F_{MD} (Figure 4.7e), are identical to those observed in Figure 4.6. Figure 4.6e and Figure 4.7e provide different values for F_{MD} at diverse τ. Conversely to Figure 4.6e, Figure 4.7e shows a maximum F_{MD} at the maximum τ.

Figure 4.8 shows the results of Figure 4.6 and Figure 4.7 at only four distinct τ and superpose them. Figure 4.8c reveals that at $\tau = 1\ s$ and $T = 550.15\ K$, it is the F_{MD} that is the best. Since the feed flow rate remains constant, increasing the catalyst mass provides more surface area for reactant molecules to adsorb, leading to higher production. However, maintaining a constant space time (e.g., 100 s) through adjustments in catalyst mass and feed flow rate guarantees consistent productivity per kg of catalyst, as demonstrated in Figure 4.8d.

Figure 4.8a, c, and d are so identical that τ can be varied by the feed flow rates or the catalyst length. These results suggest that X_1, X_2, X_4, X_{CO_2} and $\dot{Q}$, the global heat flux (the heat transferred per unit of time and per reactor wall square meter), are a function of τ regardless of how τ is changed. Increasing the catalyst mass resulted in a higher F_{MD} compared to increasing the feed flow rate, with the maximum F_{MD} observed at $\tau = 100\ s$ and $T = 553.15\ K$ (see Figure 4.8c). Table 4.7 details the results for both cases, changing feed flow rate and catalyst mass. At $\tau = 1\ s$, the simulation with an increased feed flow rate resulted in a higher productivity of combined methanol and DME. At $\tau = 100\ s$, the highest productivity was achieved using 11.9 g of catalyst. Based on these results, it is more desirable to increase the catalyst mass than the reactor inlet flow rate to ensure adequate contact between the reactive molecules and the catalyst surface. This approach increases overall production and prevents the rapid saturation of the catalyst.

Table 4.7 presents that the highest heat flux $\dot{Q}$, alongside the greatest methanol plus DME productivity per kilogram of catalyst F_{MD}/m_{cat}, is found at a space time of one second ($\tau = 1\ s$). This outcome coincides with the configuration employing the lowest catalyst mass for a fixed reactor length and the configuration with the highest feed flow rate. Per energy equation Eq. (4.38), we know that the power increases with the reaction rate which is directly proportional to the inlet molar flow. Consequently, it is consistent to obtain a higher heat flux $\dot{Q}$ when the space-time is 1 s due to the higher molar flow of reactants within smaller reactor volume and wall surface. Regardless of the space time, the conversion was the same when varying the flow rate or the length of the catalyst bed.

Table 4.7 Simulation results when varying feed flow rate and the amount of catalyst mass.

	τ (s)	T_{opt} (K)	m_{cat} (g)	$F_{t,in}$ $(mol.h^{-1})$	X_{CO_2} (%)	$F_{MD} \cdot 10^{-3}$ $(mol.h^{-1})$	F_{MD}/m_{cat} $(mol.h^{-1}.kg^{-1})$	$\dot{Q}$ $(W.m^{-2})$
Flow	109	508.15	0.83	0.02	32.92	1.46	1.76	81.03
	81	513.15	0.83	0.03	31.33	1.79	2.15	98.34
	53	523.15	0.83	0.04	29.36	2.37	2.84	127.14
	25	548.15	0.83	0.09	26.89	3.61	4.33	180.40
	10	553.15	0.83	0.22	22.50	7.15	8.57	348.49
	7	553.15	0.83	0.31	19.52	8.88	10.65	433.57
	5	553.15	0.83	0.44	16.43	10.52	12.62	514.65
	3	553.15	0.83	0.73	11.89	12.81	15.37	628.64
	1	553.15	0.83	2.18	4.96	16.33	19.58	796.30
Length	109	508.15	11.91	0.31	32.92	20.91	1.76	81.03
	81	513.15	8.93	0.31	31.33	19.23	2.15	98.34
	53	523.15	5.96	0.31	29.36	16.92	2.84	127.14
	25	548.15	2.98	0.31	26.89	12.88	4.33	180.40
	10	553.15	1.19	0.31	22.50	10.21	8.57	348.49
	7	553.15	0.83	0.31	19.52	8.88	10.65	433.57
	5	553.15	0.60	0.31	16.43	7.51	12.62	514.65
	3	553.15	0.36	0.31	11.89	5.49	15.37	628.64
	1	553.15	0.12	0.31	4.96	2.33	19.58	796.30

Since residence time is defined as the ratio of reactor volume to feed molar flow (Eq. (4.7)), and the latter parameters are directly proportional, it is expected that increasing the feed flow rate for a fixed catalyst mass, and increasing the catalyst mass for a fixed feed flow rate yield identical outcomes. Therefore, the overlapping F_{MD}/m_{cat} results presented in Figure 4.8d are as expected. At $\tau = 1\ s$, the productivity with respect to catalyst mass F_{MD}/m_{cat} was maximum.

All in all, the simulations demonstrated consistent CO_2 conversion across all investigated scenarios. However, for a space time of 100 seconds, increasing the catalyst mass resulted in superior productivity and lower global heat flux compared to varying the feed flow rate. This suggests that, for a long space time, adjusting the catalyst quantity rather than the feed flow rate is a more effective strategy to achieve both higher productivity and lower global heat flux as the wall surface area increased. It is noteworthy that the amount of catalyst needs to be re-evaluated in the context of reactor design.

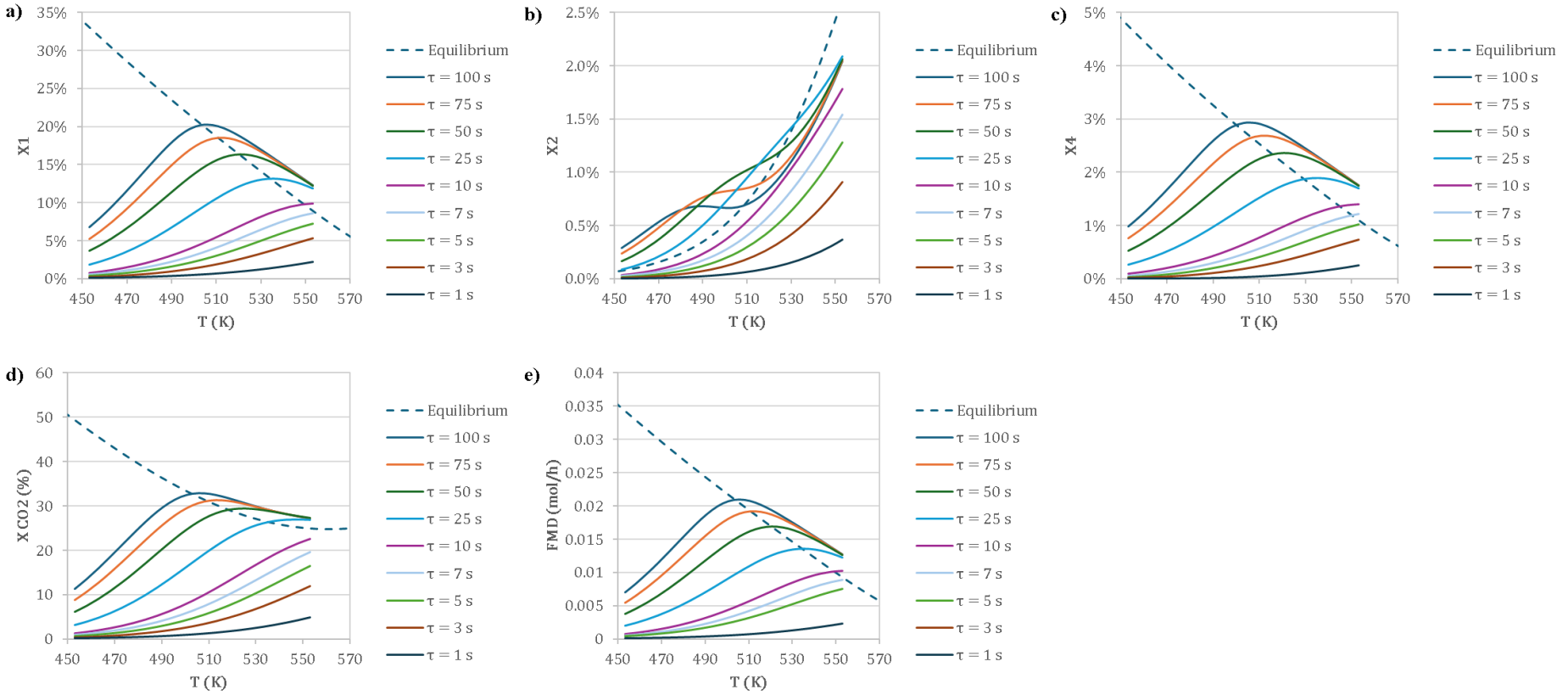

Figure 4.7 Simulation of an isothermal reactor for different set space times (τ) by changing the length of catalyst bed (H_{bed}=0.88-87.86 cm) for a) X_1, b) X_2, c) X_4, d) X_{CO_2} and e) F_{MD} versus temperature. Operating conditions: P=36 bar, T=453.15-553.15 K, $H_2/CO_2 = 3$, $N_2 = 10\%$. Refer to Table 4.6.

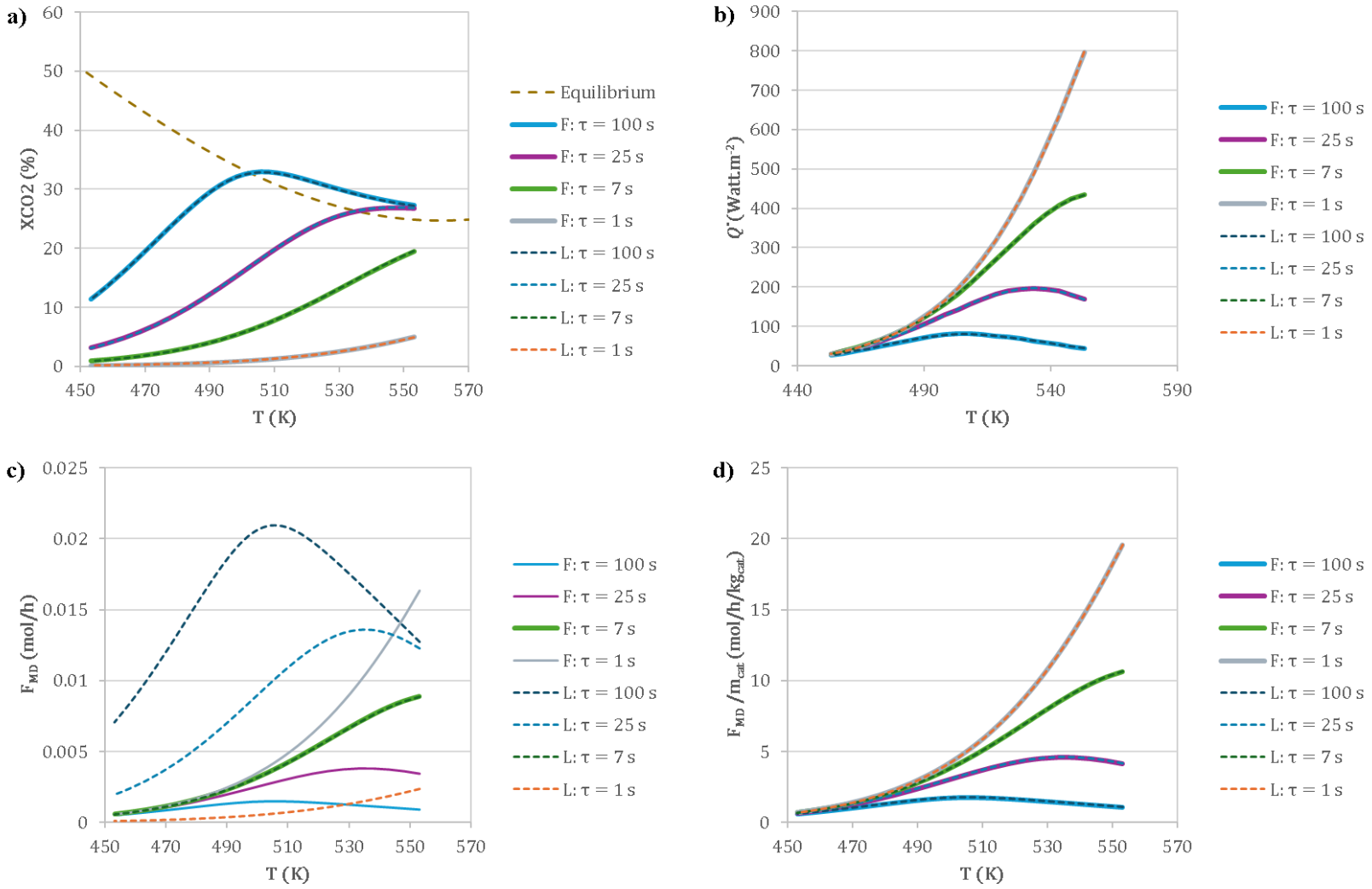

Figure 4.8 Comparison of simulations of an isothermal reactor for different set of space times (τ) by changing the feed flow rate (F) and by varying the length of catalyst bed (L) for a) X_{CO_2} (%), b) $\dot{Q}$ ($W.m^{-2}$), c) F_{MD} ($mol.h^{-1}$) and d) F_{MD}/m_{cat} ($mol.h^{-1}.kg_{cat}$) versus the temperature. Refer to Table 4.5 and Table 4.6.

4.5. A reactor optimisation by temperature progression

After completing the simulations in an isothermal fixed bed reactor and verifying that the results were as expected according to the literature, we optimised the temperature profile of the reactor. In this section, we will select the criterion to be optimised. We analyse the effects of the reactor inlet temperature, the molar feed ratio (H_2/CO_2), and the residence time (τ). This last analysis, similar to the simulation, will be performed by varying the inlet flow rate or changing the catalyst mass.

4.5.1. Choice of criterion to optimise

The optimisation criterion is dictated by the desired outcome. For instance, an industrial plant may seek to maximise CO_2 conversion, methanol production, DME production, or a combination thereof. Accordingly, we studied the influence of the optimisation criterion on the OTP obtained.

For the aim, we studied a fixed-bed reactor of 4 mm diameter and 5.9 cm length, working at 31 bar with an inlet temperature of 583.15 K and a feed flow rate of $F_{N_2} = 2.58 \cdot 10^{-2}\ mol.h^{-1}; F_{H_2} = 1.80 \cdot 10^{-1}\ mol.h^{-1}$ and $F_{CO_2} = 6.35 \cdot 10^{-2} mol.h^{-1}$. The chosen specifications reflect the reactor used in our lab experiments in Chapter 3 and a single operating condition set.

We investigated the effects of the choice of criterion, that is to maximise one outcome $X_1\ or\ X_4 or\ X_{CO_2} or\ F_{MD}$, on the 5 other outcomes $(X_1, X_2, X_4, X_{CO_2}\ and\ F_{MD})$ by comparing multiple optimisation runs. Figure 4.9 summarizes the outcomes obtained with the OTP optimisation maximising one criterion alone. For instance, when the objective was to maximise X_1 (Max. X1), the red curves shown in Figure 4.9 were obtained. Similarly, the black curve in Figure 4.9 corresponds to the maximization of X_4, and successively for X_{CO_2} and F_{MD}. The figure group the optimisations for the 4 criteria. Notably, the extent of reaction Eq. (4.33), X_1, and the combined production of methanol and twice the amount of DME (F_{MD}) all exhibited identical trends. This aligns perfectly with the overall material balance for all the chemicals involved presented in Table 4.4. According to the table, F_{MD} $\left(F_{MD} = F_{CH_3OH} + 2F_{DME}\right)$ is equal to one-third of $X_1 F_{t,in}$, bearing in mind that $F_{CH_3OH,in}$ and $F_{DME,in}$ are zero. Therefore, optimising by maximising X_1 is identical to optimising F_{MD}.

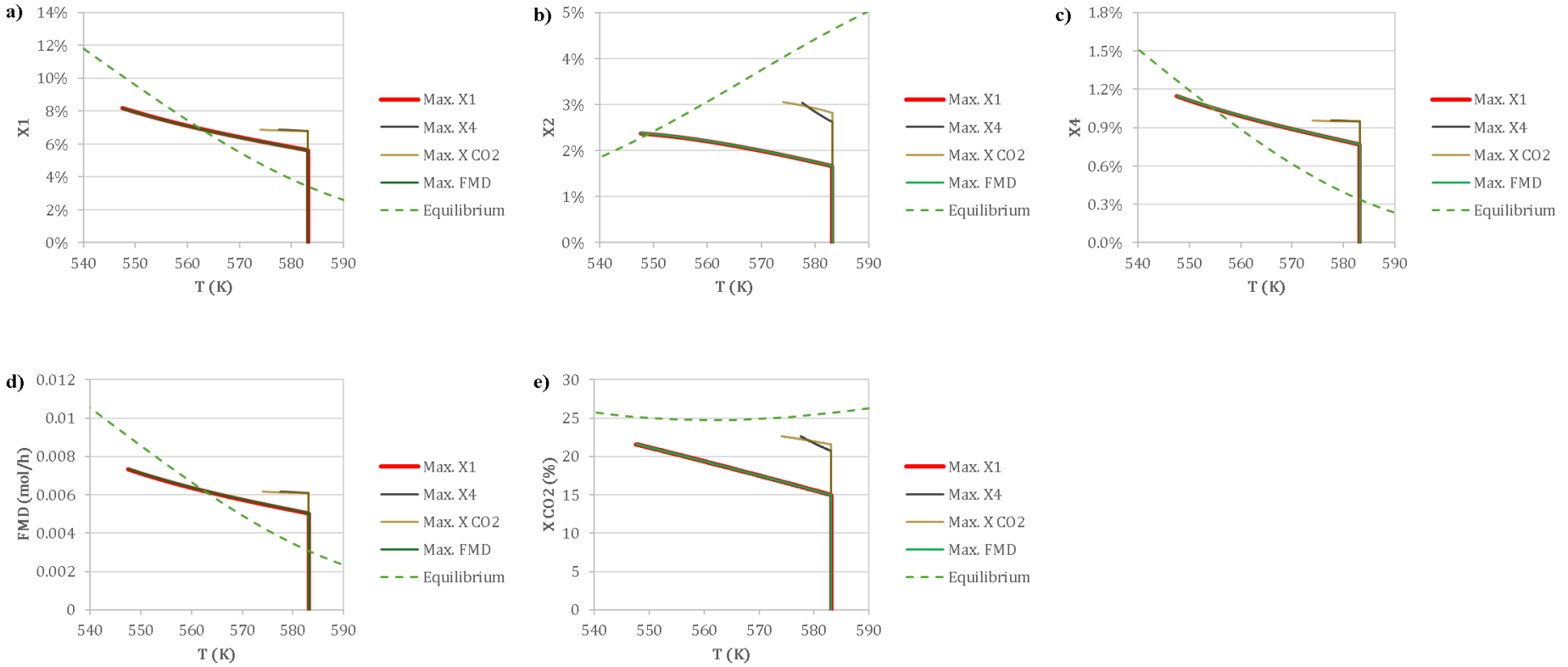

Figure 4.9 Effect of choice of criterion by maximising X_1, X_4, X_{CO_2} and methanol and DME productivity (F_{MD}) vs temperature. Operating conditions: P=31.1 bar, $F_{t,in}$=0.269 mol.h^{-1}, H_2/CO_2 = 2.8, N_2 = 10%, m_{cat}=8·10^{-4}kg, T_o=583.15 K and τ=6.8 s.

It is noted that depending on the optimized criterion, the optimal temperature progression curves will not be the same. Maximizing X_1 (and thus also F_{MD}) requires lowering the temperature to below 548 K, whereas optimisation suggests staying above 575 K if one wishes to maximize X_4 or X_{CO_2}. Our analysis revealed a trade-off between maximising X_{CO_2} and X_4, and minimising by-product formation (CO, represented by X_2). Maximising X_{CO_2} or X_4 led to higher CO_2 conversion (Figure 4.9b). Consequently, the combined production of methanol and DME is lower (Figure 4.9d). Maximising X_4 yielded results very similar to maximising X_{CO_2}, albeit with slightly lower values for X_1, X_2, X_4, X_{CO_2} and F_{MD}. The observed difference can be attributed to the elevated final temperature (577.55 K) achieved during the maximisation of X_4. Maximising either X_1 or F_{MD} led to the highest conversion into DME (X_4) and F_{MD} productivity, with minimal CO production (X_2). Based on these findings and given that we are seeking to maximise the conversion of CO_2 into DME or methanol, the order of priority for optimisation is going to be $Max.X_1 > Max.X_4 > Max.X_{CO_2}$, then, optimisation of X_1 is to be favoured. Henceforth, we maximise X_1 at each temperature step.

4.5.2. Effect of inlet temperature

Variations in reactor inlet temperature resulted in a spectrum of CO_2 conversion levels observed throughout the reactor outlet stream (length: 5.9 cm). For instance, a range of 523.15-608.15 K was tested to identify the optimal inlet temperature at 31 bar with a feed molar rate of 0.269 mol.h^{-1} and a molar ratio of $H_2/CO_2 = 2.83$ and 10% of N2 based on operating conditions of one of the laboratory experiments.

Figure 4.10 illustrates the influence of inlet temperature on the investigated parameters through the OTP profiles. For all the OTP optimisations and investigated parameters, the inlet temperatures induce different profiles which are not perfectly overlapped for high inlet temperatures, contrary to what we observed in the Figure 4.4a when studying a single reversible reaction. As observed in Figure 4.10f, CO_2 conversion at the reactor outlet increases with the reactor inlet temperature and followed by an OTP. The analysis of X_1, X_4 and F_{MD} (Figure 4.10a, Figure 4.10c and Figure 4.10d) collectively suggests that 555.15 K is the most favourable inlet temperature for the reactor under the specified operating conditions.

Regardless of higher CO_2 conversion at higher inlet temperature, Figure 4.10b shows that higher inlet temperature tends to increase CO production. Furthermore, this can be explained thermodynamically, as the RWGS reaction is endothermic while the synthesis of methanol and DME are exothermic. This conclusion is further supported by the findings in Figure 4.12.

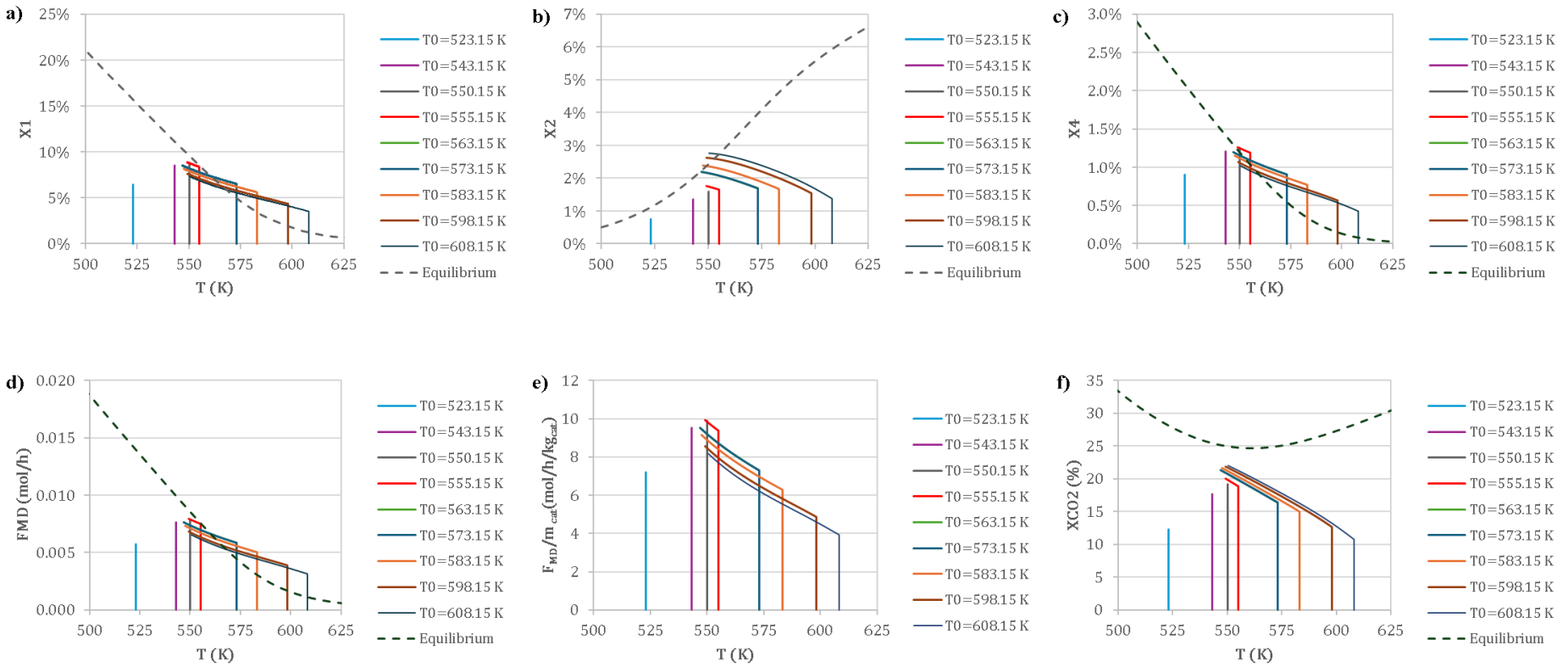

Figure 4.10 Effect of inlet temperature by optimising X1: a) X_1, b) X_2, c) X_4, d) methanol and DME productivity (F_{MD}) e) F_{MD}/m_{cat} and f) X_{CO_2} vs temperature. Operating conditions: P=31.1 bar, $F_{t,\,in}$=0.269 mol.h^{-1}, H_2/CO_2 = 2.8, N2=10%, m_{cat}=8·10^{-4}kg and τ=6.1-7.1 s.

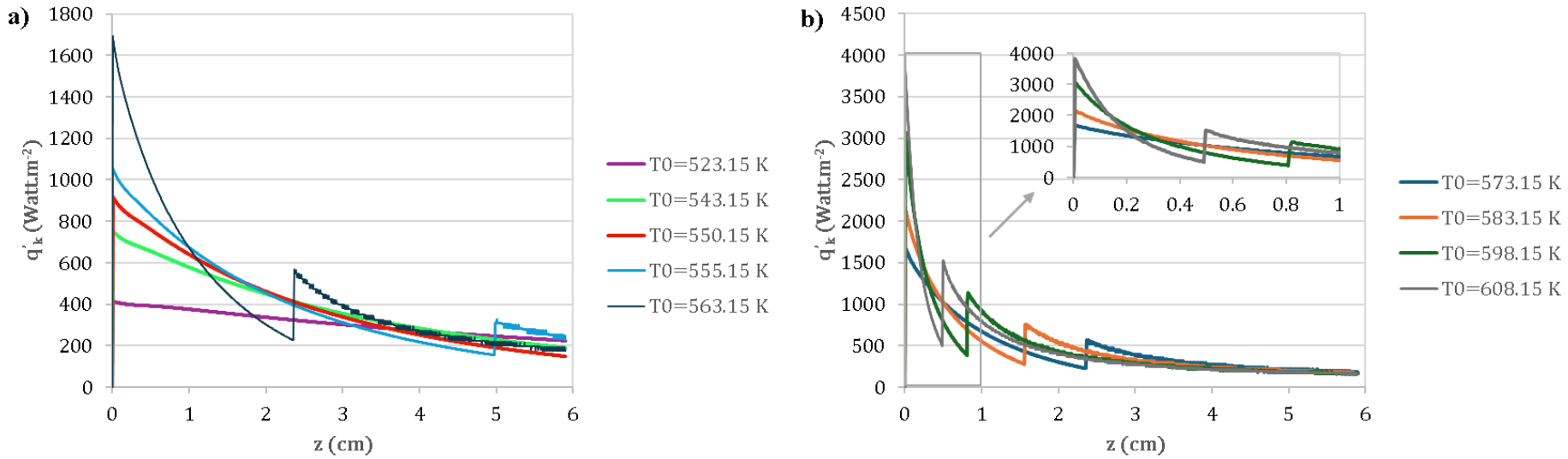

Figure 4.11 Effect of inlet temperature by optimising X1: local heat flux (q_k) vs the axial position (z) for a)T=523.15-563.15 K and b)T=573.15-608.15 K. Operating conditions: P=31.1 bar, $F_{t,in}$=0.269 mol.h^{-1}, H_2/CO_2 = 2.8, N_2 = 10%, m_{cat}=8·10^{-4}kg and τ=6.1-7.1 s.

Figure 4.11 shows the local heat flux $\dot{q_k}$ as a function of the reactor position (z) for various inlet temperature (T_0). The heat to be removed is the highest at the entrance area of the catalytic bed and decreases along its length. The higher the inlet temperature, the greater the heat to be removed at the entrance area of the catalytic bed. The heat flux to be dissipated reaches high values when the inlet temperature is elevated. A maximum value of 3820 $W.m^{-2}$ at the reactor inlet for $T_0 = 608.15\ K$, and then decreases to 160 $W.m^{-2}$ at $z = 5.9\ cm$. A distinct change in the behaviours of the curves is noticeable for inlet temperature higher than $T_0 = 550.15\ K$. Below this value, for $T_0 = 523.15, 543.15,$ and $550.15\ K$ (Figure 4.10), the OTP maintains a monotonically decreasing local heat flux, $\dot{q_k}$, profile throughout the length of reactor, explained by the fact that the OTP advocates for isothermal reactor operation. Above an inlet temperature of $T_0 = 550.15\ K$, the curves show breaks in the slope: this corresponds to conditions where the optimisation leads to the realisation of an OTP. As long as the reactor is isothermal, the power to be removed decreases steadily. When the temperature needs to decrease to remain optimal, an additional cooling term appears, contributing to the creation of extra power to be evacuated. This results in a discontinuity in the curve.

However, the optimal OTP that allows for the maximum conversion X_1 is obtained with an inlet temperature of 555.15 K, and the power to be dissipated then decreases from 1000 $W.m^{-2}$ to 200 $W.m^{-2}$ (Figure 4.11a).

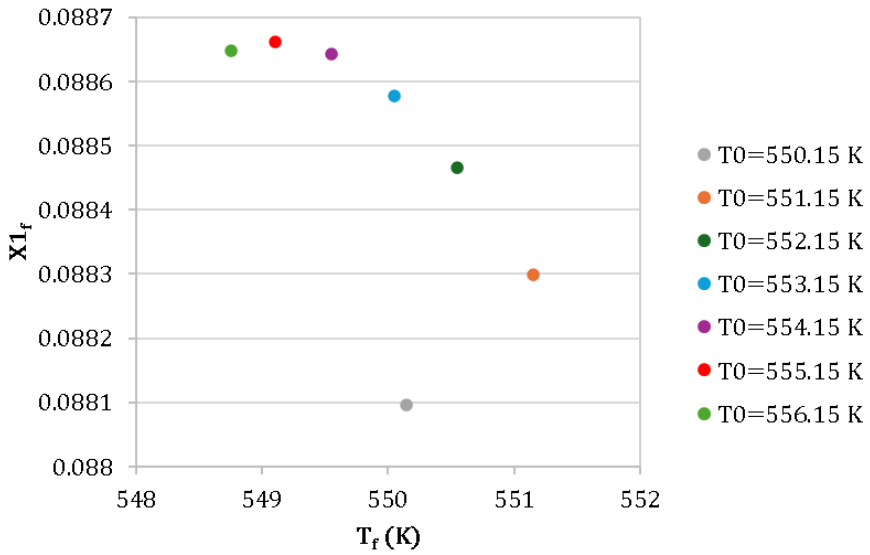

Figure 4.12 Effect of inlet temperature by optimising X_1: X_1 vs temperature at the reactor outlet. Operating conditions: P=31.1 bar, $F_{t,\,in}$=0.269 mol.h^{-1}, H_2/CO_2 = 2.8, N_2 = 10%, m_{cat}=8·10^{-4}kg and τ=6.7-6.8 s.

Figure 4.12 shows the conversion X_1 as a function of the outlet temperature, obtained over a narrower span of temperature from $550.15 - 556.15\ K$ to refine the optimal inlet temperature

value. The X_1 obtained for the different inlet temperatures are very close, as the scale is very narrow. Although, the value of X_1 is highest at $T_0 = 555.15\ K$. From Figure 4.10, we can deduce that X_4 and F_{MD} are also highest at $T_0 = 555.15\ K$. On the other hand, the conversion of CO_2 is not the best since there are other conditions where more CO is formed, which consumes CO_2 (but this is not desired in our case as this consumption of CO_2 does not produce methanol or DME). Isothermal conditions at $T_0 = 550.15\ K$ and $T_0 = 551.15\ K$ were unable to achieve a maximum CO_2 conversion or F_{MD}, underscoring the direct impact of inlet temperature on yields within the optimised temperature progression (OTP). Additionally, the lower the inlet temperature, the lower the power to be dissipated at the reactor inlet.

Between an isothermal operation with an inlet temperature $T_0 = 550.15\ K$ and an OTP with an inlet temperature $T_0 = 555.15\ K$, the results are in the end very similar. For the OTP starting at $555.15\ K$, we observe the best conversions (X_1 and X_4) and the highest production of methanol plus DME (F_{MD}). The heat to be dissipated is not significantly different from an isothermal condition at $T_0 = 550.15\ K$. In the first few centimetres of the reactor, the heat to be dissipated is comparable (isothermal versus OTP).

In this scenario, the difference between the OTP and the isothermal process with optimised inlet temperatures is not significant. This contrasts with the case of the initial $A \rightleftharpoons B$ reaction, where up to a 10% higher conversion was achieved with OTP compared to the last isothermal condition (Figure 4.4a). Unfortunately, we suspect that when there are competitive reactions involving both endothermic and exothermic processes, the benefit may be less pronounced. However, it is important to note that we did not account for CO hydrogenation to methanol, which could potentially alter our results.

Contrary to this thesis research, the study by Senthil & Sundaramoorthy, 2018 [5] focused on a single exothermic reaction in a batch reactor with a reactant A, using data reported in the literature. They demonstrated the influence of inlet temperature in the OTP, but in their work, the final fractional conversion of reactant A (x_{Af}) was not always favoured by lower initial temperatures. They achieved a maximum final conversion of $x_{Af} = 0.919$ of reactant A, by operating the batch reactor in two phases: a quick heating phase in lasting about one minute ($x_{A0} = 0.091$, $T_0 = 748.10\ K$ and a heating rate of $Q = 31000\ kW$) followed by a slow cooling phase of one hour. Their heating rate Q in all their cases was significantly higher than our results.

Similarly, Iranshahi et al., 2017 [6] optimised the inlet temperature for each of twenty segments of a fixed bed reactor for direct DME production from syngas by OTP and water removal by optimising the reactor through differential evolution algorithm (optimisation method). Through their theorical study, they achieved enhancements in DME production of

1.5%, 55% and 70% compared to the conventional reactor. In the first scenario, only the inlet temperature of each the 20 segments was optimised, resulting in 1.5% improvement. The second scenario considered water permeation (with membrane or water adsorbent as the zeolite 4A), leading to a 55% increase. The third scenario combined both optimisations, yielding a 70% improvement. Unlike our analysis, their kinetic model were selected from literature [12], and the involved reactions were methanol synthesis from CO, methanol synthesis from CO_2 and methanol dehydration to DME, all of which were considered in equilibrium. They showed good agreement with the simulation and model design of a pipe-shell reactor for DME synthesis from syngas developed by Hu et al., 2008 [13].

Omata et al., 2002 [14] performed an experimental study for DME synthesis from syngas ($3CO + 3H_2 \rightleftharpoons CH_3OCH_3 + CO_2$) with a molar ratio of H_2/CO=2:1 containing 5% CO_2, at 1-3 MPa in an isothermal reactor and a Temperature Gradient Reactor (TGR). They found CO conversion was below 80% due to equilibrium limit with the isothermal reactor ($513\ K, 2\ MPa, W/F = 30\ g.h.mol^{-1}$). However, with the TGR, the same conversion was attained with $W/F = 15\ g.h.mol^{-1}$ at $550 - 510\ K, 2\ MPa$. 90% CO conversion was possible at $3\ MPa$ and $550 - 510\ K$. In another study, they found a 5% higher CO conversion with the TGR (71%) compared to a conventional isothermal reactor (66%), effectively overcoming the equilibrium limit of the DME synthesis from syngas at high temperature and the low activity of catalyst at low temperature [9].

Another of their investigations showed that an optimised catalyst allowed a high one-pass conversion of CO ($3CO + 3H_2 \rightleftharpoons CH_3OCH_3 + CO_2$) at 82% at 1 MPa in a TGR packed with Cu-Zn-Al-Ti-Nb-V-Cr catalysts and γ-alumina, compared to 72% with a standard Cu catalyst in the TGR and 69.5% in an isothermal reactor at 523 K [8]. This investigation employed artificial neural networks (ANN) and grid search optimisation to determine the optimal temperature for each zone of the TGR. The laboratory TGR (SUS 316, 9.53 mm O.D., 7.53 mm I.D.) had five heated zones fed with syngas (H_2/CO/CO_2/N_2= 60/30/5/5), operating at $1\ MPa, W/F = 15 - 50\ g.h.mol^{-1}$.

According to these results, slightly better performances were achieved when CO_2 hydrogenation to methanol, CO hydrogenation to methanol and methanol dehydration to DME processed through the OTP. However, more improvements were observed with additional modifications, such as water removal and catalyst optimisation, always bearing in mind the equilibrium of all the reactions. This contrasts with our case, where the backward reaction of methanol dehydration to DME does not take place (non-equilibrated, as explained in Chapter 3). For single and exothermic reactions, OTP exhibited a greater impact on outcomes compared to an isothermal reactor, without any constraints. In addition to other variables

affecting the system performance, identifying the optimal inlet temperature for the reactor configuration and process conditions is crucial.

4.5.3. Effect of H_2/CO_2 ratio

Two scenarios were evaluated to assess the impact of the H_2/CO_2 ratio at the reactor inlet (maintained at 36 bar) on the conversion of CO_2, reaction progresses and productions achieved. In the first scenario, the total inlet molar flow rate was held constant, while in the second scenario, the CO_2 inlet molar flow rate was fixed and the H_2 inlet molar flow rate was calculated by imposing the molar ratio. Table 4.8 summarizes the inlet conditions established for these analyses. In all cases, the optimal inlet temperature was identified and the molar fraction of nitrogen was maintained at 10%.

When the total feed flow rate was fixed, the space-time (τ) varied slightly due to the combined effect of the inlet temperature (which fluctuated across the three H_2/CO_2 ratios of 1, 3, and 9) and the partial pressures of the reactants.

Figure 4.13 depicts the influence of varying H_2/CO_2 ratio on X_1, X_2 and X_4, while Figure 4.14 illustrates the corresponding effects on CO_2 conversion (X_{CO_2}), DME production (F_{DME}) and combined methanol and DME productivity (F_{MD}).

Table 4.8 Inlet condition set to evaluate the effect of the feed molar ratio: H_2/CO_2. H_{bed}=0.059 m, and P=36 bar.

Exp.	F_{N2} $(mol.h^{-1})$	F_{H2} $(mol.h^{-1})$	F_{CO2} $(mol.h^{-1})$	Total $(mol.h^{-1})$	H_2/CO_2	T_{ini} (K)	τ (s)
	0.031	0.140	0.140	**0.311**	1	571.15	6.50
F_t fixed	0.031	0.210	0.070	**0.311**	3	565.15	6.57
	0.031	0.252	0.028	**0.311**	9	557.15	6.67
	0.006	0.028	**0.028**	0.062	1	538.15	34.51
F_{CO2} fixed	0.012	0.084	**0.028**	0.124	3	545.15	17.04
	0.031	0.252	**0.028**	0.311	9	557.15	6.67

As shown in Figure 4.13a and Figure 4.13c, both X_1 and X_4 exhibited a positive correlation with the H_2/CO_2 molar ratio. This trend was expected as the partial pressure of H_2 increased the conversion, leading to increased yields of the desired products (X_1, X_4). Conversely, Figure 4.13b shows that while the H_2/CO_2 ratio decreases, the conversion in CO (X_2) increases, reflecting the limited H_2 availability for the desired reaction. It is explained by the fact that for a fixed total flow rate, hydrogen is the limiting reagent when the H_2/CO_2 ratio is one. Conversely, carbon dioxide becomes the limiting reagent when the H_2/CO_2 ratio is 9. When the

CO_2 flow rate is fixed, hydrogen becomes less and less limiting as the ratio increases. The molar ratio of $H_2/CO=3/1$ is the stoichiometry of the reaction.

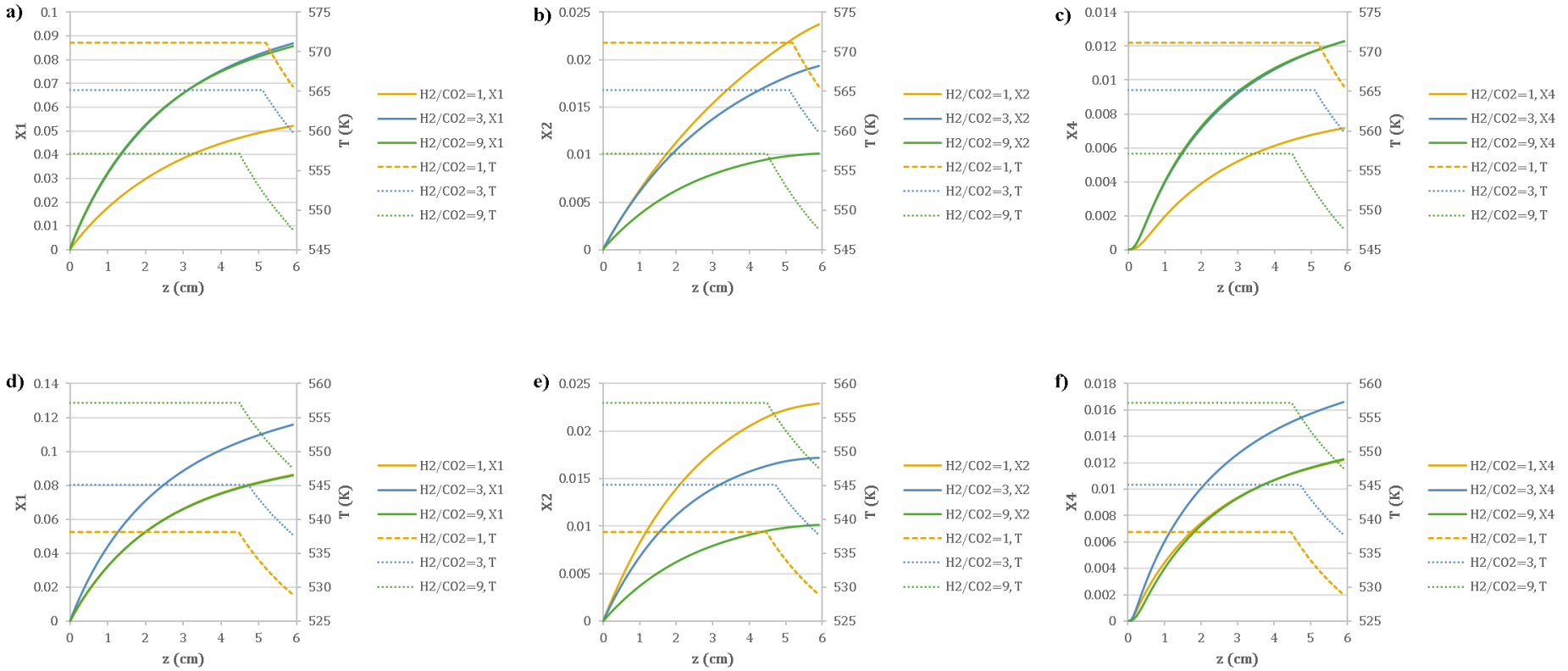

Figure 4.13 Effect of feed molar H_2/CO_2 ratio vs length of reactor (z): at a fixed input total flow a) X_1, b) X_2, c) X_4, and at a fixed CO_2 input flow rate d) X_1, e) X_2 and f) X_4. See Table 4.8 for details on operating conditions.

Interestingly, a near overlap of the X_1 and X_4 curves observed at H_2/CO_2 ratios of 3 and 9 with a fixed total feed flow rate does not occur when the CO_2 inlet molar flow rate is maintained constant. Instead, the overlap occurs for ratios of 1 and 9. This can be explained by the lower inlet temperature and reactant concentrations associated with a defined CO_2 feed flow rate. Thermodynamically, lower temperatures favour the progresses of X_1 and X_4 while suppressing X_2, as evidenced in Figure 4.13.

However, when the total inlet flow rate is held constant, the H_2/CO_2 ratio of 3 results in lower X_1 and X_4 compared to a fixed CO_2 inlet flow rate ($F_{t,infixed} = 0.311\ mol.h^{-1}$ vs $F_{tin,CO_2 in\ fixed} = 0.124\ mol.h^{-1}$). Nevertheless, for a fixed CO_2 feed flow rate, CO_2 conversion into the combined DME and methanol (X_{CO_2} and F_{MD}) is more pronounced at $H_2/CO_2 = 9$ than at ratios of 3 or 1 (Figure 4.14). This figure highlights the increasing CO_2 conversion efficiency with a higher H_2/CO_2 molar ratio. However, the DME and methanol production suggests that H_2/CO_2 ratios of 3 or 9 lead to comparable outcomes for constant total inlet flow rate.

Zhang et al., 2006 [15] evaluated the effect of feed molar ratio on methanol synthesis reaction behaviour over Cu based catalyst supported on zirconia modified γ-Al_2O_3 at T = 240 °C, P = 3.0 MPa and GHSV = 3600 h^{-1} in a micro reactor. After assessing the H_2/CO_2 molar ratio in the range of 1 to 10, they identified that CO_2 conversion improves with molar ratio. Correspondingly, the methanol selectivity was slightly upper when $H_2/CO_2 = 3$, and then decreases a little.

More recently, Stangeland et al., 2018 [16] studied the effect of feed H_2/CO_2 ratio from 1 to 10 on the thermodynamics of CO_2 hydrogenation to methanol and DME. This analysis was conducted in a temperature range of 150-350 °C and 10, 30, 50, and 100 bar using a RGIBBS reactor module in Aspen plus. They determined that getting bigger H_2/CO_2 ratio notably intensifies CO_2 conversion at all pressures. The result was ascribed to the sensitivity of methanol synthesis reaction to the H_2 partial pressure. Nonetheless, the excess of H_2 also promoted the CO formation at higher temperature. Besides, the investigators elucidated that an increasing stoichiometric H_2/CO_2 ratio can benefit methanol selectivity and restrain by-product formation. However, this will have a detrimental impact on the economic viability of the process as it will require more H_2. Their computations suggested that, whereas the total feed flow rate is constant, independent of reaction conditions, it is possible to obtain the highest methanol yield at the stoichiometric H_2/CO_2 ratio (3/1).

In light of these findings, a molar ratio of $H_2/CO_2 = 3$ was adopted for the remaining optimisation analyses presented in this chapter. This decision necessitates the continuous estimation of the inlet temperature for each scenario.

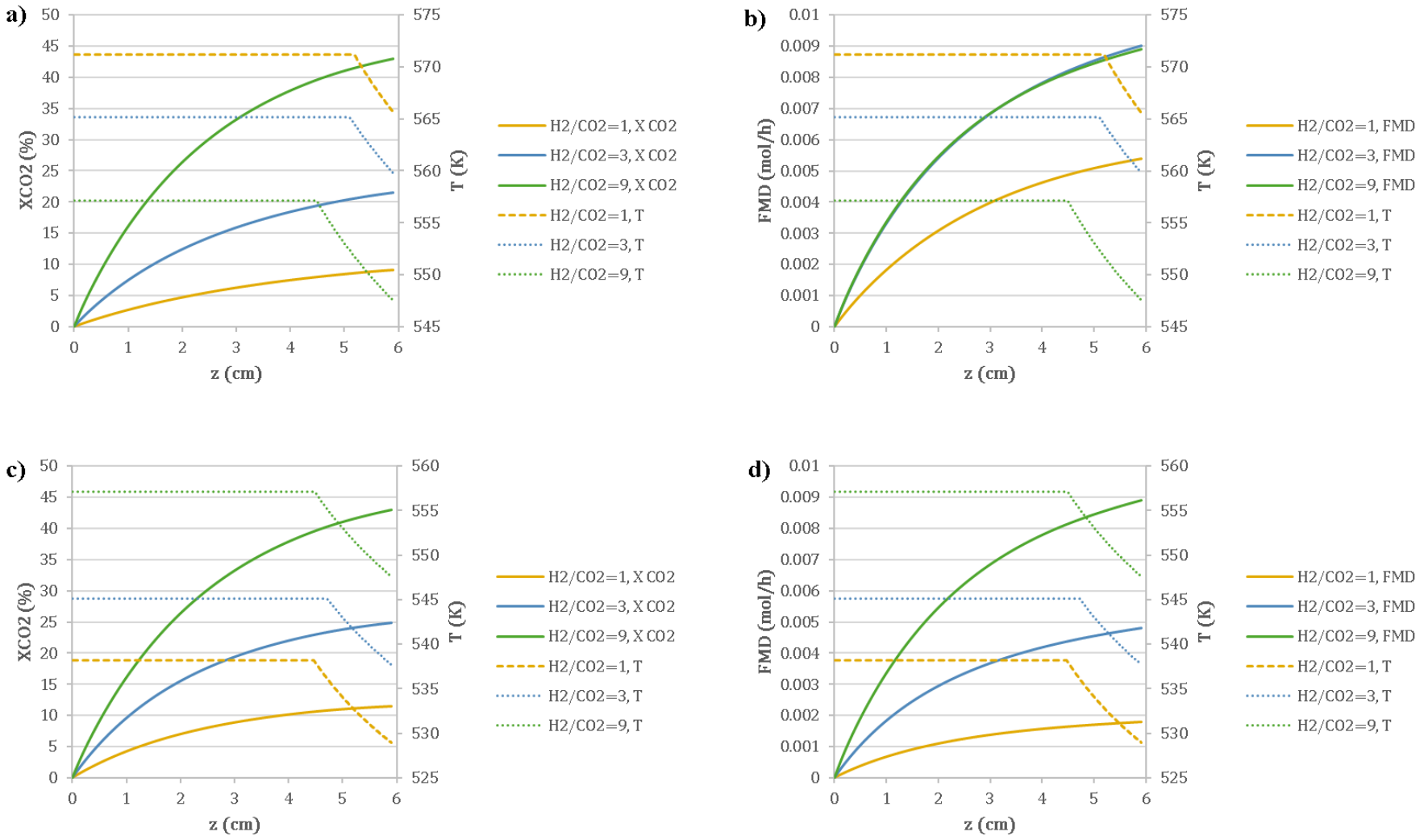

Figure 4.14 Effect of feed molar H_2/CO_2ratio vs length of reactor (z): at a fixed input total flow a) X_{CO_2}, b) F_{MD}, and at a fixed CO_2 input flow rate c) X_{CO_2}, and d) F_{MD}. See Table 4.8 for details on operating conditions.

4.5.4. Effect of space time (τ)

We assessed the effect of space-time in the OTP reactor, as with the simulations of the isothermal reactor (section 4.4), using the same approaches: varying the feed flow rate and the length of the catalyst bed. In this case, we evaluated only four space-times: 25, 7, 3, and 1 second.

The OTP reactor yielded similar conclusions to those found in the isothermal reactor simulations regarding the effect of changing the feed flow rate or the length of the catalyst bed. However, as expected due to the nature of the OTP reactor, the patterns of the curves and results differ from those in the isothermal reactor simulations. Interestingly, in the OTP reactor, higher space-times led to lower heat transfer per unit of wall surface area ($\dot{q_k}$) at the reactor outlet. For further details refer to Appendix B.

Table 4.9 presents the comparison of the results at the reactor outlet when varying the feed flow rate while keeping constant the length of the bed of reactor versus changing the length of catalyst bed and maintaining constant the feed flow rate. The combined production of methanol and DME F_{MD} increases with the mass of the catalyst and the feed flow rate. The same global $\dot{Q}$ heat flux were obtained with both methods. Similarly, local $\dot{q_k}$ heat fluxes were equal with both methods. The maximum global and local heat flux were identified for $\tau = 1\ s$.

Table 4.9 Comparison of F_{MD}, the global power Q, the outlet global heat flux $\dot{Q}$ and the local $\dot{q_k}$ heat flux of both methods for the varied space-time τ.

	τ (s)	L (m)	$F_{t,in}$ $(mol.h^{-1})$	$F_{MD} \cdot 10^{-3}$ $(mol.h^{-1})$	Q (W)	$\dot{Q}$ $(W.m^{-2})$	$\dot{q_k}$ $(W.m^{-2})$
Flow	25	6.26	0.09	3.65	0.17	216.20	1197.75 – 91.60
	7	6.26	0.31	9.18	0.35	442.90	1206.52 – 267.76
	3	6.26	0.73	14.74	0.54	692.67	1208.54 – 386.28
	1	6.26	2.18	20.51	0.76	966.99	1209.56 – 784.76
Length	25	22.36	0.31	13.04	0.61	216.20	1197.75 – 91.60
	7	6.26	0.31	9.18	0.35	442.90	1206.52 – 267.76
	3	2.68	0.31	6.32	0.23	692.67	1208.54 – 386.28
	1	0.89	0.31	2.93	0.11	966.99	1209.56 – 784.76

Senthil & Sundaramoorthy, 2018 [5] with a batch reactor volume achieved a minimal heating rate of $Q = 27000\ kW$ at $T_0 = 690.4\ K$, whereas our PFR presented lower heating rate $Q = 0.31\ W$ at $T_0 = 555.15\ K$. In a micro heat exchanger unit packed bed reactor with rectangular channels of identical dimensions of $H = 3 \times 10^{-4}\ m$, $W = 6 \times 10^{-4}\ m$ and $L = 0.15\ m$, the heat duty was found to vary between 0.4– 0.6 kW, respectively [17]. Peláez et al., 2018 [18] simulated a multi-tubular fixed-bed reactor for direct DME synthesis of $d_r = 0.02\ m$ and $L = 8.50\ m$ at

$T_0 = 518.15\ K$ and $P_0 = 40$ bar with a maximum heat flux axial profile at the reactor wall ($r = d_r/2 = 0.01\ m$) of $q = 750\ W.m^{-2}$ in the area close to the reactor inlet, which progressively decreased to 82 $W.m^{-2}$ in the reactor outlet. This is analogous to the behaviour and magnitude of the values seen in Appendix B Figure B.4f, where the heat flux through the reactor wall in the reactor inlet exhibits a maximum that progressively decreases until the reactor outlet. Likewise, Behloul et al. 2022 [19] illustrated an identical maximum in heat flux density at the reactor inlet (near 10 $kW.m^{-2}$), followed by a decrease along the axial length of the reactor, in an optimized conventional reactor–heat exchanger configuration for DME production from CO_2 hydrogenation.

It was confirmed that conversion of CO_2, reaction progresses, productivity and the heat transferred per wall unit area are highly dependent on residence time. Findings revealed that increasing the feed flow rate with a fixed mass of catalyst led to enhanced productivity and greater need of heat transfer through the reactor wall but resulted in lower conversion of CO_2 and reaction progresses as a function of residence time. In other words, augmenting the feed flow rate yielded higher production of methanol and DME and heat flux but conversions per pass are low. In contrast, adjusting the catalyst bed volume to rise residence time triggered a rise in all studied parameters: conversion of CO_2, reaction progresses, productivity and heat transferred per wall unit area. In view of these outcomes, the preferred approach is to work with a larger mass of catalyst and as long a space time as possible, rather than with a higher feed flow rate determined by production requirements. However, the price of the catalyst must be weighed against the gain in productivity obtained by increasing the quantity of catalyst. Further studies about economics and reactor designs are required to evaluate the challenges related to capital cost, catalyst deactivation, mass transfer limitations and heat management (potential hot spots and reactor cooling requirements).

4.6. Simulation of an OTP scaled-up reactor

In the previous section, X_1 was identified as the key parameter for optimisation. We established that a feed molar ratio of $H_2/CO_2 = 3$ is optimal. Furthermore, the highest space time yielded the highest conversions (approaching equilibrium) and productivity for a given configuration suggesting the benefit of having the longest catalyst bed. It is important to note that the estimation of the inlet temperature must be optimised for each scenario.

As previously discussed, the dimensions of the reactor have a direct impact on the conversion of CO_2, reaction progresses, methanol and DME productivity, and heat transferred per wall unit area. In this phase, we continue considering a non-isothermal PFR with the kinetic model validated in Chapter 3 to simulate an industrial OTP reactor.

For the simulation of an industrial reactor, the following assumptions were made:

1. The particle diameter considered for the simulations was 2000 μm. Let's discuss this value: we know that if we increase the particle diameter, we risk creating a limitation of internal diffusion and the kinetics will be affected. On the other hand, we know that this size is realistic and avoids creating excessive pressure drops. Furthermore Quezada, 2020 [20] in his kinetics, tested several particle sizes and showed no limitation of internal diffusion up to 1700 μm, but at 2500 μm. The transfer limitations will be further discussed.
2. Initially, the hydrodynamics conditions of the experimental are shown for a particle Reynolds number at 0.7. Quezada, 2020 [20] explained that the extrapolation of the results is possible if there are no external mass and heat transfer limitations. This would allow for a wider range of particle diameters, more representative of industrial catalysts, rather than being restricted to the 200 μm diameter used in his kinetic study. The author found that mass transfer limitations increased with larger particle diameters, such as 2500 μm. He clarified that the ideal scenario would maintain similar mass and heat transfer coefficients as the experimental case, minimizing pressure drop and maximizing residence time. To achieve this ideal case, he varied the Reynolds number by increasing the particle diameter, ensuring turbulent flow. In that case, nor heat or mass transfer limitations were identified for $Re = 200 - 800$. Based on those results and since the dimensions of the reactor are directly affected by the particle Reynolds number (Eq. (4.45)-(4.49)), we have also chosen to vary this parameter (Re) in conjunction with space time (τ).
3. The reactor is a plug flow, consequently the ratio of reactor height and the particle diameter must always be greater or equal to 50 $\left(H_{bed}/d_p \geq 50\right)$.
4. The loading densities of the two catalysts in the bed (ρ_{bed}) are the same as in the laboratory experiments.

This chapter will merely provide information on the behaviour of an industrial fixed bed if the kinetics are assumed to remain equal to the chemical kinetics. For the chosen reactor sizes and operating conditions, the mass and heat transfer limitations were checked with the same methods as those described in Chapter 3.

The computations were done by setting a desired space time (τ) and a precise feed flow rate of CO_2 (100 tons per day). The molar flow rate of hydrogen is three times that of CO_2. The nitrogen flow rate is assumed to be zero in all cases. The volume of the reactor was then computed from Eq. (4.14) as follows:

$$V = \frac{F_{t,in}}{C_{i0}}\tau \tag{4.42}$$

where,

$$C_{i0} = \frac{P}{RT} \tag{4.43}$$

The mass of the catalyst (m_{cat}) was determined from the catalyst loading density (ρ_{cat}) and the reactor volume (V), according to:

$$m_{cat} = V \cdot \rho_{cat} \tag{4.44}$$

Per definition, Reynolds number is:

$$Re = \frac{u\rho d_p}{\mu_m} \tag{4.45}$$

where $u\rho$ is the fluid superficial mass flow, d_p is the diameter of the particle and μ_m is the viscosity of the mixture (refer to Appendix A, Eq. (A.1) to (A.4)). Since Re, for hydrodynamics reasons, is retained and d_p is fixed, from Eq. (4.45), it is possible to compute the fluid superficial mass flow $u\rho$ as:

$$u\rho = \frac{Re\mu_m}{d_p} \tag{4.46}$$

From this, it is possible to calculate the section of the catalytic bed with the total feed mass flow rate ($\dot{m}$) and the fluid superficial mass flow.

$$S = \frac{\dot{m}}{u\rho} \tag{4.47}$$

The length of catalytic bed is given by,

$$H_{bed} = \frac{V}{S} \tag{4.48}$$

In terms of reactor section S, the diameter of the reactor is:

$$d_{bed} = \sqrt{4S/\pi} \tag{4.49}$$

Using these equations, we will now present the optimisation results. The procedure followed for this optimisation aligns with the methodology employed in Section 4.3.2 to determine the optimal temperature profile (Figure 4.5) for a constant space time and a pre-selected inlet temperature.

4.6.1. Optimal dimensions of scaled-up reactors

The operating conditions, as well as the reactor and catalyst parameters, are detailed in Table 4.10. The reactor operates at 36 bar, with a gas inlet of $3.79 \cdot 10^5\ mol.h^{-1}$, corresponding to a carbon dioxide mass flow of $4167\ kg.h^{-1}$ or $100\ ton.d^{-1}$. The inlet temperature varies depending on the fixed residence time (τ) and particle Reynolds number (Re). The particle diameter chosen was $2000\ \mu m$ to use a particle diameter (d_p) that is closer to the sizes of industrial catalysts. The reference d_p and Re were set based on simulation studies conducted by Quezada, 2020 [20] on a PFR.

Table 4.10 Operating conditions of the reactor and particle diameter parameter.

Parameters	**Value**	**Unit**
P	36	bar
H_2/CO_2	3	$-$
$F_{t,in}$	$3.79 \cdot 10^5$	$mol.h^{-1}$
d_p	$2.00 \cdot 10^{-3}$	m

Building upon the initial residence time of 25 seconds identified in Section 4.5.4, we opted to explore a wider range to evaluate its effect in conversion of CO_2, reaction progresses, methanol and DME productivity and heat transfer per unit area. Therefore, we varied the residence time from 25 to 200 seconds with increments of 25.

Table 4.11 Effect of space time and Reynolds number on reactor dimensions in a laboratory reactor and scaled-up OTP reactors. Fixed parameters: $P = 36\ bar$, H_2/CO_2=3, $F_{t,in} = 3.79 \cdot 10^5\ mol.h^{-1}$ and $d_p = 2 \cdot 10^{-3}\ m$. The fixed parameters for the reference (first line): $P = 36\ bar$, H_2/CO_2=3, $F_{t,in} = 2.71 \cdot 10^{-1}\ mol.h^{-1}$ and $d_p = 2 \cdot 10^{-4}\ m$.

$\boldsymbol{\tau}$ (s)	$\boldsymbol{Re}$ $-$	$\boldsymbol{T_0}$ (K)	$\boldsymbol{u\rho}$ $(kg.m^{-2}.s^{-1})$	$\boldsymbol{H_{bed}}$ (m)	$\boldsymbol{d_{bed}}$ (m)	$\boldsymbol{X_1}$ $-$	$\boldsymbol{Reactor}$
7.6	0.7	562.24	0.08	0.06	0.004	0.09	OTP-Lab
25	100	545.15	1.11	2.79	1.23	0.14	OTP

50	100	538.15	1.10	5.45	1.24	0.18	OTP
75	100	537.15	1.10	8.14	1.24	0.21	OTP
100	100	539.15	1.10	10.94	1.23	0.23	OTP
25	200	545.15	2.22	5.59	0.87	0.14	OTP
50	200	538.15	2.19	10.90	0.87	0.18	OTP
75	200	537.15	2.19	16.29	0.87	0.21	OTP
100	200	539.15	2.20	21.88	0.87	0.23	OTP

Table 4.11 details the optimised inlet temperature, the fluid superficial mass flow, the height and diameter of the reactor, and the corresponding reaction progress X_1 at the outlet. This analysis is conducted for reactors operating at 36 bar with a feed molar ratio $H_2/CO_2 = 3$. The first row shows an experimental point from the laboratory in a simulated OTP reactor with a particle diameter (d_p) of 200 μm and a feed flow rate $F_{t,in} = 2.71 \cdot 10^{-1} mol.h^{-1}$. The remaining rows are simulated OTP reactors which operate with $F_{t,in} = 3.79 \cdot 10^{5}\ mol.h^{-1}$ and $d_p = 2000\ \mu m$, which implied a modification in reactor dimensions (see Eq. (4.46) - (4.49)).

As clearly shown in Table 4.11, the prescribed Reynolds number determines the reactor diameter. The resulting diameters $(0.87\ m - 1.24\ m)$ fall within quite reasonable sizes for industrial applications. Lower particle Reynolds number necessitates a larger bed diameter and a shorter reactor length, but the overall reactor volume remains constant for same τ. The reactor lengths obtained are significant. For a simple fixed bed, a diameter/length ratio of 1/10 is reasonable. We can say that by setting a Reynolds number at 100, all residence times up to 100 seconds are possible. For $Re = 200$, the last two cases may be less feasible because the reactor height would be too large relative to the diameter.

The lowest conversion X_1 resulted in the laboratory reactor with 9%. For the OTP reactors, since the flow rate is the same in all cases, the larger the X_1, the more production is achieved. It is perceived that the change in conversion is related to the change in space time and not to the Reynolds number. As expected, the highest space time yielded higher conversion ($X_1 = 0.23$). Thus, based on reactor dimensions, the best compromise of presented parameters seems to be $\tau = 100$ and $Re = 100$. $\tau = 100$ and $Re = 200$ showed same X_1 and the ratio diameter/ length was higher than 1/10.

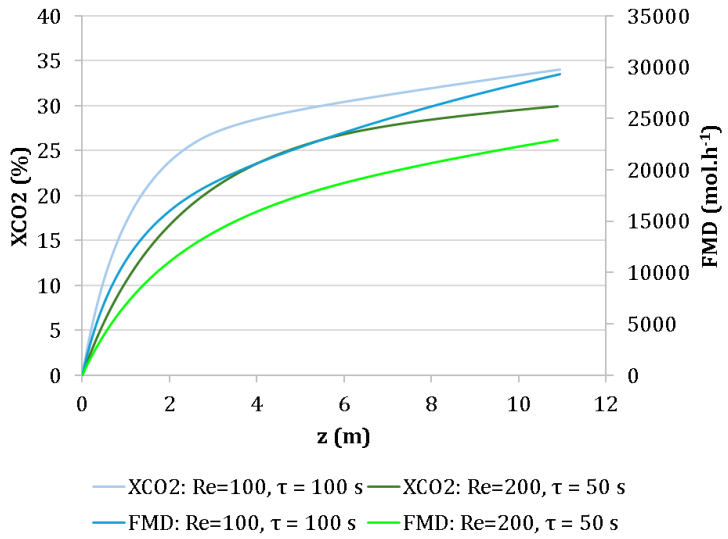

Figure 4.15 Effect of particle Reynolds number (Re) on X_{CO2} and FMD throughout the reactor. Fixed parameters: $P = 36\ bar$, $H_2/CO_2 = 3$, $F_{t,in} = 3.79 \cdot 10^5 mol.h^{-1}$ and $d_p = 2 \cdot 10^{-3} m$. Refer to Table 4.11 for more details.

Given that the ratio diameter/height close to 1/10 is maintained when $Re = 100$ and $\tau = 100\ s$, as well as with $Re = 200$ and $\tau = 50\ s$, a comparison between these two cases was decided. Figure 4.15 depicts the optimisation results attained by varying the particle Reynolds number from 100 to 200 along the entire length of the reactor, with space time of 100 and 50 seconds, respectively. The inlet temperature was selected through an iterative process, evaluating a range from 445.15 K to 589.15 K. The criterion optimised throughout these processes is still X_1.

Figure 4.15 shows that when $\tau = 100\ s, Re = 100$, the conversion of CO_2 and the combined production of methanol and DME are obviously superior ($T_f = 497.95\ K, X_{CO_2,f} = 34.04\%$, $F_{MD,f} = 29.34 \cdot 10^3\ mol.h^{-1}$) than when $\tau = 50\ s$, $Re = 200$ ($T_f = 518.45\ K, X_{CO_2,f} = 29.97\%$, $F_{MD,f} = 22.92 \cdot 10^3\ mol.h^{-1}$) with similar length of catalytic bed but higher catalytic bed volume. Based on the fact that greater catalytic bed diameter with $\tau = 100\ s$ and $Re = 100$ leads to a flow more evenly distributed and a reduction of pressure drop, we consider continuing working with these operating conditions.

4.6.2. Verification of transfer limitations

The criteria for mass and heat transfer limitations, established in Chapter 3 by Eq. (3.12), (3.15) and (3.22) for a PFR, are calculated for the scaled-up OTP reactor with $\tau = 100\ s$ and $Re = 100$. The three criteria to be met are recalled below:

1. Firstly, we verify that the criterion for analysing the external diffusion of reactants from the bulk fluid to the catalyst surface satisfies the condition $f_{ext} \ll 1$, ensuring negligible external limitation. The external resistance fraction is determined by:

$$f_{ext} = \frac{r_{obs,i}}{k_{D,i} C_{i,b}} \left(\frac{d_p}{6} \right) \tag{4.50}$$

For simpler calculation, we assume a local average observed reaction rate, r_{obs}, calculated between different points in the reactor, as per:

$$r_{obs} = \frac{F_{t,in} \cdot \left(X_{CO_2}(z_2) - X_{CO_2}(z_1) \right)}{(z_2 - z_1) \cdot (\pi \cdot d_r^2/4) \cdot (1 - \varepsilon)} \tag{4.51}$$

Considering the path followed by X_{CO_2}, as shown in Figure 4.15, and the spacing between segments $\Delta z = 0.11\ m$, we have chosen 6 points to compute r_{obs} at: 0.22 m, 0.55 m, 1.09 m, 2.08 m, 5.03 m and 10.94 m.

2. We now proceed to validate the criterion defined by Mears (C_M) to assess the negligibility of heat transfer limitation between the particle surface and the bulk fluid, namely:

$$\frac{|-\Delta H_{rx}| r_{obs}}{hT} \frac{d_p}{6} < 0.15 \frac{RT}{E_{obs}} \tag{4.52}$$

3. Finally, to confirm the absence or presence of internal mass transfer limitations, we evaluate the Weisz-Prater criterion (φ′). This criterion is expressed as:

$$\varphi' = \frac{r_{obs}}{D_e C_s} \left(\frac{d_p}{6} \right)^2 \tag{4.53}$$

Given that in Chapter 3, the outcomes for these criteria were more limiting for CO_2 than for H_2, we have decided to present only the results for CO_2 in this section.

Table 4.12 Effect of space time and Reynolds number on reactor dimensions and transfer coefficients in two scaled-up OTP reactors. Fixed parameters: $P = 36\ bar$, $H_2/CO_2 = 3$, $F_{t,in} = 3.79 \cdot 10^5 mol.h^{-1}$, $\tau = 100\ s$ and $d_p = 2 \cdot 10^{-3} m$.

z	Re	T_0	H_{bed}	d_{bed}	r_{obs}	$f_{ext,CO_2} \cdot 10^{-3}$	$C_{M,CO_2} \cdot 10^{-4}$	φ'_{CO_2}
(m)	$-$	(K)	(m)	(m)	$(mol.s^{-1}.m^{-3})$	$\ll 1$*	< 0.004*	$\ll 1$*
0.22					70.03	7.10	19.61	0.31
0.55					51.40	5.21	14.39	0.23
1.09	100	539.15	10.94	1.23	33.52	3.40	9.38	0.15
2.08					17.86	1.81	5.00	0.08
5.03					5.22	0.53	1.46	0.02

10.94	2.12	0.22	5.94	0.01

*Indicates the criterion to be met.

Table 4.12 details the optimised inlet temperature, the reactor height and diameter and observed reaction rate (r_{obs}) for calculating the three mentioned criteria, along with the corresponding outcomes. This analysis is conducted for the same conditions than those of Table 4.11.

Due to differences in temperature and reactor dimensions, particularly the diameter of the catalytic bed, we found a lower observed rate of reaction for $\tau = 100\ s$ and $Re = 100$ than for $\tau = 50\ s$ and $Re = 200$. This is normal, as the rates are always higher at the reactor inlet and decrease along the reactor length. The highest observed reaction rate was identified for the experimental point in a simulated OTP reactor for which the residence time is the lowest. This is further reflected in the outcomes of the external mass transfer limitation calculations, where the lowest value was found for $\tau = 100\ s$ and $Re = 100$. Nonetheless, the three simulated scenarios meet the defined criteria, being much smaller than the limit values, indicating negligible internal or external limitations.

4.6.3. Comparison of isothermal and OTP reactors

Table 4.13 presents the outcomes of two reactors, an OTP reactor (#1) and an isothermal reactor (#2), with a $\tau = 100\ s$ and $Re = 100$. The isothermal reactor operates at lower temperature ($514.15\ K$) compared to the inlet temperature of OTP reactor. However, the OTP reactor achieves a lower outlet temperature ($497.95\ K$). Due to the difference in temperature, $539.15\ K\ vs\ 514.15\ K$, we notice a minimal variation in reactor dimensions ($H_{OTP} = 10.94\ m, d_{OTP} = 1.23\ m$) ($H_{sim} = 9.99\ m, d_{sim} = 1.26\ m$). As shown in Table 4.13, the conversions performance (X_1 and X_{CO_2}) and the combined productivity of methanol and DME in the OTP reactor are slightly higher than in the isothermal reactor. We guess that this slight difference with the OTP reactor could be linked to the exothermic and endothermic reactions that occur competitively and in parallel. It has been demonstrated previously that when only one reaction occurs, the performance is significantly better with the OTP reactor. The comparison of the global heat flux $\dot{Q}$ is also presented, but this will be discussed further later.

Table 4.13 Comparison of reactor dimensions and transfer coefficients of a scaled-up OTP reactor (#1) and an isothermal reactor (#2). Fixed parameters: $P = 36\ bar$, $H_2/CO_2 = 3$, $F_{t,in} = 3.79 \cdot 10^5 mol.h^{-1}$ *and* $d_p = 2 \cdot 10^{-3} m$.

#	τ (s)	Re $-$	T_0 (K)	H_{bed} (m)	d_{bed} (m)	X_1 $(-)$	X_{CO_2} (%)	F_{MD} $(kmol.h^{-1})$	$\dot{Q}$ $(kW.m^{-2})$
1	100	100	539.15	10.94	1.23	0.23	34.04	29.34	33.23
2	100	100	514.15	9.99	1.26	0.22	33.11	28.07	30.20

The performance of OTP and isothermal reactors are shown in Figure 4.16. CO_2 conversion and combined methanol and DME production for the OTP reactor are slightly superior to the isothermal reactor. The increase in CO_2 conversion at the outlet is marginal (<1%), but the percentage difference of the productivity, F_{MD}, is more significant (about 4.40 % or 1263.81 $mol.h^{-1}$). It is noted that in the simulated isothermal reactor, exceeding equilibrium is possible (Figure 4.16a and Figure 4.16b). This is associated with the non-equilibrium consideration of methanol to DME reaction incorporated in the kinetic model. In the OTP reactor, X_{CO_2} and F_{MD} increase almost asymptotically to the equilibrium, as expected, leading to higher performance (Figure 4.16c and Figure 4.16d). OTP reactor allows higher CO_2 conversion and productivity than the isothermal at a shorter length (0.5 m). Starting at approximately 7 meters, the conversion and production rates of both reactors begin to converge. The non-isothermal profile of the OTP reactor contributes to enhance CO_2 conversion and productivity by continuously promoting the methanol synthesis reaction and reducing the competing RWGS reaction rate over the entire length of the reactor due to lower outlet temperature.

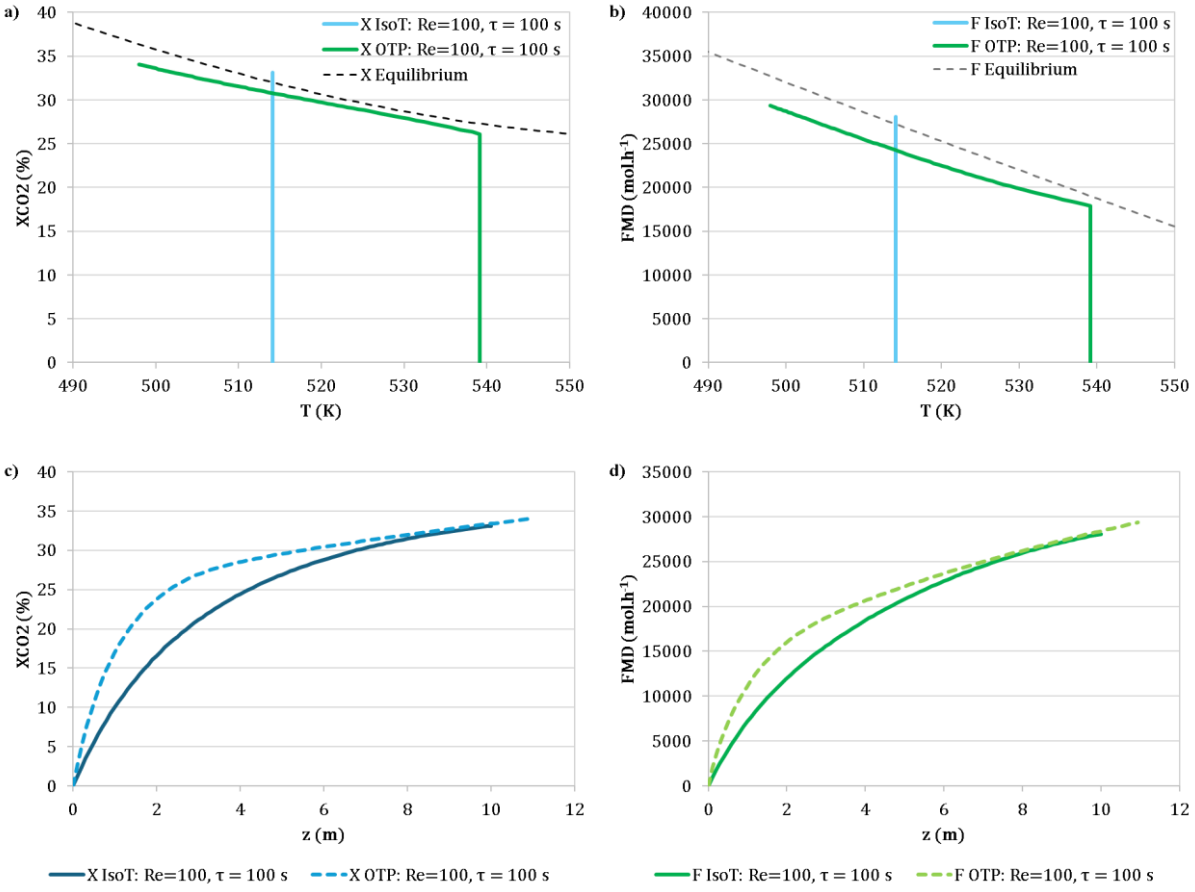

Figure 4.16 Simulated a) CO_2 conversion profile, b) combined methanol and DME production profile and evolution of c) X_{CO2} and d) F_{MD} throughout the reactor in the scaled-up isothermal (IsoT) and OTP reactors. Fixed parameters: P=36 bar, $H_2/CO_2 = 3$, $F_{t,in} = 3.79 \cdot 10^5 mol.h^{-1}$ and $d_p = 2 \cdot 10^{-3}$ m. Refer to Table 4.13 for more details.

Mitsubishi Heavy Industry (MHI) and Mitsubishi Gas Chemical Company (MGC) process for methanol synthesis employs a quasi-isothermal reactor in their process. The temperature of the catalyst bed gradually decreases from 260 °C (near-inlet) to 210 °C (at the outlet) due to heat exchange with the feed gas [21]. This supports the potential feasibility of designing and applying an OTP reactor in industrial settings.

In summary, we found that the OTP reactor offers a slight advantage over the isothermal reactor in terms of CO_2 conversion, but a more important in combined methanol and DME productivity. Moreover, maintaining isothermal conditions in industrial settings remains challenging. Operational costs can increase due to the requirements for uniform temperature control in large volumes, as well as the requirement for complex and sophisticated control systems to maintain operating conditions, avoid hotspots and temperature gradients. However, heat exchanger reactors provide a viable option for effective temperature control.

4.6.4. Thermal aspects: heat removal and heat exchanger sizing

In this part, we will look at the thermal control of the OTP and isothermal reactors to assess the technical feasibility to reach the optimum temperature profiles.

The lower the local heat flux through the reactor wall (q_k) (Eq. (4.41)) is, the easier it is to remove heat. As q_k, the heat flow to be removed through the wall depends on the reaction rates, the simpler way to reduce q_k is to increase the reactor wall surface area by using reactor heat exchangers. Based on this, on patent EP2468394A1 for multi-tubular fixed bed reactor and its use ($L_{tube} = 3 - 30\ m$) [22], and on the commercialized plate-and-shell heat exchanger Alfa-Laval Packinox used as feed/effluent heat exchangers in catalytic reforming, $d_{shell} = 1.5 - 6\ m$ and $L_{shell} = 10 - 20\ m$, we compare the performance of an isothermal reactor operating at 514.15 K with an OTP reactor having a catalyst bed of 10.94 m length ($Re\ = 100, \tau = 100\ s$). The optimal temperature of the isothermal reactor was determined through an iterative process, akin the method used in previous sections for the OTP reactor.

In Figure 4.17, we compare the temperature profile and local heat flux profile of the OTP and the isothermal reactors along the reactor length. The OTP reactor exhibits a constant temperature zone of approximately 2.63 m at 539.15 K, followed by a gradual decrease to reach 497.95 K at the reactor outlet ($z = 10.94\ m$).

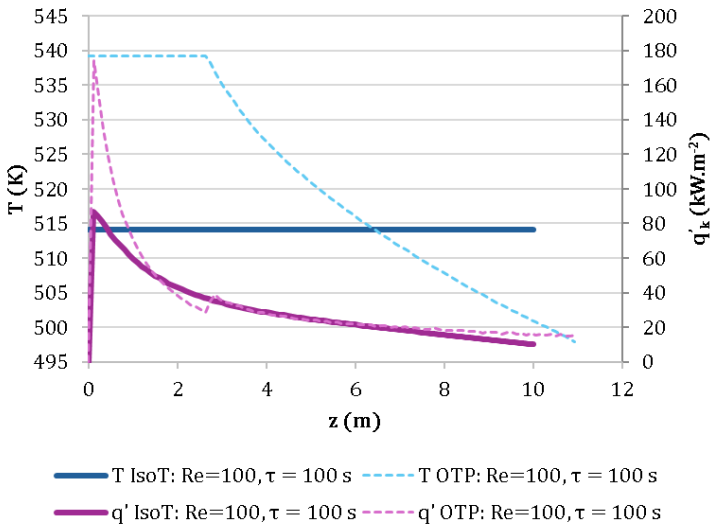

Figure 4.17 Simulated temperature and local heat flux q_k profiles in the scaled-up isothermal (IsoT) and OTP reactors. Fixed parameters: P=36 bar, $H_2/CO_2 = 3$, $F_{t,in} = 3.79 \cdot 10^5 mol.h^{-1}$ and $d_p = 2 \cdot 10^{-3}$ m. Refer to Table 4.13 for more details.

In both reactors, we observe a peak close to the inlet in the heat flux through the reactor wall that needs to be removed. The peak reaches 174.30 $kW.m^{-2}$ for the OTP reactor, while it is

almost twice as low for the isothermal reactor ($86.55\ kW.m^{-2}$). At the outlet, the heat flux is very close between the OTP and isothermal reactors and below $5.40\ kW.m^{-2}$. This disparity can be attributed to the temperature variation within the OTP reactor. Given that the OTP reactor operates with a higher inlet temperature compared to the isothermal reactor, the extents of reactions are greater at the inlet. Consequently, the higher reaction rate at the inlet leads to a greater initial heat release, necessitating efficient heat removal.

Although the OTP reactor exhibits higher local heat fluxes through the reactor wall q_k than those for the isothermal reactor, we decided to continue the study keeping only the OTP reactor due to its potential interest in the overall DME synthesis process. In the OTP reactor, the outlet temperature is indeed interesting: at $T = 497.95\ K$ and $P = 36\ bar$, the state of the water being liquid, this could simplify the separation process and be an advantage for the overall energy saving.

In many industrial applications, heat transfer in a heat exchanger occurs from one fluid to another through a solid wall. The total heat transfer Q between the fluids is expressed in a manner analogous to Newton's law of cooling, as:

$$Q = UA\left(T - T_{fluid}\right) \tag{4.54}$$

where A is the total heat transfer area (here, the surface of the reactor wall along its entire length) and U is the average overall heat transfer coefficient for that area, T is the temperature inside the reactor and T_{fluid} is the temperature of the coolant. Integrating Eq. (4.54) to Eq. (4.38), the energy balance in a reactor segment can be also written as,

$$\sum_i F_{i,0} Cp_i \Delta T + \sum_j F_0 \Delta H_{rx,j} \Delta X_j = -\pi d_r \Delta z U (T(z) - T_{coolant}) \tag{4.55}$$

with

$$q_k = \pi d_r \Delta z U (T(z) - T_{coolant}) \tag{4.56}$$

From Eq. (4.56), different evaluations can be done. We decided to analyse three scenarios:

- First, we chose to examine the profile of the product of the overall heat transfer coefficient and the heat transfer area (UdA) at a fixed coolant temperature and a fixed heat transfer area (dA). Based on Eq. (4.55), $dA = \pi d_r \Delta z$. Consequently, dA is dependent on the size of the element Δz and the chosen number of discrete segments (here, 100 segments). Since the reactor length is $10.94\ m$, then $\Delta z = 0.11\ m$.
- Secondly, dA is varied at a fixed coolant temperature $T_{coolant}$ and different fixed overall heat transfer coefficients U.

- Finally, for the third scenario, an optimal coolant temperature $T_{coolant}$ throughout the reactor is determined at a fixed dA and as a function of U.

In literature, for tubular heat exchangers with gas-liquid media (water – hydrogen containing natural gas mixtures), a design overall heat transfer coefficient of $454 - 709\ W.m^{-2}.K^{-1}$ is proposed [23]. Thus, we tested six U values uniformly distributed within this range: $455, 504, 553, 602, 651$ and $700\ W.m^{-2}.K^{-1}$.

For the first scenario, the UdA profile at a coolant temperature set *a priori* at $423.15\ K$ is presented in Figure 4.18a. The coolant temperature was set to $423.15\ K$, significantly lower than the reactor temperature ($539.15\ K$), to facilitate effective heat removal from the reactor. Since $\dot{q_k}$ and UdA are directly proportional, Figure 4.18 has the same appearance as the $\dot{q_k}$ OTP curve of Figure 4.17. During the evolution of the reaction inside the OTP reactor, the UdA exhibits a decreasing trend, starting from an initial value of $UdA = 637.59\ W.K^{-1}$ in the first segment. Since the diameter is fixed ($d_{bed} = 1.23\ m$) and the reactor segments are evenly spaced, $\Delta z = 0.11\ m$ and thus dA is constant and equal to $0.42\ m^2$. Consequently, the downward trend observed is due to the decreasing overall heat transfer coefficient U, as shown in Figure 4.18b, which is required to remove the heat along the reactor (z). In the first segment, the overall heat transfer coefficient U is equal to $1502.61\ W.m^{-2}.K^{-1}$ and even in the first 0.77 meters of the reactor, very high values of UdA, are exhibited (U exceeds $700\ W.m^{-2}.K^{-1}$).

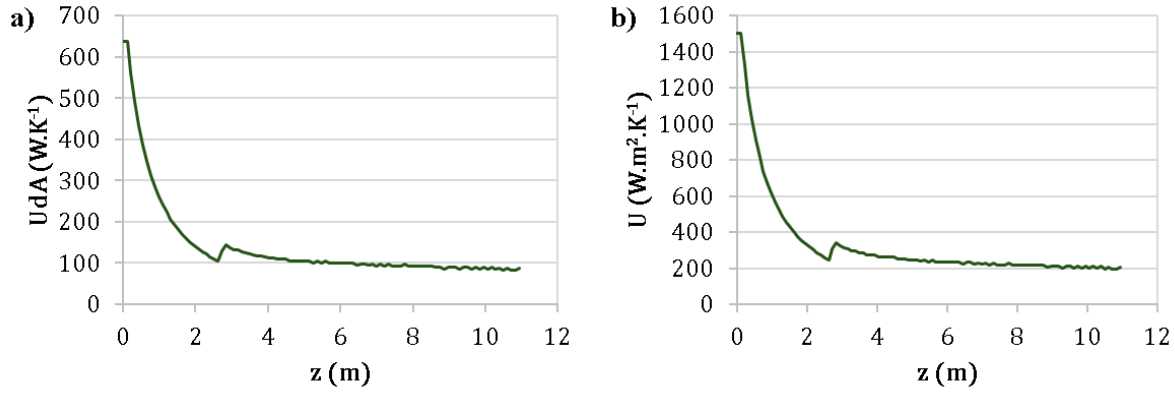

Figure 4.18 Profile of the product of a) the overall heat transfer coefficient and the heat transfer area (UdA)and b) the overall heat transfer coefficient along the simulated OTP reactor. Fixed parameters: P=36 bar, $H_2/CO_2 = 3$, $F_{t,in} = 3.79 \cdot 10^5 mol.h^{-1}$, $d_p = 2 \cdot 10^{-3}\ m$, $\Delta z = 0.11\ m$ and $T_{coolant} = 423.15\ K$. Refer to Table 4.13 for more details.

In a second scenario, we evaluated the evolution profile of the heat transfer area (partial wall surface area) (dA) along the reactor length for several overall heat transfer coefficient U with an invariable coolant temperature set *a priori* at $423.15\ K$ (Figure 4.19). The outcomes for the

six U values demonstrate a uniform trend. At the outset, fixing $U = 455\ W.m^{-2}.K^{-1}$ (the lowest value in the range studied), a large surface area of $1.40\ m^2$ is required in the first segment ($z = 0.11\ m$). But this area varies along the reactor from $1.40\ m^2$ to $0.18\ m^2$. Likewise, we identified that $U = 700\ W.m^{-2}.K^{-1}$ requires less heat transfer area, with a maximum dA of $0.91\ m^2$ and a minimum of $0.12\ m^2$ with $0.11\ m$ length segments. Since U is generally assumed to be lower than $700\ W.m^{-2}.K^{-1}$ for technical feasibility, it is worth considering a multi-zone reactor with an initial zone offering more surface area, followed by a simple fixed-bed tubular reactor. In conclusion, by fixing U, dA was computed in such a way that we have different heat exchange area along the reactor length, enabling a segmented reactor structure (Figure 4.19). For instance, between $z = 2\ m$ and $z = 10.94\ m$, the reactor could have segments with constant dA of about $0.42\ m^2$ (the reactor will be thus a simple tube). On the contrary, from the entrance to $z = 2\ m$, the reactor must have higher and variable areas along the reactor length. The segment $z = 2\ m$ could be the transition to more structured dimensions. The technical feasibility of this design remains uncertain due to manufacturing complexity and flow considerations. However, compared to the first examined scenario, it seems more achievable.

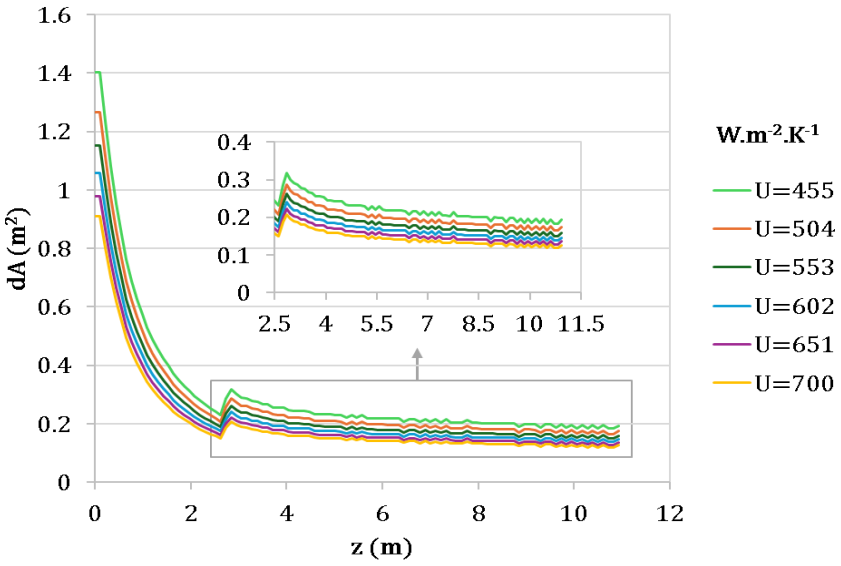

Figure 4.19 Evolution of the heat transfer surface area (dA)throughout the OTP reactor. Fixed parameters: P=36 bar, $H_2/CO_2 = 3$, $F_{t,in} = 3.79 \cdot 10^5 mol.h^{-1}$, $d_p = 2 \cdot 10^{-3}\ m$ and $T_{coolant} = 423.15\ K$. Refer to Table 4.13 for more details.

Another option, the third scenario, is to adjust the temperature of the cooling fluid. Thus, in this scenario, we assumed that U and dA are constant, with an inlet coolant temperature of 293.15 K to determine the coolant temperature along the reactor. Figure 4.20 illustrates the temperature profile that the cooling fluid should follow for various U values to remove the generated heat and maintain the optimal temperature profile in the reactor.

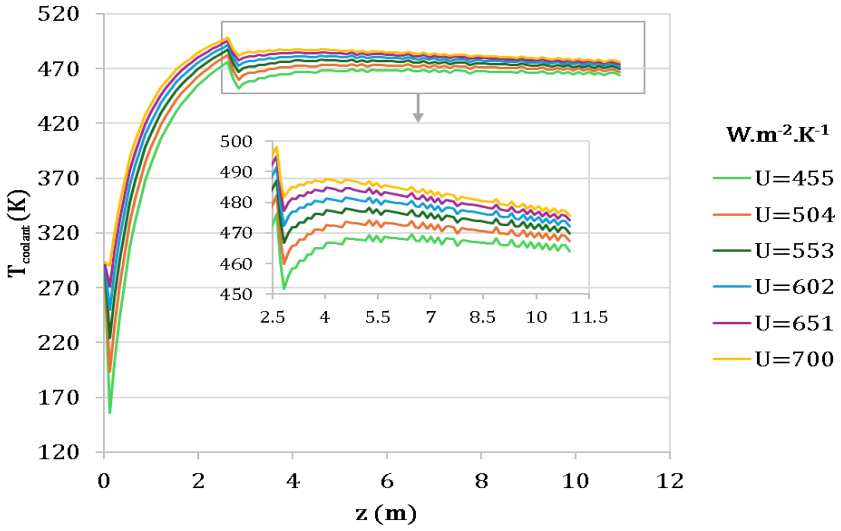

Figure 4.20 Evolution of coolant temperature along the OTP reactor. Fixed parameters: P=36 bar, $H_2/CO_2 = 3$, $F_{t,in} = 3.79 \cdot 10^5 mol.h^{-1}$ *and* $d_p = 2 \cdot 10^{-3}$ *m. Refer to Table 4.13 for more details.*

Obviously, the lower the U value, the colder the cooling fluid must be. However, it is particularly evident that at the reactor inlet, the cooling fluid temperature needs to be very low ($156.07\ K$ or $-117.08°C$ for $U = 455\ W.m^{-2}.K^{-1}$ and $20°C$ for $U = 700\ W.m^{-2}.K^{-1}$). Along the reactor, this temperature must rise to around $476 - 488\ K$ ($203 - 215°C$).

It is hardly feasible to have a cooling fluid that undergoes such a large temperature variation between the reactor inlet and outlet (over 200 to 300°C). Furthermore, the OTP induces a discontinuity when the reactor transitions from isothermal operation to a cooling mode, resulting in a sudden change in the cooling fluid temperature (around z = 2.77 m). This could be achievable with two different cooling fluids, with the second being injected at z = 2.77 m, 20 to 25°C cooler than the outlet temperature of the first fluid.

At this point, the variation is associated with the temperature change induced by the OTP (see $\dot{q}_k$ OTP and T OTP in Figure 4.17). Beyond 2.77 m, as the reaction progresses towards the reactor outlet, the coolant temperature profile flattens out, remaining quasi-constant. This behaviour is noticed in all six cases. The minimal fluctuations observed are due to the temperature changes induced by the OTP.

The feasibility challenge of the last case lies in the variation of coolant temperature throughout the reactor length, particularly in the first 2.77 meters. Nevertheless, diverse heat exchangers are used in industrial settings with variable coolant temperatures along the reactor length: multi-section heat exchangers. These heat exchangers are sectioned into multiple segments, each equipped with a dedicated coolant supply to optimise heat transfer. Based on this, we opted to simulate a multi-tubular reactor with a coolant temperature evolution. In industrial

applications for methanol and DME synthesis, multi-tubular shell-and-tube heat exchanger reactors are commonly used, as discussed in the State-of-the-Art section of this PhD thesis. While our previous analysis focused on the performance of a reactor as a single-tube reactor, a multi-tubular reactor provides a larger external surface area, leading to improved heat management, enhanced reaction rates and increased process safety.

In the patent EP2468394A1 for multi-tubular fixed bed reactor and its use for hydrocarbons production, the inventors specified that typically multi-tubular reactors have diameters ranging from 0.005-0.2 m, with a length of 3-30 m containing over at most 97% of catalyst particles, and the numbers of tubes can vary widely from 4 to 50000 [22]. According to this, a multi-tubular reactor in this thesis was calculated as follows:

The diameter of a single tube was set arbitrary in the diameter range to 0.04 m and the reactor section was calculated using Eq. (4.49), $S_{tube} = \pi d_{tube}^2/4$. The reactor in question handles a total inlet mass flow of $4739\, kg.h^{-1}$, with a constant CO_2 mass flow rate of $4167\, kg.h^{-1}$ ($100\, ton.d^{-1}$). Maintaining $Re = 100$, the fluid superficial mass flow was determined using Eq. (4.46). Based on the total mass flow rate, the number of tubes was calculated to be 958, as per:

$$N_{tubes} = \frac{\dot{m}}{u\rho S_{tube}} \tag{4.57}$$

So, the simulated multi-tubular reactor consists of 958 tubes, each of 11 m in length and 0.04 m diameter, filled with a fixed bed of catalyst particles of $d_p = 0.2\, cm$. Only a single tube is simulated, assuming identical performance for the others.

Figure 4.21 illustrates the evolution of the coolant temperature profile along the reactor length of the OTP multi-tubular reactor. The profile is plotted as a function of global heat transfer coefficient U for an inlet temperature T_0 and inlet coolant temperature $T_{0,coolant}$ of $523.15\, K$, assuming $U = 455\, W.m^{-2}.K^{-1}$ and dA constant ($0.01\, m^2$ each tube).

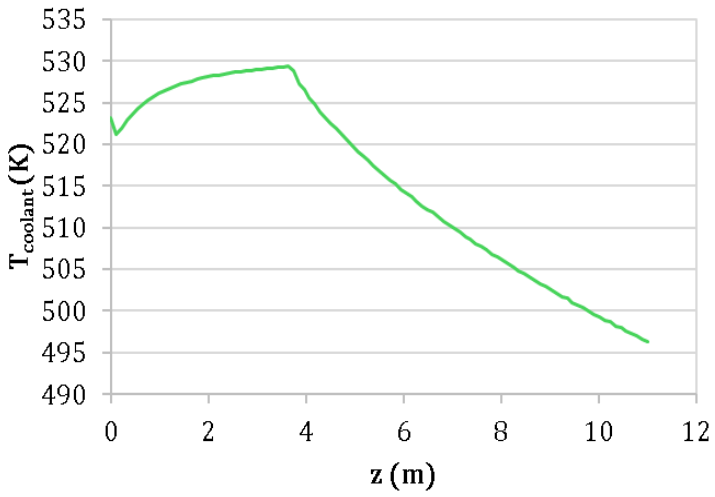

Figure 4.21 Evolution of coolant temperature along the OTP multi-tubular reactor. Fixed parameters: P=36 bar, $T_0 = 531.15\ K$, $H_2/CO_2 = 3$, $F_{t,in} = 3.79 \cdot 10^5 mol.h^{-1}$, $d_p = 2 \cdot 10^{-3}\ m$, $d_{tube} = 0.04\ m$, $L_r = 11\ m$, $\Delta z = 0.1\ m$, $N_{tubes} = 958$, $U = 455\ W.m^{-2}.K^{-1}$, $Re = 100$ *and* $\tau = 102.6\ s$.

In contrast to the outcomes observed with a single tube (Figure 4.20), variation within the first 3.6 meters is less pronounced (Figure 4.21), which is associated with the temperature change caused by the OTP. However, in the subsequent meters, there is a gradual temperature decline until the reactor outlet. This behaviour is attributed to the fact that 958 tubes (each with a diameter of 0.04 meters) provide a surface area approximately 30 times greater than a single tube with a diameter of 1.23 meters. Moreover, Eq. (4.55) demonstrates that the coolant fluid temperature is directly influenced by the term $FCp\Delta T$, where F is distributed across 958 tubes. Figure 4.22 compares the $T_{coolant}$ of the multi-tubular reactor with that of a single-tube reactor of the same dimensions and operating conditions. It is evident that also for the single-tube reactor, there is also a change in the curve at 3.6 meters.

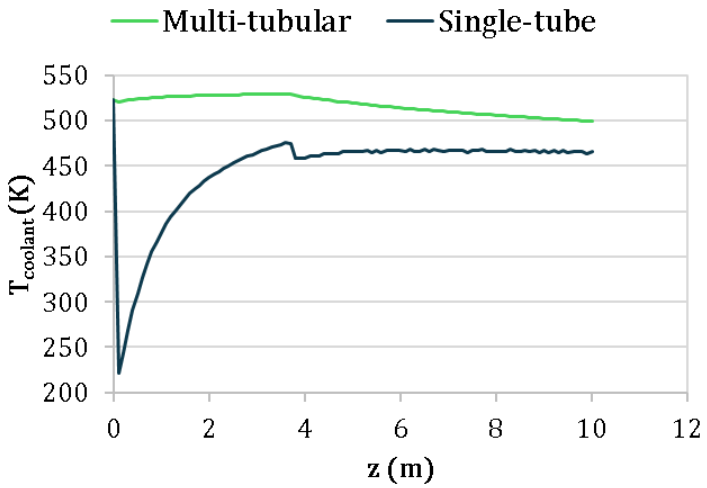

Figure 4.22 Comparison of the evolution of coolant temperature along the OTP multi-tubular reactor and the single-tube reactor. Fixed parameters: P=36 bar, $T_0 = 531.15\ K$, $H_2/CO_2 = 3$, $F_{t,in} = 3.79 \cdot 10^5 mol.h^{-1}$, $d_p = 2 \cdot 10^{-3}\ m$, $L_r = 11\ m$, $\Delta z = 0.1\ m$, $U = 455\ W.m^{-2}.K^{-1}$, $Re = 100$ *and* $\tau = 102.6\ s$. *For multi-tubular:* $d_{tube} = 0.04\ m$, $N_{tubes} = 958$. *For single-tube:* $d_r = 1.24\ m$.

We notice that the temperature profile for the $T_{coolant}$ is more feasible, as it falls within a range between 529.37 and 496.32 K, which is achievable. However, the exact profile still requires more in-depth study.

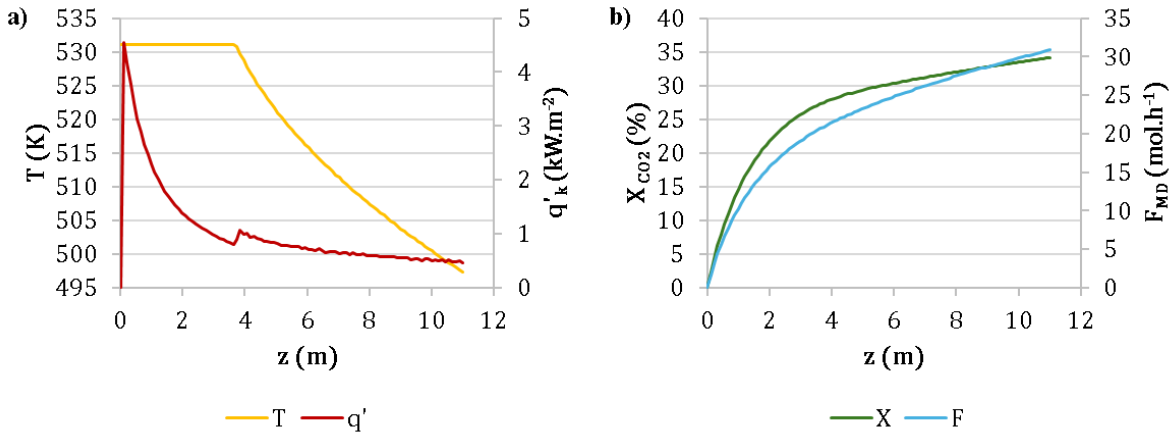

Figure 4.23 Profiles of a) the temperature and local heat flux $\dot{q}_k$ *and b)* CO_2 *conversion and combined methanol and DME production in the OTP multi-tubular reactor. Fixed parameters: P=36 bar,* $T_0 = 531.15\ K$, $H_2/CO_2 = 3$, $F_{t,in} = 3.79 \cdot 10^5 mol.h^{-1}$, $d_p = 2 \cdot 10^{-3}\ m$, $d_{tube} = 0.04\ m$, $L_r = 11\ m$, $\Delta z = 0.1\ m$, $N_{tubes} = 958$, $U = 455\ W.m^{-2}.K^{-1}$, $Re = 100$ *and* $\tau = 102.6\ s$.

Figure 4.23a shows the profile of the temperature and local heat flux $\dot{q}_k$ per tube of the simulated OTP multi-tubular reactor. The outcomes exhibit similar patterns to those of the single-tube OTP reactor in Figure 4.17. Nevertheless, the local heat flux per tube is significantly

lower in the multi-tubular reactor, with a maximum of 4.5 $kW.m^{-2}$ per tube, compared to 174.3 $kW.m^{-2}$ in the single-tube reactor, mainly due to the reduction of overall heat exchange surface area between the multi-tubular reactor and the single-tube reactor. The OTP reactor exhibits a constant temperature zone of approximately 2.63 m at 539.15 K, followed by a gradual decrease to reach 497.95 K at the reactor outlet ($z = 10.94\ m$). As expected, we observed a stable temperature zone followed by a decline towards the reactor outlet. Figure 4.23b illustrates the CO_2 conversion and combined methanol and DME production within the simulated OTP multi-tubular reactor. The model achieved a final CO_2 conversion of 34.18% and a combined rate of 30.84 $mol.h^{-1}$ for methanol and DME in a single tube, with a CO_2 input of 98.8 $mol.h^{-1}$.

Analysing the CO_2 conversion and methanol and DME productivity of a single tube of the scaled-up multi-tubular reactor, we observe that we successfully approached the thermodynamic limit through the optimal progression temperature, as illustrated in Figure 4.24. Ateka et al., 2020 [24] indicated that both CO_2 conversion and DME yield can be enhanced by incorporating recirculation, where a portion of the gases in the product stream—separated from oxygenated products (H_2O, DME, and MeOH)—is recycled. However, the process details in this thesis research attains equilibrium without recirculation, although there remains potential for improvement through its implementation. We compare the outcomes of this simulation with those available in the literature.

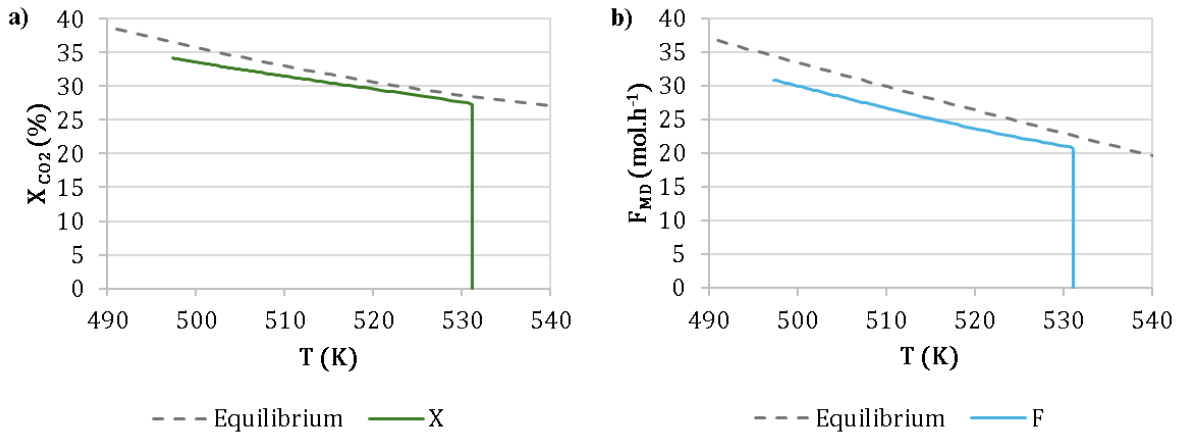

Figure 4.24 Evolution of a) CO_2 conversion and b) combined methanol and DME production as a function of the temperature in the OTP multi-tubular reactor. Fixed parameters: P=36 bar, $T_0 = 531.15\ K$, $H_2/CO_2 = 3$, $F_{t,in} = 3.79 \cdot 10^5 mol.h^{-1}$, $d_p = 2 \cdot 10^{-3}\ m$, $d_{tube} = 0.04\ m$, $L_r = 11\ m$, $\Delta z = 0.1\ m$, $N_{tubes} = 958$, $U = 455\ W.m^{-2}.K^{-1}$, $Re = 100$ and $\tau = 102.6\ s$.

Comparing the results obtained in this research with those reported in the literature is essential for validating our findings and evaluating their significance. Most investigations have been conducted using syngas and/or CO_2/CO_x, focusing specifically on CO conversion to DME

synthesis, as discussed in the State-of-the-Art section of this thesis (Chapter 1). Therefore, to evaluate our findings, we compare our results against other technologies reported in the literature, as shown in Table 4.14.

Table 4.14 Comparison of the outcomes with literature data.

$\boldsymbol{Reactor}$	$\boldsymbol{H_2/CO_x}$	$\boldsymbol{T_0\ (K)}$	$\boldsymbol{P\ (bar)}$	$\boldsymbol{X_{CO_2}}(\%)$	$\boldsymbol{Y_{DME}}(\%)$	$\boldsymbol{Ref.}$
$R-E-M\ (J'_H)$	1	518.15	70	55.33	53	[19]
$R-E-M\ (J'_H+J_{H_2O})$	1	518.15	70	81.89	80	[19]
MR	3	532.00	40	51.00	51	[25]
$PBMR$	0.25	548.15	30	70.00	60	[24]
$This\ research\ thesis$	3	531.15	36	31.88	25	-

Although the conversion of CO_2 and DME yield obtained in this study are significantly lower than those reported in the literature, we were able to achieve thermodynamic limits by following the optimal temperature progression, as shown in Figure 4.24. However, our study did not include the use of membranes, which are well known to enhance reaction productivity by removing water and preventing kinetic inhibition.

Our operating conditions deviated from those commonly stated. Regarding the feed molar ratio, our research, unlike others, did not involve the CO_2/CO mix but focused solely on CO_2 conversion. The industrial plant simulation for DME synthesis by De Falco et al., 2017 [25] utilised a membrane reactor (MR) based on the kinetic model of Lu et al., 2004 [26]. The theoretical study by Ateka et al., 2020 [24] employed a packed bed membrane reactor (PBMR) integrating the kinetic model proposed by the same research team in another publication [27]. Both studies involved CO in the inlet stream. Behloul et al., 2022 in their investigation modelled and optimised a multifunctional reactor for DME synthesis, coupling the reaction, heat exchange, and membrane separation in the Reactor-Heat Exchanger-Membrane Separator (R-E-M). Their kinetic model was based on the Nie et al., 2005 [28] model, based on the Langmuir–Hinshelwood mechanism.

Our experiments were carried out at lower pressure (36 bar) compared to the literature, based on the range evaluated in the kinetic model developed in Chapter 3 validated with the laboratory experiments carried out up to 36 bar. The PBMR investigation operated at 30 bar. Our inlet temperature was higher than those used in the R-E-M and very close to that of the MR, with only a 0.85 K difference due to a very small pressure difference, on the order of 4 bar (40 and 36 bar). The R-E-M presented the CO_2 conversion and not the mix of CO_2/CO conversion.

Despite these differences, further comparison is possible. For instance, the outcomes of the R-E-M which considers the heat flux density (J'_H) as the decision variable are comparable to ours.

However, a direct comparison is not possible when optimising both heat flux density and water molar flux density simultaneously ($J'_H + J'_{H_2O}$). For $R-E-M$ (J'_H), their pressure was nearly double ours, leading to higher CO_2 conversion and DME yield, as expected, based on the thermodynamic analysis by Stangeland et al., 2018 [16] on CO_2 hydrogenation to DME.

The development of new technologies aims to address issues of catalyst deactivation and loss during processes. Integrating a membrane into the proposed OTP multi-tubular reactor could align with this objective. A comprehensive economic assessment is essential to evaluate the feasibility of this approach.

Moreover, in his PhD thesis, Quezada, 2020 [20] proposed a staged process with reactors and separators in series to remove water during the methanol synthesis from CO_2. The main drawback of his process was that the reactors were iso-thermal and the reacting fluids had to be cooled before the separators and reheated before the feeding in the following reactors. This hindered the overall energy balance and penalized the energy savings. In this study, we calculated that both the reacting fluid and the cooling fluid temperatures were in close ranges (from 531.15 K at the inlet to 497.35 K at the outlet for the OTP multi-tubular reactor and from 529.37 K at the maximum and 496.32 K at the minimum for the cooling fluid), and that water could be liquid at the outlet reactor conditions, avoiding an additional cooling upstream the separator. Furthermore, using the reacting fluid outgoing the separator as part of the cooling fluid in the reactor heat exchanger could allow saving the heating energy needed upstream a second reactor in case of continuing the reaction.

4.7. Conclusions

In this chapter, we analysed the potential advantages of using an Optimal Temperature Profile reactor integrating the kinetic model developed in Chapter 3. Firstly, the OTP principle was explained with a single first-order reaction.

Afterwards, we examined the case of a reversible reaction in a plug flow reactor. Using the minimisation method, we have demonstrated that it is possible to achieve the same final conversion by starting with low temperatures at the reactor inlet and then increasing the temperature, compared to the while loop method that started with high temperatures and subsequently lowering them. The minimisation method "*fminunc*" suggests initially using faster reaction rates by applying high temperatures; but this makes the temperature control more complex. In contrast, *while* loop method prioritises simplicity and imposes an isothermal zone at the reactor inlet.

Simulations and optimisations confirmed that longer residence times allow higher CO_2 conversion but result in lower heat transfer per unit area. Based on these findings, adjusting the amount of catalyst is more effective than reducing the feed flow rate. Therefore, it is advisable to prioritise the longest possible residence time, although an economic assessment would be necessary (particularly concerning the costs of catalyst).

In terms of reactor optimisation, we demonstrate that the inlet temperature has an important impact on the yield of the OTP reactor. Similarly, the H_2/CO_2 feed molar ratios of 3 or 9 lead to identical outcomes. Further, lengthening the reactor improves conversion rates and DME plus methanol production.

At the end of this chapter, we simulated different OTP scaled-up reactors considering the kinetics model developed in Chapter 3, testing different particle Reynolds numbers and space times. After evaluating the heat and mass transfer limitations around and inside the particles, we found them to be negligible. Reactors operating at elevated space time (100 seconds) presented better performance, as expected, regardless of their Reynolds number. Among them, the more compact reactor design with $Re = 100$ was compared with an isothermal reactor. Our study showed that the OTP reactor offers only marginally better performance compared to the isothermal reactor. While the OTP reactor can achieve higher conversion rates for a single, first-order exothermic reaction (around 10% in our example), its advantages diminish when multiple competitive and parallel reactions, both exothermic and endothermic, are involved. However, the OTP reactor has a potential interest in the overall DME synthesis process as at the outlet reactor conditions, water is liquid, and this could simplify the separation process.

For an OTP reactor chosen under optimal operating conditions ($Re = 100$, $\tau = 103\,s$, $H_2/CO_2 = 3$, optimising X_1), we analysed the product of the overall heat transfer coefficient and the heat transfer surface area (UdA) along the reactor. We then explored how to manage heat removal and proposed three approaches: a reactor with variable U along its length, a reactor with a variable external heat exchange surface, and a reactor with a variable coolant temperature. Based on the results, the latter two scenarios seem more attainable. Given the existence of multi-section heat exchangers, allowing different temperatures along the heat exchanger, we opted for a multi-tubular OTP reactor with variable external cooling temperature and simulated its performance. The CO_2 conversion and the combined methanol and DME production in the multi-tubular OTP reactor described in this thesis reached thermodynamic equilibrium without recirculation. Future work should explore the feasibility of integrating a membrane into this reactor to address catalyst deactivation and enhance overall performance. Moreover, in case of recirculation, the wise management of fluid and heat flows should allow an enhance of conversion and energy savings.

4.8. References

[1] G. F. Froment, J. De Wilde, and K. B. Bischoff, *Chemical reactor analysis and design*, Third. John Wiley & Sons, Inc., 2011.

[2] O. Levenspiel, *Chemical Reaction Engineering*, Third. John Wiley & Sons, 2008.

[3] J. Villermaux, *Génie de la réaction chimique: conception et fonctionnement des réacteurs*, 2nd ed. Paris, 1993.

[4] J. Villermaux, "Réacteurs chimiques - Principes," *Opérations unitaires. Génie la réaction Chim.*, Mar. 1994, doi: 10.51257/a-v1-j4010.

[5] S. A. Senthil and S. Sundaramoorthy, "Optimal control policy for tracking optimal progression of temperature in a batch reactor – Some insights into the choice of objective function," *IFAC-PapersOnLine*, vol. 51, no. 1, pp. 112–117, Jan. 2018, doi: 10.1016/J.IFACOL.2018.05.019.

[6] D. Iranshahi, R. Saeedi, and K. Azizi, "Maximization of dimethyl ether production from synthesis gas by obtaining optimum temperature profile and water removal," *Fuel*, vol. 190, pp. 386–395, Feb. 2017, doi: 10.1016/J.FUEL.2016.10.118.

[7] L. Kiewidt and J. Thöming, "Predicting optimal temperature profiles in single-stage fixed-bed reactors for CO2-methanation," *Chem. Eng. Sci.*, vol. 132, pp. 59–71, Aug. 2015, doi: 10.1016/J.CES.2015.03.068.

[8] K. Omata and M. Yamada, "Artificial Neural Network and Grid Search Aided Optimization of Temperature Profile of Temperature Gradient Reactor for Dimethyl Ether Synthesis from Syngas," *Ind. Eng. Chem. Res.*, vol. 48, no. 2, pp. 844–849, Jan. 2009, doi: 10.1021/ie8008633.

[9] K. Omata, T. Ozaki, T. Umegaki, Y. Watanabe, N. Nukui, and M. Yamada, "Optimization of the Temperature Profile of a Temperature Gradient Reactor for DME Synthesis Using a Simple Genetic Algorithm Assisted by a Neural Network," *Energy & Fuels*, vol. 17, no. 4, pp. 836–841, Jul. 2003, doi: 10.1021/ef0202438.

[10] F. Logist, P. M. Van Erdeghem, I. Y. Smets, and J. F. Van Impe, "Generic Optimal Temperature Profiles for a Class of Jacketed Tubular Reactors," *IFAC Proc. Vol.*, vol. 41, no. 2, pp. 12923–12928, Jan. 2008, doi: 10.3182/20080706-5-KR-1001.02185.

[11] F. Logist, I. Y. Smets, and J. F. Van Impe, "Derivation of generic optimal reference temperature profiles for steady-state exothermic jacketed tubular reactors," *J. Process Control*, vol. 18, no. 1, pp. 92–104, Jan. 2008, doi: 10.1016/J.JPROCONT.2007.05.001.

[12] R. Vakili, H. Rahmanifard, P. Maroufi, R. Eslamloueyan, and M. R. Rahimpour, "The effect of flow type patterns in a novel thermally coupled reactor for simultaneous direct dimethyl ether (DME) and hydrogen production," *Int. J. Hydrogen Energy*, vol. 36, no. 7, pp. 4354–4365, Apr. 2011, doi: 10.1016/j.ijhydene.2010.12.135.

[13] Y. Hu, Z. Nie, and D. Fang, "Simulation and model design of pipe-shell reactor for the direct synthesis of dimethyl ether from syngas," *J. Nat. Gas Chem.*, vol. 17, no. 2, pp. 195–200, Jun. 2008, doi: 10.1016/S1003-9953(08)60051-1.

[14] K. Omata, Y. Watanabe, T. Umegaki, G. Ishiguro, and M. Yamada, "Low-pressure DME synthesis with Cu-based hybrid catalysts using temperature-gradient reactor," *Fuel*, vol. 81, no. 11–12, pp. 1605–1609, Jul. 2002, doi: 10.1016/S0016-2361(02)00080-7.

[15] Y. Zhang, J. Fei, Y. Yu, and X. Zheng, "Methanol synthesis from CO2 hydrogenation over Cu based catalyst supported on zirconia modified γ-Al2O3," *Energy Convers. Manag.*, vol. 47, no. 18–19, pp. 3360–3367, Nov. 2006, doi: 10.1016/J.ENCONMAN.2006.01.010.

[16] K. Stangeland, H. Li, and Z. Yu, "Thermodynamic Analysis of Chemical and Phase Equilibria in CO2 Hydrogenation to Methanol, Dimethyl Ether, and Higher Alcohols," *Ind. Eng. Chem. Res.*, vol. 57, no. 11, pp. 4081–4094, 2018, doi: 10.1021/ACS.IECR.7B04866/ASSET/IMAGES/LARGE/IE-2017-04866G_0013.JPEG.

[17] H. H. Koybasi, C. Hatipoglu, and A. K. Avci, "Sustainable DME synthesis from CO2–rich syngas in a membrane assisted reactor–microchannel heat exchanger system," *J. CO2 Util.*, vol. 52, p. 101660, Oct. 2021, doi: 10.1016/j.jcou.2021.101660.

[18] R. Peláez, P. Marín, F. V Díez, and S. Ordóñez, "Direct synthesis of dimethyl ether in multi-tubular fixed-bed reactors: 2D multi-scale modelling and optimum design," *Fuel Process. Technol.*, vol. 174, pp. 149–157, 2018, doi: 10.1016/j.fuproc.2018.02.025.

[19] C. R. Behloul, J.-M. Commenge, and C. Castel, "Modeling and Optimization of Mass and Heat Flux Profiles in a Multifunctional Reactor for CO2 and H2 Valorization to Dimethyl Ether," *Ind. Eng. Chem. Res.*, vol. 61, no. 41, pp. 15301–15315, Oct. 2022, doi: 10.1021/acs.iecr.2c02713.

[20] M. J. Quezada, "Hydrogénation catalytique de CO_2 en méthanol en lit fixe sous chauffage conventionnel et sous plasma à DBD," Normandie Université, 2020.

[21] M. Ebrahimzadeh Sarvestani, O. Norouzi, F. Di Maria, and A. Dutta, "From catalyst development to reactor Design: A comprehensive review of methanol synthesis techniques," *Energy Convers. Manag.*, vol. 302, p. 118070, Feb. 2024, doi:

10.1016/J.ENCONMAN.2024.118070.

[22] G. Leendert Bezemer, T. Joris Remans, and J. Volkert Zander, "EP2468394A1 - Multi-tubular fixed bed reactor and its use," *Google Patents*, 2010. https://patents.google.com/patent/EP2468394A1/en# (accessed Jul. 22, 2024).

[23] D. W. Green and R. H. Perry, "Perry's Chemical Engineers' Handbook," 2008. doi: 10.1036/0071422943.

[24] A. Ateka, J. Ereña, J. Bilbao, and A. T. Aguayo, "Strategies for the Intensification of CO2 Valorization in the One-Step Dimethyl Ether Synthesis Process," *Ind. Eng. Chem. Res.*, vol. 59, no. 2, pp. 713–722, Jan. 2020, doi: 10.1021/acs.iecr.9b05749.

[25] M. De Falco, M. Capocelli, and A. Giannattasio, "Membrane Reactor for one-step DME synthesis process: Industrial plant simulation and optimization," *J. CO2 Util.*, vol. 22, pp. 33–43, Dec. 2017, doi: 10.1016/j.jcou.2017.09.008.

[26] W. Z. Lu, L. H. Teng, and W. De Xiao, "Simulation and experiment study of dimethyl ether synthesis from syngas in a fluidized-bed reactor," *Chem. Eng. Sci.*, vol. 59, no. 22–23, pp. 5455–5464, Nov. 2004, doi: 10.1016/J.CES.2004.07.031.

[27] A. Ateka, J. Ereña, J. Bilbao, and A. T. Aguayo, "Kinetic modeling of the direct synthesis of dimethyl ether over a CuO-ZnO-MnO/SAPO-18 catalyst and assessment of the CO2 conversion," *Fuel Process. Technol.*, vol. 181, pp. 233–243, Dec. 2018, doi: 10.1016/j.fuproc.2018.09.024.

[28] Z. Nie, H. Liu, D. Liu, W. Ying, and D. Fang, "Intrinsic Kinetics of Dimethyl Ether Synthesis from Syngas," *J. Nat. Gas Chem.*, vol. 14, pp. 22–28, 2005.

5. General Conclusions and Perspectives

5.1. General conclusions

This thesis aimed to study the hydrogenation of CO_2 into a higher value-added molecule, with the goal of maximising CO_2 consumption and increasing the production of the target molecule. Among potential products of CO_2 hydrogenation identified in the literature, three molecules were prioritised: methane, methanol and dimethyl ether (DME). Given that DME synthesis was identified as the least researched, it was selected as the case of study.

Catalyst optimisation, reactor design, and process innovation constitutes the primary pillars for enhancing process performance. Based on this, we tested two catalysts for methanol synthesis (a commercial CuZnO-Al_2O_3, CZA-C, and a developed CuZnO-Al_2O_3, CZA-D) and two commercial zeolites (HZSM-5 and HY) for methanol dehydration to DME in a fixed bed reactor to compare their performance. A physical mixture of catalysts allowed for one-step DME synthesis. CZA-C proved to be the most performant catalyst, attributed to its preparation method and composition, particularly the presence of magnesium, which increases stability and activity. Both zeolites displayed similar outcomes, with HZSM-5 performing slightly better than HY.

An analysis of the experimental results for a kinetic study was conducted with the CZA-C + HZSM-5 mixture. Increasing the temperature favoured CO_2 conversion. Beyond 560 K, DME yield declined while CO yield continued to increase. Several coupled phenomena were observed at this temperature. Above 540 K, it was possible to exceed thermodynamic limit for DME yield while keeping CO yield below its thermodynamic limit, despite changing operating conditions. This was most noticeable in the first three experimental runs. The overshooting of thermodynamic equilibrium was linked to the presence of zeolite and the methanol dehydration reaction, specifically to the retention of water in the zeolite pores. A shift in the CO yield curve was evident above 540 K across all experiments. Elevated pressure, feed molar ratio (H_2/CO_2) and Gas Hourly Space Velocity (GHSV) positively impacted CO_2 conversion, methanol and DME yields. Considering the unexpected behaviour of GHSV in the reaction, catalyst deactivation of CZA-C and/or water adsorption on the zeolite were hypothesised for the development of the kinetic model.

A kinetic model was developed considering CO_2 hydrogenation to methanol, the Reverse Water Gas Shift (RWGS) reaction, and methanol dehydration to DME in a plug flow reactor. Kinetic parameters were estimated based on experimental data, incorporating catalyst deactivation.

The model used the Langmuir–Hinshelwood approach with one type of active site for methanol synthesis (adapted from Quezada, 2020 [1]) and a novel relationship for DME synthesis was ultimately proposed, building upon the work of Ortega et al., 2018 [2] based on the model of Klusáček & Schneider, 1982 [3]. Experimental results were explained using an irreversible reaction to better represent the catalyst tests carried out. The model effectively explained experimental observations and was validated through regression analysis.

The potential advantages of an Optimal Temperature Profile (OTP) reactor were assessed using the developed kinetic model. Simulations and optimisations confirmed that adjusting catalyst mass is more effective than decreasing feed flow rate to increase the residence time in enhancing conversion rates and combined DME and methanol production, but with potential heat flux implications. Therefore, balancing feed flow rate with catalyst mass is crucial for optimal performance. Our study showed that an OTP reactor operating at an inlet temperature of 539.15 K and 36 bar offers a minimal advantage in terms of CO_2 conversion over an isothermal fixed bed reactor but should offer a greater advantage considering the overall process. The combined DME and methanol production presented a better performance at the reactor output of 1263.80 $mol.h^{-1}$ over an isothermal reactor operated at 514.15 K and 36 bar. However, for a single reaction, better performance is achieved by using an OTP reactor.

Lastly, three OTP multi-tubular heat exchanger reactor configurations were evaluated. Reactors with variable heat transfer area or coolant temperature along the reactor length were deemed more industrially feasible than those with varying overall heat transfer coefficient. Based on existing multi-section heat exchangers, an OTP multi-tubular reactor with variable coolant temperature was simulated. It consisted of 958 tubes, each 11 meters in length and 0.04 meters of diameter, handling an inlet mass flow rate of CO_2 of 94677 $mol.h^{-1}$ (i.e. 100 $ton.d^{-1}$) distributed across the 958 tubes. The reactor achieved 34.18% CO_2 conversion and a combined methanol and DME production rate of 30.84 $mol.h^{-1}$ per tube at 36 bar and an inlet temperature of 531.15 K. CO_2 conversion and combined methanol and DME production approached equilibrium limits without recirculation. The economic assessment of examined reactor was beyond the scope of this investigation.

The findings presented in this PhD thesis contribute to the advancement of CO_2 hydrogenation research and provide a basis for future research.

5.2. Perspectives

Building upon the analogous results obtained with CZA-C+HZSM-5 and CZA-C+HY in this PhD thesis for one-step DME synthesis from CO_2 hydrogenation, extended experiments are recommended to evaluate the long-term performance of CZA-C+HY. Additionally, the lack of information in the literature regarding exceeding equilibrium DME yields and the shift in CO yield at temperatures up to 540 K in one-step DME synthesis necessitates further experimental investigation in this temperature range to elucidate these phenomena. Employing thermocouples along the reactor length would enable a detailed temperature profile analysis, verifying if there may exist any relation with thermal characteristics of the reactor. In these terms, the use of a larger reactor is recommended to prevent flow-related disturbances.

Furthermore, monitoring water adsorption by the zeolite throughout the reaction process would help for clarifying the unexpected GHSV behaviour. A comparative study of fresh and used catalysts (CZA + zeolite) might provide insights into this phenomenon. Additionally, analysing catalyst deactivation is critical to comprehend the decline in catalyst activity and/or yield over time for improving catalyst performance and longevity. Although this analysis was not conducted in the current investigation, it is strongly recommended for future studies.

Another point of discussion is the catalyst performance. Developing a catalyst aimed at eliminating CO by-product formation during the CO_2 hydrogenation is a crucial step towards process optimisation. Since this is an area of focus for chemists, we suggest leaving this subject in their hands for further investigation.

Since the developed kinetic model did not account for the reaction of CO hydrogenation to methanol, experiments with $H_2/(CO_2+CO)$ in the feed mixtures should be performed to evaluate the influence of this reaction on the system and how it might shift the proposed kinetic model.

For the development of a new reactor, further evaluations are required for a pilot unit with a 2D model of the Optimal Temperature Progression (OTP) reactor, which was assessed using our kinetic model for an industrial process handling 100 tonnes of CO_2. The model should consider the mass and energy balances in radial and axial coordinates. This would allow to calculate more accurately the new reactor behaviour considering the kinetics along the reactor length and the concentration of compounds across the reactor radius.

Reactor configuration optimisation is another area of interest. In the case of outlet recirculation, which can potentially enhance the conversion of CO_2 (even though we have already achieved conversion close to the equilibrium, about 30% without recirculation), the inlet optimal temperature for the OTP necessitates deeper assessment. Considering the results

of the minimisation method (*fminunc*) in Chapter 4, where the identification of the optimal inlet temperature implied, in most of the cases, an increment of temperature for the OTP; it would be beneficial to assess whether recirculating the outlet gases at a lower temperature, rather than a higher one (*while loop* method), is preferable due to the requirement for water condensation for separation in the process, which necessitates cooling the gases. A comprehensive economic analysis is needed to determine the most cost-effective approach, including evaluating the trade-off between lower inlet temperatures and slower reaction rates versus higher inlet temperatures and achieving same final performance.

The development and testing of a new reactor with variable surface area along the reactor length to follow the OTP and effectively manage heat removal is proposed. This reactor concept could be combined with low inlet temperatures and controlled coolant temperature variation. Exploring the integration of plate-shell heat exchangers, such as Alfa-Laval Packinox, into an OTP reactor design is also reasonable. Integrating a hydrophilic membrane into the OTP plate heat exchanger reactor to enhance performance could be of interest. A thorough techno-economic assessment is essential to evaluate the feasibility of these reactor concepts.

5.3. References

[1] M. J. Quezada, "Hydrogénation catalytique de CO_2 en méthanol en lit fixe sous chauffage conventionnel et sous plasma à DBD," Normandie Université, 2020.

[2] C. Ortega, M. Rezaei, V. Hessel, and G. Kolb, "Methanol to dimethyl ether conversion over a ZSM-5 catalyst: Intrinsic kinetic study on an external recycle reactor," *Chem. Eng. J.*, vol. 347, pp. 741–753, Sep. 2018, doi: 10.1016/j.cej.2018.04.160.

[3] K. Klusáček and P. Schneider, "Stationary catalytic kinetics via surface concentrations from transient data: Methanol dehydration," *Chem. Eng. Sci.*, vol. 37, no. 10, pp. 1523–1528, Jan. 1982, doi: 10.1016/0009-2509(82)80010-9.

6. Scientific Production

1. L. Duran Martinez, I. Pitault, I. Polaert, Optimisation de l'hydrogénation du CO_2 en Di-Méthyl-Ether par la conduite optimale de température du réacteur, Société Française de Génie des Procédés (SFGP), 15-17 October 2024. Oral.

2. L. Duran Martinez, I. Pitault, I. Polaert, Optimization of Temperature Profile for di-methyl ether synthesis by CO_2 hydrogenation, CAMURE12-ISMR11: 12th International Symposium on Catalysis in Multiphase Reactors and the 11th International Symposium on Multifunctional Reactors, 8-11 September 2024. Oral.

3. L. E. Duran Martinez, I. Polaert, I. Pitault, Amélioration de la conversion de CO_2 en molécules valorisables par la synthèse du DME : Expériences et modélisation cinétique, Société Française de Génie des Procédés (SFGP), 7-10 November 2022. Oral.

4. M. J. Quezada Feliz, L.E. Duran Martinez, A. Ledoux, I. Polaert, Carbon dioxide hydrogenation into methanol: from Cu/Zn catalyst pellets kinetics to process modelling, CHISA 2021: International Congress of Chemical and Process Engineering, 15-18 March 2021 (Virtual). Poster.

APPENDIX

Appendix A

Data and Equations for Transport Phenomena Calculations

A.1. Mass transfer limitation

The viscosity of the pure components has been calculated from the theory of Chapman and Enskog [1]:

$$\mu = \frac{26.69(MT)^{1/2}}{\sigma^2 \Omega_v} \tag{A.1}$$

where μ is the fluid dynamic viscosity ($Pa \cdot s$), M is the molecular weight ($g.mol^{-1}$), T is the temperature (K), σ is the hard-sphere or collision diameter (m) and Ω_v is the collision integral. Neufeld et al., 1972 [2] proposed an empirical equation to compute the collision integral:

$$\Omega_v = [A(T^*)^{-B}] + C[exp(-DT^*)] + E[exp(-FT^*)] \tag{A.2}$$

where $T^* = kT/\varepsilon$ (k is Boltzmann's constant and ε is the minimum of the pair-potential energy), $A = 1.16145$, $B = 0.14874$, $C = 0.52487$, $D = 0.77320$, $E = 2.16178$, and $F = 2.43787$.

Mixture viscosity (μ_m) was determined by the method of Wilke, 1950 [3]:

$$\mu_m = \sum_{i=1}^{n} \frac{y_i \mu_i}{\sum_{j=1}^{n} y_j \varphi_{ij}} \tag{A.3}$$

where,

$$\varphi_{ij} = \frac{\left[1 + \left(\mu_i/\mu_j\right)^{0.5} \left(M_j/M_i\right)^{0.25}\right]^2}{\left[8(1 + M_i/M_j)\right]^{0.5}} \tag{A.4}$$

y_i is the i component molar fraction.

The molecular diffusivity of the mixture (D_i) used in Eq. (3.13) to compute the Sherwood number was computed per the proposition of Fairbanks & Wilke, 2002 [4]:

$$D_{m,i} = \frac{1 - y_i}{\sum_{j \neq i} \frac{y_j}{D_{ij}}} \tag{A.5}$$

with

$$D_{ik} = \frac{0.00266T^{1.5}}{PM_{ij}^{0.5}\sigma_{ij}^2\Omega_D} \tag{A.6}$$

where,

$$\Omega_D = A/(T^*)^B + C/exp(DT^*) + E/\,exp(FT^*) + G/\,exp(HT^*) \tag{A.7}$$

with $T^* = kT/\varepsilon_{ij}$, $A = 1.06036$, $B = 0.15610$, $C = 0.19300$, $D = 0.47635$, $E = 1.03587$, $F = 1.52996$, $G = 1.76474$ and $H = 3.89411$.

where,

$$\varepsilon_{ij} = \left(\varepsilon_i \varepsilon_j\right)^{0.5} \tag{A.8}$$

$$\sigma_{ij} = \frac{\sigma_i + \sigma_j}{2} \tag{A.9}$$

In order to calculate Schmidt number in Eq. (A.7), density was computed by:

$$\rho = \frac{P\sum_{i=1}^{n} y_i M_i}{RT} \tag{A.10}$$

All gas properties were taken from Poling et al., 2001 [1] and they are available in Table A.1.

Table A.1 Gas properties [1].

Component	$\boldsymbol{M_i}$ $(\boldsymbol{g.mol^{-1}})$	$\boldsymbol{\varepsilon/k}$ $(\boldsymbol{K})$	$\boldsymbol{\sigma_i}$ (Å)
CO_2	44.01	195.2	3.941
CO	28.01	91.7	3.69
CH_3OH	32.04	481.8	3.626
CH_3OCH_3	46.07	395	4.307
H_2	2.02	59.7	2.827
H_2O	18.02	809.1	2.641
N_2	28.01	71.4	3.798

A.2. Heat transfer limitation

For the computation of Mears criterion, the heat transfer coefficient of fluid, h ($J.m^{-2} \cdot s^{-1} \cdot K^{-1}$), is given by:

$$h = \frac{Nu \cdot \lambda_m}{d_p} \tag{A.11}$$

where λ_m is the thermal conductivity of the gas mixture. Wassiljewa Equation proposed [1]:

$$\lambda_m = \sum_{i=1}^{n} \frac{y_i \lambda_{f,i}}{\sum_{j=1}^{n} y_j A_{ij}} \tag{A.12}$$

Mason and Saxena, 1958 [5] recommended:

$$A_{ij} = \frac{\varepsilon \left[1 + \left(\mu_i/\mu_j\right)^{0.5} \left(M_j/M_i\right)^{0.25}\right]^2}{\left[8(1 + M_i/M_j)\right]^{0.5}} \tag{A.13}$$

The authors suggested $\varepsilon = 1.065$, Poling et al., 2001 [1] mentioned that Tandon and Saxena in 1965 proposed $\varepsilon = 0.85$. Accordingly, Poling et al., 2001 [1] considered $\varepsilon = 1$. In this work, $\varepsilon = 1$ has been assumed, thus $A_{ij} = \varphi_{ij}$.

λ_f is the vapor thermal conductivity of i component determined by means of values from the Design Institute for Physical Properties (DIPPR) of the American Institute of Chemical Engineers (AIChE) of implicated components calculated by [6]:

$$\lambda_{f,i} = \frac{C1T^{C2}}{1 + C3/T + C4/T^2} \tag{A.14}$$

the constants for the calculations are as follows:

Table A.2 Vapor Thermal Conductivity of Components ($W.m^{-1}.K^{-1}$) *[6].*

Component	C1· 10^{-4}	C2	C3	C4
CO_2	$3.69 \cdot 10^4$	−0.3838000	964.00	$1.86 \cdot 10^6$
CO	5.9882	0.6863000	57.13	501.92
CH_3OH	$5.80 \cdot 10^{-3}$	0.0341770	0	0
CH_3OCH_3	$5.9975 \cdot 10^2$	0.2667000	1018.60	$1.10 \cdot 10^6$
H_2	$2.6530 \cdot 10$	0.7452000	12.00	0
H_2O	$6.20 \cdot 10^{-2}$	1.3973000	0	0
N_2	3.3143	0.7722000	16.32	373.72

Nusselt Nu dimensionless number was calculated by Kunii and Levenspiel [7]:

$$Nu = 2 + 1.8Re^{1/2}Pr^{1/3} \tag{A.15}$$

Prandtl Pr dimensionless number was determined by:

$$Pr = \frac{\mu_m C_{p,m} C_m}{\rho \lambda_m} \tag{A.16}$$

where C_m $(mol.m^{-3})$ is the concentration of the mixture and Cp_m $(J.mol^{-1}.K^{-1})$ is ideal gas heat capacity of the mixture, this last is calculated by,

$$Cp/R = a0 + a1 \cdot T + a2 \cdot T^2 + a3 \cdot T^3 + a4 \cdot T^4 \tag{A.17}$$

Values of constants are presented in the table below.

Table A.3 Ideal Gas Heat Capacities at 298.15 K ($J.mol^{-1}\,K^{-1}$) [1] .

Component	$a0$	$a1 \cdot 10^3$	$a2 \cdot 10^5$	$a3 \cdot 10^8$	$a4 \cdot 10^{11}$
CO_2	3.259	1.356	1.502	−2.374	1.056
CO	3.912	−3.913	1.182	−1.302	0.515
CH_3OH	4.714	−6.986	4.211	−4.443	1.535
CH_3OCH_3	4.361	6.07	2.899	−3.581	1.282
H_2	2.883	3.681	−0.772	0.692	−0.213
H_2O	4.395	−4.186	1.405	−1.564	0.632
N_2	3.539	−0.261	0.007	0.157	−0.099

A.3. References

[1] B. E. Poling, J. M. Prausnitz, and J. P. (John P. O'Connell, *The properties of gases and liquids*. McGraw-Hill, 2001.

[2] P. D. Neufeld, A. R. Janzen, and R. A. Aziz, "Empirical Equations to Calculate 16 of the Transport Collision Integrals Ω(il, si)* for the Lennard-Jones (12–6) Potential," *J. Chem. Phys.*, vol. 57, no. 3, pp. 1100–1102, Aug. 1972, doi: 10.1063/1.1678363.

[3] C. R. Wilke, "A Viscosity Equation for Gas Mixtures," *J. Chem. Phys.*, vol. 18, no. 4, pp. 517–519, Apr. 1950, doi: 10.1063/1.1747673.

[4] D. F. Fairbanks and C. R. Wilke, "Diffusion Coefficients in Multicomponent Gas Mixtures," *Ind. Eng. Chem.*, vol. 42, no. 3, pp. 471–475, Mar. 2002, doi: 10.1021/IE50483A022.

[5] E. A. Mason and S. C. Saxena, "Approximate Formula for the Thermal Conductivity of Gas Mixtures," *Phys. Fluids*, vol. 1, pp. 361–369, 1958, doi: 10.1063/1.1724352.

[6] D. W. Green and R. H. Perry, "Perry's Chemical Engineers' Handbook," 2008. doi: 10.1036/0071422943.

[7] J. Villermaux, *Génie de la réaction chimique: conception et fonctionnement des réacteurs*, 2nd ed. Paris, 1993.

Appendix B

Effect of space time (τ) on the OTP

B.1. Changing feed flow rate

Table B.1 shows the established conditions to assess the effect of changing the feed flow rate, but with same molar ratio of $H_2/CO_2 = 3$. It is important to note that the catalyst mass (0.85 g), inlet temperature (563.15 K) and pressure (36 bar) remained the same in all cases. Figure B.1 illustrates the results of this optimisation, by maximising X_1.

Table B.1 Inlet conditions set to evaluate the effect of changing total feed flow rate for a feed molar flow ratio of $H_2/CO_2 = 3$, T=563.15 K and P=36 bar.

Exp.	F_{N2} $(mol.h^{-1})$	F_{H2} $(mol.h^{-1})$	F_{CO2} $(mol.h^{-1})$	Total $(mol.h^{-1})$	H_{bed} (cm)	τ (s)
1	0.009	0.059	0.020	0.087	6.26	25.00
2	0.031	0.210	0.070	0.311	6.26	7.00
3	0.072	0.488	0.163	0.723	6.26	3.00
4	0.217	1.465	0.488	2.170	6.26	1.00

Figure B.1 confirms that operating the reaction with a longer space time, τ, improves the conversion of CO_2 and reaction progresses X_1 and X_4. The highest CO_2 conversion and reaction progresses X_1, X_2 and X_4 were identified with $\tau = 25\ s$, being nearer to the equilibrium curve. However, as the space time increased, which meant a lower total feed flow rate, the combined production of methanol and DME diminished. Figure B.1e shows the lowest productivity at $\tau = 25\ s$.

Figure B.2 illustrates the conversion of CO_2, reaction progresses and production along the entire reactor. It is visible that X_2 with τ equal to 25 and to 7 seconds are very close at the output of the reactor. It is interesting to observe that when $\tau = 25\ s$, X_2 passes through a maximum and then descends very close to the output when $\tau = 7\ s$. The lowest results for the conversion of CO_2 to CO (X_2) were obtained at $\tau = 1\ s$. X_1, X_4, and X_{CO_2} display similar curve-shapes, but with different order of magnitude. The shorter space time ($\tau = 1\ s$) seems to be not sufficient for the reaction completion since conversion of CO_2 and reaction progresses are lower and there are more reactant molecules for the same amount of catalyst. Higher space time led to lower productivity and lower heat transfer per unit of wall surface area ($\dot{q_k}$). These are

associated with slower reaction rates and lower concentrations of reactants, allowing a more complete conversion of CO_2 into products of interest.

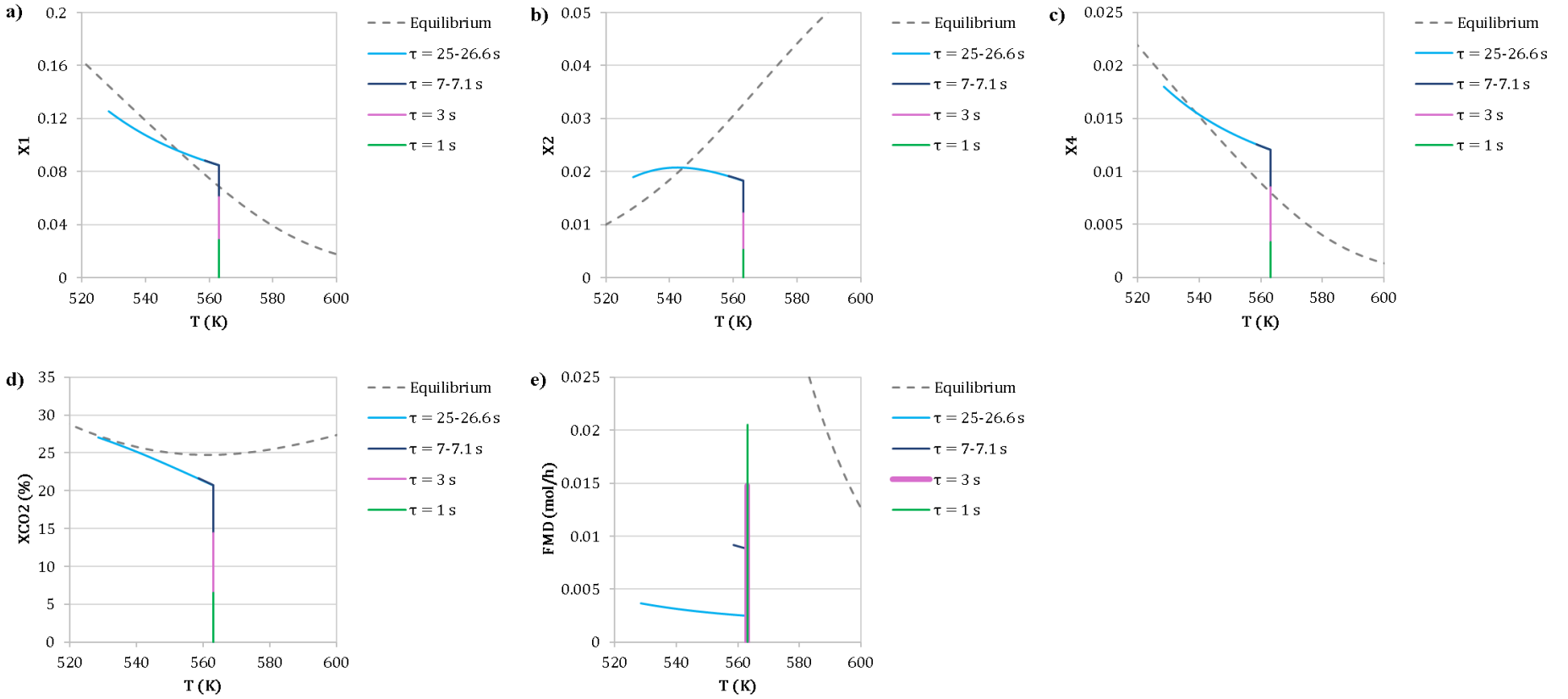

Figure B.1 Optimisation of X_1 at 563.15 K: Effect of space time (τ) vs temperature by varying the total feed flow rate from 0.091 – 2.013 mol.h^{-1} for $H_2/CO_2 = 3$ and P=36 bar at a fixed catalyst mass a) X_1, b) X_2, c) X_4, d) X_{CO2} and e) F_{MD}. Refer to Table B.1 for specific operating conditions.

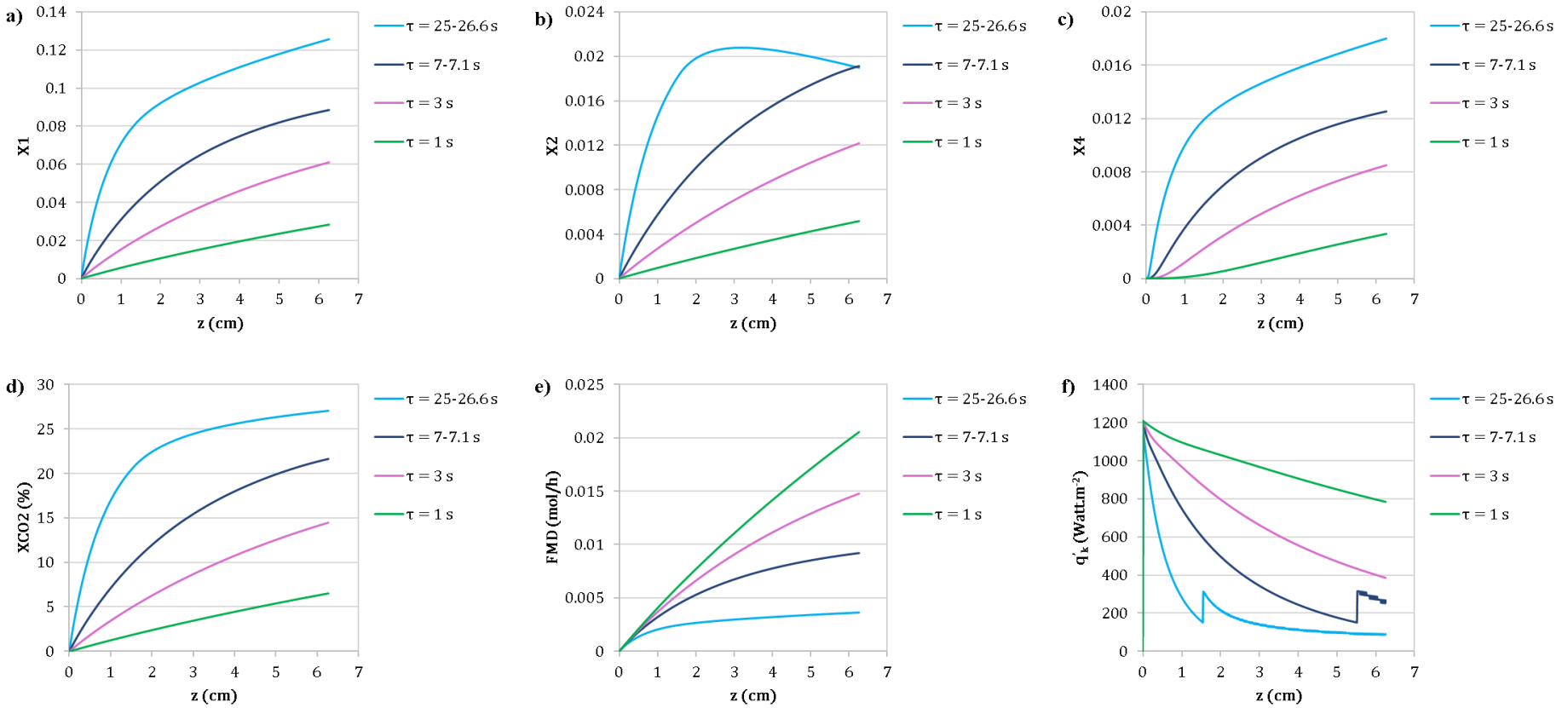

Figure B.2 Optimisation of X_1 at 563.15 K: Effect of space time (τ) along the entire reactor by varying the total feed flow rate from 0.09 – 2.01 mol.h^{-1} for $H_2/CO_2 = 3$, T=563.15 K and P=36 bar at a fixed catalyst mass a) X_1, b) X_2, c) X_4, d) X_{CO2}, e) F_{MD} and f) $\dot{q}_k$. Refer to Table B.1 for specific operating conditions.

B.2. Changing amount of catalyst mass

Table B.2 outlines the prescribed parameters for examining the influence of modifying the length of the catalyst bed, and thus the catalyst mass, while maintaining a constant molar ratio of $H_2/CO_2 = 3$. Under these conditions, the inlet temperature (563.15 K), pressure (36 bar), and feed flow rate (0.311 mol.h^{-1}) remained unchanged. The outcomes of this optimisation are displayed in Figure B.3.

Table B.2 Inlet conditions set to evaluate the effect of changing the length of catalyst bed for a feed molar ratio of $H_2/CO_2 = 3$, T=563.15 K and P=36 bar.

Exp.	F_{N2} $(mol.h^{-1})$	F_{H2} $(mol.h^{-1})$	F_{CO2} $(mol.h^{-1})$	Total $(mol.h^{-1})$	H_{bed} (cm)	τ (s)
1	0.031	0.210	0.070	0.311	22.36	25.00
2	0.031	0.210	0.070	0.311	6.26	7.00
3	0.031	0.210	0.070	0.311	2.68	3.00
4	0.031	0.210	0.070	0.311	0.89	1.00

Adjustment of the length of the catalytic bed led to identical conversion of CO_2 and reaction progresses as in the scenario where the total feed flow rate was modified (Figure B.3a, b, c, d identical to Figure B.1 a, b, c, d). Conversely, the maximum achievable production of methanol and DME was achieved at the maximum space time of $\tau = 25\ s$ (Figure B.3e) i.e. for a maximum quantity of catalyst. This can be explained by the fact that the same amount of reactant molecules has more catalyst surface to interact with, as the flow rate remained constant, but the catalyst mass was increased.

Figure B.4 shows the conversion of CO_2, reaction progresses and methanol and DME production across the entire reactor. It is observed that the lengthening of the reactor meant an improvement in conversion of CO_2, reaction progresses, combined methanol and DME production. The local heat flux ($\dot{q_k}$) at the reactor outlet was inferior for a longer catalyst bed ($\tau = 25\ s$).

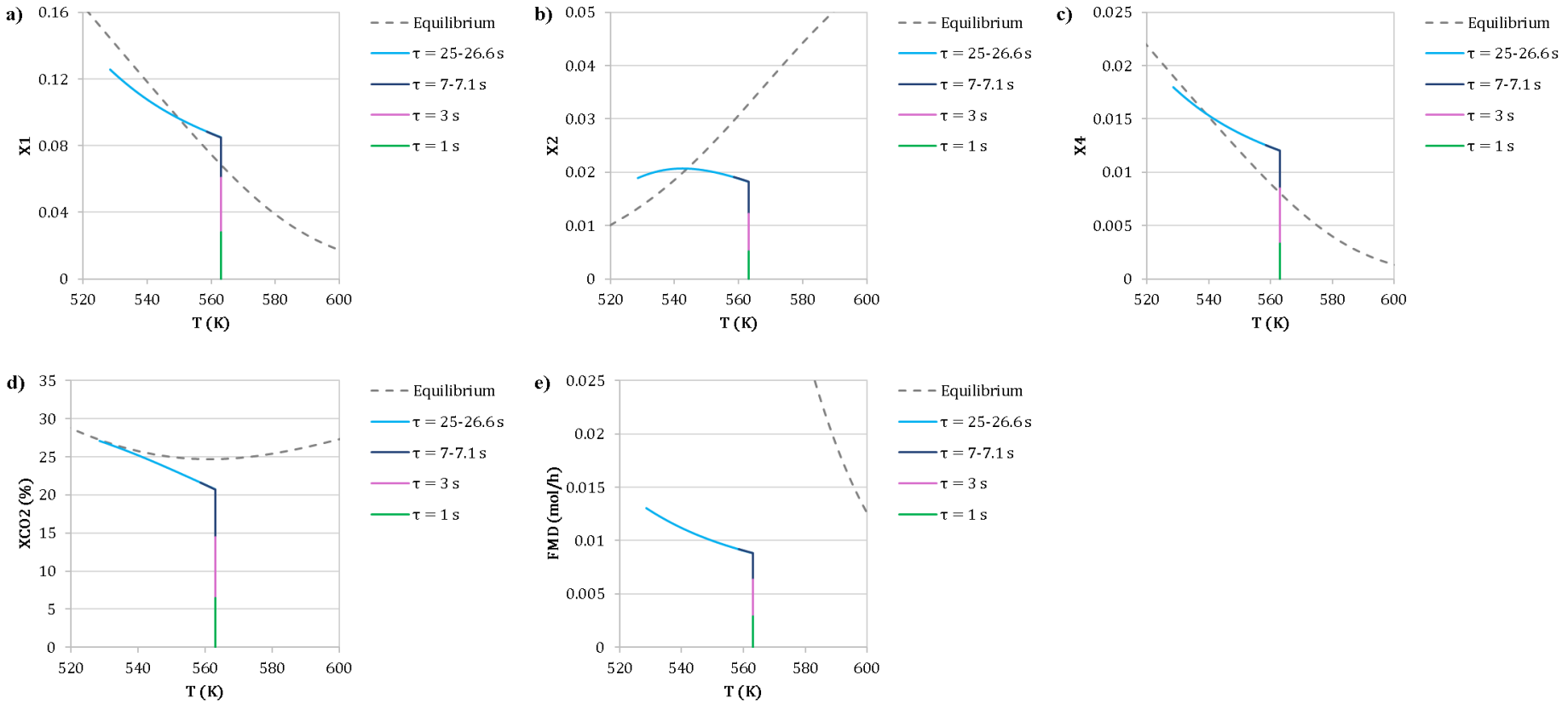

Figure B.3 Optimisation of X_1 at 563.15 K: Effect of space time (τ) along the entire reactor vs temperature by changing the length of catalyst bed (z) from 0.89 – 22.36 cm for $H_2/CO_2 = 3$, T=563.15 K and P=36 bar at a fixed molar flow a) X_1, b) X_2, c) X_4, d) X_{CO2} and e) F_{MD}. Table B.2 outlines the specific operating parameters.

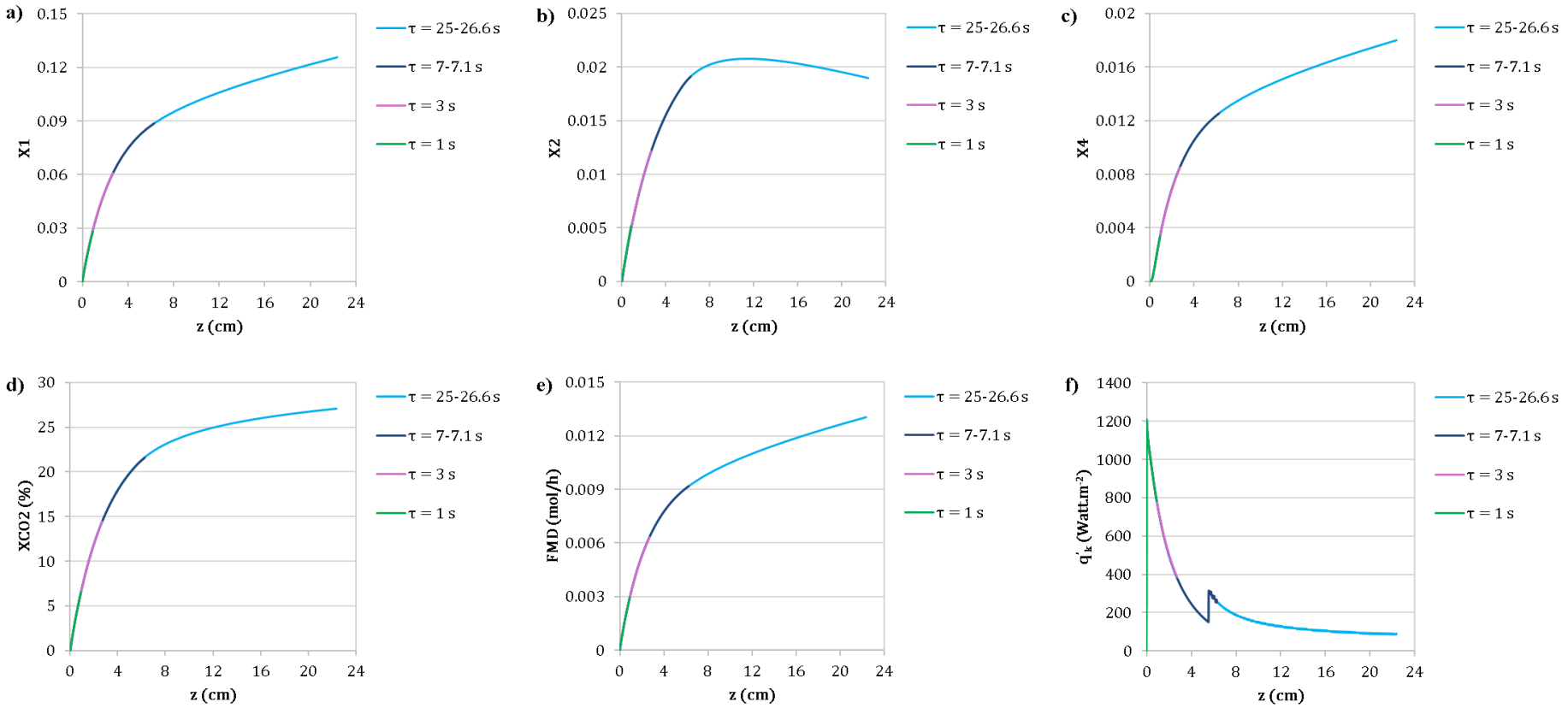

Figure B.4 Optimisation of X_1 at 563.15 K: Effect of space time (τ) along the entire reactor by changing the length of catalyst bed (z) from 0.89 – 22.36 cm for $H_2/CO_2 = 3$, T=563.15 K and P=36 bar at a fixed molar flow a) X_1, b) X_2, c) X_4, d) X_{CO2}, e) F_{MD} and f) q'_k. Table B.2 outlines the specific operating parameters.